Modelling the feeding process for aluminium production

Attila Kovács

Mansfield College

University of Oxford

A thesis submitted for the degree of

Doctor of Philosophy

Michaelmas 2020

Statement of Originality

All the work in this thesis has been done by the author, unless otherwise indicated. Chapter 2 has been published in as a journal paper Kovács et al. [50].

Abstract

In this thesis, we build and solve various mathematical models to describe the interplay between alumina particles and a cryolite bath that takes place in a Hall-Héroult cell, which is the foundational process for aluminium production. We aim to understand the heat and mass transfer mechanisms taking place in order to gather insights into the aluminium production process and use these insights to suggest process improvements.

First, we examine the problem of adding a cold alumina particle to a bath of hot cryolite. We develop a spherically symmetric model to describe heat and mass transfer between the particle and the surrounding material, allowing for freezing and melting of the cryolite close to the particle and its subsequent dissolution. We solve this model numerically using the method of lines using the early-time asymptotic solution to initiate the numerical scheme. We explore the behaviour as we vary the key dimensionless parameters. We also consider the model in the limits of small superheat and of small Stefan number. Using these asymptotic solutions, we find approximate expressions for the freezing, melting, and dissolution timescales, with freezing being the fastest effect and dissolution the slowest. Also, using the early-time solution, we determine constraints on the parameters for which shell growth is possible. Our results predict that increasing the superheat or decreasing the particle size should decrease the time it takes for a particle to dissolve, in accordance with practical experience. Furthermore, we note that the temperature changes are localised to a 5–10 particle radii.

Second, we formulate a one-dimensional model for the phase-changing infiltration into a porous alumina raft placed on top of the cryolite. We simplify our model in the limit of small superheat. We solve the equations using the same approach as in Chapter 2 with the method of lines, using the early-time asymptotic solution to initiate the numerical scheme. We find that the early-time problem can exhibit a stable and an unstable solution

and in certain parameter regions, these solutions disappear altogether. Furthermore, depending on the heat loss through the top of the raft, the model can undergo a discontinuous change in behaviour which corresponds to the clogging of the pore space. Additionally, near clogging, we find power-law behaviour of the frozen cryolite fraction and the location of the infiltration and solidification fronts.

Third, we formulate a model for the disintegration of a spherical clump of alumina particles. We solve the problem numerically with the method of lines and see that, for certain parameters, the solution behaves like a travelling dissolution front, while in other regimes there is bulk dissolution. We investigate the travelling dissolution front by using the method of matched asymptotic expansions to reduce the full problem. The asymptotic expressions match well with the numerical solutions up to the order that would be expected.

In Chapter 5 we formulate a model for the phase-changing infiltration into a spherical clump of alumina particles, which physically corresponds to a larger batch that is entirely enclosed by the cryolite. We find that many of the results in Chapter 3 carry over, such as the multiple solutions for early time, the late time clogging, or the fact that the phase-changing front is slower than the isothermal one. The presence of clogging in this model is especially interesting as it is caused by the slowing down of the front, as opposed to the cooling at the top, which was the case in Chapter 3.

Finally, we summarize the findings and offer possible extensions to our models in Chapter 6 and present our mathematical findings in an approachable way in Chapter 7. The alumina feeding is a process with many interacting parts producing complex behaviour. In this thesis we shed light on a few problems, but the research is not over.

Acknowledgements

There are many people whom I would like to thank for making this thesis happen and for being there for me during my years in Oxford. First and foremost, I thank my supervisors: **Chris Breward**, **Jim Oliver**, and **Andreas Münch**. They were always pushing me to be better, making me question everything, and at the same time, they were always being enthusiastic and helpful. I appreciate all of their hard work and guidance, during these years I've learned a lot from them.

I would also like to thank all my Norwegian supervisors: **Svenn-Anton Halvorsen**, **Ellen Nordgård-Hansen**, **Eirik Manger**, and **Kristian Einarsrud**, they were always enthusiastic about the project. I also thank my examiners: **Ian Hewitt**, **Ian Griffiths**, **Peter Howell**, and **Thomas Witelski** for all of their valuable suggestions.

I've met plenty of new and interesting people during my time in Oxford, most importantly the people of InFoMM, whom I also need to thank: **Colin**, **Jonathan**, **Laura**, **Amanda**, **Sarah**. I would also like to thank Cohort 3, you are the most awesome people I know: **Alissa**, **Ana**, **Clint**, **Fede**, **Jonathan**, **Joe**, **Kris**, **Mel**, **Ollie**, **Raquel**, **Scott**, and also **Helen**. We shared many good memories over these years and hopefully many more in the future. I want to thank my office mates: **Ferran**, **Ben**, **Hamza**, **Ellen** and **Mattie** for making the everyday work fun and engaging. I would also thank all the numerous students and professors of the university I came into contact with, I've learned a lot from you. I would also like to thank **Henrik** for being a good friend through all these years.

Last, but not least, I would like to thank my parents **Ágnes** and **József** for supporting me for all these years that I've spent learning about the world.

This work is supported by the EPSRC Centre For Doctoral Training in Industrially Focused Mathematical Modelling (EP/L015803/1) in collaboration with NORCE and Hydro Aluminium. Furthermore, this work is partly funded by SFI Metal Production, Centre for Research-based Innovation, 237738. Financial support from the Research Council of Norway and the partners of SFI Metal Production is gratefully acknowledged.

Contents

Chapter 1

Introduction

Synopsis

In this chapter we describe the Hall-Héroult process, which is the main aluminium-producing industrial process in the world. We then focus our attention on the addition of the raw material, alumina, into the production cell. We formulate industrially relevant questions and a plan for the different mathematical models that we will use to answer these questions.

Aluminium plays a big role in today's society, but it does not appear naturally in its pure state. In 1821, Pierre Belthier identified that bauxite ore could be used as a suitable raw material for making aluminium, and the first metallic form was produced in small amounts in 1825 by Hans Christian Ørsted [49]. Since the production of aluminium was difficult, at first it was mainly used for luxury goods such as sculptures and royal cutlery. More widespread use of aluminium had to wait until the late 19^{th} century, when Charles Martin Hall and Paul Héroult independently discovered a scalable electrolytic process for producing high purity aluminium from alumina. Since this process requires a large amount of electrical energy, production plants were built near large sources of cheap electricity, such as hydroelectric generators. This led to the aluminium industry forming close connections with energy companies. For example,

Hydro Aluminium, one of the industrial partners in this project, produces both energy and aluminium [41].

Aluminium has many advantageous properties. It has a high strength to density ratio, especially when alloyed with other metals, resulting in wide use in the aerospace industry where weight and strength are of utmost importance [56].

It is also a good conductor of both heat and electrical current and is used in the electronics industry for heat-sinks [53], and even for the thick conducting wires used in making aluminium. At the same time, aluminium is capable of low-temperature superconductivity and is used in the building of quantum computers [30, 101].

Aluminium can also be used for making mirrors and solar cells, due to its high reflectivity [1]. It forms an aluminium oxide layer when in contact with air which prevents further degradation [55], unlike steel which rusts. It has become a widely used material in the transportation industry as well because of its very good shock absorbance due to the ductility of aluminium [62, 87]. One of its most important properties that underlies aluminium's everyday use is that it is fully recyclable without any loss of quality.

Aluminium also has disadvantages, for example, even small-amplitude periodic loads can cause material failure, an effect known as fatigue [81]. Steel, on the other hand, has an apparent endurance limit, which means that if the amplitude of the load is smaller than half of the ultimate tensile strength, then the cycles that can be achieved are practically unlimited. Aluminium also has a lower melting point than most metals which makes it easier to produce and recycle, but also makes it more sensitive to heat loads.

The focus of our research is the Hall-Héroult process, which is widely used to make millions of tons of aluminium every year. However, due to the harsh temperature and chemical conditions inside a Hall-Héroult cell, experimental measurements are quite hard, a detailed description of the process is still not well known, and sophisticated

mathematical models are rarely employed to help understand the process. Our interest is on one particular aspect of the Hall-Héroult process, namely the feeding of alumina into the processing bath. The alumina is added at room temperature as solid particles[1] containing bound water and has to dissolve into a bath of electrolyte fluid, before the electrolytic processes turning alumina into liquid aluminium can take place.

The goal of the Hall-Héroult process (a schematic of a Hall-Héroult cell is shown in Figure 1.1) is to make aluminium (Al) from alumina (Al_2O_3) by using electrolysis [28, 33, 82]. Depending on the level of detail one wants to take, there are different ways of expressing the basic idea, but in general the electrochemical process can be summarized by two electrochemical reactions, one that occurs on the surface of the anode:

$$2\,Al_2O_3 + 12\,NaF + 3\,C \longrightarrow 12\,Na^+ + 12\,e^- + 4\,AlF_3 + 3\,CO_2, \tag{1.0.1}$$

and another one that occurs on the cathode

$$AlF_3 + 3\,e^- + 3\,Na^+ \longrightarrow Al + 3\,NaF. \tag{1.0.2}$$

Inside the electrolyte the conserved Na^+ ions carry the current. From these two balance equations we can see that the sodium ions are conserved in the system, so we can also write down an overall cell reaction as

$$2\,Al_2O_3 + 3\,C \longrightarrow 4\,Al + 3\,CO_2, \tag{1.0.3}$$

which summarizes that, in order to produce aluminium, the cell uses up both the alumina and the carbon of the anode and produces CO_2[2]. This means that the cell generates large amounts of greenhouse gases and also that, after some time, the anode

[1] The alumina particles can be comprised of γ-alumina or α-alumina, each of which has a different crystal structure.

[2] In fact, 1.4 kg of CO_2 for every kg of aluminium [82].

needs to be replaced. In recent years, there has been a huge endeavour to find different anode compositions that eliminate these disadvantages by using inert anodes [76]. For example, a good candidate material for an inert anode has been discovered in a joint cooperation between Alcoa, Rio Tinto and Apple, but they have not released any further details [19].

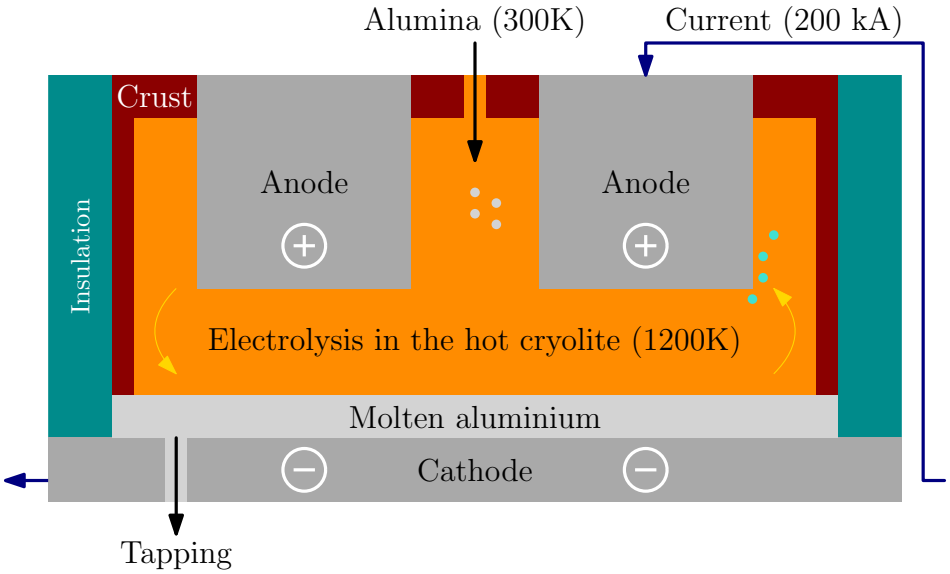

Figure 1.1: Schematic of a Hall-Héroult cell. The electrolyte fluid resides between the anode and the cathode. The molten aluminium product is collected on the cathode surface. The cell interior is bounded by a crust of solidified electrolyte and additional insulation.

In order for reactions (1.0.1) and (1.0.2) to work in the region between the anode and the cathode, the alumina needs to be dissolved into the electrolyte fluid. This fluid is a mixture of fluoride- and aluminium-based molten salts created by melting cryolite (Na_3AlF_6) with additional chiolite ($Na_5Al_3F_{14}$) along with small amounts of other materials that differ company by company. The electrolyte fluid inside an aluminium cell is usually called *a cryolite bath* or *molten cryolite*, but cryolite is not the only component. In general, the electrolyte is made of many different ionic species constantly reacting with each other [27]. The only cation is Na^+, but there are usually multiple anions such as AlF_4^-, AlF_3^-, F^-, as well as the oxofluoride species formed by the alumina dissolution, including $Al_2O_2F_4^{2-}$, $Al_2O_2F_6^{4-}$, and there is still debate on

exactly which ions make up the bath. One of the controversies is about the form of alumina in the bath, and whether it is in a molecular form or reacts with the bath to produce multiple different fluoride species [29, page 45]. A simplistic view that we will adopt is that the electrolyte fluid is made up of two different components, a substance that we will call cryolite that makes up the bulk of the fluid and a dilute alumina component.

If the electrolyte has a high enough concentration of alumina in the electrolysis region (usually around 3 % volume fraction), then it is observed that the process is stable, but both larger and smaller alumina concentrations are detrimental [29]. At low concentrations, a detrimental process, called the *anode effect* occurs. This is characterised by a large jump in the operating voltage of the cell, with the reaction at the anode adversely affecting the anode material and increasing wear by generating bubbles of harmful gases (e.g. CF_4, C_2F_6). The exact mechanism of the anode effect is not known, but in general it is viewed as a shift in the main reaction pathway from the desired one to an undesirable one [29]. If, however, the bath is saturated with alumina, the feeding is inefficient and the excess undissolved alumina can aggregate, sink to the bottom of the cell, contaminate the aluminium product, and form hard-to-dissolve sludge.

1.1 Feeding of alumina

In order to maintain a 3 % volume fraction of alumina in the electrolyte, a feeder mechanism is used which penetrates the crust of the molten electrolyte every few minutes (the top of the fluid usually freezes because the outside temperature is below the freezing temperature of the cryolite) and supplies a dose of alumina particles [51, 103] with mean radius on the order of 100 µm. The dose may penetrate into the liquid cryolite as individual particles or as clumps of particles, or can float on the

surface as rafts. Since the temperature of the alumina is low (slightly higher than room temperature) and the temperature of the cryolite is close to its melting point (5–10 K above), there is momentary local freezing of the cryolite over the surface of the dose. This local freezing can cause rafts to persist for a long time at the surface.

The falling of rafts through the molten aluminium is undesirable and when they settle at the bottom of the cell they are called sludge. Once the frozen cryolite layers have melted, the alumina dissolves (both melting and dissolution are rapid for a small particle and slow for agglomerates) and it is transported to the electrolysis region between the anode and the cathode by advection, diffusion, and with the bulk flow generated by multiple effects (e.g. bubbling, magnetohydrodynamical forces, buoyancy) with a velocity of several cm/s. We also note that the solid alumina particles and the rafts have a porous structure [60, 77], which may influence the dissolution reaction. We will look at this effect with more detail in Chapter 4. The feeding of alumina can be divided into the following stages (see Figure 1.2):

- **A**, falling of the granular dose in the air;
- **B**, impacting of the dose on the cryolite surface and subsequent agglomeration of particles, forming a floating *raft*;
- **C**, sinking of different types of agglomerates from the surface in the cryolite; and
- **D** and **E**, floating of alumina agglomerates on top of liquid aluminium with the possibility of sinking in the liquid aluminium to the bottom of the cell forming a *sludge*.

Each of the stages involve multiple different effects. In the following sections we will summarize the physical mechanisms and related research done for each of the stages.

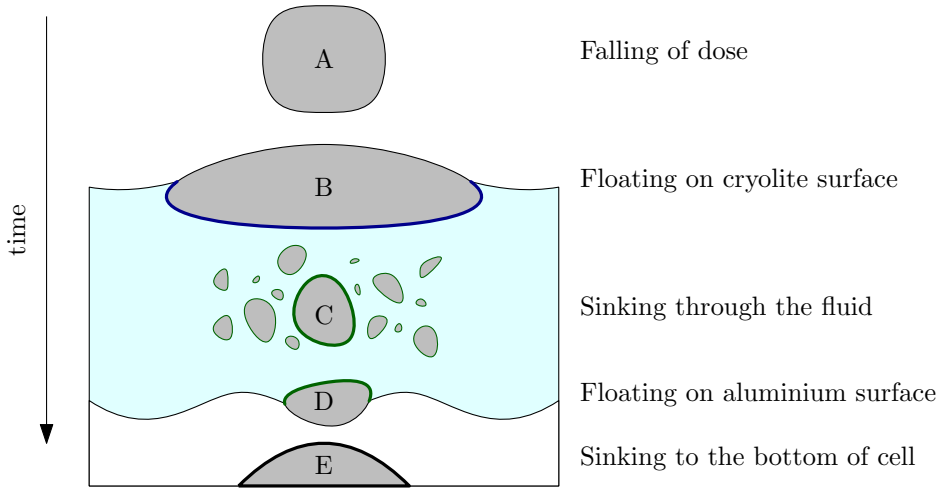

Figure 1.2: Chronology of the feeding process resulting in raft and sludge.

1.1.1 Falling

The first stage of the feeding of alumina is the *falling of a granular dose* after release under the influence of gravity and the convective air flow generated by temperature differences between the cryolite and the outside environment. This convective current influences the dispersion of the dose on the surface of the cell.

1.1.2 Rafting

In the second stage of the process, the *dose impacts on the surface of the fluid*. Here, there are at least three different interacting factors that affect the behaviour: the granularity of the dose, the chemical reaction between the particles and the electrolyte, and the huge temperature gradients between the particles and the fluid.

To study the effect of granularity, we need to know how a group of particles interact with each other and with the surface, what makes them float or sink [97], and how the fluid infiltrates between the particles. A similar problem in everyday life is the addition of chocolate powder onto the surface of a glass of milk. Without enough stirring, the powder can float on top of the milk for a considerable amount of time and, even if it breaks up, it often forms dry agglomerates enclosed in wet powder. The

floating of agglomerates has been investigated by Kaszás et al. [44, 45, 46] in a series of papers; they first investigate the flotation of a single spherical particle, then measure the infiltration rate for a solid disk-like porous alumina lump. Dassylva-Raymond et al. [9] set up a model for the alumina aggregate, which contains most of the effects that Walker [100] identifies in his measurements on aggregates, such as the phase change and infiltration of the cryolite, the γ-α phase change of alumina, and the amount of gas produced in the process. They analyse their moisture evolution model numerically and conclude that the model correctly predicts the frozen layer thickness on a single agglomerate and the mass of the alumina agglomerate when compared with Walker's measurements [100].

Another problem associated with this stage is the dissolution reaction between the particles and the electrolyte, and a key question is how fast the dissolution (the degradation of the structure) is compared to the infiltration (the flow of cryolite into the structure). Related problems in geoscience are, for example, the permeation of acid into a porous rock [36] or the melting of snow [61]. In the former, the mathematical model involves tracking the concentrations of soluble minerals and acid, while in the latter, the mathematical model involves equations describing the evolution of the volume fractions of ice, water and air along with the associated heat transfer problem. In the rafts formed in the Hall-Héroult process, there are four phases present: a porous matrix, frozen cryolite, liquid cryolite, and gas. Moreover, the frozen cryolite is not present when the particles are submerged and so heat transfer plays a crucial role in the evolution of the alumina particles. Thus it is difficult to translate the preexisting results.

While the most important reaction taking place is the dissolution of alumina into the cryolite, a side reaction between the cryolite and the bound water content of the particles also occurs instantaneously. This reaction releases gases, the effect of which is not well known, but might include the cracking of the particles, pushing particles

around, increasing pressure in an agglomerate, or decreasing the infiltration speed.

An added complication is that the bath is hot and the particles are cold, with temperature below the freezing temperature of the liquid cryolite. This causes liquid to solid phase change in the vicinity of the particles (or the rafts). This freezing behaviour is complicated because the bath consists of multiple components, each with their own melting points. This is shown by Lavoie, Taylor, and Metson [51] and Walker [100], who identify multiple infiltration fronts into an agglomerate of alumina of chiolite and cryolite by observing that the infiltration front temperatures coincide with the melting points of the chiolite and cryolite. The presence of any frozen layer surrounding particles or infiltrated into the raft inhibits the mass transfer of alumina into the bath by substantially reducing the dissolution rate. Nevertheless, the temperature of the bath causes the frozen material to eventually melt away, but this frozen material affects the initial infiltration behaviour. The particles themselves also undergo a crystal structure change that occurs at temperatures achieved during the infiltration process [100]. It is widely believed that γ–alumina contributes to the stability and cohesion of rafts, since it promotes the merging and bonding of the particles.

Since the freezing is rapid, nonequilibrium effects can also have a role in the process. A related problem is transient infiltration of liquid into a capillary tube, which has been investigated by numerous authors (e.g. [66, 67]). Another interesting related study has been done by Epstein [20], who investigates a growing freezing crust on the interface between two fluids. A more macroscale problem of this transient solidifying problem is presented by Bunk and King [7], who consider the spreading of basal melts and find various different solidification regimes depending on the parameters.

There have been several studies that explicitly focus on the feeding of alumina into the Hall-Héroult cell. Walker [100] studies the dissolution of alumina mainly experimentally, but also builds a simple model for the heat-transfer-controlled freezing.

In the experiments, he uses large spherical and cylindrical lumps of alumina powder and measures the temperature at different points of the lump. He observes that a frozen cryolite layer forms around the lumps and that this frozen layer behaves qualitatively as predicted by his simple model. He also shows that, even though there is a frozen layer, cryolite fluid still infiltrates into the specimen even before this frozen layer melts away. This suggests that the freeze layer is not impermeable, but is more like a mushy region [106], which is a region that contains multiple distinct phases of the same material. Another noteworthy observation is that some components of the fluid penetrate further into the aggregate than others, which he attributes to the fact that the two components have different liquidus temperatures and even when one of them freezes out of the mixture the other part can still penetrate. Finally he mentions that through the process the alumina material itself changes phase between α and γ-alumina, absorbing heat.

Østbø [72] investigates the effect of the phase change of the alumina from α- to γ-alumina when added to the cell and conducts a large number of experiments. The main conclusion that he draws is that the phase change of alumina has a big effect on the agglomeration behaviour: during phase change platelets (plate-like α-alumina structures) are generated and these grow together and make the particle agglomerate mechanically resistant to shear. He also shows that the agglomerate can break apart due to 'snowflaking', in which small parts of the raft separate and start to sink; this can be attributed to a loss of structural integrity of the raft at certain points.

Hofer [37] prescribes a flow and formulates a model for the evolution of alumina inside the cryolite liquid, consisting of a convection-diffusion equation for the concentration of the alumina and a population balance equation for the alumina particles and solves the problem numerically using finite elements, with the aim of optimizing the locations of the alumina feeding points. In his mathematical model, the particles are added straight into the population balance equation in the fluid with a given

distribution and neglecting the multitude of effects that occur on the surface. Thus the model does not consider rafts. This modelling framework has also been used by other authors to investigate various aspects of the Hall-Héroult cell [6, 18, 109].

1.1.3 Sinking

In the third stage of the process, either single particles or larger agglomerates (fully or partially infiltrated) sink through the cryolite fluid. The main processes taking place are the infiltration of fluid into the agglomerate, the dissolution of alumina particles, the sinking of the agglomerate, and the bulk liquid flow.

If the agglomerates have not been completely infiltrated before they become completely submerged, there will be gas trapped inside them. Subsequently, further infiltration will compress this gas, which will increase the pressure and hinder the infiltration. This effect is exacerbated by the production of additional gas due to a reaction between liquid cryolite and the bound water inside the alumina particles.

Experimental research on the feeding and dissolution of alumina particles in the Hall-Héroult process focuses on, for example, how the particle dissolution time depends on the bath concentration [90, 91], the size of the alumina particles [90], the initial heating of the particles [91], and the effect of stirring, which accelerates the dissolution by dispersing the alumina particles [34, 91].

The particle dissolution problem is well known in the scientific literature spanning many fields including pharmaceutics, where it is an important part of the drug delivery process [16, 57, 80], the metallurgical industry, where it is used to model corrosion [85], and environmental science, where it is used to model polymer dissolution [54, 115]. The dissolution reaction is dependent on difference between the (constant) concentration of alumina in the particles and the alumina dissolved in the liquid cryolite. The concentration of alumina dissolved in the liquid cryolite increases due to the dissolution reaction and evolves due to diffusion and the bulk fluid flow. The bulk fluid flow is

turbulent and is driven by the electric field, temperature variations in the bath, the upward flow of bubbles, and the downward flow of aggregates and particles [51]. If the spherical particles are small enough, they are convected with the bulk flow, while if they are larger, gravity will also be important. In a related area, Dierich and Nikrityuk [12] and Dierich, Nikrityuk, and Ananiev [13] present a model for the melting and freezing of a group of ice particles rising due to buoyancy in a fluid column which they explore using direct numerical simulation. They find that the particles shift from the wall to the centre of the column due to the Saffman force (a lifting force acting on a particle in a shearing viscous flow). In another related area, Gan, Feng, and Hu [26] build and solve a model for the sedimentation of hot and cold (compared to the fluid) particles in a fluid and they observe that, in their model, a group of cold particles disperse meanwhile a group of hot particles aggregate.

Of course, all these processes depends on the local temperature. The fluid flow is likely to break any local particle-based symmetries and generate asymmetric phase boundaries. Models involving asymmetric phase boundaries have been formulated for numerous physical situations, for example [10, 13, 26, 40, 71].

1.1.4 Sludging

The last stage involves the behaviour of agglomerates on top of the liquid aluminium. Depending on their size and velocity, they can either penetrate the surface of the liquid aluminium or float on the top. Severe problems are caused by penetration, since the dissolution process stops and there is no way of getting rid of the agglomerate, which is often called a *sludge*. A milder case is when the aggregate floats, which can contaminate the end product due to surface reactions and slow down the aggregate dissolution as the sludge/aluminium interface behaves differently than the sludge/electrolyte one. In a successful process, the alumina particles and clumps all dissolve before reaching the aluminium layer.

1.2 Material properties

Due to the extreme operating conditions of the cell, the material properties of the cryolite bath cannot be accurately measured and, in some cases such as the diffusivity of alumina in cryolite, there is no accurately known value. However, an order of magnitude assumption can be made by looking at similar materials. The melting point and the temperature of the cryolite are more accurately known; they depend on the composition of the bath so, depending on the exact cell type, these values can vary slightly. Since the solid alumina particles contain bound water (and probably some voids), the precise value of the alumina density depends on the source material and is less than that of pure alumina but more than that of cryolite, so the particles themselves tend to sink in the liquid. An overview of the best guesses for key material parameters can be found in Table 1.1.

1.3 Key questions and plan for the thesis

The key industrially questions that we are interested in answering are as follows.

- *How long does it take to dissolve an alumina dose completely and what controls the timescale?*
- *How much cryolite freezes during the process and how important is it?*
- *What parameters control whether a dose will aggregate or disperse?*
- *What parameters control whether a dose will float or sink?*

Our overarching aim is to build a mathematical model of *the feeding stage* that can inform the design of cells leading to the more efficient production of aluminium. In this thesis, we will investigate the behaviour of various agglomerates in, and on top of, the fluid.

In Chapter 2, we will start by investigating the behaviour of a single cold solid particle of alumina submerged in an unbounded cryolite bath. We will formulate a heat and mass transfer problem for a sphere including the phase-change of the cryolite and we will solve this model in two industrially relevant limits (small superheat, and small Stefan number). We will also solve the full model numerically and compare the behaviour with our asymptotic solutions.

In Chapter 3, we will change our focus and formulate a mathematical model for the phase-changing infiltration of a cold porous structure, in order to determine the expected behaviour of a raft floating on top of the liquid. We will investigate this problem in the relevant small-superheat limit and use asymptotics to solve for the early-time behaviour. Furthermore, we will solve the model numerically, and compare these with asymptotic solutions near clogging, that is, when the pore space becomes completely filled with frozen cryolite.

In Chapter 4 we will formulate a model for the diffusion-driven dissolution of a porous structure, in order determine how an alumina clump, that detaches from the main raft, dissolves while sinking in the cryolite. We will solve this model numerically and explore two qualitatively different behaviours, that emerge, namely bulk dissolution and travelling front solutions, both of which we will also investigate using asymptotics.

In Chapter 5 we investigate how an alumina clump behaves if it is placed into the cryolite bath quickly, so that gas is trapped inside. We will combine the models in Chapters 2 and 3 and investigate this model in three different limits. Our aim will be to determine how the presence of gas modifies the infiltration behaviour.

In Chapter 6 we will draw together our conclusions and discuss recommendations for future work, while in Chapter 7, we will summarize the results for an industrial perspective.

Parameter	Symbol	Value	Sources
Alumina			
initial temperature	T_A	373 K	[41]
melting temperature	T_m^A	2300 K	[2]
heat conductivity	k_a	4–16 W/(m K)	[2, 41]
specific heat capacity	c_p	1200 J/(kg K)	[2, 41]
density	ρ_p	2000–2500 kg/m^3	[41][29, p.47]
diffusivity in cryolite	D	1.5×10^{-9} m^2/s	[41]
far-field concentration	C_f	62 kg/m^3	[41]
saturation concentration	C_s	165 kg/m^3	[41]
Frozen cryolite			
melting point	T_m	1200–1230 K	[29, p.43][82, p.52]
heat conductivity	k_s	1.5 W/(m K)	[41]
specific heat capacity	c_s	1450 J/(kg K)	[41]
density	ρ_s	2090 kg/m^3	[41][29, p.54]
Molten cryolite			
bath temperature	T_c	1223–1243 K	[72, 100, 108]
heat conductivity	k_c	0.8 W/(m K)	[41]
specific heat capacity	c_c	1900 J/(kg K)	[42]
density	ρ_c	2070 kg/m^3	[29, p.45]
latent heat of solidification	L	530×10^3 J/kg	[41]
dynamic viscosity	μ_c	2.7×10^{-3} Pa s	[29, p.56]
Environment			
typical particle size	a	50×10^{-6} m	[41][29, p.65]
raft size	s	$0.1 \times 0.1 \times 0.05$ m	[41]
top temperature	T_{top}	1000 K	[41]
addition rate	Q	16×10^{-3} kg/s	[41]
porosity	ϕ	0.3–0.45	[47, T 2.1][29, p.66]
volumetric heat transfer	h	1×10^6 W/(m^3 K)	[48]

Table 1.1: Table showing the key material and physical parameters in the Hall-Héroult process.

Chapter 2

Solid alumina particle in a cryolite bath

Synopsis

In this chapter, we investigate the spherically symmetric dissolution of an initially cold alumina particle in a bath of molten cryolite. The cryolite initially freezes on the particle, forming a shell that must melt before the particle can dissolve. We derive asymptotic solutions valid in the limits of small-superheat and of small Stefan number. In the small-superheat limit, the evolution of the boundary exhibits a two-scale behaviour. In the small Stefan number limit, we find that the behaviour of a particle is limited by either the dissolution (in the case where the temperature differences are small) or by heat transfer (when both the latent heat is large and the temperature gradients are large). Our asymptotic predictions are validated by comparing with solutions found using a front-fixing numerical scheme that we initiate using the early-time asymptotics.

2.1 Introduction

We first focus on the simple problem of single, cold, solid alumina particle surrounded by liquid cryolite, as a paradigm for the feeding process where a single particle becomes

rapidly submerged. Our aim is to explore the freezing and subsequent melting of the cryolite around the particle and then its dissolution into the bath. This is contrast to previous studies, which focus on the dissolution of clumps of alumina particles. The low temperature of the feedstock compared to the bath, which is maintained only slightly above the melting point to save energy, leads to three distinct process stages in the single-particle case: first, some of the cryolite bath freeze into a shell around the particle; second, this shell melts; third, after the shell has vanished, the alumina particle dissolves into the cryolite. The first two stages are heat-transfer-driven phase changes and are observed in experiments in which porous alumina lumps are dropped onto the cryolite [100]. All three stages involve the motion of a free boundary.

Moving boundary problems are ubiquitous in many disciplines such as materials science, geosciences, biology, and even finance. There is a considerable amount of mathematical literature on spherically symmetric moving boundary problems dealing with bubble nucleation [78], bubble dissolution [15], and mass-transfer-controlled dissolution of an isolated sphere [16]. Due to its rich mathematical structure, the inward solidification of a suddenly cooled liquid sphere has also been extensively studied, for example, in [35, 58, 59, 73, 75, 84, 86]. Pedroso and Domoto [73] formulate a spherically symmetric model involving the temperature inside and outside the liquid sphere and the position of the freezing front. They utilize a small Stefan number approximation to formulate asymptotic solutions to the problem. However, their analysis breaks down as the freezing front approaches the centre of the sphere. By considering the region close to the centre of the sphere when freezing is nearly complete, this issue is rectified for early time in [75], and improved for later time in [86]. Similar issues arise in solidification problems in a cylindrical geometry, which was analysed in Soward [84], and for an N-dimensional sphere in Herrero and Velázquez [35]. In contrast to these one-phase models McCue, Wu, and Hill [59] included temperature evolution in both phases, leading to a two-phase Stefan problem which they analyse

in the small Stefan number limit to find approximate solutions for the movement of the boundary. Furthermore, Dewynne and Hill [11] investigates the integral forms of the equations to calculate bounds for the evolution of the radius. The coupling of heat transfer and liquid flow is investigated in Huppert [39], where the behaviour of a hot liquid flowing over a cold solid plane is analysed.

The paper most relevant to our analysis is Ehrich, Yun-Ken, and Schwerdtfeger [17], in which the problem of a metal particle immersed in its melt is considered. They formulate a two-phase Stefan problem similar to our model, with the difference that the contribution of the melt is lumped into the boundary condition using Newton's law of cooling with a constant convective coefficient. We will comment on the differences and similarities as they arise. Our aim in this chapter is to formulate and solve a mathematical model to describe the freezing, melting and dissolution process for a single alumina particle, which is an essential building block for understanding alumina feeding and distribution in the Hall-Héroult process.

We will present the mathematical model in Section 2.2. We then nondimensionalise and analyse the thermal problem in Section 2.3 and present the analysis for the dissolution problem in Section 2.4. Finally, we summarise the results and present the conclusions in Section 2.5.

2.2 Mathematical model

We consider a spherically symmetric geometry in which a solid spherical alumina particle is immersed in a stationary cryolite bath. We suppose that the initial temperature, T_p^*, of the particle is much lower than the melting temperature, T_m^*, of the cryolite. The cryolite is initially at a temperature T_c^*, which is slightly higher than the melting temperature. Thus, a frozen shell of cryolite will form on the surface of the particle, which will then melt away as the temperature equilibrates. We neglect

bulk cryolite flow for simplicity and we also initially neglect the radial flow in the cryolite caused by the phase change during the freezing and melting stages, motivated by the small difference (1 %) in the densities between frozen and molten cryolite; we revisit this assumption in Section 2.5.2.

2.2.1 Thermal problem

We denote by t the time since the instantaneous immersion of the particle in the bath and by r the radial coordinate from the centre of the particle. We split the domain into three regions as shown in Figure 2.1: the solid alumina particle of radius a occupies $0 < r < a$; the frozen cryolite shell occupies $a < r < R(t)$, where $R(t)$ is the position of the interface between the frozen and unfrozen region; and finally the molten cryolite resides in $r > R(t)$.

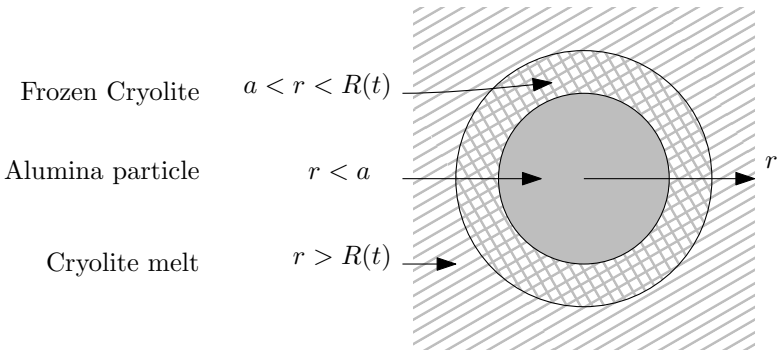

Figure 2.1: Geometry of the phase-change problem for a spherical particle of radius a with a frozen shell located at $a < r < R(t)$.

Conservation of heat energy and Fourier's law for heat conduction [32] give the governing equations in each region, namely

$$\rho_p c_p \frac{\partial T_p}{\partial t} = \frac{k_p}{r}\frac{\partial^2}{\partial r^2}(rT_p) \quad \text{in} \quad 0 < r < a, \tag{2.2.1a}$$

$$\rho_s c_s \frac{\partial T_s}{\partial t} = \frac{k_s}{r}\frac{\partial^2}{\partial r^2}(rT_s) \quad \text{in} \quad a < r < R(t), \tag{2.2.1b}$$

$$\rho_c c_c \frac{\partial T_c}{\partial t} = \frac{k_c}{r}\frac{\partial^2}{\partial r^2}(rT_c) \quad \text{in} \quad r > R(t), \tag{2.2.1c}$$

where $T_i(r,t)$ are the temperatures, ρ_i are the densities, c_i are the specific heat capacities at constant pressure, and k_i are the thermal conductivities; here $i \in \{p, s, c\}$, where p denotes the *particle*, s denotes the frozen *shell* of cryolite and c denotes the molten *cryolite*.

We assume that the temperature and the heat flux are continuous at the boundary between the particle and the frozen cryolite shell, so that

$$T_p = T_s, \quad k_p \frac{\partial T_p}{\partial r} = k_s \frac{\partial T_s}{\partial r} \quad \text{on} \quad r = a. \tag{2.2.2}$$

On the moving boundary between the frozen and molten cryolite, $r = R(t)$, we assume that the temperature is continuous and equal to the cryolite melting temperature T_m^*. We further assume that there is a jump in the thermal flux caused by the phase change. Thus, we write

$$T_s = T_c = T_m^*, \quad k_s \frac{\partial T_s}{\partial r} - k_c \frac{\partial T_c}{\partial r} = \rho_s L \dot{R} \quad \text{on} \quad r = R(t), \tag{2.2.3}$$

where L is the latent heat of solidification of the cryolite, which is assumed to be constant. The Stefan condition given in (2.2.3) is different from the condition used in [17], where they assume Newton's law of cooling at the edge of frozen cryolite rather than modelling the heat transfer in the liquid. We note that, by writing $T_s = T_p$ on $r = a$ and $T_s = T_c = T_m^*$ on $r = R(t)$, we are explicitly excluding situations where the initial temperature of the particle is above the melting temperature. In these situations, no frozen cryolite layer exists and we have to solve a different thermal problem coupled with the dissolution problem given in Section 2.2.2.

Finally, we assume that the temperature at the centre of the particle is finite, and that the temperature far away from the particle is given, so that

$$T_p \quad \text{bdd} \qquad \text{as} \quad r \to 0, \tag{2.2.4a}$$

$$T_c \to T_c^* \qquad \text{as} \quad r \to \infty, \tag{2.2.4b}$$

where T_c^* is the far-field cryolite temperature, which we note is normally a few degrees above T_m^*.

Initially, the temperatures in the particle and the cryolite are spatially homogeneous and there is no frozen shell so that the initial conditions are given by

$$T_p = T_p^* \quad \text{for} \quad 0 < r < a \quad \text{at} \quad t = 0, \tag{2.2.5a}$$

$$T_c = T_c^* \quad \text{for} \quad r > a \quad \text{at} \quad t = 0, \tag{2.2.5b}$$

$$R = a \qquad\qquad\qquad \text{at} \quad t = 0, \tag{2.2.5c}$$

where T_p^* is the initial temperature of the particle (slightly above room temperature). The equations (2.2.1)–(2.2.5) form a classical two-phase Stefan problem [3, 24, 59] in the cryolite, with an added region for the particle. We note that, in contrast, the model of [17] is a one-phase Stefan problem involving two domains (particle and shell). The key material and physical parameters are presented in Table 1.1.

We are interested in determining the thickness of the frozen shell. We define the freezing time, t_F, to be the time at which the thickness of the frozen shell is maximal, which we denote by R_F, and the melting time, t_M, to be the time at which the frozen shell has melted away to zero thickness. We are also interested in the time of complete dissolution of the particle, denoted by t_D. A schematic of the process, indicating the timescales, is shown in Figure 2.2. Our phase change model is only valid up to t_M, after which the frozen shell region and the moving boundary disappears. After t_M we have to solve a standard heat conduction problem in the particle and the cryolite and our interest turns to how the particle dissolves.

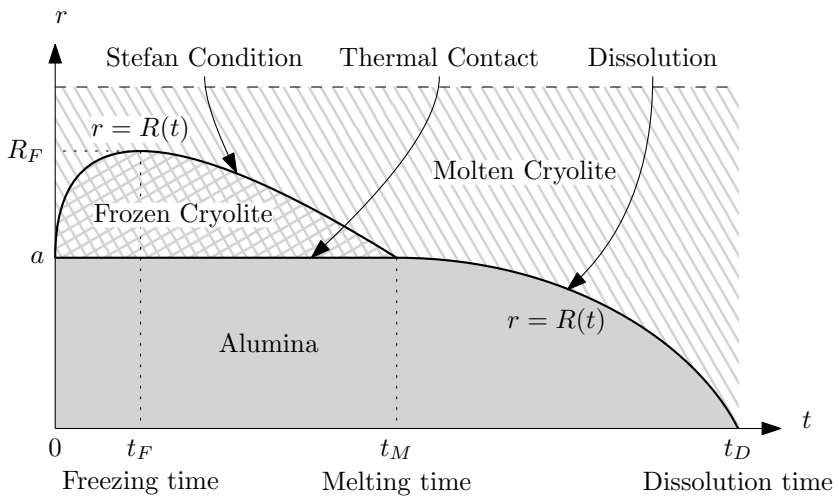

Figure 2.2: Schematic of the heat conduction and dissolution problems. The freezing model (in Section 2.2.1) is valid for $0 < t < t_M$, while the dissolution model (in Section 2.2.2) is valid for $t_M < t < t_D$. The maximum shell radius is denoted by R_F.

2.2.2 Dissolution problem

As soon as the frozen shell has melted, the behaviour of the particle is described by a well-known mass-transfer based problem. The pure dissolution of a particle has been investigated before by e.g. [15, 16], and here we summarise concisely the argument.

The alumina dissolved in the molten cryolite makes up about 3 % (by mass) of the bath, so we define the dilute concentration of alumina in the bath as $C(r,t)$ (with units $\mathrm{kg/m^3}$). Assuming spherical symmetry and that the transport of dissolved alumina is due to diffusion and advection, the governing conservation of mass equation is given by

$$\frac{\partial C}{\partial t} + \frac{1}{r^2}\frac{\partial}{\partial r}\left(r^2 u_r C - r^2 D \frac{\partial C}{\partial r}\right) = 0 \quad \text{in} \quad r > R(t), \tag{2.2.6}$$

where $u_r(r,t)$ is the radial velocity of the molten cryolite caused by the motion of the edge of the dissolving particle, and D is the alumina diffusivity in the molten cryolite. Assuming that the cryolite has constant density, conservation of mass implies that the velocity field in the molten cryolite satisfies

$$\frac{1}{r^2}\frac{\partial}{\partial r}\left(r^2 u_r\right) = 0 \quad \text{in} \quad r > R(t), \tag{2.2.7}$$

which can be immediately integrated to give

$$u_r = \frac{A(t)}{r^2}, \tag{2.2.8}$$

for some function $A(t)$, which we will determine later.

We note that, in this dissolution model, we include the velocity due to the movement of the boundary because the density difference between the alumina and the molten cryolite is substantial (see Table 1.1).

At the surface of the particle, we assume that the alumina in the cryolite is in thermodynamic equilibrium with the particle and that the concentration of alumina in the cryolite is equal to a given saturation concentration C_s. Far away from the particle, we also assume that the concentration is at a known value C_f. These conditions read

$$C = C_s \quad \text{on} \quad r = R(t), \tag{2.2.9}$$

$$C \to C_f \quad \text{as} \quad r \to \infty. \tag{2.2.10}$$

We note that, in general, the saturation concentration is a function of temperature. However, for simplicity we take it to be a constant.

We have two more conditions due to the moving boundary. They can be derived (see Scriven [78]) by considering conservation of total mass and alumina mass relative to the moving boundary, and are given by

$$(u_r - \dot{R})\rho_c = -\dot{R}\rho_p \quad \text{on} \quad r = R(t), \tag{2.2.11}$$

$$(u_r - \dot{R})C_s - D\frac{\partial C}{\partial r} = -\dot{R}\rho_p \quad \text{on} \quad r = R(t), \tag{2.2.12}$$

where ρ_c is the density of the molten cryolite, ρ_p is the density of the alumina particle, and $\dot{R} = \mathrm{d}R\,/\,\mathrm{d}t$. Solving (2.2.11) and (2.2.12) for the two unknowns, u_r and $\dot{R}$, we

obtain[1]

$$u_r = \dot{R}\left(1 - \frac{\rho_p}{\rho_c}\right) \quad \text{on} \quad r = R(t), \tag{2.2.13}$$

$$\dot{R} = \frac{D}{\rho_p(1 - C_s/\rho_c)}\frac{\partial C}{\partial r} \quad \text{on} \quad r = R(t). \tag{2.2.14}$$

Finally, the initial concentration in the bath and the position of the boundary are given by

$$C = C_f \quad \text{in} \quad r > a \quad \text{at} \quad t = t_M, \tag{2.2.15a}$$

$$R = a \quad \text{at} \quad t = t_M. \tag{2.2.15b}$$

Before proceeding, we use (2.2.13) to find $A(t)$ in (2.2.8) and hence the velocity distribution in the cryolite, which reads

$$u_r = \left(1 - \frac{\rho_p}{\rho_c}\right)\frac{R^2\dot{R}}{r^2}. \tag{2.2.16}$$

We see that, since the density of the particle ρ_p is greater than that of the cryolite, decreasing the radius induces outward flow.

2.3 Analysis of the thermal problem

2.3.1 Nondimensionalisation

We nondimensionalise (2.2.1)–(2.2.5) using the scalings

$$r = a\tilde{r}, \quad t = \frac{\rho_p c_p a^2}{k_p}\tilde{t}, \quad R = a\tilde{R}, \quad T_i = T_p^* + (T_c^* - T_p^*)\tilde{T}_i. \tag{2.3.1}$$

[1] We note that these conditions are valid even when the density of the molten cryolite is not uniform.

We note that the temperature scale is chosen so that the dimensionless temperature varies between 0 and 1 initially, while the time scale is chosen to be the diffusive time scale inside the particle. Dropping the tildes, the heat equations in (2.2.1) become

$$\frac{\partial T_p}{\partial t} = \frac{1}{r}\frac{\partial^2}{\partial r^2}(rT_p) \quad \text{in} \quad 0 < r < 1, \tag{2.3.2a}$$

$$\frac{\partial T_s}{\partial t} = \frac{\kappa_2}{r}\frac{\partial^2}{\partial r^2}(rT_s) \quad \text{in} \quad 1 < r < R(t), \tag{2.3.2b}$$

$$\frac{\partial T_c}{\partial t} = \frac{\kappa_3}{r}\frac{\partial^2}{\partial r^2}(rT_c) \quad \text{in} \quad r > R(t). \tag{2.3.2c}$$

The boundary and interface conditions (2.2.2), (2.2.3) and (2.2.4a) become

$$T_p = \mathrm{O}(1) \quad \text{as} \quad r \to 0, \tag{2.3.3a}$$

$$T_p = T_s, \quad \beta\frac{\partial T_p}{\partial r} = \frac{\partial T_s}{\partial r} \quad \text{on} \quad r = 1, \tag{2.3.3b}$$

$$T_c = T_s = \theta_m, \quad \frac{\partial T_s}{\partial r} - \nu\frac{\partial T_c}{\partial r} = \frac{\dot{R}}{\mathrm{St}} \quad \text{on} \quad r = R, \tag{2.3.3c}$$

$$T_c \to 1 \quad \text{as} \quad r \to \infty. \tag{2.3.3d}$$

The initial conditions (2.2.5) become

$$T_p = 0 \quad \text{in} \quad 0 < r < 1 \quad \text{at} \quad t = 0, \tag{2.3.4a}$$

$$T_c = 1 \quad \text{in} \quad r > 1 \quad \text{at} \quad t = 0, \tag{2.3.4b}$$

$$R = 1 \quad \text{at} \quad t = 0. \tag{2.3.4c}$$

The dimensionless parameters are given by

$$\kappa_2 = \frac{\rho_p c_p k_s}{\rho_s c_s k_p}, \quad \kappa_3 = \frac{\rho_p c_p k_c}{\rho_c c_c k_p}, \quad \theta_m = \frac{T_m^* - T_p^*}{T_c^* - T_p^*}, \tag{2.3.5}$$

$$\beta = \frac{k_p}{k_s}, \qquad \nu = \frac{k_c}{k_s}, \qquad \mathrm{St} = \frac{\rho_p c_p (T_c^* - T_p^*) k_s}{\rho_s k_p L}. \tag{2.3.6}$$

Here, κ_2 is the ratio of the thermal diffusivities of the frozen cryolite and the solid alumina, κ_3 is the ratio of the thermal diffusivities of the molten cryolite and the solid alumina, θ_m is the dimensionless melting temperature of the cryolite, β is the ratio of the thermal conductivity of alumina to that of the frozen cryolite, ν is the ratio of the thermal conductivity of the molten cryolite to that of the frozen cryolite, and St is the Stefan number, which is the ratio of the heat required to warm up a unit volume of cryolite from the particle temperature to the cryolite temperature to the heat required to change the phase of a unit volume of cryolite from liquid to solid.

Parameter	Sym.	Value
Diffusivity ratio	κ_2	0.074–0.37 (0.13)
Diffusivity ratio	κ_3	0.03–0.15 (0.05)
Melting temperature	θ_m	0.95–1 (0.98)
Conduction of particle	β	2.7–10.7 (7)
Conduction of melt	ν	(0.5)
Stefan number	St	0.19–0.95 (0.34)
Dissolution number	σ	0.05
Density ratio	ρ_r	0.97–1.2 (1.1)

Table 2.1: Dimensionless parameters, and ranges of values, with mean physical properties written in parentheses, calculated from Table 1.1.

The typical values for each dimensionless parameter are given in Table 2.1, calculated using the data in Table 1.1. We see that the Stefan number and the diffusivity ratios, κ_2 and κ_3, are small, while the dimensionless melting temperature θ_m is close to 1.

We will consider three different scenarios. First, we will investigate the model as $t \to 0$ to gain insight into the early-time behaviour and derive an appropriate initial condition with which to initiate our numerical scheme. We will then use asymptotic analysis to explore the small superheat limit ($\theta - 1 \ll 1$), and the small Stefan number limit ($\mathrm{St} \ll 1$).

2.3.2 Early-time behaviour

Anticipating that, for early-time, the frozen shell is thin and that temperature changes will be restricted to small regions near the interfaces, we seek an asymptotic self-similar solution of the form

$$T_i \sim f_i(\eta), \quad R \sim 1 + 2\lambda\sqrt{t}, \tag{2.3.7}$$

where $\eta = (r-1)/2\sqrt{t} = \mathrm{O}(1)$ as $t \to 0^+$, and λ is a constant. At leading order as $t \to 0$ the Stefan problem (2.3.2)–(2.3.4) reduces to the similarity formulation given by

$$f_p'' + 2\eta f_p' = 0 \quad \text{in} \qquad \eta < 0, \tag{2.3.8a}$$

$$f_s'' + \frac{2\eta}{\kappa_2} f_s' = 0 \quad \text{in} \quad 0 < \eta < \lambda, \tag{2.3.8b}$$

$$f_c'' + \frac{2\eta}{\kappa_3} f_c' = 0 \quad \text{in} \qquad \eta > \lambda, \tag{2.3.8c}$$

with boundary conditions

$$f_p \to 0 \qquad \text{as} \quad \eta \to -\infty, \tag{2.3.9a}$$

$$f_p = f_s, \quad \beta f_1' = f_2' \qquad \text{on} \quad \eta = 0, \tag{2.3.9b}$$

$$f_s = f_c = \theta_m, \quad f_2' - \nu f_3' = \frac{\lambda}{\mathrm{St}} \quad \text{on} \quad \eta = \lambda, \tag{2.3.9c}$$

$$f_c \to 1 \qquad \text{as} \quad \eta \to \infty. \tag{2.3.9d}$$

We note that the boundary conditions (2.3.9a) and (2.3.9d) follow from matching with outer regions (away from the inner boundary layer regions near $r = 1$) in which T_p and $T_c - 1$ are exponentially small as $t \to 0$. The solution to (2.3.8)–(2.3.9) is given by

$$f_p(\eta) = \theta_m \frac{1 + \operatorname{erf}(\eta)}{1 + \sqrt{\kappa_2}\beta \operatorname{erf}\left(\lambda/\sqrt{\kappa_2}\right)}, \tag{2.3.10a}$$

$$f_s(\eta) = \theta_m \frac{1 + \sqrt{\kappa_2}\beta \operatorname{erf}\left(\eta/\sqrt{\kappa_2}\right)}{1 + \sqrt{\kappa_2}\beta \operatorname{erf}\left(\lambda/\sqrt{\kappa_2}\right)}, \tag{2.3.10b}$$

$$f_c(\eta) = \frac{(\theta_m - 1)\operatorname{erf}\left(\eta/\sqrt{\kappa_3}\right) + \operatorname{erf}\left(\lambda/\sqrt{\kappa_3}\right) - \theta_m}{\operatorname{erf}\left(\lambda/\sqrt{\kappa_3}\right) - 1}, \tag{2.3.10c}$$

in $\eta < 0$, $0 < \eta < \lambda$ and $\eta > \lambda$, respectively, with the Stefan condition (2.3.9c) providing a transcendental equation for λ, which we write as

$$\lambda = \frac{\mathrm{St}\beta\theta_m}{\sqrt{\pi}} \left(\frac{\mathrm{e}^{-\lambda^2/\kappa_2}}{1 + \beta\sqrt{\kappa_2}\operatorname{erf}\left(\lambda/\sqrt{\kappa_2}\right)} - \frac{\nu(1-\theta_m)}{\beta\theta_m\sqrt{\kappa_3}} \frac{\mathrm{e}^{-\lambda^2/\kappa_3}}{1 - \operatorname{erf}\left(\lambda/\sqrt{\kappa_3}\right)} \right). \tag{2.3.11}$$

We require λ to be positive for the boundary to move outwards initially. This places a restriction on the possible parameter values for which freezing is possible. From (2.3.11) we find that $\lambda > 0$ if

$$\frac{\sqrt{\kappa_3}\beta\theta_m}{\nu(1-\theta_m)} > 1. \tag{2.3.12}$$

In the limit $\mathrm{St} \to 0$, equation (2.3.11) gives

$$\lambda \sim \mathrm{St}\frac{\beta\theta_m}{\sqrt{\pi}} \left(1 - \frac{\nu(1-\theta_m)}{\sqrt{\kappa_3}\beta\theta_m} \right). \tag{2.3.13}$$

We will compare this prediction with the small-t limit of a small-St asymptotic solution in Section 2.3.5.

In the limit $\mathrm{St} \to \infty$, we find that $\lambda \to \lambda_\infty$, where λ_∞ is the unique positive root of the equation

$$\frac{\beta\theta_m\sqrt{\kappa_3}}{\nu(1-\theta_m)} = \mathrm{e}^{-\lambda_\infty^2(1/\kappa_3 - 1/\kappa_2)} \frac{1 + \beta\sqrt{\kappa_2}\operatorname{erf}\left(\lambda_\infty/\sqrt{\kappa_2}\right)}{1 - \operatorname{erf}\left(\lambda_\infty/\sqrt{\kappa_3}\right)}, \tag{2.3.14}$$

and thus, in this limit, the interface speed is independent of St.

In Figure 2.3 we plot the left-hand side (blue) and the right-hand side (black) of

(2.3.14) as a function of λ_∞, using the parameter values given in Table 2.1. We see that the two curves intersect at one point, showing that there is a unique positive root at least for the physically relevant parameters values. We note that, when $\kappa_3 > \kappa_2$, the right-hand side increases monotonically from 1, so there will always be a solution in this case.

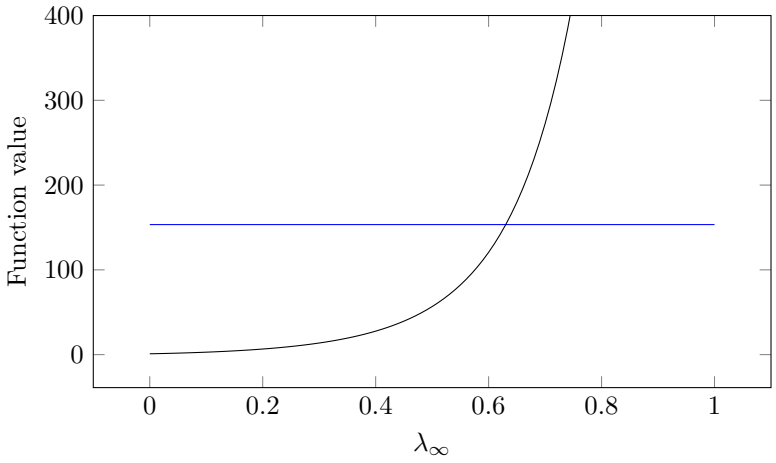

Figure 2.3: Graph of the left-hand side (blue) and the right-hand side (black) of (2.3.14). The two curves intersect at one point giving a unique positive root for the parameters $\beta = 7$, $\nu = 0.5$, $\kappa_2 = 0.13$, $\kappa_3 = 0.05$, and $\theta_m = 0.98$.

In Figure 2.4 (left) we show a representative early-time solution given by (2.3.10) and (2.3.11) for three different (early) times. We see that, as time increases, the temperature in the particle increases and the temperature in the molten cryolite decreases, as expected. We see that a "kink" develops in the temperature profile at the outer edge of the frozen shell because of the jump in the heat flux due to the latent heat requirement. In Figure 2.4 (right) we show how λ varies with the Stefan number and we compare the solution from (2.3.11) with the asymptotic solutions for small and large Stefan numbers given by (2.3.13) and (2.3.14), for three values of θ_m. We see excellent agreement in the appropriate limits.

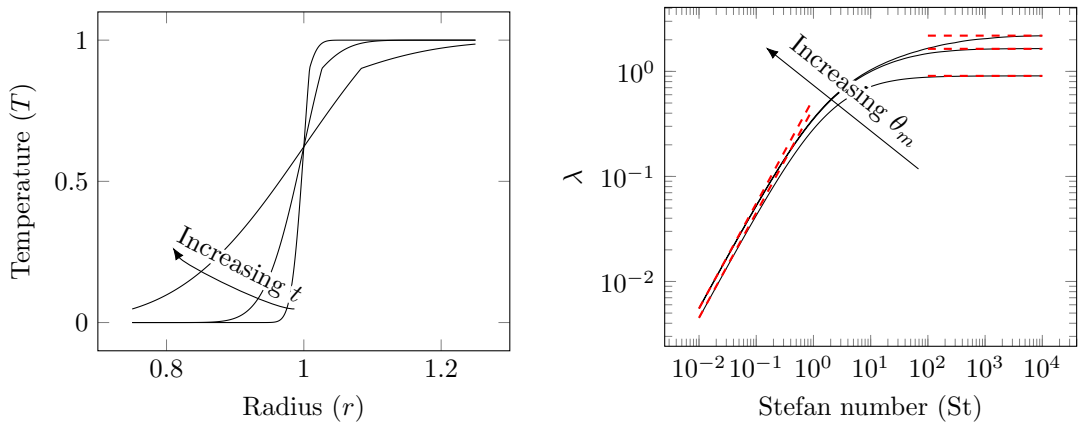

Figure 2.4: Left: Graph showing how the temperature varies with r, given by (2.3.10) and (2.3.11) for $t = 10^{-4}, 10^{-3}, 10^{-2}$. The kink denotes the position of the frozen shell. Right: Graph showing λ vs Stefan number given by (2.3.11) for three different $1 - \theta_m = 10^{-1}, 10^{-2}, 10^{-3}$ with all other parameters equal to 1. The red lines depict the solution given by (2.3.13) and (2.3.14).

2.3.3 Numerical results

We solve (2.3.2)–(2.3.4) numerically using method of lines. We apply boundary fixing transformations given by

$$r = 1 + \xi(R(t) - 1) \quad (0 < \xi < 1), \quad r = R(t) + \zeta \quad (\zeta > 0), \tag{2.3.15}$$

in regions $1 < r < R(t)$ and $r > R(t)$, respectively. Our spatial discretisation uses central differences and we solve the resulting system of nonlinear ODEs using `NDSolve` in `Wolfram Mathematica 12.1` with the inbuilt adaptive backward differentiation method in time. Since there is no frozen shell initially, we use the early-time asymptotic solutions given by (2.3.10) and (2.3.11) to resolve the initial behaviour and to start our simulation at a small, nonzero time (we choose $t = 10^{-4}$). We checked convergence in the usual manner by increasing the spatial resolution and decreasing the error tolerances.

To see the overall behaviour of the model we present results for a range of parameters (in Figures 2.5–2.9). Then, in Figure 2.10, we will present the behaviour for the typical

operating parameters given in Table 1.1. In Figure 2.5, we present the solution for the temperature T (left) and for the shell thickness R (right) in the case in which $\theta_m = 0.95$, with all other parameters set equal to unity. We see that a frozen shell immediately forms around the particle and that the particle heats up. We see that the cryolite is cooled slightly in a region close to the particle. We also see that the frozen shell thickness reaches a maximum and then begins to thin. When the shell has completely melted, the temperature in the particle is approximately constant.

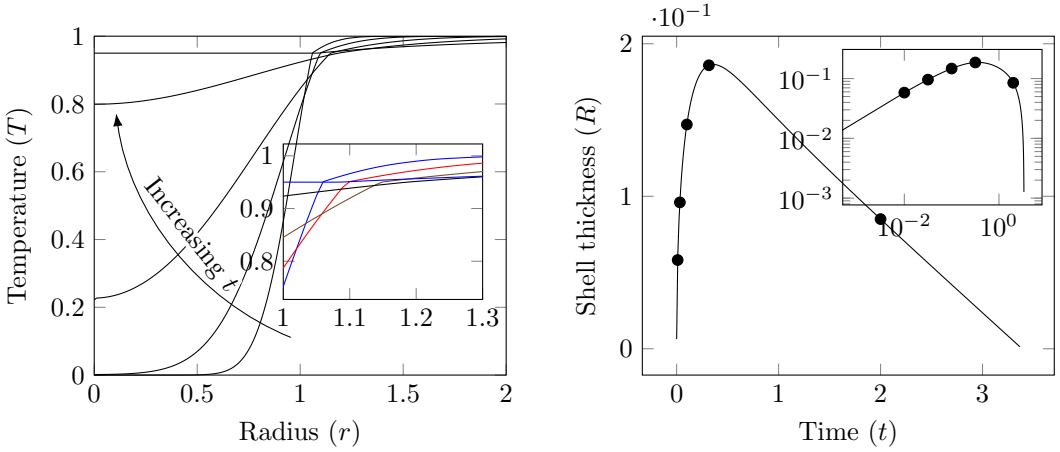

Figure 2.5: Left: Graph showing the temperature versus radius, given by solving (2.3.2)–(2.3.4) numerically at times $t = 10^{-2}, 10^{-1.5}, 10^{-1}, 10^{-0.5}, 2$. Right: Graph showing how the shell thickness varies with time. The points marked with a circle correspond to the curves in the temperature plot. $\theta_m = 0.95$; all other parameters set equal to 1. The inset in the left figure shows a zoom in near $r = 1$, meanwhile the inset in the right figure shows the boundary evolution on a logarithmic scale.

Next we examine the effect of varying the Stefan number. In Figure 2.6 (left) we show log-log plots of the frozen shell thickness varying in time for three different Stefan numbers. We note that, motivated by (2.3.63) which we will derive in Section 2.3.5, an appropriate scaled shell thickness is given by $3(R-1)/(\mathrm{St}\beta\theta_m)$, which bounds the scaled thickness by 1. We see that the numerical solutions converge to the small Stefan number solution in the appropriate limit, and that the early-time solution (2.3.10) and (2.3.11) holds for multiple decades. We see that there is a small increase in the scaled shell thickness as we decrease the Stefan number. However, since the scaled

shell thickness converges to some shape $F(t)$ as $\mathrm{St} \to 0$, the actual radius

$$R \sim 1 + \frac{1}{3}\mathrm{St}\beta\theta F \tag{2.3.16}$$

decreases as the Stefan number decreases, which motivates the investigation of the small Stefan number limit.

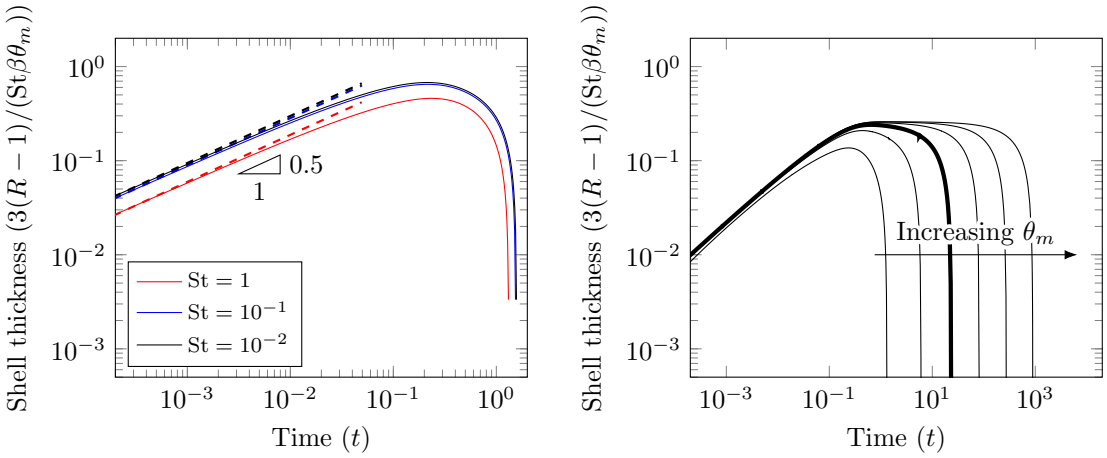

Figure 2.6: Left: Scaled shell thickness vs time. The solid lines show the numerical solutions given by (2.3.7) and (2.3.11) for $\mathrm{St} = 10^{-2}, 10^{-1}, 1$; the dashed lines represent the early-time solutions found in Section 2.3.2. Right: Scaled shell thickness as a function of time for different values of θ_m. The lines correspond to logarithmically distributed $1 - \theta_m$ values between 10^{-4} and 10^{-1}, with all other parameters set equal to 1. The thick black line corresponds to $\theta_m = 0.99$.

In Figure 2.6 (right), we see that increasing θ_m (the dimensionless melting temperature) significantly increases the melting time, introducing a two-timescale behaviour, namely rapid freezing followed by slow melting, and slightly increases the scaled shell thickness. In Figure 2.7, we see that decreasing ν has the same effect as increasing θ_m; meanwhile increasing β significantly increases both the thickness of the frozen shell and the melting time. Physically, these correspond to making the cryolite region non-conductive, decreasing the superheat, and making the particle very conductive, respectively.

Finally, we investigate the behaviour of the melting and freezing times, t_M and t_F,

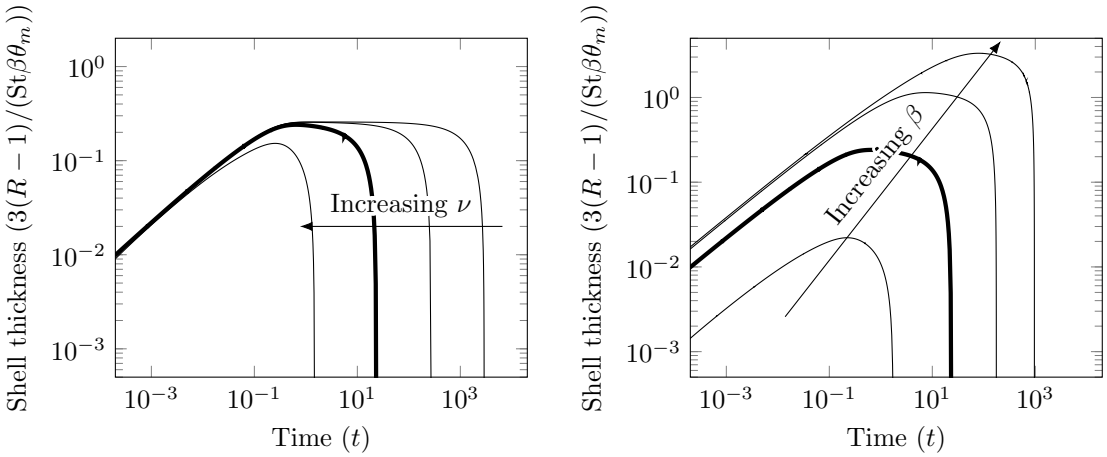

Figure 2.7: Graphs showing the shell thickness as a function of time for different β and ν values ranging from 10^{-2} to 10^2. $\theta_m = 0.99$, with all other parameters set equal to 1.

as θ_m changes for $\mathrm{St} = 1$. In Figure 2.8, we show graphs of the behaviour as $1 - \theta_m$ changes. We see that as $\theta_m \to 1^-$, the melting time t_M scales with $1/(1 - \theta_m)$ (shown as a dashed line in Figure 2.8 (left)). We note that the freezing time t_F depends only weakly on the superheat, which means that the freezing is governed mainly by the time it takes for the temperature to equilibrate inside the particle.

2.3.4 Small superheat limit

As noted earlier, the temperature in the bath is near to the melting temperature so that we can write $\theta_m = 1 - \varepsilon$, where $0 < \varepsilon \ll 1$. In this limit, motivated by the behaviour in Figure 2.6 (right), we expect the problem to separate onto two different timescales: the freezing timescale, in which $t = \mathrm{O}(1)$, and then the melting timescale, in which $t = \mathrm{O}(1/\varepsilon)$. In the limit $\varepsilon \ll 1$, we expand the dependent variables in powers of ε, and, on the freezing timescale, we have that $T_c^{(0)} = 1$ and that $T_p^{(0)}$ and $T_s^{(0)}$ satisfy the same problem as (2.3.2)–(2.3.4), but with $T_c^{(0)} = 1$ everywhere in $r > R(t)$. In general there is no analytical solution for this problem. However, we can make progress because we are mainly interested in the steady state the system achieves on

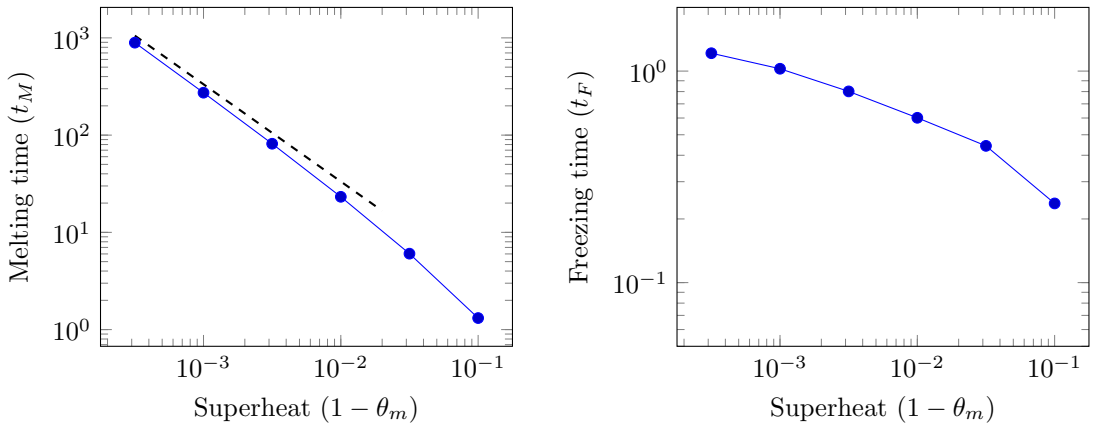

Figure 2.8: Left: Melting time as a function of the superheat. For small values the behaviour is $t \sim 1/(1-\theta_m)$ (dashed line). Right: Freezing time vs superheat. All other parameters are set equal to 1.

the freezing timescale so that we can match to the melting timescale. Crossing out the time derivatives in (2.3.2a) and (2.3.2b), we can solve for $\bar{T}_p$, $\bar{T}_s$, and R_F where bars denote the steady state versions of T_p, T_s, and R. By integrating the right-hand side of (2.3.2a) and (2.3.2b), and applying the boundary conditions (2.3.3) we deduce that, in steady state,

$$\bar{T}_p = 1 \quad \text{in} \quad 0 < r < 1, \quad \bar{T}_s = 1 \quad \text{in} \quad 1 < r < R_F, \tag{2.3.17}$$

which means that the particle and the shell heats up to the bath temperature, as we would expect intuitively. The leading-order boundary position, R_F, is determined using the total energy of the system. As described in [17] for a similar model, integrating (2.3.2a) and using (2.3.3a) gives[2]

$$\frac{\mathrm{d}}{\mathrm{d}t}\int_0^1 r^2 T_p^{(0)}\,\mathrm{d}r = \int_0^1 r^2 \frac{\partial T_p^{(0)}}{\partial t}\,\mathrm{d}r = \int_0^1 \frac{\partial}{\partial r}\left(r^2 \frac{\partial T_p^{(0)}}{\partial r}\right)\mathrm{d}r = \left.\frac{\partial T_p^{(0)}}{\partial r}\right|_{r=1}, \tag{2.3.18}$$

[2]We recall that $\frac{1}{r}\frac{\partial^2}{\partial r^2}(rT) = \frac{1}{r^2}\frac{\partial}{\partial r}\left(r^2\frac{\partial T}{\partial r}\right)$.

while integrating (2.3.2b) gives

$$\int_1^{R^{(0)}(t)} r^2 \frac{\partial T_s^{(0)}}{\partial t}\,\mathrm{d}r = \kappa_2 \int_1^{R^{(0)}(t)} \frac{\partial}{\partial r}\left(r^2 \frac{\partial T_s^{(0)}}{\partial r}\right)\mathrm{d}r = \kappa_2 \left(R^{(0)^2}\left.\frac{\partial T_s^{(0)}}{\partial r}\right|_{r=R^{(0)}} - \left.\frac{\partial T_s^{(0)}}{\partial r}\right|_{r=1}\right). \tag{2.3.19}$$

We use Leibniz rule to transform the left-hand side of (2.3.19), to get

$$\frac{\mathrm{d}}{\mathrm{d}t}\int_1^{R^{(0)}(t)} r^2 T_s^{(0)}\,\mathrm{d}r - \dot{R}^{(0)} R^{(0)^2}\left.T_s^{(0)}\right|_{r=R^{(0)}} = \kappa_2 \left(R^{(0)^2}\left.\frac{\partial T_s^{(0)}}{\partial r}\right|_{r=R^{(0)}} - \left.\frac{\partial T_s^{(0)}}{\partial r}\right|_{r=1}\right). \tag{2.3.20}$$

We multiply (2.3.18) by β and divide (2.3.20) by κ_2, and add the two equations and appeal to (2.3.3b) and (2.3.3c) (remembering that $T_c^{(0)} = 1$), to find that

$$\frac{\mathrm{d}}{\mathrm{d}t}\left[\beta \int_0^1 r^2 T_p^{(0)}\,\mathrm{d}r + \frac{1}{\kappa_2}\int_1^{R^{(0)}(t)} r^2 T_s^{(0)}\,\mathrm{d}r\right] = \dot{R}^{(0)} R^{(0)^2}\left(\frac{1}{\kappa_2} + \frac{1}{\mathrm{St}}\right), \tag{2.3.21}$$

which we solve along with the conditions (2.3.4a) and (2.3.4c) to give

$$\beta \int_0^1 r^2 T_p^{(0)}\,\mathrm{d}r + \frac{1}{\kappa_2}\int_1^{R^{(0)}(t)} r^2 T_s^{(0)}\,\mathrm{d}r = \frac{1}{3}\left(R^{(0)^3} - 1\right)\left(\frac{1}{\kappa_2} + \frac{1}{\mathrm{St}}\right). \tag{2.3.22}$$

As $t \to \infty$, $T_p^{(0)} \to 1$, $T_s^{(0)} \to 1$, and $R^{(0)} \to R_F$, and thus we find from (2.3.22) that the maximum radius, R_F, is given by

$$R_F = \sqrt[3]{1 + \beta \mathrm{St}}. \tag{2.3.23}$$

We note that the maximum shell size given by (2.3.23) is identical to that predicted in [17], which is to be expected since energy is conserved in both models. This solution is, however, only valid for $t \ll 1/\varepsilon$; on the timescale $t = \mathrm{O}(1/\varepsilon)$ the boundary shrinks due to heat transfer from the cryolite. To resolve this late-time behaviour, we introduce

the scalings

$$T_c = 1 - \varepsilon \hat{T}_c(r, \tau), \quad R = \hat{R}(\tau), \tag{2.3.24}$$

into (2.3.2)–(2.3.4) using the long timescale given by

$$\tau = t\varepsilon = \mathrm{O}(1). \tag{2.3.25}$$

Expanding the dependent variables in powers of ε, the leading-order problem for $\hat{T}_c$ is given by

$$0 = \frac{\kappa_3}{r}\frac{\partial^2}{\partial r^2}\left(r\hat{T}_c^{(0)}\right) \quad \text{in} \quad r > \hat{R}^{(0)}(\tau), \tag{2.3.26}$$

$$\hat{T}_c^{(0)} = 1 \quad \text{on} \quad r = \hat{R}^{(0)}(\tau), \tag{2.3.27}$$

$$\hat{T}_c^{(0)} \to 0 \quad \text{on} \quad r \to \infty, \tag{2.3.28}$$

$$\hat{R} = R_F \quad \text{at} \quad \tau = 0, \tag{2.3.29}$$

$$\frac{\partial \hat{R}^{(0)}}{\partial \tau} = \nu \frac{\partial \hat{T}_c^{(0)}}{\partial r} \quad \text{at} \quad r = \hat{R}^{(0)}(\tau), \tag{2.3.30}$$

where we have used the fact that $T_s^{(0)} = 1$ (because the particle and the shell temperature are already equilibrated on this longer timescale) in order to simplify (2.3.30). The leading-order problem can be solved readily to give

$$\hat{T}_c^{(0)} = \frac{\hat{R}^{(0)}(\tau)}{r}. \tag{2.3.31}$$

Substituting (2.3.31) into (2.3.30) gives the boundary evolution at long times as

$$\hat{R}^{(0)}(\tau) = \sqrt{R_F^2 - 2\nu\tau}; \tag{2.3.32}$$

which gives the melting time as

$$t_M \sim \frac{R_F^2}{2\varepsilon\nu} \quad \text{as} \quad \varepsilon = 1 - \theta_m \to 0^+. \tag{2.3.33}$$

Hence, we have an expression that is valid for calculating the melting time in the limit of small superheat. Since [17] do not consider superheat, they present no expression for the melting time t_M, though they do provide expressions in the large diffusivity limit and find that the radius decreases linearly with time.

2.3.5 Small Stefan number limit

In the small Stefan number limit, the thickness of the frozen shell is small (as is shown in Figure 2.6) because the interface speed found in (2.3.13) is O(St) as St $\to 0$ and the cryolite is hard to freeze in this limit. From the Stefan condition (2.3.3c), we see that, in this limit, R is constant at leading order. Thus, when St $\ll 1$, we introduce a local coordinate, $\bar{r}$, in the thin shell by defining

$$R = 1 + \mathrm{St}R^{(1)}, \quad r = 1 + \mathrm{St}\bar{r}. \tag{2.3.34}$$

Substituting (2.3.34) into (2.3.2)–(2.3.4) and assuming that the dependent variables can be expanded in the form $T_i \sim T_i^{(0)} + \mathrm{St}\, T_i^{(1)}$ as St $\to 0$, we find that conduction of heat across the frozen layer is dominant so that, at leading order,

$$\frac{\partial^2 T_s^{(0)}}{\partial \bar{r}^2} = 0 \quad \text{for} \quad 0 < \bar{r} < R^{(1)}, \tag{2.3.35}$$

with leading-order boundary conditions given by

$$T_s^{(0)} = \theta_m \quad \text{on} \quad \bar{r} = R^{(1)}, \quad \frac{\partial T_s^{(0)}}{\partial \bar{r}} = 0 \quad \text{on} \quad \bar{r} = 0. \tag{2.3.36}$$

The solution to (2.3.35) and (2.3.36) is simply

$$T_s^{(0)} = \theta_m, \tag{2.3.37}$$

i.e. the temperature through the frozen shell is equal at leading order to the melting temperature. To obtain an equation for the interface position, we have to consider the O(St) problem in the shell, which reads

$$\frac{\partial^2 T_s^{(1)}}{\partial \bar{r}^2} = 0 \quad \text{for} \quad 0 < \bar{r} < R^{(1)}, \tag{2.3.38}$$

with boundary conditions

$$T_s^{(1)} = 0 \quad \text{on} \quad \bar{r} = R^{(1)}, \tag{2.3.39}$$

$$\frac{\partial T_s^{(1)}}{\partial \bar{r}} = \beta \left.\frac{\partial T_p^{(0)}}{\partial r}\right|_{r=1} \quad \text{on} \quad \bar{r} = 0. \tag{2.3.40}$$

The solution for $T_s^{(1)}$ is

$$T_s^{(1)} = \beta \left.\frac{\partial T_p^{(0)}}{\partial r}\right|_{r=1} \left(\bar{r} - R^{(1)}\right), \tag{2.3.41}$$

and we see from (2.3.41) that the flux is preserved through the shell and so we can write (2.3.3c) as

$$\dot{R}^{(1)}(t) = \beta \left.\frac{\partial T_p^{(0)}}{\partial r}\right|_{r=1^-} - \nu \left.\frac{\partial T_c^{(0)}}{\partial r}\right|_{r=1^+}, \tag{2.3.42}$$

with

$$R^{(1)} = 0 \quad \text{at} \quad t = 0. \tag{2.3.43}$$

Thus, at leading order, the temperatures of the particle and cryolite bath are equal to the melting temperature at the boundary, which is linearised onto $R = 1$, while the flux of heat out of each of these regions controls the evolution of the thickness of the frozen shell.

2.3.5.1 Leading-order solution in the alumina particle

In the particle, the leading-order problem is given by

$$\frac{\partial T_p^{(0)}}{\partial t} = \frac{1}{r}\frac{\partial^2}{\partial r^2}\left(rT_p^{(0)}\right) \quad \text{in} \quad 0 < r < 1 \quad \text{for} \quad t > 0, \tag{2.3.44}$$

with the boundary and initial conditions given by

$$T_p^{(0)} \quad \text{bdd} \qquad \text{as} \qquad r \to 0 \quad \text{for} \quad t > 0, \tag{2.3.45a}$$

$$T_p^{(0)} = \theta_m \qquad \text{on} \qquad r = 1 \quad \text{for} \quad t > 0, \tag{2.3.45b}$$

$$T_p^{(0)} = 0 \qquad \text{in} \quad 0 \leq r \leq 1 \quad \text{at} \quad t = 0. \tag{2.3.45c}$$

Noting that $rT_p^{(0)}$ satisfies a one-dimensional problem in Cartesian variables, we use Fourier series theory to find that the solution is given by

$$T_p^{(0)}(r,t) = \theta_m \left(1 + 2\sum_{j=1}^{\infty} \frac{(-1)^j}{j\pi r} \sin(j\pi r) \mathrm{e}^{-j^2\pi^2 t}\right). \tag{2.3.46}$$

Hence, the heat flux at the boundary is given by

$$\beta \frac{\partial T_p^{(0)}}{\partial r}\bigg|_{r=1^-} = 2\beta\theta_m \sum_{j=1}^{\infty} \mathrm{e}^{-j^2\pi^2 t} \quad \text{for} \quad t < t < t_M. \tag{2.3.47}$$

The infinite sum is a strictly decreasing function of time, which tends to 0 as $t \to \infty$. As $t \to \infty$, $T_p^{(0)} \to \theta_m$ although we note that the solution is only physically relevant for $t < t_M$. For early-times, motivated by [59, Eq. 2.12] we use the transformation given by

$$w(z) = \sum_{n=1}^{\infty} \mathrm{e}^{-n^2\pi z}, \quad 1 + 2w(z) = z^{-1/2}(1 + 2w(1/z)), \tag{2.3.48}$$

to rewrite the right-hand side of (2.3.47) using the fact that it is equal to $2\beta\theta_m w(\pi t)$; hence as $t \to 0$, the heat flux is more conveniently written as

$$\beta \frac{\partial T_p^{(0)}}{\partial r}\bigg|_{r=1^-} = \beta\theta_m \left(-1 + \frac{1}{\sqrt{\pi t}} \left(1 + 2 \sum_{j=1}^{\infty} \mathrm{e}^{-j^2/t} \right) \right). \tag{2.3.49}$$

Thus, the leading-order behaviour of the heat flux at small times is given by

$$\beta \frac{\partial T_p^{(0)}}{\partial r}\bigg|_{r=1^-} \sim \frac{\beta\theta_m}{\sqrt{\pi t}} \quad \text{as} \quad t \to 0. \tag{2.3.50}$$

2.3.5.2 Leading-order solution in the molten cryolite

The leading-order problem for $T_c^{(0)}$ is given by

$$\frac{\partial T_c^{(0)}}{\partial t} = \frac{\kappa_3}{r} \frac{\partial^2}{\partial r^2} \left(r T_c^{(0)} \right) \quad \text{in} \quad r > 1 \quad \text{for} \quad t > 0, \tag{2.3.51}$$

with the following boundary and initial conditions

$$T_c^{(0)} = \theta_m \quad \text{on} \quad r = 1 \quad \text{for} \quad t > 0, \tag{2.3.52a}$$

$$T_c^{(0)} \to 1 \quad \text{as} \quad r \to \infty \quad \text{for} \quad t > 0, \tag{2.3.52b}$$

$$T_c^{(0)} = 1 \quad \text{in} \quad r \geq 1 \quad \text{at} \quad t = 0. \tag{2.3.52c}$$

This problem admits the similarity solution given by

$$T_c^{(0)}(r,t) = 1 + \frac{(1-\theta_m)\left(\operatorname{erf}\left(\frac{r-1}{2\sqrt{\kappa_3 t}} \right) - 1 \right)}{r}, \tag{2.3.53}$$

for $r > 1$ and $0 < t < t_M$.

The flux through the phase boundary $r = 1$ is

$$\nu \frac{\partial T_c^{(0)}}{\partial r}\ (1^+, t) = \nu(1-\theta_m) \left(\frac{1}{\sqrt{\kappa_3 \pi t}} + 1 \right) \quad \text{for} \quad t > 0. \tag{2.3.54}$$

Since all the parameters are positive and $\theta_m < 1$, the heat flux is positive for all time with

$$\nu \frac{\partial T_c^{(0)}}{\partial r}\ (1^+, t) \sim \nu \frac{1-\theta_m}{\sqrt{\kappa_3 \pi t}} \quad \text{as} \quad t \to 0. \tag{2.3.55}$$

In Figure 2.9, we show the temperature distributions in the particle and in the cryolite, found by solving (2.3.2)–(2.3.4), for various times while the frozen region exists. We see that the particle warms up and the cryolite cools, as expected from (2.3.46).

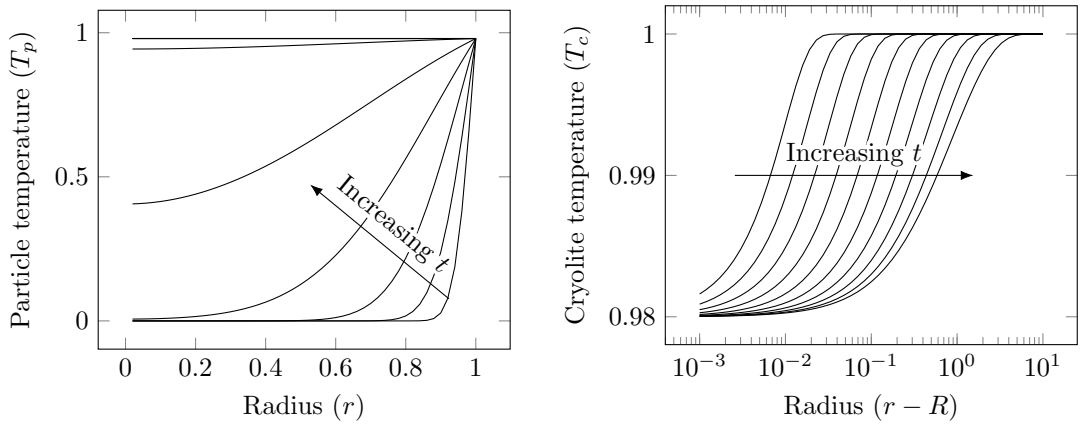

Figure 2.9: Graphs showing the temperature distribution in the particle given by (2.3.46) (left) and cryolite given by (2.3.53) (right) at different times (uniformly logarithmically distributed between $t = 10^{-3}$ and $t = 164$). The parameters are $\beta = 7$, $\nu = 0.5$, $\kappa_3 = 0.05$, and $\theta_m = 0.98$. Note that both figures have the same number of lines at the same times, but on the left multiple lines collapse onto the spatially uniform state.

We note that if we move away from the boundary by 5–10 particle diameters, the cryolite temperature is close to the undisturbed bath temperature. This suggests a critical length scale which distinguishes between well distributed and closely packed particles.

2.3.5.3 Motion of the freezing surface

Now that we have expressions for the fluxes, namely (2.3.49) and (2.3.54), we can substitute them into the Stefan condition (2.3.43), to find that

$$\dot{R}^{(1)}(t) = 2\beta\theta_m \sum_{j=1}^{\infty} \mathrm{e}^{-\pi^2 j^2 t} - \nu(1-\theta_m)\left(\frac{1}{\sqrt{\pi\kappa_3 t}} + 1\right). \tag{2.3.56}$$

We integrate (2.3.56) and apply the initial condition $R^{(1)} = 0$ to obtain

$$R^{(1)} = \beta\theta_m \left(\frac{1}{3} - 2\sum_{j=1}^{\infty} \frac{\mathrm{e}^{-\pi^2 j^2 t}}{\pi^2 j^2}\right) - \nu(1-\theta_m)\left(t + \frac{2\sqrt{t}}{\sqrt{\pi\kappa_3}}\right). \tag{2.3.57}$$

We plot $R^{(1)}(t)$ in Figure 2.10. We see that the frozen shell grows on a short timescale, reaches a maximum and then melts away again over a longer timescale. If we consider the special case $\theta_m = 1$, in which the bath is everywhere at the melting temperature, then the second term in (2.3.57) disappears and the liquid will freeze and form a shell which will grow until its thickness reaches $\beta/3$. Using (2.3.56) and (2.3.57), we find that the freezing time, t_F, and the melting time, t_M, are given implicitly by

$$0 = 2\beta\theta_m \sum_{j=1}^{\infty} \mathrm{e}^{-\pi^2 j^2 t_F} - \nu(1-\theta_m)\left(\frac{1}{\sqrt{\pi\kappa_3 t_F}} + 1\right), \tag{2.3.58}$$

$$0 = \beta\theta_m \left(\frac{1}{3} - 2\sum_{j=1}^{\infty} \frac{\mathrm{e}^{-\pi^2 j^2 t_M}}{\pi^2 j^2}\right) - \nu(1-\theta_m)\left(t_M + \frac{2\sqrt{t_M}}{\sqrt{\pi\kappa_3}}\right). \tag{2.3.59}$$

It is useful to rearrange the terms in (2.3.56) to further investigate the behaviour by writing

$$\frac{\dot{R}^{(1)}}{\beta\theta_m} = 2\sum_{j=1}^{\infty} \mathrm{e}^{-\pi^2 j^2 t} - \delta\left(\frac{1}{\sqrt{\pi\kappa_3 t}} + 1\right), \tag{2.3.60}$$

with

$$\delta = \frac{\nu(1-\theta_m)}{\beta\theta_m}. \tag{2.3.61}$$

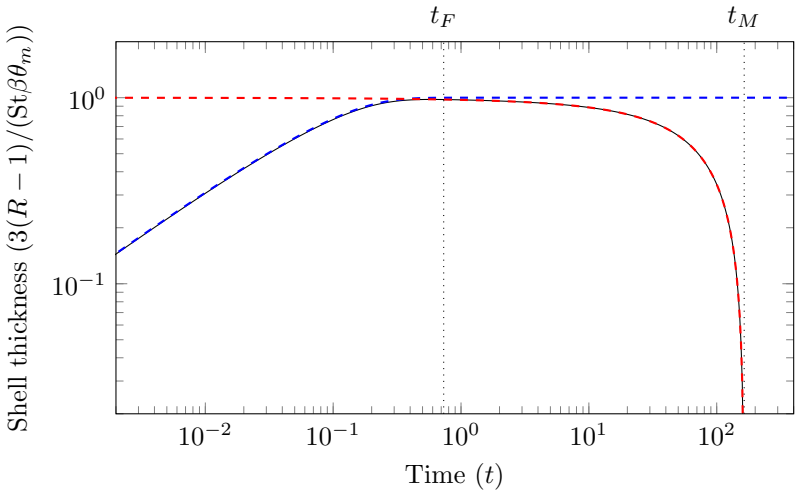

Figure 2.10: Graph showing the scaled shell thickness given by (2.3.57) as a function of time (black). Fast freezing given by (2.3.62) (blue) tends to a constant value given by (2.3.63), while the slow melting effect given by (2.3.66) (red) can be used to provide an approximation for the melting time given by (2.3.67) as $\theta_m \to 1$. t_F is given by (2.3.71). The parameters are $\beta = 7$, $\nu = 0.5$, $\kappa_3 = 0.05$, $\theta_m = 0.98$.

Substituting in the parameters in Table 1.1, we find that $\delta \approx 10^{-3}$ and that the solution to (2.3.60) in the limit $\delta \ll 1$, with initial condition given by $R^{(1)} = 0$, is

$$\frac{R^{(1)}}{\beta\theta_m} = \frac{1}{3} - \frac{2}{\pi^2}\sum_{j=1}^{\infty}\frac{\mathrm{e}^{-\pi^2 j^2 t}}{j^2}. \tag{2.3.62}$$

This gives us the maximum radius in the large-time limit of the $t = \mathrm{O}(1)$ problem as

$$R^{(1)} = \frac{\beta\theta_m}{3}, \tag{2.3.63}$$

and thus we predict that

$$R_F \sim 1 + \frac{\mathrm{St}\beta\theta_m}{3} \quad \text{as} \quad \delta \to 0, \quad \mathrm{St} \to 0. \tag{2.3.64}$$

Setting $\theta_m = 1$ in (2.3.64), we recover the same formula for R_F as in the small Stefan number limit of (2.3.23). For large time, we rescale $t = T/\delta$, so that (2.3.60) becomes,

at leading order in δ,

$$\frac{1}{\beta\theta_m}\frac{\mathrm{d}R^{(1)}}{\mathrm{d}T} = -1. \tag{2.3.65}$$

We solve (2.3.65) and match with the long-time behaviour of the shorter time problem given by (2.3.63), to find that

$$\frac{R^{(1)}}{\beta\theta_m} = \frac{1}{3} - T, \tag{2.3.66}$$

which gives us an explicit estimate for the melting time as

$$t_M = \frac{1}{\delta} = \frac{\beta\theta_m}{\nu(1-\theta_m)}, \tag{2.3.67}$$

which is consistent with (2.3.33). For $t \ll 1$ the behaviour of (2.3.56) is

$$\dot{R}^{(1)} \sim \frac{\theta_m\beta}{\sqrt{\pi t}}\left(1 - \frac{\nu}{\beta\sqrt{\kappa_3}}\frac{1-\theta_m}{\theta_m}\right) > 0 \quad \text{as} \quad t \to 0, \tag{2.3.68}$$

where again we have made use of (2.3.48). Since all the parameters are positive, in order for the cryolite to freeze, we require

$$\frac{\sqrt{\kappa_3}\beta\theta_m}{\nu(1-\theta_m)} > 1. \tag{2.3.69}$$

We find a simple upper bound for the freezing time by noticing that the cryolite temperature distribution results in constant steady-state heat flux. As the sum in (2.3.57) rapidly decreases, we balance

$$\nu(1-\theta_m) \approx 2\beta\theta_m \mathrm{e}^{-\pi^2 t}, \tag{2.3.70}$$

which yields

$$t_F \approx \frac{1}{\pi^2}\log\left(\frac{2}{\delta}\right). \tag{2.3.71}$$

We note that, in (2.3.69) and (2.3.71), the main parameters are κ_3 (see (2.3.6)) and δ

which represents the ratio of the heat transfer rates in the cryolite and the alumina particle, and describes how intensive the heat flow is between the regions. If δ is small, the timescale for solidification is much smaller than the melting and so we expect a shell to form. Conversely, if δ is large then the temperatures equilibrate fast and no freezing is possible.

In Figure 2.11, we compare the numerical solutions of the full system (2.3.2)–(2.3.4) with the asymptotic solutions given by (2.3.57). We see that the numerical solutions converge to the small Stefan number solution in the appropriate limit.

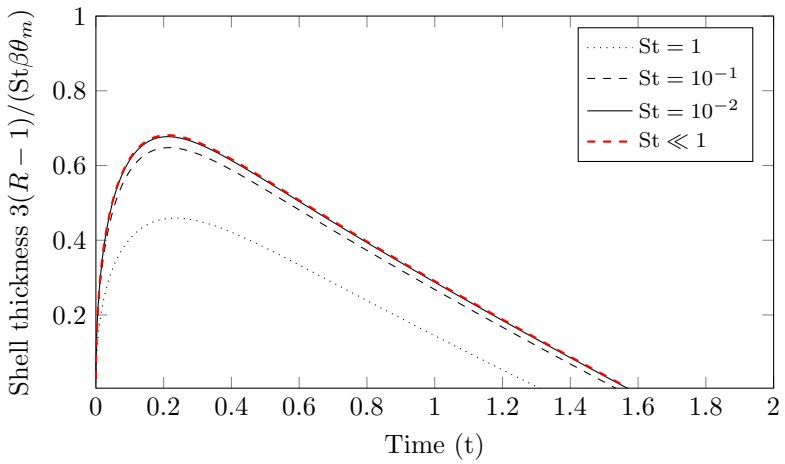

Figure 2.11: Graph showing the scaled shell thickness as a function of time for different Stefan numbers The black curves correspond to numerical solutions and the small-St limit in red from Section 2.3.5.

2.4 Analysis of the dissolution problem

2.4.1 Nondimensionalisation

Since we assume that dissolution can only start after complete melting of the frozen shell, we nondimensionalise[3] the system (2.2.6)–(2.2.16) using the scalings

$$r = a\hat{r}, \quad R = a\hat{R}, \quad t - t_M = \frac{a^2}{D\sigma}\tau, \quad C = C_f + (C_s - C_f)\hat{C}. \tag{2.4.1}$$

Eliminating the liquid velocity, the dimensionless system (2.2.6)–(2.2.16) can be written, dropping the hats, as

$$\frac{\partial C}{\partial \tau} = \frac{1}{r^2}\frac{\partial}{\partial r}\left(\frac{r^2}{\sigma}\frac{\partial C}{\partial r} - (1-\rho_r)R^2\frac{\mathrm{d}R}{\mathrm{d}\tau}C\right) \quad \text{in} \quad r > R(\tau), \tag{2.4.2a}$$

with boundary conditions

$$C = 1, \quad \frac{\mathrm{d}R}{\mathrm{d}\tau} = \frac{\partial C}{\partial r} \quad \text{on} \quad r = R(\tau), \tag{2.4.2b}$$

$$C \to 0 \quad \text{as} \quad r \to \infty, \tag{2.4.2c}$$

and initial conditions

$$C = 0 \quad \text{at} \quad \tau = 0 \quad \text{in} \quad r > 1, \tag{2.4.2d}$$

$$R = 1 \quad \text{at} \quad \tau = 0, \tag{2.4.2e}$$

where we have introduced the dimensionless parameters

$$\sigma = \frac{C_s - C_f}{\rho_p(1 - C_s/\rho_c)}, \qquad \rho_r = \frac{\rho_p}{\rho_c}, \tag{2.4.3}$$

[3]It is worth noting that there are two natural choices for the timescale: the dissolution timescale that we used in (2.4.1), which balances the two terms in the second boundary condition in (2.2.14), and the diffusive timescale a^2/D, representing the balance in the governing equation (2.4.2a).

where σ is the dissolution Stefan number, and ρ_r is the density ratio of the alumina to the cryolite. We see in Table 2.1 that $\sigma = 0.05$ and $\rho_r = 2$. We will now investigate the early-time behaviour of (2.4.2) analytically, then numerically in Section 2.4.3, and finally in the small-σ limit in Section 2.4.4.

2.4.2 Early-time behaviour

To initiate our the numerical simulations, it is necessary to derive the early-time behaviour (as C is discontinuous initially at $r = R$). The analysis is similar to that for the temperature problem presented in Section 2.3.2. The concentration is exponentially small except in a boundary layer in which we assume that the asymptotic similarity solution is given by

$$C \sim f(\eta), \quad R \sim 1 - 2\lambda\sqrt{\tau}/\sqrt{\sigma} \tag{2.4.4}$$

with $\eta = \sqrt{\sigma}(r-1)/(2\sqrt{\tau}) = \mathrm{O}(1)$ as $\tau \to 0^+$, where λ is a constant that needs to be found as part of the solution. After substituting (2.4.4) into (2.4.2) and expanding for small τ, we find that the leading-order equation for f is given by

$$2\eta f'(\eta) + f''(\eta) = 0, \tag{2.4.5}$$

while the boundary and matching conditions are given by

$$f(-\lambda) = 1, \quad f(\eta) \to 0 \quad \text{as} \quad \eta \to \infty. \tag{2.4.6}$$

The solution to (2.4.5) and (2.4.6) is

$$f(\eta) = \frac{1 - \mathrm{erf}(\eta)}{1 + \mathrm{erf}(\lambda)}, \tag{2.4.7}$$

where λ is the unique positive root of the transcendental equation

$$\lambda\sqrt{\pi}(1+\operatorname{erf}(\lambda)) = \sigma \mathrm{e}^{-\lambda^2}. \tag{2.4.8}$$

Equation (2.4.7) is often referred to as the Neumann Solution. The asymptotic behaviour of λ for small and large σ are given by

$$\lambda \sim \sigma/\sqrt{\pi} \quad \text{as} \quad \sigma \to 0, \tag{2.4.9}$$

$$\lambda \sim \log^{1/2}(\sigma/\sqrt{2\pi}) \quad \text{as} \quad \sigma \to \infty. \tag{2.4.10}$$

These limits are shown in Figure 2.12, along with the solution to (2.4.8), showing excellent agreement in both limits.

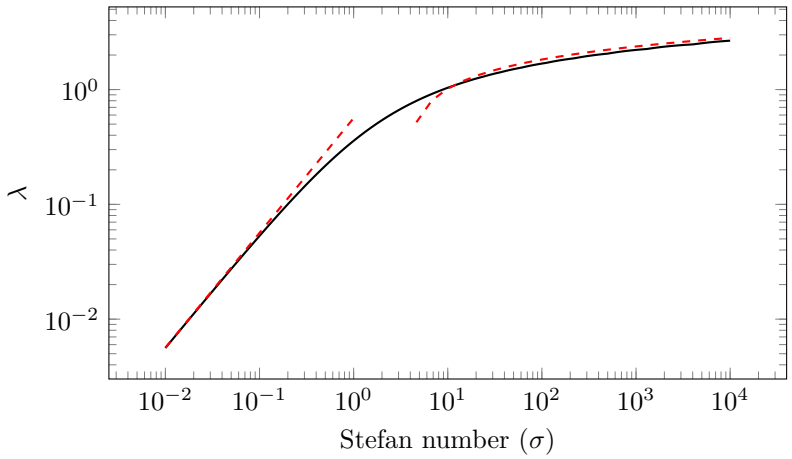

Figure 2.12: Graph showing λ given by (2.4.8) as σ varies, along with the two asymptotic limits (2.4.10).

2.4.3 Numerical results

We use (2.4.4), (2.4.7) and (2.4.8) to initiate our numerical simulations to (2.4.2). We solve the model using the method of lines with a discretisation analogous to the one described in Section 2.3.3. We define the dissolution time, τ_D, to be the time τ at

which $R = 0$. We show how the radius of the particle varies with scaled time τ/τ_D for various values of σ in Figure 2.13 (left). We see that, for small σ, the numerical results agree with the small-σ asymptotic result that we will derive in (2.4.13). For large σ, we see that the numerical results agree with the small-time solution presented in (2.4.4) and (2.4.10).

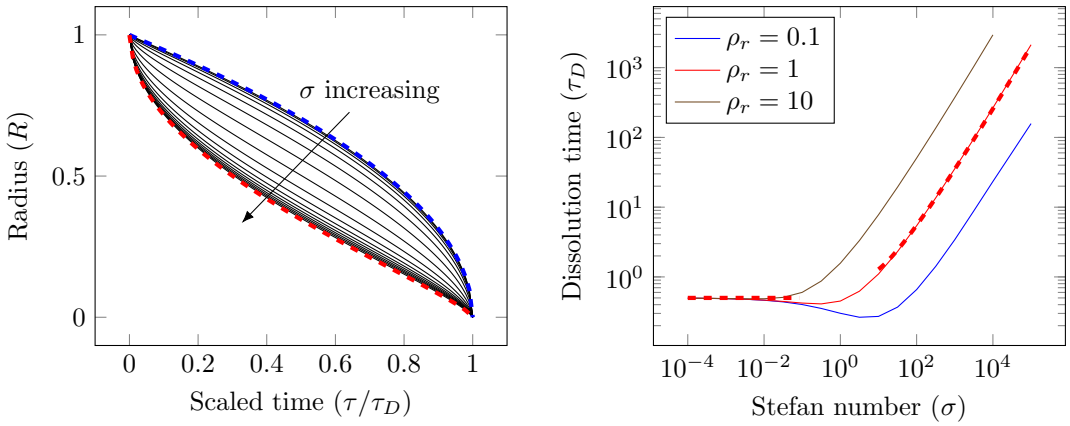

Figure 2.13: Left: $R(\tau)$ for varying σ for $\rho_r = 1$. The lines range between $\sigma = 10^{-4}, \cdots, 10^5$. The red dashed line is the small-time solution, while the blue dashed line is the small-σ solution given by (2.4.13). Right: Dissolution time for varying Stefan number (σ) for different ρ_r values showing the non-monotonicity at $\sigma \approx 1/\rho_r$. Note that the two asymptotic limits are denoted with dashed red lines.

The dissolution time, τ_D, is also an important prediction of our model. In Figure 2.13 (right), we plot the dissolution time as a function of σ for different σ values. We note that, in the small-σ limit, τ_D tends to a constant, while the behaviour for large σ is more complicated. At first sight the scaling looks like σ, however $\sigma/\log(\sigma)$ (shown with a red dashed line in Figure 2.13 (right)) looks like a more appropriate candidate, hinting at logarithmic behaviour in this limit, but we do not explore this further. The final observation that we make is that the t_D-σ curve is non-monotonic when $\rho_r < 1$; there is a minimum dissolution time which occurs when $\sigma \approx 1/\rho_r$.

In Figure 2.13, we also see that, in the small-σ limit, the dependence on the density disappears. Physically this means that, if the boundary is moving slowly, then the induced liquid movement due to the phase change is also small and the density ratio

only changes the higher-order dynamics.

2.4.4 Small-σ limit

In this section, we will consider the physically relevant limit of small σ by expanding

$$R \sim R^{(0)} + \sigma R^{(1)}, \quad C \sim C^{(0)} + \sigma C^{(1)} \quad \text{as} \quad \sigma \to 0. \tag{2.4.11}$$

A regular perturbation analysis shows that the leading-order solution is quasi-steady with (2.4.2) giving

$$C^{(0)} = \frac{R^{(0)}}{r}, \qquad \frac{\mathrm{d}R^{(0)}}{\mathrm{d}\tau} = -\frac{1}{R^{(0)}}; \tag{2.4.12}$$

applying the initial condition $R^{(0)}(0) = 1$ then gives

$$R^{(0)} = \sqrt{1 - 2\tau}. \tag{2.4.13}$$

We can see from (2.4.13) that complete dissolution occurs at $\tau_D \sim 1/2$ as $\sigma \to 0$, after which the particle ceases to exist. This result has been calculated by many authors, e.g. [16]. By undoing the nondimensionalisation, we see that the leading-order dissolution time t_D is given by

$$t_D - t_M \sim \frac{a^2}{2D\sigma} = \frac{a^2\rho_p(1 - C_s/\rho_c)}{2D(C_s - C_f)} \quad \text{as} \quad \sigma \to 0. \tag{2.4.14}$$

2.5 Conclusions

2.5.1 Summary of scales

In Figure 2.14, we plot t_F, t_M and t_D given by (2.3.58), (2.3.59) and (2.4.14) as a function of $\beta\theta_m\sqrt{\kappa_3}/\nu(1 - \theta_m)$, where δ is defined in (2.3.61). There are two qualitatively different regimes. Below the freeze limit (shown by the vertical dot-

dashed line given by (2.3.12)) the particle simply dissolves, since the heat transfer in the cryolite is fast enough that the cryolite temperature remains above the freezing temperature and no freezing occurs. However, above this limit, freezing, melting, and dissolution all occur. The actual operating regime is shown as a vertical dotted line. We also see that the dissolution takes the largest amount of time, except in the limit $\delta \to 0$ corresponding to $\theta_m \to 1$, where the melting takes over. A similar behaviour is shown in Huppert [39] for the related problem of turbulent flow of lava over a cold surface.

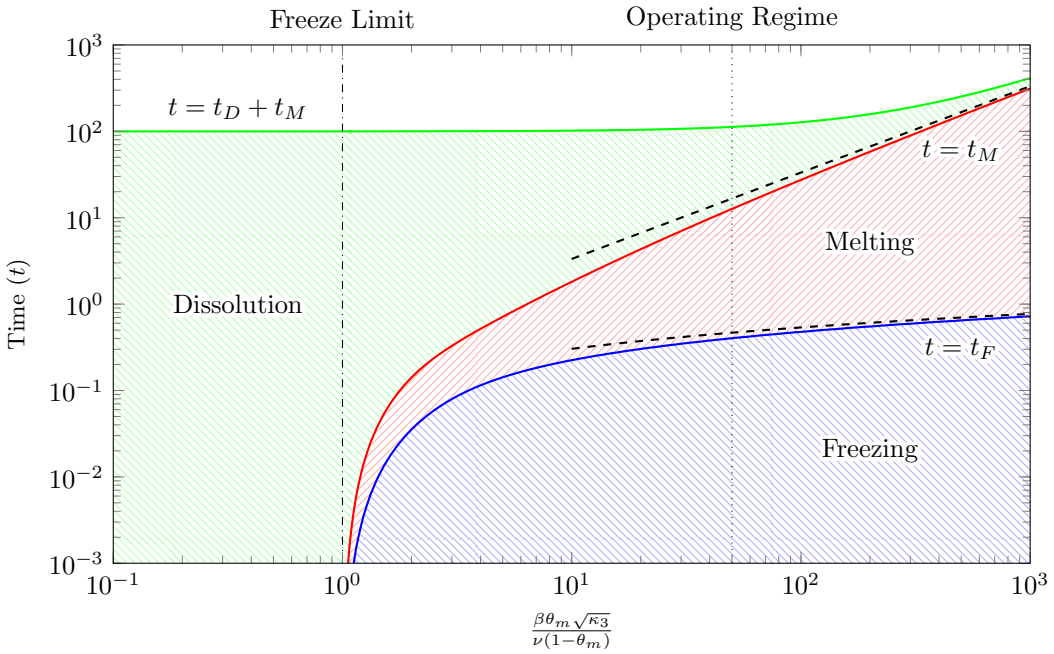

Figure 2.14: Graph showing t_F, t_M and t_D given by (2.3.58), (2.3.59) and (2.4.14) as a function of $\beta\theta_m\sqrt{\kappa_3}/\nu(1-\theta_m)$, coloured blue, red and green, respectively. The parameters are $\mathrm{St} = 0.34$, $\beta = 7$, $\nu = 0.5$, $\kappa_3 = 0.05$, and $\theta_m = 0.98$. Dashed lines are given by (2.3.67) and (2.3.71) and are valid as $\delta \to 0$. The dotted vertical line indicate the operating regime of the Hall-Héroult cell, and the freeze limit is given by (2.3.12).

We use the data to obtain analytical predictions for the dimensional freezing time t_F, melting time t_M, and dissolution time t_D for a 50 µm particle, which we find to be

$$t_F \approx \frac{a^2 c_p \rho_p}{\pi^2 k_p} \log\left(\frac{2(T_m^* - T_p^*)k_p}{(T_c^* - T_m^*)k_c}\right) \approx 500\,\mu\mathrm{s}, \tag{2.5.1}$$

from (2.3.71),

$$t_M \sim \frac{a^2 c_p \rho_p}{3k_p} \frac{(T_m^* - T_p^*)k_p}{(T_c^* - T_m^*)k_c} \approx 100\,\text{ms}, \tag{2.5.2}$$

from (2.3.67) and

$$t_D \sim \frac{a^2 \rho_p (1 - C_s/\rho_c)}{2D(C_s - C_f)} \approx 17\,\text{s}, \tag{2.5.3}$$

from (2.4.14). The ratios of these three timescales are independent of a and, for the parameters given in Table 1.1, are $t_D/t_M \approx 170$ and $t_M/t_F \approx 200$. We note that the approximations for the melting and freezing times are only strictly valid when the dimensionless melting temperature is close to the cryolite temperature, i.e. $1 - \theta_m$ is small (as is true in our case), and that our results only depend on one property of the frozen cryolite, namely the dimensional melting temperature T_m^*. We also note that the dissolution timescale t_D is a factor of 10 smaller than that observed by Haverkamp and Welch [34], which is likely due to the difference between dissolving one particle rather than dissolving a powder.

2.5.2 Bulk flow

We now revisit our modelling assumption concerning the neglect of the bulk flow. If we consider a stationary solid alumina particle of radius a in a background cryolite flow with average speed U, with dynamic viscosity μ_c, then the particle Reynolds number is given by

$$\text{Re} = \frac{aU\rho_c}{\mu_c}. \tag{2.5.4}$$

Assuming $U \approx 10\,\text{cm/s}$ and using the other parameters in Table 1.1, we find that $\text{Re} \approx 4$, which means that the particle is in the "Stokes drag" regime. The governing equation for the location $\mathbf{r}$ of the particle, assuming Stokes drag given by

$$F_d = 6\pi\mu_c a U, \tag{2.5.5}$$

can be written as

$$\frac{4}{3}\pi\rho_p a^3\ddot{\mathbf{r}} = 6\pi\mu_c a(\mathbf{u}-\dot{\mathbf{r}}) + \frac{4}{3}\pi(\rho_p-\rho_c)a^3\mathbf{g}. \tag{2.5.6}$$

We scale (2.5.6) using

$$r = H\hat{r}, \quad \mathbf{u} = U\hat{\mathbf{u}}, \quad T = \frac{H}{U}\hat{t}, \tag{2.5.7}$$

where $H \approx 100\,\text{cm}$ is the typical depth of the bath. Using these scales the nondimensional equation is

$$\text{Stk}\,\ddot{\mathbf{r}} = \mathbf{u} - \dot{\mathbf{r}} - \text{G}\,\mathbf{k}, \tag{2.5.8}$$

where $\mathbf{u}$ is the velocity of the cryolite and $\mathbf{k}$ is the unit vector in the vertical direction and where

$$\text{Stk} = \frac{2\rho_p U a^2}{9\mu_c H} \approx 10^{-5}, \tag{2.5.9}$$

$$\text{G} = \frac{2(\rho_p-\rho_c)ga^2}{9U\mu_c} \approx 10^{-3}. \tag{2.5.10}$$

Since both Stk and G are small, we conclude that both inertia and gravity can be neglected compared to drag, and hence the particles follow the flow. This also means that the relative velocity between the flow and particle is small, so we are justified in neglecting the influence of flow on the freezing, melting and dissolution, and hence we are permitted to use spherically symmetric geometry. These assumptions break down when Stk and G are O(1), which occurs for particles with a millimetre or bigger radii.

2.5.3 Summary

In this chapter, we have examined the problem of adding a cold alumina particle to a bath of hot cryolite. We developed a spherically symmetric model to describe heat and mass transfer between the particle and the surrounding material, allowing for freezing and melting of the cryolite close to the particle and its subsequent dissolution.

We solved this model numerically with the method of lines, using the early-time asymptotic solution to initiate the numerical scheme. We explored the behaviour as we varied the key dimensionless parameters. We also considered the problem in the limits of small superheat and of small Stefan number. Using these asymptotic solutions, we found approximate expressions for the freezing, melting, and dissolution timescales, with freezing being the fastest effect and dissolution the slowest. Also, using the early-time solution, we determined constraints on the parameters for which shell growth is possible. Our results predict that increasing the superheat or decreasing the particle size should decrease the time it takes for a particle to dissolve, in accordance with practical experience. Furthermore, the temperature changes are localised to a 5–10 particle radii region. Our goal is to use the insight we have found for the single-particle situation as a building block towards a more realistic model for the feeding of alumina particles into the Hall-Héroult cell.

Chapter 3

A porous alumina raft on a cryolite bath

Synopsis

In this chapter, we develop a one-dimensional Stefan-type model for the imbibition of molten cryolite into a cold porous lump of alumina. In the small overheat limit, we analyse the small-time behaviour using the method of matched asymptotic expansions seeking locally self-similar solutions that describe analytically the competition between imbibition and freezing. Depending on the balance between these effects, the problem exhibits two self-similar solutions (one being stable and the other unstable) or no solution, signalling a case where the molten cryolite freezes first on the exterior before imbibition occurs. Our asymptotic predictions are validated by direct numerical simulations that are also used to investigate late time behaviour. In particular, we predict the depth of the imbibition layer before the cryolite freezes.

3.1 Introduction

Having considered what happens to an isolated particle in an unbounded bath in Chapter 2, we now turn our attention to the more realistic case of a cold porous

alumina raft floating on the surface of the cryolite, which is experimentally studied in [46]. In this chapter, we focus on the interplay between two mechanisms: the imbibition of the cryolite into, and the freezing of cryolite inside, a porous raft when it is floating on the top of the cryolite bath, see Figure 3.1.

In Figure 3.1 (right) we show a microscope image, reproduced from [44] (with permission) that depicts a slice of a raft, where the light grey areas are the alumina particles and the darker grey areas are the frozen cryolite. In the experimental image, three distinct regions are visible; the uninfiltrated region on the top left (labelled I), the liquid region on the bottom right (labelled II), and a region where both the alumina particles and the cryolite are present (labelled III). Since the porous medium is cold, we expect that the cryolite freezes as it infiltrates. One possibility is that the liquid solidifies on the outer surface of the raft. Another possibility is that the liquid infiltrates into the porous medium and solidifies inside the pores, which has been observed experimentally. However, frozen cryolite cannot be the only phase in the porespace, since in that case the infiltration front would not be able to propagate. We thus assume that the infiltration involves a mushy region, which is a region containing both solid and liquid cryolite at the same temperature. The region marked as III in Figure 3.1 (right) is thus split into two: a mushy region (consisting of liquid and solid cryolite, and alumina) and an infiltrated region (consisting of liquid cryolite and alumina). This structure permits the solidification and flow of the cryolite at the same time, and these types of models have been used in many different contexts such as the growth of sea ice [23, 104] and the infiltration of metals [63]. We note that, since the cryolite in the raft has to solidify before imaging can take place, details of the mushy region cannot be seen in the image so the line separating the two regions is illustrative to aid the subsequent presentation of the model. The darker solid region in the bottom right is the background for the SEM image and does not represent a physical region.

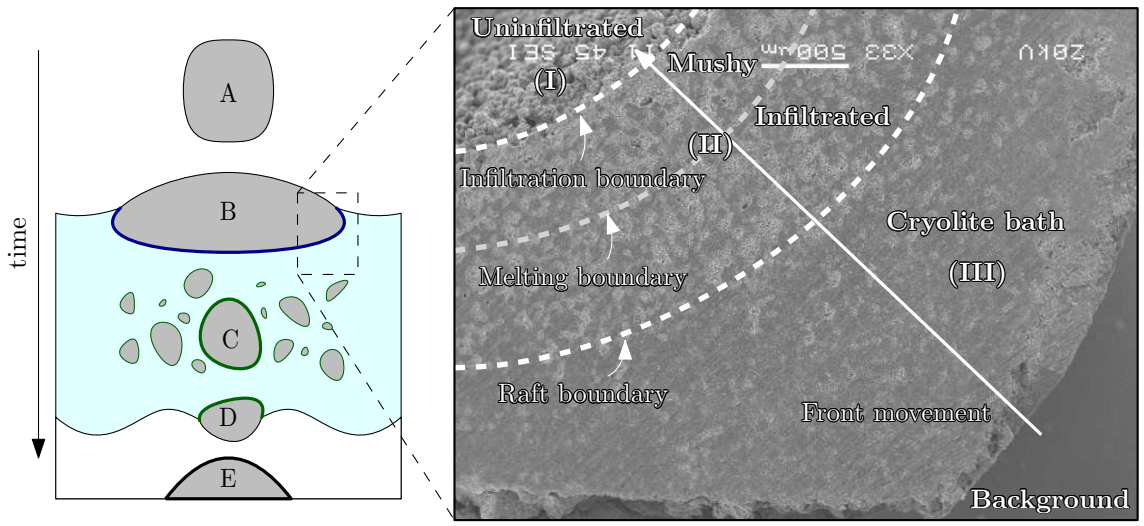

Figure 3.1: Chronology of the process (left), with the focus of this chapter denoted with B. Image of a raft (right) showing the different regions that will be used in our mathematical model. The background image (right) is an experiment from [44], reproduced with permission.

We show a schematic of the problem in Figure 3.2 (left) in which we see the raft partially submerged at the top surface of the cryolite bath. An infiltration front penetrates into the porous medium vertically upwards, while below this front there is a melting front which separates a mushy region containing both liquid and solid cryolite as well as alumina particles from a region which is saturated with liquid cryolite. Throughout this chapter, we will analyse a one-dimensional model, see Figure 3.2 (right), which is relevant in practice because the vertical thickness, H, of a raft is much smaller than the horizontal width, L. We assume that the bottom surface of the raft is at some given fixed depth H_d.

The model that we formulate is similar to the one used by Mortensen et al. [63] to model the infiltration of metal into fibrous performs, but with a number of differences. They use the same general regions and governing equations that we introduce, except for the pure liquid region which is not present in their model. They investigate a different microstructure, so their permeability function differs in form. In addition, the geometry they consider is also different: they investigate a problem where metal

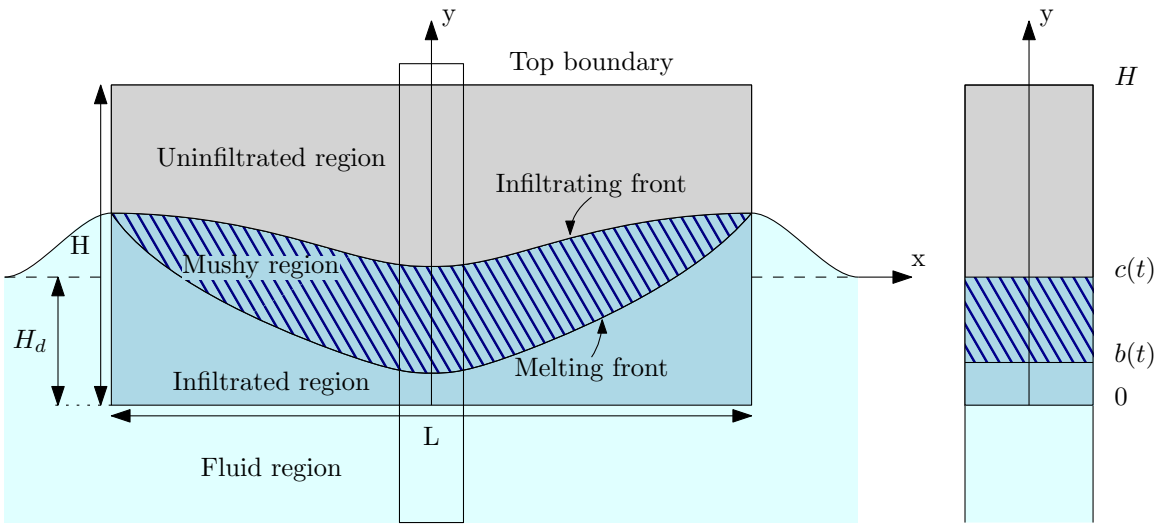

Figure 3.2: Geometry of a rectangular raft with the different regions inside at early time. We consider $H/L \ll \mathrm{O}(1)$ in our current model and only investigate the vertical variation corresponding to the y axis. See text for details.

is injected into an adiabatic or cooled mould. They observe the appearance of fully solidified or clogged regions, which appear at the sides of the cylindrical mould. They do not observe finite time clogging at the front during the process. For the unidirectional case, they find a similarity solution, which they use to explore the behaviour of the infiltrating front.

There is also a substantial body of research on the infiltration of liquid into a partially cooled capillary tube [21, 22, 66], where the behaviour can be rather complex, including the emergence of ice-bands along the inner surface of the pipe, or the phenomenon of freeze-shut, which is the clogging of a pipe from freezing from the sides. In the context of porous media, averaging techniques have been used to derive macroscopic equations for a solidifying liquid in porous media [67], but this model is only applicable where the porous medium is fully saturated, hence can not be used for problems containing an infiltration front, such as ours. A similar model has been used to model crust infiltration in a Hall-Héroult cells [110], where they assume that the cryolite is a binary liquid. They investigate the model numerically and validate it against experimental measurements.

Related models have been used to describe liquid-gas phase change in porous media as well. An example of this is the formation of salt precipitate during evaporation of water in porous medium [93, 95, 96]. In these papers, the authors consider the propagation of an evaporating front in a porous medium saturated with water containing salt. They model the vapour region using Clapeyron's equations, the liquid region with the heat equation and a concentration equation for the salt, and they prescribe continuity and phase-change conditions on the evaporating front. They find that their model exhibits multiple solutions to their early-time similarity solution, due to salt precipitation decreasing the porosity at the front.

In contrast with the solid particle problem considered in Chapter 2, where the frozen layer forms around the particle, in the case of imbibition and freezing of a raft we expect that qualitatively different behaviours can occur depending on the size of different parameters. If the porous medium is densely packed, we expect that the resulting behaviour is similar to a solid body which is covered by a surface freeze. However, if the porous medium is loosely packed, then we expect that the liquid can infiltrate the porous medium and freeze around the particles. Our aim is to develop a model that can capture these two limits. We note that, if the top surface of the raft is sufficiently cold, infiltration may stop at some finite time due to complete freezing of the cryolite at the infiltrating front.

The structure of this chapter is the following. In Section 3.2 we formulate a multi-phase model for liquid cryolite infiltrating into a porous medium. We nondimensionalise this model in Section 3.3, and then consider the small superheat limit in Section 3.4. We investigate the early-time behaviour of the problem in Section 4.5, determining whether an infiltrating solution exists and investigate the effect of varying the parameters on the existence of solutions. We solve the problem numerically in Section 3.6 to determine the influence of the ambient temperature above the raft on the behaviour. Using the numerical results as a guide we investigate the near clogging behaviour

in Section 3.7 and investigate the stability of the multiple solutions in Section 3.8. Finally, we discuss the results in Section 3.9.

3.2 Mathematical Model

We use t to denote the time since the porous raft was placed on top of the liquid and y to denote the vertical spatial coordinate with origin at the bottom surface of the porous medium. We initially consider two regions; a *semi-infinite bath* located in $y < 0$, denoted as Ω_b, and an *uninfiltrated porous medium*, residing in $0 < y < H$, and denoted as Ω_u, where H is the height of the porous medium as shown in Figure 3.3.a. In practice the temperature in these two regions are different. Initially, the bath temperature T_b^* is above the melting temperature of the cryolite T_m^*, and the porous medium is at some temperature smaller than T_m^* denoted as T_a^*.

In an isothermal situation, if the liquid wets the porous medium, the liquid then imbibes due to the capillary pressure difference generated by the small liquid menisci inside the porous medium; these menisci displace the air in the pores as they move. This continues until the imbibed height becomes so large that the weight of the liquid slows down and stops this process [98, 102].

In the nonisothermal case, the liquid can freeze and, if the porous medium is cool enough, then the problem turns into a Stefan problem (which is similar to the single-particle problem considered in Chapter 2) where the liquid freezes on the outside of the porous medium, and this layer then recedes as the porous region heats up. If buoyancy effects due to the temperature gradient are important, they will generate convective flows in the bath liquid, possibly forming mushy regions instead of a sharp freezing front on the outer surface (see [105]).

It is also possible for the freezing and infiltration to balance, which gives rise to an infiltrating front on which phase-change also occurs. In this case, the liquid will

propagate into the porous medium and freeze on the surface of the alumina particles. In the rest of this section, we will describe a model for this infiltrating and freezing situation (we will see that the isothermal imbibition is a straightforward limit of our model).

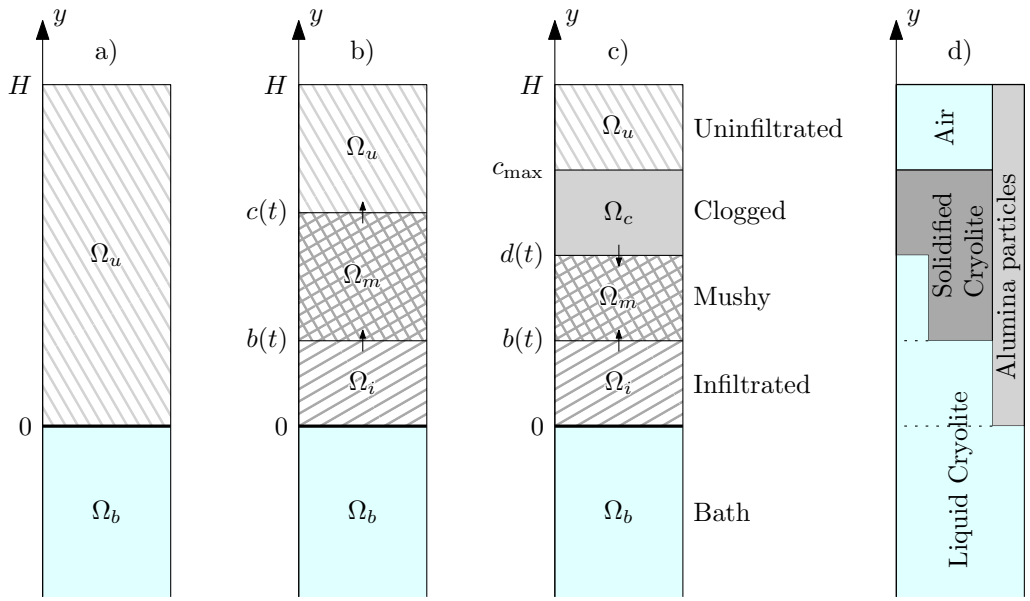

Figure 3.3: Schematics showing the evolution of the domains in our model from (a) the initial time, through (b) early-time infiltration, to (c) late-time clogging. The constituents in each of the regions are shown in (d).

For the infiltrating situation, we introduce the additional regions shown in Figure 3.3.b; an *infiltrated porous medium* region in which the cryolite is liquid, which we denote by Ω_i in $0 < y < b(t)$ and a *mushy* region in which there is a mixture of solid and liquid cryolite, which we denote by Ω_m for $b(t) < y < c(t)$. We denote the location of the *melting front* by $b(t)$ and *infiltration front* by $c(t)$. If the infiltration front reaches the top of the raft, we denote that time with t_i. If the liquid cryolite at $c(t)$ completely freezes, then $c(t) = c_{\max}$, the maximum penetration height, subsequently. We call the time at which this happens the clogging time, t_c. After the clogging time, a region of completely frozen cryolite can develop. We denote this frozen region by Ω_c, and assume that it lies in $d(t) < y < c_{\max}$, where $d(t)$ denotes the position of the *clogging front* (see Section 3.2.5 for more discussion). We assume that the

different constituents in the pore space are in a thermal equilibrium locally, so we can describe the state of the infiltrated porous medium using one local temperature[1]. We denote the temperature in each region as $T_b(y,t)$, $T_i(y,t)$, $T_m(y,t)$, $T_u(y,t)$ and $T_c(y,t)$, and the average liquid cryolite flow speed in each region as $u_b(y,t)$, $u_i(y,t)$ and $u_m(y,t)$, remembering that there is no flow in Ω_u or Ω_c. We denote the pressure in each of the regions by $p_b(y,t)$, $p_i(y,t)$ $p_m(y,t)$, respectively. We denote the volume fraction of *alumina particles* as ϕ_a (which we take to be a constant since we are only considering the temperature problem and not dissolution), the volume fraction of *air* as $\phi_{\text{air}}(y,t)$, the volume fraction of *liquid cryolite* by $\phi_c(y,t)$ and the volume fraction of *frozen cryolite* by $\phi_s(y,t)$ We summarize the constituents present in each region in Figure 3.3.d.

We denote densities as ρ_a, ρ_c, ρ_s, specific heat capacities as c_a, c_c, c_s and heat conductivities as k_a, k_c, k_s and k_{air}, where a denotes alumina, c denotes cryolite, and s denotes frozen cryolite. Furthermore, we denote the viscosity of the liquid cryolite as μ_c and the gravitational acceleration as g.

In the following sections, we describe the equations that hold in each region, and will then present the boundary and initial conditions.

3.2.1 Bath region

In the cryolite bath located in $y < 0$, the temperature T_b, velocity u_b and the pressure p_b are governed by conservation of energy, conservation of mass and conservation of momentum and are given by

$$\rho_c c_c \frac{\partial T_b}{\partial t} + \rho_c c_c u_b \frac{\partial T_b}{\partial y} = k_c \frac{\partial^2 T_b}{\partial y^2}, \tag{3.2.1}$$

$$\frac{\partial u_b}{\partial y} = 0, \tag{3.2.2}$$

[1]This assumption can be relaxed by writing down the full microscale problem then using some procedure like homogenisation or averaging obtain the macroscale equations [67].

$$-\frac{\partial p_b}{\partial y} - \rho_c g + \mu_c \frac{\partial^2 u_b}{\partial y^2} = 0, \tag{3.2.3}$$

where we assumed that the liquid inertia is negligible in the bath region.

3.2.2 Infiltrated region

We assume that as the cryolite penetrates into the porous medium, it saturates each pore. In this infiltrated region, we assume that the liquid flow is described by Darcy's equation. Furthermore, we assume that the transport of energy is due to advection by the liquid in the pore space and by conduction in both phases. The governing conservation of energy, mass and momentum equations for the temperature T_i, average velocity u_i and pressure p_i in this region, $0 < y < b(t)$, are

$$\widehat{\rho c}\frac{\partial T_i}{\partial t} + \phi_c \rho_c c_c u_i \frac{\partial T_i}{\partial y} = k_i \frac{\partial^2 T_i}{\partial y^2}, \tag{3.2.4}$$

$$\frac{\partial}{\partial y}\left(\phi_c u_i\right) = 0, \tag{3.2.5}$$

$$-\frac{K(\phi_c)}{\phi_c \mu_c}\left(\frac{\partial p_i}{\partial y} + \rho_c g\right) = u_i, \tag{3.2.6}$$

remembering that there is no air or solid cryolite in this region, so that $\phi_a = 1 - \phi_c$. We use mixture properties given in [47], namely

$$\widehat{\rho c} = \phi_c \rho_c c_c + (1 - \phi_c)\rho_a c_a, \quad k_i = k_c^{\phi_c} k_a^{1-\phi_c}; \tag{3.2.7}$$

$K(\phi_c)$ is the permeability function, which we assume is given by the Carman-Kozeny relationship [47] namely

$$K(\phi_c) = \frac{a^2 \phi_c^3}{180(1 - \phi_c)^2}, \tag{3.2.8}$$

where a is the average diameter of the particles and the pores.

3.2.3 Mushy region

Due to the initial temperature difference between the cryolite bath and the porous medium, we expect that the cryolite changes phase from liquid to solid in some parts of the porous medium. We consider the situation where, as the liquid infiltrates, some, but not all of it, freezes, forming a *mushy region*. We thus need to track how much of the liquid solidifies and thus how much of the liquid infiltrates further into the porous medium. Here, we consider the simplest possible model of a mushy region closely following [63], remembering that more complicated problems, such as the solidification of liquids with multiple components [64] or solidification in the presence of convection [105], require more complicated constitutive laws. The main assumptions for our mushy-region model are the following:

- The constituents (liquid cryolite, frozen cryolite and the alumina particles) are in thermal equilibrium on the microscale, at a temperature equal to the constant melting temperature T_m^*.
- The timescales for freezing and melting are shorter than the timescale of the infiltration, so phase change occurs only in thin layers at the boundaries of the mushy region.
- Since freezing occurs instantaneously at the infiltration front, the frozen cryolite is laid down inside the mushy region as the front moves and, at a given position, does not vary with time once the front has passed.

The equations governing the temperature T_m, average velocity u_m, pressure p_m, frozen cryolite fraction ϕ_s and liquid cryolite fraction ϕ_c in this mushy region in $b(t) < y < c(t)$ are given by the following conservation of energy, mass, and momentum equations

$$T_m = T_m^*, \tag{3.2.9}$$

$$\frac{\partial \phi_s}{\partial t} = 0, \tag{3.2.10}$$

$$\frac{\partial \phi_c}{\partial t} + \frac{\partial}{\partial y}\left(\phi_c u_m\right) = 0, \tag{3.2.11}$$

$$-\frac{K(\phi_c)}{\phi_c \mu_c}\left(\frac{\partial p_m}{\partial y} + \rho_c g\right) = u_m, \tag{3.2.12}$$

along with the condition of 'no voids', which reads

$$\phi_c + \phi_s + \phi_a = 1. \tag{3.2.13}$$

Here, $K(\phi_c)$ is the permeability function given in (3.2.8), μ_c is the viscosity of the liquid cryolite, ρ_c is the density of the liquid cryolite, g is the gravitational acceleration, and ϕ_a is the alumina fraction.

3.2.4 Uninfiltrated region

In the uninfiltrated region, we neglect the contribution to the temperature field due to the air, since its heat capacity is much smaller than that for alumina. We assume that the heat transfer in this region is only due to conduction in the particle-air mixture, hence the temperature T_u for $c(t) < y < H$ is governed by

$$\phi_a \rho_a c_a \frac{\partial T_u}{\partial t} = k_p \frac{\partial^2 T_u}{\partial y^2}. \tag{3.2.14}$$

There are many ways to model the heat conductivity of a porous matrix, which in itself is a whole field of study (e.g. [14, 32, 47]). We consider that the raft microstructure can be modelled accurately by a packed bed of spheres, and in this case the effective heat conductivity coefficient is given by (see [47])

$$k_p = k_a^{\phi_a} k_{air}^{1-\phi_a}. \tag{3.2.15}$$

3.2.5 Clogged region

If the top of the raft is cold enough, the liquid cryolite at the infiltration front may completely freeze, preventing further front motion. We call the time at which this happens the *clogging time*, t_c. At $t = t_c$, we suppose that the infiltrating front is at position $c_{\max}$ and thus, since the volume fraction of liquid cryolite reaches zero at the infiltration front, the pores become completely blocked, so that $\phi_s\left(c_{\max}, t_c\right) = 1 - \phi_a$. A *clogging front*, located at $y = d(t)$, initiates from $y = c_{\max}$ and moves backwards through the mushy region, freezing material as it moves. The governing equation for the temperature, T_c, in the clogged region $d(t) < y < c_{\max}$ reads

$$\widehat{\rho c}_f \frac{\partial T_c}{\partial t} = k_f \frac{\partial^2 T_c}{\partial y^2}, \tag{3.2.16}$$

where the mixture properties (analogously to (3.2.7)) are given by

$$\widehat{\rho c}_f = (1 - \phi_a)\rho_s c_s + \phi_a \rho_a c_a, \quad k_f = k_a^{\phi_a} k_s^{1-\phi_a}. \tag{3.2.17}$$

3.2.6 Boundary and initial conditions

In order to close the model, we apply the following boundary and initial conditions, which couple together the different regions. We assume that, in the far-field, deep in the bath, the temperature T_b tends to a constant given by

$$T_b \to T_b^* \quad \text{as} \quad y \to -\infty, \tag{3.2.18}$$

where T_b^* denotes the far-field temperature of the cryolite bath.

At the interface at $y = 0$ between the porous medium and the liquid, we assume that the pressure is given by the hydrostatic head, corresponding to placing the base of the porous medium below the free surface by a given amount and keeping it there,

as illustrated in Figure 3.2. In order to model free-floating, this height should change as the weight of the porous medium changes, but we assume that the position is fixed, and that the timescale of mechanical equilibration is faster than all the timescales in our model. Hence, we write

$$p_i = p_0 + \rho_c g H_d \quad \text{at} \quad y = 0, \tag{3.2.19}$$

where H_d is the distance of the bottom of the raft from the undisturbed liquid surface, and p_0 is the atmospheric pressure. Additionally, we assume that the temperature and heat flux are continuous across this boundary and write

$$T_b = T_i \qquad \text{at} \quad y = 0, \tag{3.2.20}$$

$$k_c \frac{\partial T_b}{\partial y} = k_i \frac{\partial T_i}{\partial y} \quad \text{at} \quad y = 0. \tag{3.2.21}$$

At the interface between the infiltrated layer and the mushy region at $y = b(t)$, we assume that the total mass of the cryolite is conserved through the moving boundary using

$$\phi_c^+ \rho_c (u_m - \dot{b}) - \phi_c^- \rho_c (u_i - \dot{b}) = \phi_s^+ \rho_s \dot{b} \quad \text{at} \quad y = b(t), \tag{3.2.22}$$

where, since the volume fractions ϕ_c and ϕ_s does not need to be continuous across $y = b$, $+$ and $-$ denote the values of the variables on $y = b^+$ and $y = b^-$, respectively. The left-hand side of (3.2.22) denotes the discontinuity in the flux of the liquid across the interface, caused by phase change on the right-hand side.

We assume that the temperature is continuous at $y = b(t)$, which means that the temperature is equal to the melting temperature. We also assume that the pressure is continuous across this boundary, and thus we write

$$T_i = T_m^* \quad \text{at} \quad y = b(t), \tag{3.2.23}$$

$$p_i = p_m \quad \text{at} \quad y = b(t). \tag{3.2.24}$$

We assume that melting happens instantaneously, and hence the difference in heat fluxes must balance the latent heat necessary to melt the frozen material. This is equivalent to stating that energy must be conserved at the moving boundary and thus we write

$$\phi_c^+ \rho_c h_c (u_m - \dot{b}) - \phi_s^+ \rho_s h_s \dot{b} = \phi_c^- \rho_c h_c (u_i - \dot{b}) - k_i \frac{\partial T_i}{\partial y} \quad \text{at} \quad y = b(t), \tag{3.2.25}$$

where h_c is the enthalpy of the liquid cryolite and h_s is the enthalpy of the solid cryolite. Equation (3.2.25) can be simplified using mass conservation (3.2.22) and using the fact that the latent heat of solidification L is defined to be the difference between the enthalpies of the solid and liquid at a given temperature [38], i.e.

$$L = h_c - h_s \quad \text{at} \quad T = T_m^*. \tag{3.2.26}$$

Since we know that the temperature at this interface is continuous and is given by the solidification temperature, we reduce (3.2.25) to the more commonly used form

$$\phi_s^+ \rho_s L \dot{b} = -k_i \frac{\partial T_i}{\partial y} \quad \text{at} \quad y = b(t). \tag{3.2.27}$$

Using similar arguments as before, the temperature at the infiltrating front is also held at the melting temperature, thus

$$T_u = T_m^* \quad \text{at} \quad y = c(t). \tag{3.2.28}$$

At this front, we also assume that the liquid pressure is given by the capillary

contribution

$$p_m = p_0 - \frac{\gamma}{r(\phi_c)} \quad \text{at} \quad y = c(t), \tag{3.2.29}$$

where p_0 is the atmospheric pressure, γ is the surface tension of the microscale air-cryolite interfaces, and r represents the pore radius, which we assume depends on the local volume fraction of liquid cryolite ϕ_c. This radius and, in general, the capillary pressure are also dependent on the microstructure evolution which, for a general porous medium, is hard to characterise. We would expect that, in the case where the porosity does not change much, this effect will be negligible, but that the contribution might be substantial when the pores are small. We follow [47] and suppose that $r(\phi_c)$ is given by the square root of the permeability thus we write

$$r(\phi_c) = \sqrt{K} = \frac{a}{\sqrt{180}} \frac{\phi_c^{3/2}}{1 - \phi_c}. \tag{3.2.30}$$

This function has the desired property that it tends to a constant as the volume fraction of frozen cryolite tends to zero (i.e. $\phi_s = 1 - \phi_a - \phi_c \to 0$, which implies $\phi_c \to 1 - \phi_a$), and tends to zero (giving large suction pressure) when the solid fraction is large. Other models are also possible that have these behaviours; an example is

$$r(\phi_c) = \left| \frac{\phi_c}{1 - \phi_a} \right|^n, \tag{3.2.31}$$

where $n > 0$ is some exponent. With increasing n we get stronger effect and if $n = 0$ we neglect this effect and simply have $r(1 - \phi_a) = 1$. In the absence of any concrete physical evidence for picking one form over another, we choose to use (3.2.30) in our model.

We also conserve energy and mass across the moving front $c(t)$, which can be

written analogously to (3.2.22) and (3.2.27) as

$$\phi_s^- \rho_s L \dot{c} = -k_p \frac{\partial T_u}{\partial y} \quad \text{at} \quad y = c(t), \tag{3.2.32}$$

$$\phi_c^- \rho_c (u_c - \dot{c}) = \phi_s^- \rho_s \dot{c} \qquad \text{at} \quad y = c(t). \tag{3.2.33}$$

At the top of the raft, we assume that the surface is open to the atmosphere, so a natural boundary condition to prescribe is Newton's law of cooling [32, p. 19], which reads

$$-k_p \frac{\partial T_u}{\partial y} = h(T_u - T_{top}) \quad \text{at} \quad y = H, \tag{3.2.34}$$

where T_{top} is the ambient temperature and h is the convective coefficient. We note that, as $h \to 0$, the boundary becomes insulated, while as $h \to \infty$, the boundary is at the prescribed ambient temperature.

After clogging has occurred, we need to prescribe different boundary conditions. At the stationary infiltration front at $y = c_{\max}$, we replace (3.2.28), (3.2.29) and (3.2.32) with

$$T_c = T_u \qquad \text{at} \quad y = c_{\max}, \tag{3.2.35}$$

$$k_s \frac{\partial T_c}{\partial y} = k_p \frac{\partial T_u}{\partial y} \quad \text{at} \quad y = c_{\max}, \tag{3.2.36}$$

remembering that we only need 2 conditions since $c_{\max}$ is known. Meanwhile, on the *clogging front* $y = d(t)$ we write the Stefan conditions

$$\phi_c^-(d(t)) \rho_s L \dot{d} = k_s \frac{\partial T_c}{\partial y} \qquad \text{at} \quad y = d(t), \tag{3.2.37}$$

$$\rho_c \phi_c^- (u_i - \dot{d}) - \rho_s \phi_s^- \dot{d} = -\rho_s \phi_s^+ \dot{d} \quad \text{at} \quad y = d(t), \tag{3.2.38}$$

$$T_u = T_m^* \qquad \text{at} \quad y = d(t), \tag{3.2.39}$$

where we note that in (3.2.37) the liquid fraction ϕ_c^- is a function of position (given

from the previous stage), and hence this clogged problem is similar to a problem with spatially varying latent heat, which has been previously investigated for the shoreline problem [99] and for power-law functions [114].

Initially, we assume that the porous medium is dry, and thus the infiltrating and melting boundaries are at the bottom of the raft, i.e.

$$b = c = 0 \quad \text{at} \quad t = 0. \tag{3.2.40}$$

We assume that the temperature of the external cryolite and the uninfiltrated porous medium are given, and so we write

$$T_u = T_a^* \quad \text{in} \quad 0 < y < H \quad \text{and} \quad T_b = T_b^* \quad \text{in} \quad y < 0 \quad \text{at} \quad t = 0, \tag{3.2.41}$$

where T_a^* is the initial temperature of the porous raft, H is the height of the porous medium and T_b^* is the initial temperature of the cryolite bath (which is identical to the far-field temperature). We note that, in general, the temperature of the air around the raft and the initial temperature of the raft can be different; however for simplicity we will take them to be the same, assuming that the temperature of the particles is in equilibrium with the environment before the porous raft made contact with the bath. We further note that, since $b = c = 0$ at $t = 0$, we do not need to prescribe ϕ_s or ϕ_c, nor T_i, T_m or T_c initially.

Equations (3.2.1)–(3.2.24), (3.2.27)–(3.2.30) and (3.2.32)–(3.2.41) form a closed system describing the raft infiltration problem. In Figure 3.4, we present an overview of the different regions in the (y, t) plane for the two cases of full and partial infiltration.

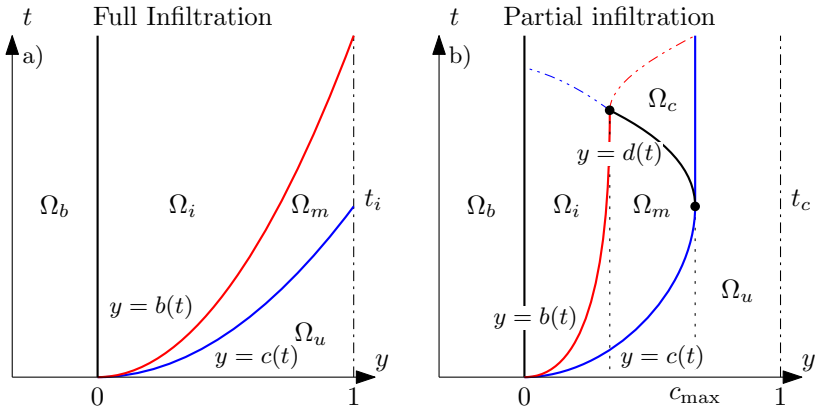

Figure 3.4: Overview of the location of the different regions and moving fronts in the (y, t) plane for the two possible qualitatively different solutions. The Ωs denote the different regions, meanwhile $b(t)$, $c(t)$, and $d(t)$ denote the positions of the infiltration, melting, and clogging fronts, respectively.

3.3 Nondimensionalisation

We use (3.2.2), (3.2.3) and (3.2.19) to solve for the pressure in the cryolite bath, which gives a hydrostatic pressure distribution which we write as

$$p_b = p_0 - \rho_c g(y - H_d) \quad \text{in} \quad y < 0. \tag{3.3.1}$$

We thus nondimensionalize our model for the raft infiltration problem using the scalings

$$y = H\hat{y}, \quad t = \frac{H^2}{\alpha_p}\hat{t}, \quad T = T_a^* + (T_b^* - T_a^*)\hat{T}, \quad K = \frac{a^2}{180}\hat{K}, \tag{3.3.2}$$

$$b = H\hat{b}, \quad c = H\hat{c}, \quad d = H\hat{d}, \quad r = a\hat{r}, \tag{3.3.3}$$

$$p = p_0 + \rho_c g H_d - \rho_c g H\hat{y} + \left(\frac{\gamma}{a} + \rho_c g H_d\right)\hat{p}, \quad u = \frac{\alpha_p}{H}\hat{u}, \tag{3.3.4}$$

where we note that we have used the same nondimensionalisation for T, p, and u in each region and we have thus omitted the subscripts. We note that α_p is the thermal

diffusivity of the porous medium, and is given by

$$\alpha_p = \frac{k_p}{\phi_a \rho_a c_a}, \tag{3.3.5}$$

where k_p is defined in (3.2.15). Substituting (3.3.2)–(3.3.4) into (3.2.1)–(3.2.24), (3.2.27)–(3.2.30) and (3.2.32)–(3.2.41) and subsequently dropping the hats, the dimensionless model for T_b, u_b, T_i, u_i, p_i, T_m, u_m, p_m, ϕ_s, T_u, in the case of no clogging, reads

$$\frac{\partial T_b}{\partial t} + u_b \frac{\partial T_b}{\partial y} = \alpha_{cp} \frac{\partial^2 T_b}{\partial y^2} \quad \text{in} \quad y < 0, \tag{3.3.6a}$$

$$\frac{\partial u_b}{\partial y} = 0, \quad \frac{\partial p_b}{\partial y} = 0 \quad \text{in} \quad y < 0, \tag{3.3.6b}$$

$$\frac{\partial T_i}{\partial t} + q\phi_c u_i \frac{\partial T_i}{\partial y} = \alpha_{ip} \frac{\partial^2 T_i}{\partial y^2} \quad \text{in} \quad 0 < y < b(t), \tag{3.3.6c}$$

$$\frac{\partial}{\partial y}(\phi_c u_i) = 0, \quad u_i = -\mathrm{Be} \frac{K(\phi_c)}{\phi_c} \frac{\partial p_i}{\partial y} \quad \text{in} \quad 0 < y < b(t), \tag{3.3.6d}$$

$$T_m = \theta_m \quad \text{in} \quad b(t) < y < c(t), \tag{3.3.6e}$$

$$\frac{\partial \phi_s}{\partial t} = 0, \quad \frac{\partial \phi_c}{\partial t} + \frac{\partial}{\partial y}(\phi_c u_m) = 0 \quad \text{in} \quad b(t) < y < c(t), \tag{3.3.6f}$$

$$u_m = -\mathrm{Be} \frac{K(\phi_c)}{\phi_c} \frac{\partial p_m}{\partial y} \quad \text{in} \quad b(t) < y < c(t), \tag{3.3.6g}$$

$$\frac{\partial T_u}{\partial t} = \frac{\partial^2 T_u}{\partial y^2} \quad \text{in} \quad c(t) < y < 1, \tag{3.3.6h}$$

where $K(\phi_c) = \phi_c^3/(1-\phi_c)^2$. The boundary conditions are

$$T_b \to 1 \quad \text{as} \quad y \to -\infty, \tag{3.3.7a}$$

$$T_b = T_i, \quad p_i = 0, \quad k_{ci} \frac{\partial T_b}{\partial y} = \frac{\partial T_i}{\partial y} \quad \text{on} \quad y = 0, \tag{3.3.7b}$$

$$T_i = \theta_m, \quad \frac{1}{k_{if} \alpha_{sp} \mathrm{St}} \phi_s \dot{b} = -\frac{\partial T_i}{\partial y} \quad \text{on} \quad y = b(t), \tag{3.3.7c}$$

$$p_i = p_m, \quad \phi_c^-(u_i - \dot{b}) = \phi_c^+(u_m - \dot{b}) - \phi_s^+\rho_r\dot{b} \quad \text{on} \quad y = b(t), \tag{3.3.7d}$$

$$T_u = \theta_m, \quad \frac{1}{k_{pf}\alpha_{sp}\mathrm{St}}\phi_s\dot{c} = -\frac{\partial T_u}{\partial y} \quad \text{on} \quad y = c(t), \tag{3.3.7e}$$

$$p_m = c(t)(1-\beta)Q + \left(1 - \frac{1}{r(\phi_c)}\right)\beta - 1 \quad \text{on} \quad y = c(t), \tag{3.3.7f}$$

$$\phi_s^-\rho_r\dot{c} = \phi_c^-\rho_c(u_c - \dot{c}) \quad \text{on} \quad y = c(t), \tag{3.3.7g}$$

$$\frac{\partial T_u}{\partial y} = -\mathrm{Nu}(T_u - \theta_e) \quad \text{on} \quad y = 1, \tag{3.3.7h}$$

where $r(\phi_c) = \frac{\phi_c^{3/2}}{1-\phi_c}$. Finally, the initial conditions become

$$c = b = 0 \quad \text{at} \quad t{=}\,0. \tag{3.3.8a}$$

$$T_u = 0 \quad \text{in} \quad 0 < y < 1, \quad T_b = 1 \quad \text{in} \quad y < 0 \quad \text{at} \quad t{=}\,0, \tag{3.3.8b}$$

When clogging occurs, for $t > t_c$ the system for T_b, u_b, T_i, u_i, T_m, ϕ_s, T_c, T_u reads

$$\frac{\partial T_b}{\partial t} + u_b\frac{\partial T_b}{\partial y} = \alpha_{cp}\frac{\partial^2 T_b}{\partial y^2} \quad \text{in} \quad y < 0, \tag{3.3.9a}$$

$$\frac{\partial u_b}{\partial y} = 0, \quad \frac{\partial p_b}{\partial y} = 0 \quad \text{in} \quad y < 0, \tag{3.3.9b}$$

$$\frac{\partial T_i}{\partial t} + q\phi_c u_i\frac{\partial T_i}{\partial y} = \alpha_{ip}\frac{\partial^2 T_i}{\partial y^2} \quad \text{in} \quad 0 < y < b(t), \tag{3.3.9c}$$

$$\frac{\partial}{\partial y}(\phi_c u_i) = 0, \quad u_i = -\mathrm{Be}\frac{K(\phi_c)}{\phi_c}\frac{\partial p_i}{\partial y} \quad \text{in} \quad 0 < y < b(t), \tag{3.3.9d}$$

$$T_m = \theta_m \quad \text{in} \quad b(t) < y < d(t), \tag{3.3.9e}$$

$$\frac{\partial \phi_s}{\partial t} = 0, \quad \frac{\partial \phi_c}{\partial t} + \frac{\partial}{\partial y}(\phi_c u_m) = 0 \quad \text{in} \quad b(t) < y < d(t), \tag{3.3.9f}$$

$$u_m = -\mathrm{Be}\frac{K(\phi_c)}{\phi_c}\frac{\partial p_m}{\partial y} \quad \text{in} \quad b(t) < y < d(t), \tag{3.3.9g}$$

$$\frac{\partial T_c}{\partial t} = \alpha_{fp}\frac{\partial^2 T_c}{\partial y^2} \quad \text{in} \quad d(t) < y < c_{\max}, \tag{3.3.9h}$$

$$\frac{\partial T_u}{\partial t} = \frac{\partial^2 T_u}{\partial y^2} \qquad \text{in} \quad c_{\max} < y < 1, \tag{3.3.9i}$$

with boundary conditions given by

$$T_b \to 1 \qquad \text{as} \quad y \to -\infty, \tag{3.3.10a}$$

$$T_b = T_i, \quad k_{ci}\frac{\partial T_b}{\partial y} = \frac{\partial T_i}{\partial y} \qquad \text{on} \quad y = 0, \tag{3.3.10b}$$

$$T_i = \theta_m, \quad \frac{1}{k_{if}\alpha_{sp}\mathrm{St}}\phi_s\dot{b} = -\frac{\partial T_i}{\partial y} \qquad \text{on} \quad y = b(t), \tag{3.3.10c}$$

$$\phi_c^-(u_i - \dot{b}) = \phi_c^+(u_m - \dot{b}) - \phi_s^+\rho_r\dot{b} \qquad \text{on} \quad y = b(t), \tag{3.3.10d}$$

$$T_c = \theta_m, \quad \frac{1}{k_{sf}\alpha_{sp}\mathrm{St}}\phi_c^-\dot{d} = -\frac{\partial T_u}{\partial y} \qquad \text{on} \quad y = d(t), \tag{3.3.10e}$$

$$-\phi_s^+\rho_r\dot{b} = \phi_c^-(u_i - \dot{b}) - \phi_s^-\dot{b} \qquad \text{on} \quad y = d(t), \tag{3.3.10f}$$

$$T_c = T_u, \quad \frac{\partial T_c}{\partial y} = k_{pf}\frac{\partial T_u}{\partial y} \qquad \text{on} \quad y = c_{\max}, \tag{3.3.10g}$$

$$\frac{\partial T_u}{\partial y} = -\mathrm{Nu}(T_u - \theta_e) \qquad \text{on} \quad y = 1. \tag{3.3.10h}$$

The initial conditions for the clogged case are the solutions to (3.3.6)–(3.3.8) evaluated at $t = t_c$. We have introduced the following 18 dimensionless parameters. We collate these into two groups of nine. The first group is:

$$q = \frac{1}{\phi_c + \phi_a\frac{\rho_a c_a}{c_c\rho_c}}, \quad \mathrm{Be} = \frac{(\gamma/a + \rho_c g H_d)\,a^2}{180\alpha_p\mu_c}, \quad \theta_m = \frac{T_m^* - T_a^*}{T_b^* - T_a^*}, \quad \mathrm{Nu} = \frac{Hh}{k_p}, \quad \rho_r = \frac{\rho_s}{\rho_c},$$
$$\mathrm{St} = \frac{(T_b^* - T_a^*)c_s}{L}, \quad \beta = \frac{\gamma/a}{(\gamma/a + \rho_c g H_d)}, \quad \theta_e = \frac{T_{top} - T_a^*}{T_b^* - T_a^*}, \quad Q = \frac{H}{H_d}, \tag{3.3.11}$$

where q is the ratio of heat capacities of the liquid and the total heat capacity in the infiltrated region, Be is the *Bejan number*, which is a nondimensional pressure drop, θ_m is the dimensionless melting temperature, Nu is the *Nusselt number*, which is a measure of how easy it is to exchange energy between the porous medium and the

surrounding atmosphere, ρ_r is the density ratio of frozen to liquid cryolite, St is the *Stefan number*, which is the ratio of *sensible* heat (the heat required to change the temperature of a given mass of substance) to the latent heat (the heat required to change the phase of a given mass of substance), β is ratio of the pore pressure and the total pressure, θ_e is the dimensionless ambient temperature, and Q is the depth ratio, indicating how much of the raft is above the surface of the cryolite bath. In the absence of experimental data, we will assume $Q = 1$, that is, the top surface of the raft is level with the bath surface, and we will vary Nu to explore the effect of heat transfer at the top of the raft on the behaviour of the system.

The second group of parameters involves the ratios of the different thermal diffusivities α_{cp}, α_{ip}, α_{sp}, α_{fp} and heat conductivities k_{ci}, k_{if}, k_{st}, k_{sp}, k_{pf}, denoted by $\alpha_{ij} = \alpha_i/\alpha_j$ and $k_{ij} = k_i/k_j$, where the thermal diffusivities are given by

$$\alpha_c = \frac{k_c}{\rho_c c_c}, \quad \alpha_s = \frac{k_s}{\rho_s c_s}, \quad \alpha_i = \frac{k_a^{\phi_a} k_c^{\phi_c}}{\rho_a c_a \phi_a + \phi_c \rho_c c_c}, \quad \alpha_f = \frac{k_a^{\phi_a} k_s^{\phi_s}}{\rho_a c_a \phi_a + \rho_s c_s \phi_s}, \tag{3.3.12}$$

and where α_p is defined in (3.3.5). In Table 3.1 we present the typical values of the dimensionless parameters using the typical values of the dimensional parameters presented in Table 1.1. We note that the "superheat" $1 - \theta_m$ is small and that Be is large. Furthermore, α_{cp}, α_{sp} and $1 - \beta$ are also small, but we do not focus on those limits in this analysis. We note that we do not have an experimentally provided value for the convective coefficient, h. Thus, the size of the Nusselt number is unknown and, consequently, we will explore the behaviour of the model as the Nusselt number varies.

3.4 Small-superheat approximation

Since the melting temperature θ_m is near 1, we seek an asymptotic solution for small $\varepsilon = 1 - \theta_m$.

Parameter		Value
Diffusivity ratio	α_{cp}	0.36
Diffusivity ratio	α_{ip}	2.06
Diffusivity ratio	α_{sp}	0.89
Diffusivity ratio	α_{fp}	2.99
Conductivity ratio	k_{ci}	0.22
Conductivity ratio	k_{if}	2.42
Conductivity ratio	k_{pf}	0.6
Conductivity ratio	k_{sf}	0.56
Conductivity ratio	k_{sp}	10.23
Relative heat capacity	q	1.23
Effect of pore-size change	β	0.92
Bejan number	Be	25
Top temperature	θ_e	0.05
Melting temperature	θ_m	0.98
Stefan number	St	2.55
Density ratio	ρ_r	1.001
Height ratio	Q	1
Nusselt number	Nu	not known

Table 3.1: Non-dimensional parameters using the mean physical properties presented in Table 1.1.

3.4.1 Unclogged problem

We expand the dependent variables in powers of ε (for example, writing $T_b = T_b^{(0)} + \mathrm{O}(\varepsilon)$ as $\varepsilon \to 0$), and we find that the solutions to the leading-order problems for T_b, T_i and T_m from (3.3.6a), (3.3.6c), (3.3.6e), (3.3.7a)–(3.3.7c) and (3.3.8b) are $T_b^{(0)} = T_i^{(0)} = T_m^{(0)} = 1$. This also means that the melting front in the leading-order problem does not move, with (3.3.7b) giving $b^{(0)} = 0$. The remaining equations provide the leading-order problem for $c^{(0)}(t)$, $u_m^{(0)}(y,t)$, $T_u^{(0)}(y,t)$, and

$$S^{(0)}(y,t) := \frac{\phi_s^{(0)}(y,t)}{1-\phi_a}, \tag{3.4.1}$$

where $S^{(0)}$ represents the fraction of the pore space that is solid. Substituting our expansions into (3.3.6), dropping terms of $\mathrm{O}(\varepsilon)$ or smaller and dropping the order

notation, the leading-order problem for the remaining unknowns becomes

$$\frac{\partial}{\partial y}\left((1-S)u_m\right) = 0 \qquad \text{in} \qquad 0 < y < c(t), \tag{3.4.2a}$$

$$\frac{\partial S}{\partial t} = 0 \qquad \text{in} \qquad 0 < y < c(t), \tag{3.4.2b}$$

$$(1-S)u_m = -\hat{\mathrm{Be}}\hat{K}(S)\frac{\partial p_m}{\partial y} \qquad \text{in} \qquad 0 < y < c(t), \tag{3.4.2c}$$

$$\frac{\partial T_u}{\partial t} = \frac{\partial^2 T_u}{\partial y^2} \qquad \text{in} \quad c(t) < y < 1, \tag{3.4.2d}$$

where we have defined $\hat{K}(S) = K((1-\phi_a)(1-S))$ and

$$\hat{\mathrm{Be}} = (1-\phi_a)\mathrm{Be} = \frac{a^2\left(\gamma/a + \rho_c g H_d\right)(1-\phi_a)}{180\alpha_p \mu_c}. \tag{3.4.3}$$

The leading-order boundary conditions are given by

$$p_m = 0 \qquad \text{at} \quad y = 0, \tag{3.4.4a}$$

$$T_u = 1, \quad AS\dot{c} = -\frac{\partial T_u}{\partial y} \qquad \text{at} \quad y = c(t), \tag{3.4.4b}$$

$$p_m = B(S), \quad \dot{c} = u\frac{1-S}{1+S(\rho_r - 1)} \qquad \text{at} \quad y = c(t), \tag{3.4.4c}$$

$$T_u = 0 \qquad \text{at} \quad y = 1, \tag{3.4.4d}$$

where

$$A = \frac{(1-\phi_a)}{\alpha_{sp} k_{pf} \mathrm{St}} = \frac{(1-\phi_a)\rho_s L}{\phi_a \rho_a c_a (T_b^* - T_a^*)}, \quad B(S) = -\frac{1}{r((1-\phi_a)(1-S))}. \tag{3.4.5}$$

We note that $B(S)$ is the capillary pressure which depends on the volume fraction of frozen cryolite. The initial conditions are given by

$$T_u = 0 \quad \text{at} \quad t = 0 \quad \text{in} \quad 0 < y < 1, \tag{3.4.6a}$$

$$c = 0 \quad \text{at} \quad t = 0. \tag{3.4.6b}$$

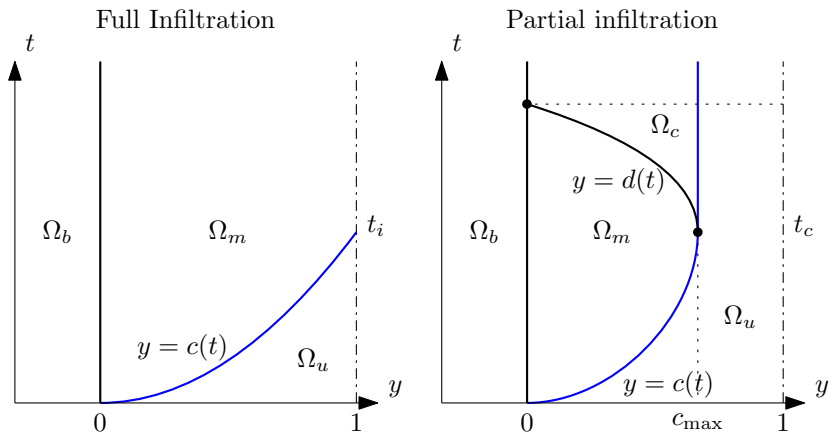

Figure 3.5: Sketch of the small-superheat limit and the two possible outcomes depending on the value of Nu. For the partial infiltration, after t_c the geometry of the problem changes, requiring a different model which is presented in Section 3.4.2.

Equations (3.4.2a)–(3.4.2c) describe the problem in the mushy region, meanwhile (3.4.2d) describes the heat-transfer problem in the uninfiltrated region.

In order to make the system as compact as we can for solving it numerically, we integrate (3.4.2a) and (3.4.2b) and apply (3.4.4c) to find

$$S(y,t) = S(y), \quad (1 - S(y))u_m = \dot{c}\,(1 + S(c(t))(\rho_r - 1))\,, \tag{3.4.7}$$

where $(1 - S(y))u_m$ is the liquid flux, and $S(y)$ the spatial distribution of solid cryolite after it has been deposited by the front. In order to simplify the notation slightly, we will also define $S_c(t) = S(c(t))$. We integrate (3.4.2c) and use (3.4.4a) to find that

$$\dot{c}(1 + S_c(t)(\rho_r - 1))I(t) = -B(S_c(t)), \tag{3.4.8}$$

where I, the total resistance of the flow across the infiltrated region, is given by

$$I(t) = \int_0^{c(t)} \left(\hat{\mathrm{Be}}\hat{K}(S(y))\right)^{-1} \mathrm{d}y\,. \tag{3.4.9}$$

Using the Leibniz integral rule, we differentiate (3.4.9) to get an evolution equation

for $I(t)$, which is given by

$$\dot{I} = \dot{c}\Big(\hat{\mathrm{Be}}\hat{K}(S_c(t))\Big)^{-1}; \tag{3.4.10}$$

we note that, by inserting $c(0) = 0$ into (3.4.9), we arrive at the initial condition $I(0) = 0$.

Thus, the system (3.4.2a) to (3.4.6b) can be reduced to solving

$$\frac{\partial T_u}{\partial t} = \frac{\partial^2 T_u}{\partial y^2} \quad \text{in} \quad c(t) < y < 1, \tag{3.4.11}$$

and

$$\dot{c} = \frac{J(S_c(t))}{I}, \quad \dot{I} = \frac{J(S_c(t))}{\hat{\mathrm{Be}} I \hat{K}(S_c(t))}, \tag{3.4.12}$$

where $S_c(t)$ is calculated from

$$S_c(t) = -\left.\frac{\partial T_u}{\partial y}\right|_{y=c} \frac{I}{AJ(S_c(t))}. \tag{3.4.13}$$

and, for simplicity, we introduce the function $J(S)$ given by

$$J(S) = \frac{-B(S)}{(1 + S(\rho_r - 1))}. \tag{3.4.14}$$

The boundary and initial conditions are

$$T_u = 1 \quad \text{at} \quad y = c(t), \quad \frac{\partial T_u}{\partial y} = -\mathrm{Nu}\,(T_u - \theta_e) \quad \text{at} \quad y = 1, \tag{3.4.15}$$

$$T_u = 0 \quad \text{for} \quad 0 < y < 1 \quad \text{at} \quad t = 0, \tag{3.4.16}$$

$$c = 0, \quad I = 0 \quad \text{at} \quad t = 0. \tag{3.4.17}$$

We have reduced the problem to a coupled system comprising a partial differential equation for $T(y,t)$, two ordinary differential equations for $c(t)$, $I(t)$, and an algebraic equation for $S_c(t)$, along with appropriate boundary and initial conditions.

3.4.2 Clogged problem

Again, we seek an asymptotic solution for small $\varepsilon = 1 - \theta_m$. We expand all the dependent variables in (3.3.9) and (3.3.10) in the form $T_b = T_b^{(0)} + \mathrm{O}(\varepsilon)$ as $\varepsilon \to 0$ and find that the leading order solution is $T_b^{(0)} = T_i^{(0)} = T_m^{(0)} = 1$ with $b^{(0)} = 0$. The remaining equations for the leading-order versions of $T_u(y,t)$ and $T_c(y,t)$ are

$$\frac{\partial T_u}{\partial t} = \frac{\partial^2 T_u}{\partial y^2} \quad \text{in} \quad c_{\max} < y < 1, \tag{3.4.18a}$$

$$\frac{\partial T_c}{\partial t} = \alpha_{fp}\frac{\partial^2 T_c}{\partial y^2} \quad \text{in} \quad d(t) < y < c_{\max}, \tag{3.4.18b}$$

with boundary conditions

$$T_c = 1, \quad k_{pf}A(1 - S(d))\dot{d} = \frac{\partial T_c}{\partial y} \quad \text{at} \quad y = d(t), \tag{3.4.18c}$$

$$T_c = T_u, \quad \frac{\partial T_c}{\partial y} = k_{pf}\frac{\partial T_u}{\partial y} \quad \text{at} \quad y = c_{\max}, \tag{3.4.18d}$$

$$\frac{\partial T_u}{\partial y} = -\mathrm{Nu}(T_u - \theta_e) \quad \text{at} \quad y = 1, \tag{3.4.18e}$$

where the initial conditions, and $S(y)$, are given by the state of the system at the end of the previous, unclogged, stage, namely

$$S = S_{clog}(y) \quad \text{at} \quad t = t_c, \quad \text{in} \quad c_{\max} < y < 1, \tag{3.4.18f}$$

$$T_u = T_{clog}(y) \quad \text{at} \quad t = t_c, \quad \text{in} \quad c_{\max} < y < 1, \tag{3.4.18g}$$

$$q = c_{\max} \quad \text{at} \quad t = t_c. \tag{3.4.18h}$$

In the rest of the chapter, we will work with these small-superheat approximations and investigate their behaviour at early time using asymptotic methods, and later times numerically.

3.5 Early-time solution

We seek an asymptotic self-similar solution to the system (3.4.11)–(3.4.17) of the form

$$T_u \sim g(\eta), \quad c \sim 2\lambda_c\sqrt{t}, \quad I \sim 2\lambda_I\sqrt{t}, \quad S_c \sim \bar{S}, \tag{3.5.1}$$

where $\eta = y/(2\sqrt{t}) = \mathrm{O}(1)$ as $t \to 0^+$ and the function $g(\eta)$ and constants λ_c, λ_I and $\bar{S}$ are to be determined. It follows from (3.4.11) and (3.4.15) that the system that we need to solve is

$$g'' + 2\eta g' = 0 \quad \text{in} \quad \eta > \lambda_c, \tag{3.5.2}$$

with

$$g = 1 \quad \text{on} \quad \eta = \lambda_c, \quad g \to 0 \quad \text{as} \quad \eta \to \infty, \tag{3.5.3}$$

which has the solution

$$g(\eta) = \frac{\operatorname{erfc}(\eta)}{\operatorname{erfc}(\lambda_c)}. \tag{3.5.4}$$

Using (3.4.12) and (3.4.13), we solve for λ_I and λ_c to find that

$$\lambda_I = \sqrt{\frac{J(\bar{S})}{2\hat{\mathrm{Be}}\hat{K}(\bar{S})}}, \quad \lambda_c = \sqrt{\frac{\hat{\mathrm{Be}}J(\bar{S})\hat{K}(\bar{S})}{2}}, \tag{3.5.5}$$

where we have taken the positive square root for λ_I (giving that the front moves into the porous medium initially). Equation (3.4.13) implies that $\bar{S}$ satisfies

$$\frac{1}{A} = \sqrt{\pi}\exp\left(G(\bar{S})^2\right)\operatorname{erfc}(G(\bar{S}))G(\bar{S})\bar{S}, \tag{3.5.6}$$

where $G(\bar{S}) = \sqrt{\hat{\mathrm{Be}}J(\bar{S})\hat{K}(\bar{S})/2}$. Equation (3.5.6) is similar to conditions that arise in one-phase Stefan problems [31] but, in our case, the nonlinear function $G(\bar{S})$ complicates further analysis. Here, we know that G is positive when $0 < \bar{S} < 1$ and that $G(0) = G(1) = 0$, because of the form of the permeability function. We plot the

left-hand side and the right-hand side of (3.5.6) in Figure 3.6 to show that there are either 0, 1 or 2 roots (the intersections between the blue and black curves) depending on the values of the parameters $\hat{\text{Be}}$ and A due to the nonmonotonicity of $G(\bar{S})$. If $A < 1$, then no solution is possible because the right-hand side of (3.5.6) lies strictly between 0 and 1. Interestingly, a similar observation was found in a different setting, namely the modelling of liquid infiltration into a hot porous media with an evaporating front [94].

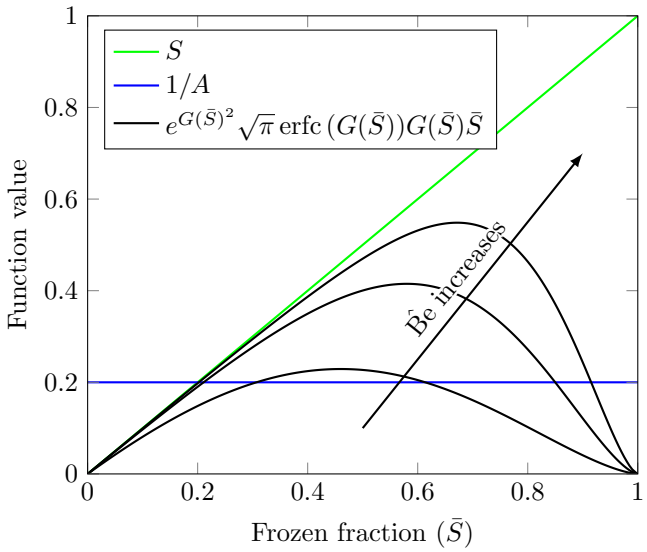

Figure 3.6: Graph showing the left-hand side of (3.5.6) (blue) and the right-hand side of (3.5.6) (black) as a function of frozen fraction, $\bar{S}$, for $\hat{\text{Be}} = 10, 100, 500$.

One immediate implication of the fact that we can have 0, 1 or 2 solutions to the early-time problem is that the infiltrating solution outlined in this chapter does not always exist. When our infiltrating model predicts no solutions, instead a qualitatively different solution must occur. One possible alternative solution is that the cryolite solidifies on the external surface of the porous medium, giving a similar problem to the one considered in Chapter 2. We show the region of parameter space where we expect to get zero or two solutions in Figure 3.7. We show the current operating conditions as a shaded ellipse, where the size of the disc indicates our uncertainty in the parameters. We see that the operating regime is close to the boundary between

two and zero solutions, suggesting that small changes in the feedstock might result in large changes in the behaviour of the system. We see that the centre of the ellipse is in the region where no infiltrating solution are possible, which suggests that a porous raft placed on the cryolite bath would exhibit surface freezing initially. We also conclude that, in order to prevent the initial freezing of the cryolite on the surface of the raft, it is more important to increase A than increase $\hat{\mathrm{Be}}$, for example by heating up the raft before putting it into the cryolite.

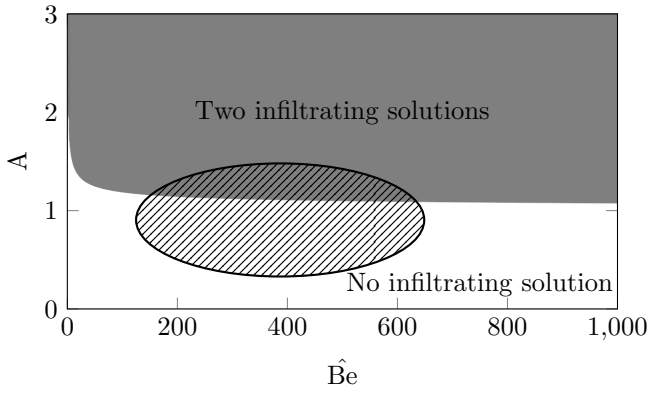

Figure 3.7: Regime diagram of the possible solutions of (3.5.6) varying A and $\hat{\mathrm{Be}}$. The parameter values corresponding to the operating regime are marked by a shaded ellipse.

In Figure 3.8 we plot the temperature in the uninfiltrated region and the frozen fraction as a function of the similarity variable. We see that the solution that corresponds to higher frozen fraction propagates slower than the one with the smaller frozen fraction, since the λ_c value is smaller.

In the rest of the section, we vary the parameters to see what effect they have on the solutions. In each case we plot $\bar{S}$ versus $\hat{\mathrm{Be}}$. First, we vary ρ_r to investigate the effect of density change on the behaviour of the roots of (3.5.6), and we show the results in Figure 3.9 (left) for $\rho_r = 1/2, 1, 2$ (we do not anticipate a large change in ρ_r from the parameter uncertainty in Table 1.1). We see that, for a given $\hat{\mathrm{Be}}$ there are either 0, 1 or two solutions, and the region of parameter space in which there are no solutions increases as ρ_r increases. We also see that the lower value of $\bar{S}$ is

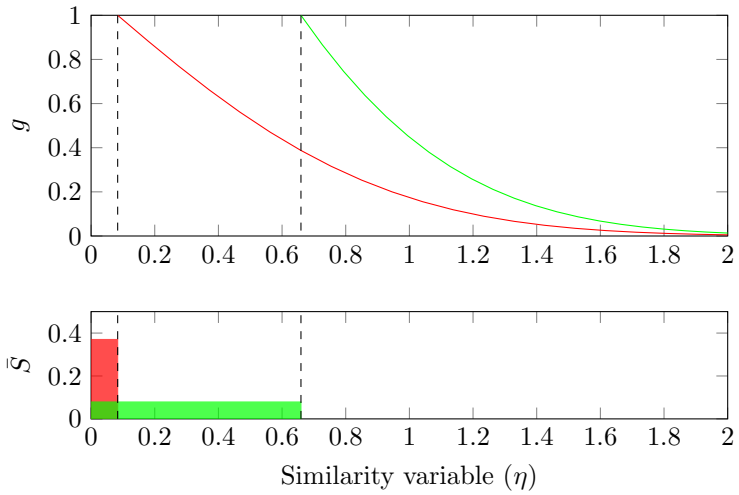

Figure 3.8: Temperature and frozen fraction as a function of the similarity variable. The solution in red is the unstable one and the green is the stable one. The parameters are $A = 10$, $\hat{\text{Be}} = 10$. The vertical lines indicate the two values of λ_c and thus the positions of the two potential infiltrating fronts.

independent of ρ_r for $\hat{\text{Be}}$ large.

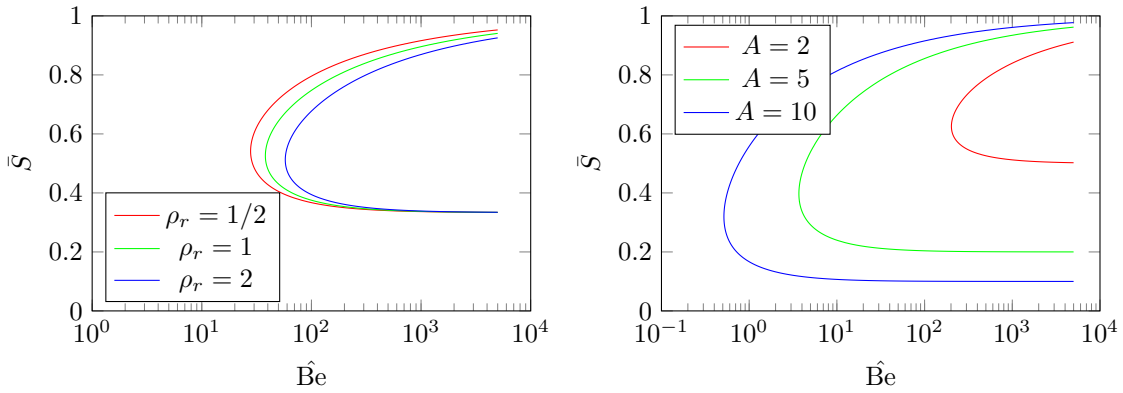

Figure 3.9: Scaled frozen fraction as a function of $\hat{\text{Be}}$ for (left) different values of density ratio given by $\rho_r = 1/2, 1, 2$, with $A = 5$, and (right) for different values of A given by $A = 2, 5, 10$ for $\rho_r = 1$.

Since

$$A = \frac{L\rho_s(1-\phi_a)}{c_a\rho_a(T_b^* - T_a^*)\phi_a}, \tag{3.5.7}$$

is the ratio of the heat released by freezing the cryolite present in the pore space to the heat needed to raise the temperature of the particles, A corresponds to how easy it is to freeze the material. If this ratio is less then one, then it means that the cold

particles that make up the porous medium can freeze more cryolite than the amount that can fit in the pore space. Since the freezing process is faster than all the other processes in the model, this shows up as non-existence of solutions. In Figure 3.9 (right), as we increase A we see that the lower value of $\bar{S}$ decreases, and that the region of space in which we have two solutions increases. This can also be seen in Figure 3.6, where we see that, for a given A, solutions only exist above a critical value of $\hat{\mathrm{Be}}$.

In all cases, there are values of $\hat{\mathrm{Be}}$ for which there are no solutions to this early-time problem. We recall that $\hat{\mathrm{Be}}$:

$$\hat{\mathrm{Be}} = \frac{(\gamma/a + \rho_c g H_d)\, a^2(1-\phi_a)}{180\alpha_p \mu_c}, \tag{3.5.8}$$

so, in terms of the physical parameters, we would not expect to have an infiltrating solution when, for example, the viscosity of the liquid is large, or the driving pressure is small.

3.6 Numerical results

To solve (3.4.11)–(3.4.17) numerically, we map (3.4.11) to a fixed domain $0 < \zeta < 1$ using

$$\zeta = \frac{y - c(t)}{1 - c(t)}, \tag{3.6.1}$$

then discretise spatially using central differences. We solve the resulting set of ODEs along with (3.4.12) and (3.4.13) using an adaptive backward differentiation method with `NDSolve` implemented in `Mathematica 12.1`. As in Chapter 2, since initially there is no infiltrated region, we use the small-time similarity solution in Section 3.5 to initiate our solver by prescribing the small-time solution at $t = 10^{-5}$. We solve the clogged model (3.4.18) similarly, by transforming $d(t) < y < c_{\max}$ to a fixed domain

$0 < \xi < 1$ using

$$\xi = \frac{y - d(t)}{c_{\max} - d(t)}, \tag{3.6.2}$$

and solve (3.4.18) using the method of lines. We note that we do not need to map (3.4.18a) to a fixed domain, because during this stage of the process this region does not have a moving boundary.

We present the solution to (3.4.11)–(3.4.13) in Figure 3.10, where we show the evolution of the temperature through the raft at different times during the infiltration phase (left) and the backwards freezing phase (right). We show the temperature distribution at $t = t_c$ as red lines and the clogging position as a vertical dotted line (in Figure 3.10 (right)), which partitions the region into frozen (to the left of the line) and dry regions (to the right of the line). We see in Figure 3.10 (left) that, as the infiltration front moves, the temperature gradient becomes steeper, while in Figure 3.10 (right), we see that the temperature gradient decreases as the clogging front moves.

In Figure 3.11 (left), we show the deposited frozen fraction as a function of position during the infiltrating phase. We see that, as the front moves in, the frozen fraction initially remains constant at $\bar{S}$, the value given by the early time solution (3.5.6), then gradually increases and reaches 1 at a finite time. To further evaluate the behaviour of the frozen fraction near the blow-up, in Figure 3.11 (right) we also show the liquid fraction near the clogging point; we see that the numerics suggest, and further analysis (in Section 3.7) near the clogging time confirms, that the frozen fraction follows a power law given by $1 - S \sim (t - t_c)^{1/4}$.

Finally, we show the vertical position of the infiltration front (black) and the clogging front (blue) as a function of time in Figure 3.12. We see that the numerical solution (solid lines) closely follows the early time solution denoted by a dashed red line, but then stops because $\dot{c} \to 0$ as $t \to t_c$. After this, a clogging front (blue) is initiated which moves in the opposite direction. We might expect this front to move

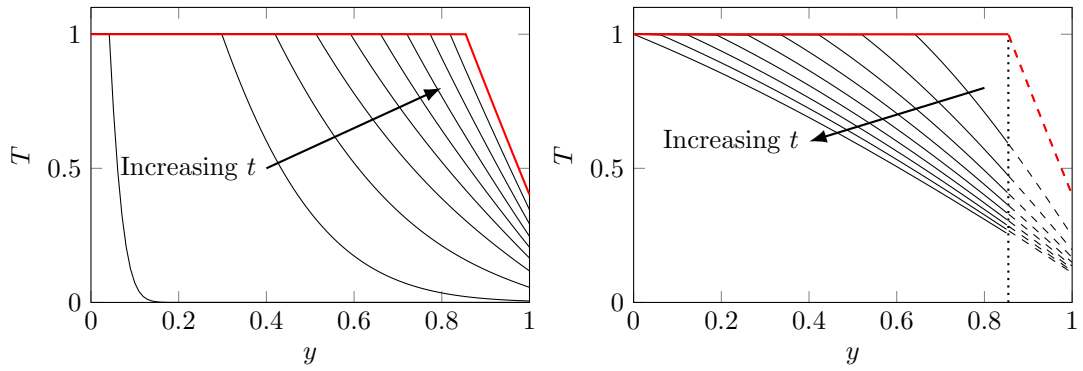

Figure 3.10: Graphs showing the spatial distribution of temperature at different times (left) during the infiltration phase, given by solving (3.4.11)–(3.4.17) for T_m and T_u, and (right) during the backwards freezing stage, given by solving (3.4.18) for T_m, T_c and T_u. The temperature distribution when the pores clog is shown in red. The vertical solid line denotes the clogging position. Parameters are $\hat{\mathrm{Be}} = 10$, $A = 10$, and $\mathrm{Nu} = 10$.

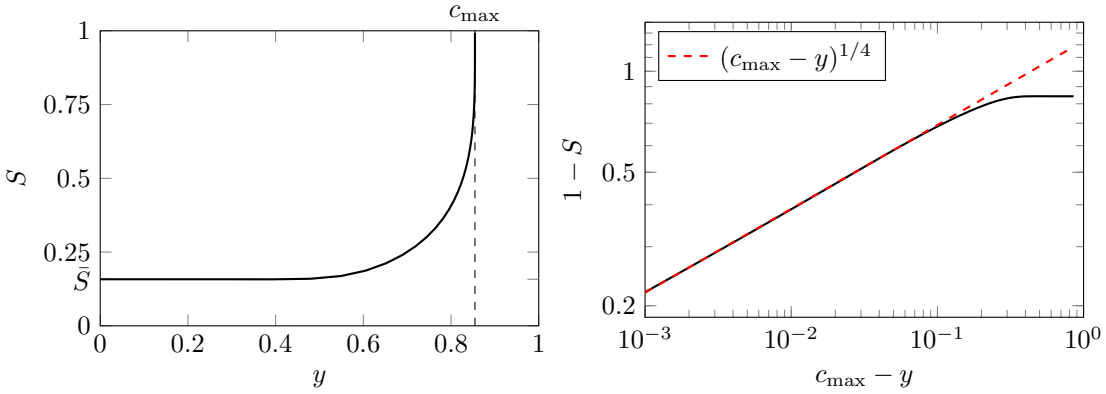

Figure 3.11: Graphs showing the deposited frozen fraction as a function of the vertical position (left) and the liquid fraction as a function of the distance from $c_{\max}$ (right) at the clogging time. The $\bar{S}$ in the left-hand graph denotes the value of the frozen fraction using the similarity solution given by (3.5.6). Parameters are $\hat{\mathrm{Be}} = 10$, $A = 10$, and $\mathrm{Nu} = 10$.

according to a $\sqrt{t}$ law. However, on closer inspection (right), we can see that, at early times ($t - t_c \ll \mathrm{O}(1)$), the front moves like $(t - t_c)^{4/5}$. This is due to the fact that S is now spatially dependent and looks like a power-law near t_c, which introduces a deviation from the $\sqrt{t}$ behaviour. We expect that this behaviour is only valid locally near t_c. In order to check this, we plot the distance of the clogging front from the maximum infiltration point $c_{\max}$ in Figure 3.12 (right), which shows that at small times the $(t - t_c)^{4/5}$ law is appropriate, but at later times it changes to $\sqrt{t - t_c}$.

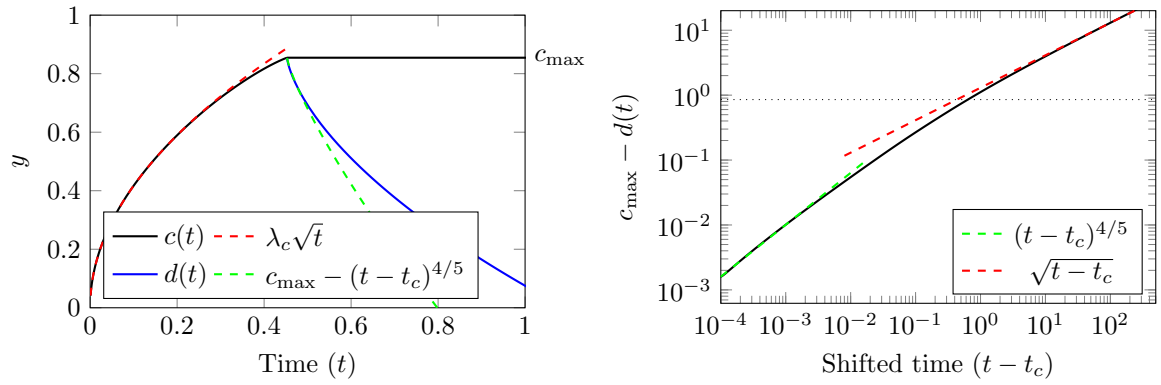

Figure 3.12: Left: Graphs showing the location of the infiltration front (black) and the clogging front (blue) along with asymptotic solutions in dashed (right). Right: Graph showing the position of the shifted clogging front location $c_{\max} - d(t)$ as a function of the shifted time $t - t_c$ along with the asymptotic limits in dashed lines. Dotted line denotes the boundary of the porous medium. Parameters are $\hat{\mathrm{Be}} = 10$, $A = 10$, and $\mathrm{Nu} = 10$.

We now investigate the effect of changing the Nusselt number on the stopping time t_{stop} given by

$$t_{\text{stop}} = \min(t_i, t_c), \tag{3.6.3}$$

where t_i denotes the time at which the infiltration front reaches the top surface of the raft, and t_c denotes the time at which the infiltration front clogs.

In Figure 3.13 we show how the infiltration time changes as we change Nu for different ambient temperatures θ_e. We see that, as we decrease the ambient temperature θ_e, the infiltration time increases from the isothermal infiltration time given by

$$t_{iso} = \frac{\hat{\mathrm{Be}} K(1 - \phi_a)}{2}, \tag{3.6.4}$$

found by solving Darcy flow with infiltration boundary condition (3.4.4c) without any freezing or melting. Thus phase change slows down the propagation of the infiltration front. We see that, for a given θ_e, there is a value of Nu at which we switch between complete and partial infiltration. This value, which we call Nu^*, gives the maximum stopping time for a given value of θ_e. We observe that, as θ_e increases, Nu^* increases.

We recall that, in the large Nusselt number limit, the temperature at the top of the raft is equal to the temperature in the atmosphere, which is less than the melting temperature. We thus expect the front to clog and stop because the temperature has to pass through the freezing temperature at some internal point in the raft. Conversely, in the small Nusselt number limit, the liquid infiltrates without clogging, since the top of the raft significantly reduces energy loss to the atmosphere.

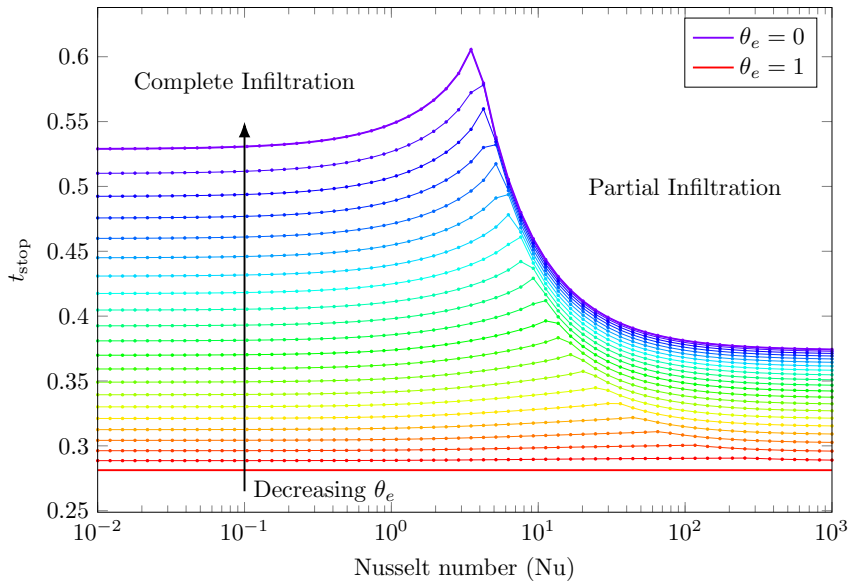

Figure 3.13: Stopping time t_{stop} given by (3.6.3) as a function of Nu for different ambient temperatures $\theta_e = 0, 0.05, \ldots, 1$. The red line without markers corresponds to isothermal infiltration calculated from (3.6.4).

In Figure 3.14, we show how the infiltration height, $c_{\max}$, varies as a function of Nu and θ_e, along with the boundary $\text{Nu}^*(\theta_e)$ that separates the solutions in which complete infiltration occurs from those in which partial infiltration occurs. We see qualitatively what we would expect intuitively, namely that, if the ambient temperature θ_e is low and the convective cooling Nu is strong enough, the front will stop, while if the temperature is above a certain value, then no clogging can happen.

In Figure 3.15 we plot S_c, given by (3.4.13), versus time, initiating the simulations with initial conditions close to the similarity solutions given by (3.5.6). We see that the similarity solution with the smaller value of $\bar{S}$ attracts the solutions, while the

similarity solution with the larger value of $\bar{S}$ repels them. This suggests that the root with smaller $\bar{S}$ is stable, and the other one is unstable. We will explore the linear stability of these solutions in Section 3.8.

3.7 Near clogging analysis

We see in Figures 3.11 and 3.12 that the liquid fraction $1 - S(c(t))$ before the clogging, and $d(t)$ after the clogging, show power-law behaviour in t. In this section we aim to explain these power-law behaviours by further analysis of (3.4.11)–(3.4.13) with a method analogous to the one presented in [4].

For simplicity, we set $\rho_r = 1$ (i.e. we assume that there is no density difference between the liquid and frozen cryolite) and we set $B(S) = -1$ (i.e. we assume that the capillary pressure does not change with frozen fraction), giving $J(S) = 1$. This makes the analysis simpler to follow, but should not change the qualitative behaviour. Furthermore, we let $S_c(t) = S(c(t))$. With these simplifications, (3.4.11)–(3.4.13)

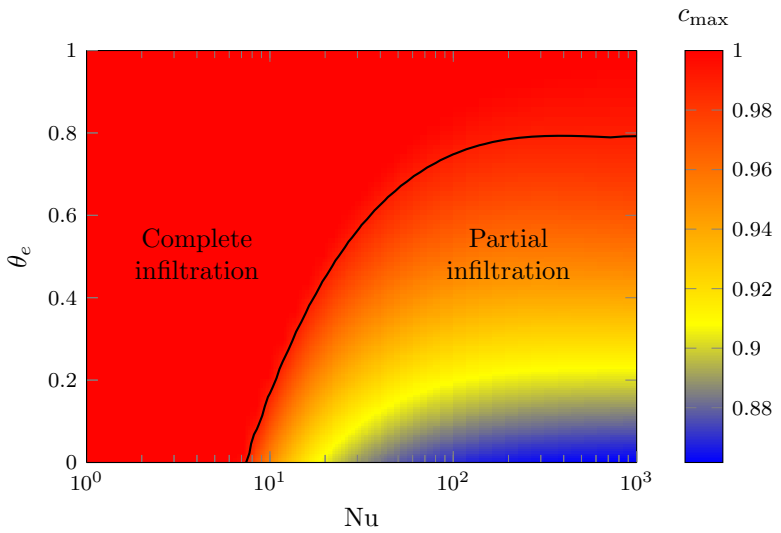

Figure 3.14: Contour plot of $c_{\max}$ as a function of Nu and θ_e, showing where the complete and partial infiltration happen in the parameter space. The black line is $\mathrm{Nu}^*(\theta_e)$. For $\mathrm{Nu} < \mathrm{Nu}^*$ the front always infiltrates completely for all ambient temperatures.

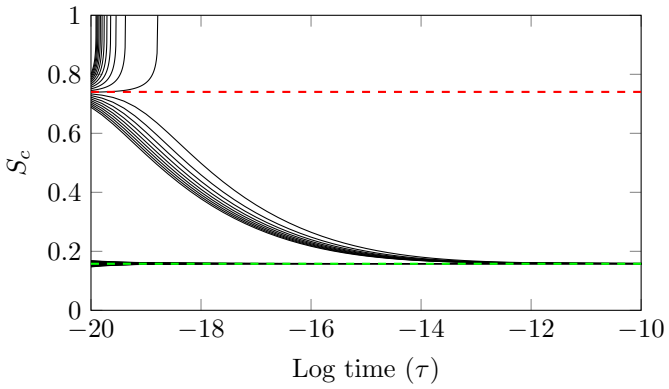

Figure 3.15: Graph of S_c given by (3.4.13) as a function of τ, for various initial conditions close to the similarity solutions. The red dashed line is the unstable similarity solution, while the green dashed line is the stable similarity solution. The parameters are $\hat{\mathrm{Be}} = 10$, $A = 10$, and $\phi_0 = 0.5$.

become

$$\frac{\partial T_u}{\partial t} = \frac{\partial^2 T_u}{\partial y^2} \quad \text{in} \quad c(t) < y < 1, \tag{3.7.1}$$

$$\dot{c} = \frac{1}{I}, \quad \dot{I} = \frac{1}{\hat{\mathrm{Be}} I \hat{K}(S_c)}, \quad S_c = -\frac{I}{A} \left. \frac{\partial T_u}{\partial y} \right|_{y=c}, \tag{3.7.2}$$

with boundary and initial conditions given by

$$T_u = 1 \quad \text{at} \quad y = c(t), \quad \frac{\partial T_u}{\partial y} = -\mathrm{Nu}\,(T_u - \theta_e) \quad \text{at} \quad y = 1, \tag{3.7.3}$$

$$T_u = 0 \quad \text{for} \quad 0 < y < 1 \quad \text{at} \quad t = 0, \tag{3.7.4}$$

$$c = 0, \quad I = 0 \quad \text{at} \quad t = 0, \tag{3.7.5}$$

and $\hat{K}$ is given by

$$\hat{K}(S_c) = \frac{(1-\phi_0)^3}{(1-(1-\phi_0)(1-S_c))^2}(1-S_c)^3, \tag{3.7.6}$$

where we note that $\hat{K} \to 0$ as $S_c \to 1$, which makes the problem singular due to the second equation in (3.7.2). In order to aid our analysis, we plot our numerical solutions for c, S_c, and I near clogging in Figure 3.16, along with guesses for the

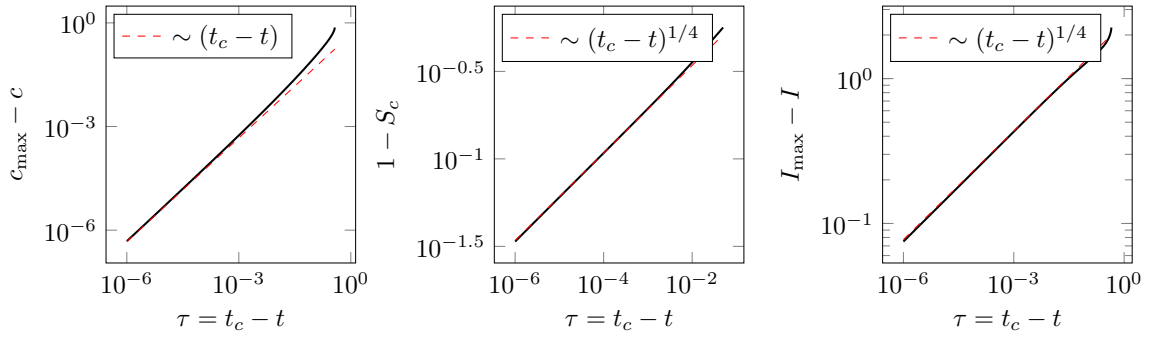

Figure 3.16: Figures showing the power-law relationships between $c_{\max} - c$, $1 - S_c$, $I_{\max} - I$, and $t_c - t$. The solid lines are the numerical solutions of the problem, meanwhile the red dashed lines are the near-clogging asymptotic expressions given by (3.7.21), (3.7.25) and (3.7.26). Parameters are $\hat{\mathrm{Be}} = 10$, $A = 10$, and $\mathrm{Nu} = 10$.

power-law behaviour (these guesses will be shown to be justified later). In each case, the subscript max refers to the value of these functions at the clogging time, we note from Figure (3.10), that T_u is approximately linear even before we approach the clogging time. Our goal is to analyse the near-clogging behaviour, so we recast the variables using

$$t = t_c - \varepsilon\tau, \quad c(t) = c_{\max} - \varepsilon\xi(\tau), \quad I(t) = I_{\max} - \varepsilon^{1/4}\zeta(\tau), \tag{3.7.7}$$

$$S_c(t) = 1 - \varepsilon^{1/4}\sigma(\tau), \quad T_u(t, y) = T_{\mathrm{u,max}}(y) + \mathrm{o}(1), \tag{3.7.8}$$

where ε is an arbitrary small parameter and we have picked the powers of ε to be consistent with Figure 3.16, and t_c, $c_{\max}$, $I_{\max}$, and $T_{\mathrm{u,max}}$ are unknown. We substitute (3.7.7) and (3.7.8) into (3.7.1)–(3.7.5) to find that

$$\frac{\partial^2 T_{\mathrm{u,max}}}{\partial y^2} = 0, \tag{3.7.9}$$

$$\frac{\mathrm{d}\xi}{\mathrm{d}\tau} = \frac{1}{I_{\max} - \varepsilon^{1/4}\zeta}, \tag{3.7.10}$$

$$\frac{\mathrm{d}\zeta}{\mathrm{d}\tau} = \frac{\varepsilon^{3/4}}{\hat{\mathrm{Be}}\hat{K}(1 - \varepsilon^{1/4}\sigma)(I_{\max} - \varepsilon^{1/4}\zeta)}, \tag{3.7.11}$$

$$A(1 - \varepsilon^{1/4}\sigma) = -(I_{\max} - \varepsilon^{1/4}\zeta)\left.\frac{\mathrm{d}T_{\mathrm{u,max}}}{\mathrm{d}y}\right|_{y = c_{\max} - \varepsilon\xi}. \tag{3.7.12}$$

with boundary conditions

$$T_{\mathrm{u,max}} = 1 \quad \text{at} \quad y = c_{\max} - \varepsilon\xi, \quad \frac{\partial T_{\mathrm{u,max}}}{\partial y} = -\mathrm{Nu}\,(T_{\mathrm{u,max}} - \theta_e) \quad \text{at} \quad y = 1, \tag{3.7.13}$$

and initial conditions

$$\xi = 0, \quad \zeta = 0, \quad \sigma = 0 \quad \text{at} \quad \tau = 0. \tag{3.7.14}$$

We expand the nonlinear terms and collect the leading-order equations in ε to find

$$\frac{\partial^2 T_{\mathrm{u,max}}}{\partial y^2} = 0, \tag{3.7.15}$$

$$\frac{\mathrm{d}\xi}{\mathrm{d}\tau} = \frac{1}{I_{\max}}, \tag{3.7.16}$$

$$\frac{\mathrm{d}\zeta}{\mathrm{d}\tau} = \frac{1}{\hat{\mathrm{Be}}(1-\phi_0)^3\sigma^3 I_{\max}}, \tag{3.7.17}$$

$$A = -I_{\max}\left.\frac{\mathrm{d}T_{\mathrm{u,max}}}{\mathrm{d}y}\right|_{y=c_{\max}}. \tag{3.7.18}$$

We solve (3.7.15) along with (3.7.13) to find that

$$T_{\mathrm{u,max}} = \frac{1 + (1 - c_{\max}\theta_e)\mathrm{Nu} - (1-\theta_e)\mathrm{Nu}\,y}{1 + (1 - c_{\max})\mathrm{Nu}}. \tag{3.7.19}$$

We immediately see from (3.7.18) that

$$I_{\max} = \frac{A\,(1 + (1 - c_{\max})\mathrm{Nu})}{(1-\theta_e)\mathrm{Nu}}. \tag{3.7.20}$$

Integrating (3.7.16), we find that

$$\xi = \frac{\tau}{I_{\max}}, \tag{3.7.21}$$

which is a linear relationship between the front position and the time to clogging (as

shown in Figure 3.16). In order to further proceed, we need to consider the $\mathrm{O}(\varepsilon^{1/4})$ version of (3.7.12), which reads

$$-\sigma = \frac{\zeta}{A}\left.\frac{\mathrm{d}T_{\mathrm{u,max}}}{\mathrm{d}y}\right|_{y=c_{\max}}. \tag{3.7.22}$$

We substitute for $\mathrm{d}T_{\mathrm{u,max}}/\,\mathrm{d}y$ from (3.7.18) to yield

$$\sigma = \frac{\zeta}{I_{\max}}, \tag{3.7.23}$$

and thus (3.7.17) reduces to

$$\frac{\mathrm{d}\sigma}{\mathrm{d}\tau}\sigma^3 = \frac{1}{\hat{\mathrm{Be}}(1-\phi_0)^3 I_{\max}^2}. \tag{3.7.24}$$

We note that the terms on the right-hand side of (3.7.24) are independent of τ, and hence we integrate (3.7.24) and choose the physically relevant (positive real) solution to find

$$\sigma = \left(\frac{4\tau}{\hat{\mathrm{Be}}(1-\phi_0)^3 I_{\max}^2}\right)^{1/4}, \tag{3.7.25}$$

which we then substitute into (3.7.23) to get

$$\zeta = I_{\max}\left(\frac{4\tau}{\hat{\mathrm{Be}}(1-\phi_0)^3 I_{\max}^2}\right)^{1/4}. \tag{3.7.26}$$

Thus, we have recovered all the power-law behaviour we saw in Figures 3.10, 3.11 and 3.16, namely $I_{\max} - I \sim 1 - S_c \sim (t_c - t)^{1/4}$ and $c_{\max} - c \sim (t_c - t)$ for the system near clogging. The remaining unknowns t_c and $c_{\max}$ still need to be determined by numerical calculations. The dashed lines on Figure 3.16 are plotted using (3.7.21), (3.7.25) and (3.7.26) and show good agreement with the numerical solutions in the $\tau \to 0$ limit.

We conclude by presenting the power laws in terms of the original variables, giving

$$S(y) = 1 - (c_{\max} - y)^{1/4} \left(\frac{4}{\hat{\mathrm{Be}}(1-\phi_0)^3 I_{\max}} \right)^{1/4} \tag{3.7.27}$$

$$I = I_{\max} - (t_c - t)^{1/4} \left(\frac{4 I_{\max}^2}{\hat{\mathrm{Be}}(1-\phi_0)^3} \right)^{1/4}, \tag{3.7.28}$$

$$c = c_{\max} - \frac{(t_c - t)}{I_{\max}}. \tag{3.7.29}$$

3.7.1 After clogging power law

In the previous section, we derived the power-law behaviour of the solution just before clogging. From Figure 3.12, we see that, after the clogging, $c_{\max} - d(t)$ is also described by power-law behaviour, which we now derive using the same methods as in the previous section. We introduce shifted coordinates given by

$$t = t_c + \varepsilon\tau, \quad d(t) = c_{\max} - \varepsilon^{4/5}\xi(\tau), \quad S_d(t) = 1 - \varepsilon^{1/5}\sigma(\tau), \tag{3.7.30}$$

$$T_u = T_{\mathrm{u,max}}(y,t) + O(\varepsilon^{4/5}), \quad T_c = 1 - \varepsilon^{4/5} T_{\mathrm{c,max}}(\eta,\tau), \tag{3.7.31}$$

and, again, we choose the exponents of ε to be consistent with the numerical behaviour observed in Figures 3.12 and 3.16, we use a scaled spatial coordinate in the completely frozen region, given by $\eta = (c_{\max} - y)/\varepsilon^{4/5}$ since, after clogging, this region is $\mathrm{O}(\varepsilon^{4/5})$, and consequently this determines the choice of scaling for T_c. With these scalings, the leading-order version of (3.4.18) becomes

$$\frac{\partial T_{\mathrm{u,max}}}{\partial \tau} = 0 \quad \text{in} \quad c_{\max} < y < 1, \tag{3.7.32a}$$

$$\frac{\partial^2 T_{\mathrm{c,max}}}{\partial \eta^2} = 0 \quad \text{in} \quad 0 < \eta < \xi(\tau), \tag{3.7.32b}$$

and the boundary conditions are

$$T_{\mathrm{c,max}} = 0, \quad k_{pf} A\sigma \frac{\mathrm{d}\xi}{\mathrm{d}\tau} = \frac{\partial T_{\mathrm{c,max}}}{\partial \eta} \quad \text{at} \quad \eta = \xi(t), \tag{3.7.32c}$$

$$T_{\mathrm{u,max}} = 1 \quad \text{at} \quad y = c_{\max}, \quad \eta = 0, \tag{3.7.32d}$$

$$k_{pf} \frac{\partial T_{\mathrm{u,max}}}{\partial y} = -\frac{\partial T_{\mathrm{c,max}}}{\partial \eta} \quad \text{at} \quad y = c_{\max}, \quad \eta = 0, \tag{3.7.32e}$$

$$\frac{\partial T_{\mathrm{u,max}}}{\partial y} = -\mathrm{Nu}(T_{\mathrm{u,max}} - \theta_e) \quad \text{at} \quad y = 1, \tag{3.7.32f}$$

and finally, the initial conditions are

$$T_{\mathrm{u,max}} = \frac{1 + (1 - c_{\max}\theta_e)\mathrm{Nu} - (1 - \theta_e)\mathrm{Nu}\, y}{1 + (1 - c_{\max})\mathrm{Nu}} \quad \text{at} \quad \tau = 0, \tag{3.7.32g}$$

$$\xi = 0 \quad \text{at} \quad \tau = 0. \tag{3.7.32h}$$

First, we solve (3.7.32a) and (3.7.32g), giving

$$T_{\mathrm{u,max}} = \frac{1 + (1 - c_{\max}\theta_e)\mathrm{Nu} - (1 - \theta_e)\mathrm{Nu}\, y}{1 + (1 - c_{\max})\mathrm{Nu}}. \tag{3.7.33}$$

We then solve (3.7.32b), (3.7.32c), and (3.7.32e) giving that

$$T_{\mathrm{c,max}} = \frac{k_{pf}(1 - \theta_e)\mathrm{Nu}}{1 + (1 - c_{\max})\mathrm{Nu}} (\eta - \xi). \tag{3.7.34}$$

Thus, from (3.7.34) and (3.7.32c) we see that

$$A\sigma \frac{\mathrm{d}\xi}{\mathrm{d}\tau} = \frac{(1 - \theta_e)\mathrm{Nu}}{1 + (1 - c_{\max})\mathrm{Nu}}. \tag{3.7.35}$$

We recall from (3.4.2b) that the volume fraction of frozen cryolite laid down in the porespace during infiltration does not change in time and hence $S(y)$ is known in

$0 < y < c_{\max}$ and, from (3.7.27), is given by

$$1 - S(y) = (c_{\max} - y)^{1/4} \left(\frac{4}{\hat{\mathrm{Be}}(1-\phi_0)^3 I_{\max}} \right)^{1/4}. \tag{3.7.36}$$

Substituting (3.7.30) and (3.7.31) into (3.7.36) and evaluating at $y = d(t)$ we find that

$$\sigma = \left(\frac{4\xi}{\hat{\mathrm{Be}}(1-\phi_0)^3 I_{\max}} \right)^{1/4}. \tag{3.7.37}$$

We use (3.7.37) to eliminate σ in (3.7.35) and we write the resulting equation as

$$\xi^{1/4} \frac{\mathrm{d}\xi}{\mathrm{d}\tau} = \frac{(1-\theta_e)\mathrm{Nu}}{A\,(1 + (1-c_{\max})\mathrm{Nu})} \left(\frac{\hat{\mathrm{Be}}(1-\phi_0)^3 I_{\max}}{4} \right)^{1/4}. \tag{3.7.38}$$

We integrate (3.7.38) to find

$$\xi = \left(\frac{5(1-\theta_e)\mathrm{Nu}}{4A\,(1 + (1-c_{\max})\mathrm{Nu})} \right)^{4/5} \left(\frac{\hat{\mathrm{Be}}(1-\phi_0)^3 I_{\max}}{4} \right)^{1/5} \tau^{4/5}, \tag{3.7.39}$$

which we use to find the evolution of d using (3.7.30). We plot the solution given by (3.7.39) in Figure 3.12 and see that there is close agreement with the numerical solution.

3.8 Stability of the similarity solutions

We have seen from the early-time nonlinear system that it can have 0, 1, or 2 solutions and that numerically we can follow only one of them. This is a characteristic case of a saddle-node bifurcation, where changing a parameter changes the number of equilibria of the system. In this section, we investigate the stability of these equilibria analytically to show which can occur in practice. For clarity, we consider $B(S) = -1$ and $\rho_r = 1$, motivated by the fact that changing these parameters should not change

the qualitative behaviour of the two solutions. We expect that the same argument holds for the non-simplified case. It is useful to first transform to a coordinate system moving with the front; we use

$$x = y - c(t), \tag{3.8.1}$$

so that $y = c(t)$ corresponds to $x = 0$. We use $\dot{c} = 1/I(t)$ to remove all of the explicit dependence on the front position $c(t)$ from (3.3.6)–(3.3.10) and the resulting system is

$$\frac{\partial^2 T}{\partial x^2} = -\frac{1}{I}\frac{\partial T}{\partial x} + \frac{\partial T}{\partial t}, \tag{3.8.2}$$

$$I\dot{I} = H\left(I \left.\frac{\partial T}{\partial x}\right|_{x=0}\right), \tag{3.8.3}$$

with

$$T = 1, \quad \text{on} \quad x = 0, \quad T \to 0, \quad \text{as} \quad x \to \infty, \tag{3.8.4}$$

where

$$H(\Theta) = \frac{1}{\hat{\mathrm{B}}\mathrm{e}K((1-\phi_0)(1+\frac{\Theta}{A}))}, \tag{3.8.5}$$

K is given by (3.7.6), and ϕ_0 is the volume fraction of the alumina particles. We introduce the similarity variables

$$\eta = \frac{x}{2\sqrt{t}}, \quad s = \log(t), \tag{3.8.6}$$

and look for a solution of the form

$$T(x,t) = g(\eta, s), \quad I(t) = 2e^{s/2}\lambda_I(s). \tag{3.8.7}$$

Substituting from (3.8.7) into (3.8.2)–(3.8.5), we find that the coupled problem for g and λ_I is

$$\left(2\eta + \frac{1}{\lambda_I}\right)\frac{\partial g}{\partial \eta} + \frac{\partial^2 g}{\partial \eta^2} = 4\frac{\partial g}{\partial s}, \tag{3.8.8}$$

$$H\left(\lambda_I \left.\frac{\partial g}{\partial \eta}\right|_{\eta=0}\right) = 2\lambda_I \left(\lambda_I + 2\frac{\mathrm{d}g}{\mathrm{d}s}\right), \tag{3.8.9}$$

with

$$g = 1 \quad \text{at} \quad \eta = 0, \quad g \to 0 \quad \text{as} \quad \eta \to \infty. \tag{3.8.10}$$

Since we are interested in the stability of the solutions, we consider the following ansatz

$$g = g^{(0)}(\eta) + \varepsilon g^{(1)}(\eta) e^{\Lambda s}, \quad \lambda_I = \lambda_I^{(0)} + \varepsilon \lambda_I^{(1)} e^{\Lambda s}, \tag{3.8.11}$$

where $g^{(0)}(\eta)$ is the steady state solution to (3.8.8)–(3.8.10) in which $\lambda_I = \lambda_I^{(0)}$, given by

$$g^{(0)\prime\prime} + \left(2\eta + \frac{1}{\lambda_I^{(0)}}\right) g^{(0)\prime} = 0, \tag{3.8.12}$$

$$H(\lambda_I^{(0)} g^{(0)\prime}(0)) = 2{\lambda_I^{(0)}}^2, \tag{3.8.13}$$

$$g^{(0)} = 1 \quad \text{at} \quad \eta = 0, \quad g^{(0)} \to 0 \quad \text{as} \quad \eta \to \infty. \tag{3.8.14}$$

We have already solved an analogue of (3.8.12)–(3.8.14) in Section 3.5, giving an error function for $g^{(0)}$ and some constant for $\lambda_I^{(0)}$ (multiple solutions still apply; we present the two solutions in Figure 3.17). The equations for the perturbations $g^{(1)}(\eta)$ and $\lambda_I^{(1)}$ form an eigenvalue problem which we write as

$$-\frac{\lambda_I^{(1)}}{{\lambda_I^{(0)}}^2} g^{(0)\prime}(\eta) + \left(2\eta + \frac{1}{\lambda_I^{(0)}}\right) g^{(1)\prime}(\eta) + g^{(1)\prime\prime}(\eta) = 4\Lambda g^{(1)}(\eta), \tag{3.8.15}$$

$$H'(\lambda_I^{(0)} g^{(0)\prime}(0))(\lambda_I^{(1)} g^{(0)\prime}(0) + \lambda_I^{(0)} g^{(1)\prime}(0)) = 4(1+\Lambda)\lambda_I^{(0)}\lambda_I^{(1)}, \tag{3.8.16}$$

$$g^{(1)} = 0 \quad \text{on} \quad \eta = 0, \quad g^{(1)} \to 0 \quad \text{as} \quad \eta \to \infty. \tag{3.8.17}$$

We solve for $\lambda_I^{(1)}$ from (3.8.16) and substitute into (3.8.15), and then, after some

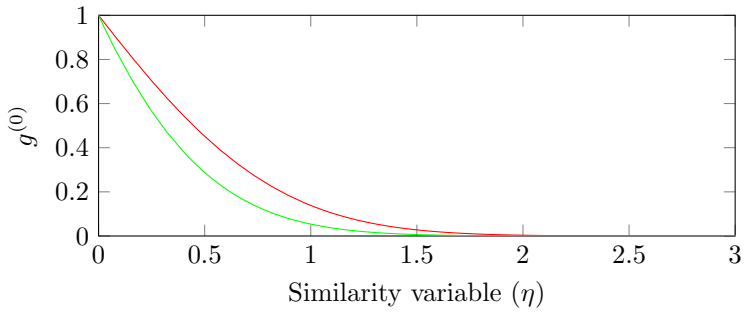

Figure 3.17: Graph showing the two solutions of (3.8.12)–(3.8.14) as a function of the similarity variable. The parameters are $A = 10$, $\hat{\mathrm{Be}} = 4$, $\phi_0 = 1/2$.

simplifications, we arrive at the following equation for $g^{(1)}$

$$4\Lambda g^{(1)} - \frac{g^{(0)\prime}(\eta)H'(\Theta)}{-4(1+\Lambda){\lambda_I^{(0)}}^2 + H'(\Theta)\Theta} g^{(1)\prime}(0) = \left(2\eta + \frac{1}{\lambda_I^{(0)}}\right) g^{(1)\prime} + g^{(1)\prime\prime}, \tag{3.8.18}$$

$$g^{(1)} = 0 \quad \text{on} \quad \eta = 0, \quad g^{(1)} \to 0 \quad \text{as} \quad \eta \to \infty, \tag{3.8.19}$$

where H is given by (3.8.5).

We discretise (3.8.18) and (3.8.19) using finite differences on $\eta \in [0, L]$, where L is chosen to be large and can be considered a numerical parameter. We multiply (3.8.18) by the denominator of the second term, then discretise in η, the state vector $\mathbf{g^{(1)}} = \{g^{(1)}\left(i\frac{L}{N}\right) \mid 0 < i < N\}$, where N is the number of grid points of the discretisation, satisfies

$$(\Lambda^2\mathbf{A} + \Lambda\mathbf{B} + \mathbf{C})\mathbf{g^{(1)}} = \mathbf{0}, \tag{3.8.20}$$

where the matrices $\mathbf{A}$, $\mathbf{B}$ and $\mathbf{C}$ are given by

$$\mathbf{A} = 16{\lambda_I^{(0)}}^2\mathbf{I}, \tag{3.8.21}$$

$$\mathbf{B} = (16{\lambda_I^{(0)}}^2 - 4\lambda_I^{(0)}H'(\Theta)g^{(0)}(0))\mathbf{I} - (4\lambda_I^{(0)}\mathbf{I} + 8{\lambda_I^{(0)}}^2\boldsymbol{\eta})\mathbf{D} + (-4{\lambda_I^{(0)}}^2)\mathbf{D}^2, \tag{3.8.22}$$

$$\mathbf{C} = (\lambda_I^{(0)}H'(\Theta)g^{(0)\prime}(0) - 4{\lambda_I^{(0)}}^2)\mathbf{D}^2 + (H'(\Theta)\mathbf{f}_0'(\eta))\mathbf{G}\mathbf{D} \tag{3.8.23}$$

$$+ (2\boldsymbol{\eta}\lambda_I^{(0)}H'(\Theta)g^{(0)\prime}(0) + H'(\Theta)g^{(0)\prime}(0)\mathbf{I} - 8\boldsymbol{\eta}{\lambda_I^{(0)}}^2 - 4\lambda_I^{(0)}\mathbf{I})\mathbf{D}, \tag{3.8.24}$$

and

$$\eta_{ij} = \begin{cases} i\frac{L}{N} & i = j \\ 0 & i \neq j \end{cases}, \quad G_{ij} = \begin{cases} 1 & i = j \\ 0 & i \neq j \end{cases}, \quad D_{ij} = \frac{N}{L} \begin{cases} 0 & i = j \\ 1 & i = j + 1 \\ -1 & i = j - 1 \end{cases}, \tag{3.8.25}$$

and $\mathbf{I}$ is the identity matrix. This is a *quadratic eigenvalue problem*, which can be solved by many different methods, and can even be transformed into a *generalized eigenvalue problem* [92, Eq. 2.13]. Since we are only interested in the dominant eigenvalues, we choose the grid size to be small and use Arnoldi iteration to find the largest eigenvalues. We note that, instead of solving the quadratic eigenvalue problem (3.8.18)–(3.8.19), we could have instead solved the linear eigenvalue problem (3.8.15)–(3.8.17). We choose to solve the quadratic eigenvalue problem since, in this case, we only need to discretise $g^{(1)}$.

Here we point out that we multiplied (3.8.18) with a term that is dependent on the eigenvalue. This operation is only valid if that term is non zero, and hence we need to take care in evaluating the eigenvalues by removing the spurious eigenvalue that is induced by this multiplication. Interestingly this spurious eigenvalue turns out to be the largest one for the stable solution.

Having implemented the discretisation and chosen a solver, we investigate the behaviour of the spectrum of eigenvalues for (3.8.18) and (3.8.19). In Figure 3.18 we plot the 10 largest eigenvalues for both of the solutions we saw in Figure 3.17, for $A = 10$, $\hat{\mathrm{B}}\mathrm{e} = 4$, and $\phi_0 = 1/2$. We vary the number of discretization points, N, and see that the eigenvalues are converged for as low as 256 discretization points. We calculate from (3.8.13) that the two values of $\lambda_I^{(0)}$ are 0.75 and 5.81. We see that, for $\lambda_I^{(0)} = 0.75$, all of the eigenvalues have negative real part, while, for $\lambda_I^{(0)} = 5.81$, two

of the eigenvalues have positive real part. Combining (3.7.2) and (3.8.7), we find that

$$\dot{c} = \frac{e^{-s/2}}{2\lambda_I} \quad \text{and} \quad S_c = \frac{\lambda_I g'(0)}{A}, \tag{3.8.26}$$

and thus we see that the stable solution has a lower amount of frozen cryolite and a faster moving front than the unstable solution.

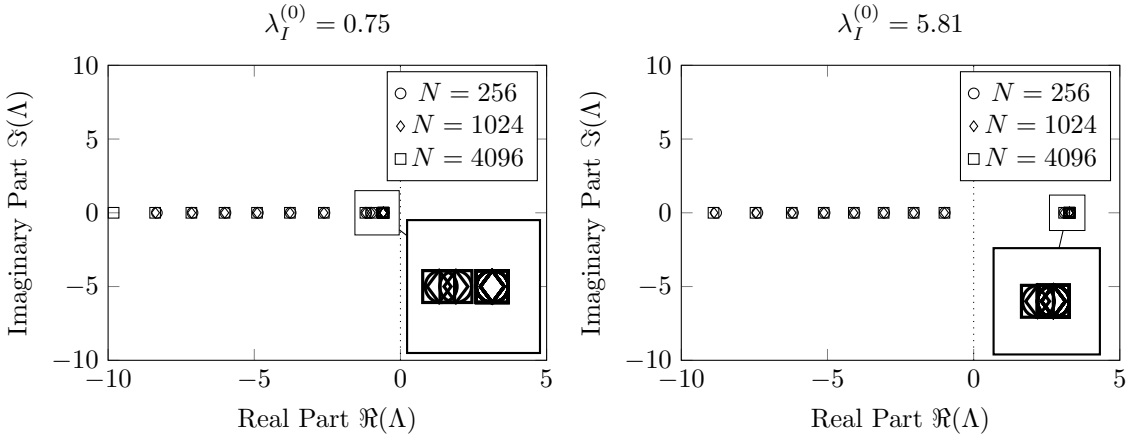

Figure 3.18: Plot of the 10 largest eigenvalues for the two different solutions of the similarity problem (3.8.15)–(3.8.17). The different symbols are for different number of discretization points, N. The parameters are $A = 10$, $\hat{\mathrm{Be}} = 4$, $\phi_0 = 1/2$. The insets show the largest eigenvalues.

The truncated and discretised system (3.8.20)–(3.8.25) converges to the semi-infinite continuous problem (3.8.18)–(3.8.19) when the two limits $L \to \infty$ and $\Delta\eta = L/N \to 0$ are simultaneously taken. We investigate the convergence of the truncated system by fixing one of L and $\Delta\eta$ and varying the other. First, we investigate the effect of increasing the computational domain, L, as shown in Figure 3.19. We see that, by increasing the computational domain by a factor of 64, the roots change, but the critical eigenvalue is not affected by this change, so we expect that our results are still valid in the $L \to \infty$ limit. To further check this, we plot the eigenfunctions in Figure 3.20 and note that all of them exhibit exponentially decaying tails. We also compare the eigenvalue calculation to the solution of the original nonlinear initial value problem, then estimate the coefficient of the exponential decay, which should

coincide with the eigenvalue. We present the results in Figure 3.21, where we plot the solutions to the nonlinear system (3.8.8)–(3.8.10), linear system, and the eigenvalue calculation (3.8.18) and (3.8.19). We see that the three different solutions are on top of each other and hence we can be confident in our numerical schemes.

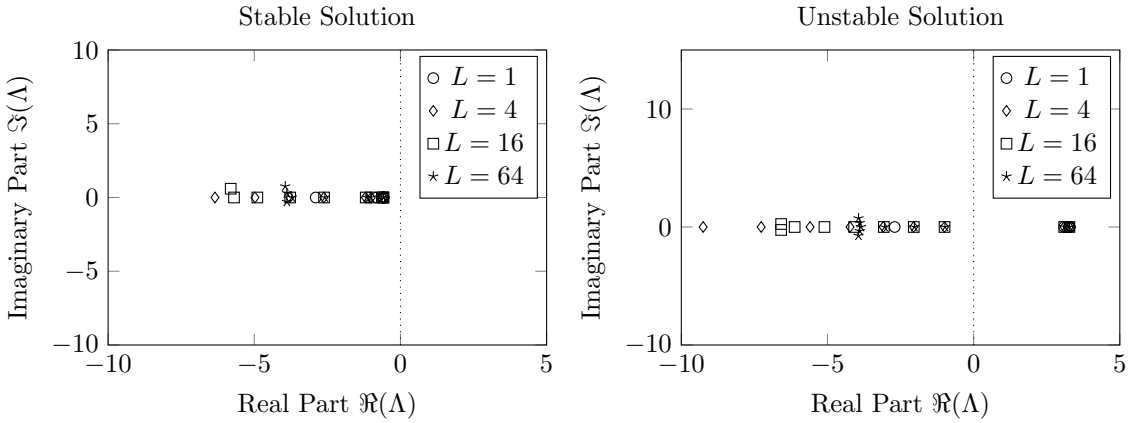

Figure 3.19: Plot of the 5 largest eigenvalues for the two different solutions of the similarity problem (3.8.15)–(3.8.17). The degree of discretisation is fixed at $N = 2048$ and the computational domain length L is varied. The parameters are $A = 10$, $\hat{\text{Be}} = 4$, $\phi_0 = 1/2$. For the stable solution on the left $\lambda_I^{(0)} = 0.75$, while for the unstable solution on the right $\lambda_I^{(0)} = 5.81$.

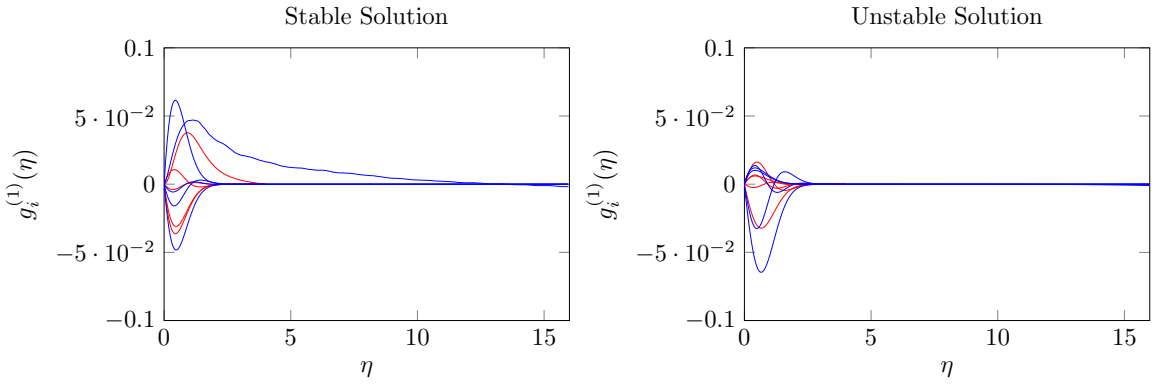

Figure 3.20: Plot of the eigenfunctions corresponding to the 5 largest eigenvalues for the two different solutions of the similarity problem (3.8.15)–(3.8.17). The red lines are for $L = 4$, while the blue lines are for $L = 16$. In both cases $N = 2048$. The parameters are $A = 10$, $\hat{\text{Be}} = 4$, $\phi_0 = 1/2$. For the stable solution on the left $\lambda_I^{(0)} = 0.75$, while for the unstable solution on the right $\lambda_I^{(0)} = 5.81$.

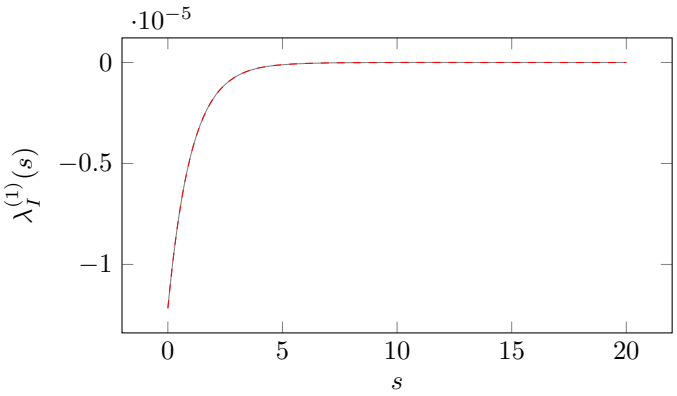

Figure 3.21: Plot of the perturbation $\lambda_I^{(1)}(s)$ as a function of the logarithm of time. We plot the result of the eigenvalue calculation given by (3.8.11), (3.8.18) and (3.8.19) with red dashed line and the nonlinear initial value problem given by (3.8.8)–(3.8.10) with grey. The parameters are $A = 10$, $\hat{\mathrm{Be}} = 4$, $\phi_0 = 1/2$.

3.9 Conclusions

In this chapter, we considered the problem of phase changing infiltration of cryolite into a cold porous raft of alumina floating on top of a slightly superheated cryolite bath. We formulated a one-dimensional mathematical model to investigate the infiltration behaviour in the industrially relevant small-superheat limit. We found that the early-time problem had a solution of similarity form which we used to initialize our numerical solver. We verified both methods by comparing them in the intermediate limit.

We used the early time solution to find that, depending on the parameters, there can either be multiple solutions to the model (a stable and an unstable pair of similarity solutions as shown in Figure 3.15) or no solutions, which suggests that external freezing occurs instead. We show the location of these regimes in the $(\hat{\mathrm{Be}}, A/\hat{\mathrm{Be}})$ parameter space in Figure 3.7, where $\hat{\mathrm{Be}}$ is the Bejan number, and A is the modified Stefan number. This regime plot can be used to predict how the qualitative behaviour of the system changes as a function of the process parameters. We used linear stability analysis to show that the stable solution is the one which has less frozen cryolite.

After investigating the early-time behaviour, we turned our attention to late-time

behaviour. We find that, depending on the size of the key dimensionless parameters the Nusselt number (that controls the heat transfer through the top of the porous alumina raft) and the ambient temperature, there are two qualitatively different possibilities for the end state of the raft (see Figure 3.14). If the heat transfer is small enough, then the front infiltrates the raft fully, resulting in a raft where the void space is filled with a mixture of liquid and solid. If, however, the heat transfer is large enough, we find that the infiltration front stops and a clogging front is created instead. This new front moves backwards through the raft resulting in a dry region near the top of the raft, which is above a region completely filled with frozen cryolite and particles. Additionally, we show that the infiltration time is non-monotonic when phase change is included in the model (see Figure 3.13).

We investigated the near-clogging problem further and found that the early time similarity solution transitions to a different type of solution which exhibits power-law behaviour as $t \to t_c^-$, where t_c is the clogging time. In addition to this, we investigate the early time evolution after the clogging time. We find that the front speed is described by a $(t - t_c)^{4/5}$ law after clogging (see Figures 3.11 and 3.12). This is a transient effect, and the behaviour transitions to $\sqrt{t}$ at longer timescales. These results improve our understanding of the infiltration of alumina rafts by molten cryolite, highlighting that small deviations from the operating conditions can fundamentally alter the behaviour.

Chapter 4

Dissolution of a spherical clump of alumina

Synopsis

In this chapter, we formulate a mathematical model for the dissolution of a spherical porous clump of alumina. We solve numerically the resulting system of equations using the method of lines and find that two qualitatively different behaviours are possible: bulk dissolution and localized dissolution near the boundary. The second behaviour corresponds to a travelling front solution which we analyse using the method of matched asymptotic expansions, resulting in a system similar to the one presented in Chapter 2 for a solid sphere. We compare the numerical results of the model with the travelling front solutions, showing agreement between them. Thus, we establish the dependence of the dissolution time of the spherical clump on the material parameters.

4.1 Introduction

After considering the evolution of a single solid particle in liquid cryolite in Chapter 2, and the imbibition of cryolite into a porous raft in Chapter 3, we turn our attention to a different stage of the alumina feeding process: the dissolution of a porous clump

of alumina. Motivated by the timescales described in previous chapters, we assume that any cryolite infiltration has already reached an equilibrium. In particular, we assume that the front has fully infiltrated into the porous clump, so that there are no dry pockets inside (we will relax this assumption in Chapter 5). In order to simplify our modelling, we assume that the clump is spherical and submerged in cryolite. This assumption should be reasonable for a clump that detached from the main raft (see Figure 4.1; clumps shown in C). Lastly, we assume that the porous clump maintains its structural integrity during the dissolution.

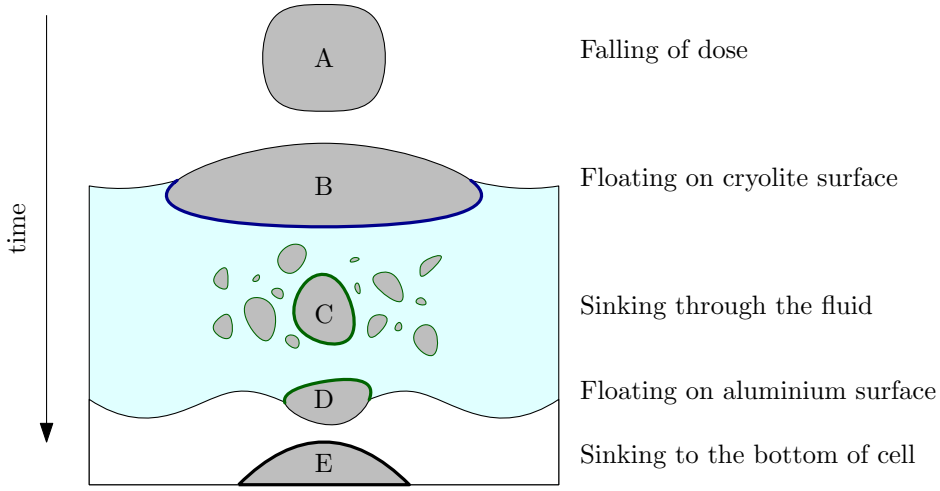

Figure 4.1: Schematic showing stages of the alumina feeding process. The focus in this chapter are the clumps in C.

There are three main questions that we would like to answer:

- How fast does the porous medium dissolve (what is the timescale)?
- What is the primary dissolution mechanism (dissolve from the bulk, or from the surface)?
- How do these answers depend on the parameters of the model (e.g. the porosity of the alumina clump)?

In general, we aim to determine how to minimise the dissolution time.

Porous medium dissolution has been investigated by many authors before. For example, Fujita [25] considers a problem in which a diffusing substance interacts with a dissolving medium, and formulates a sharp interface model in planar and cylindrical geometries. Chadam et al. [8] are among the first to incorporate flow via Darcy's equation and couple this with the conservation of mass for the fluid and a dissolved species. They solve the model in a planar geometry for constant velocity fronts and investigate the limit of a large density solid, finding that the planar front is often unstable. Hinch and Bhatt [36] consider a similar model, where the pore space of the porous medium consists of two different reacting species, a mobile acid and an immobile dissoluble mineral. They consider that the porosity does not change, but the permeability is dependent on the concentration of the dissoluble material. They solve the problem in the planar case and further investigate the small-permeability-change limit of the problem and find that the planar front is unstable in certain parameter regimes. Szymczak and Ladd [88] investigate the reactive dissolution of a rock matrix. Since previous studies suggest that the dissolution fronts might be unstable, they focus on a particular type of nonplanar solution called fracture dissolution, which is a dissolution type where channels form and penetrate into the porous medium. Kang et al. [43] uses the Lattice-Boltzmann method to investigate the microscale behaviour of a dissolving porous medium and they find planar front propagation (face dissolution), uniform dissolution, and worm holing (in which channels form inside the rock matrix) in different parameter regimes. Zhao, Hobbs, and Ord [111, 112] and Zhao et al. [113] investigate the planar form of the equations that form the basis of our model, though we do not take account of the flow of the cryolite and we work with a specific form of the constitutive law describing the dissolution. They investigate the travelling front solutions, however in their model the porosity cannot increase up to unity so that there is always some amount of porous media left, in contrast to our model in which we allow for complete dissolution. They formulate a finite element

numerical scheme that they validate by considering the evolution of the constant speed planar front by transforming the equations into the moving frame. As the dissolution progresses, the porosity increases to one and the problem exhibits a sharp front. A review of the methods applicable to finding sharp-front solutions for nonlinear diffusion equations is presented by Sherratt [79], who provides a detailed derivation for a version of Fisher's equation with degenerate diffusion with $u(x,t)$ satisfying $u_t = (uu_x)_x + u(1-u)$.

In the following sections, we formulate a model for the diffusion-driven dissolution of a spherical porous alumina particle, then solve this model numerically using the method of lines and asymptotically in two different limits, before comparing these predictions.

4.2 Mathematical model

We consider the diffusion-driven dissolution of a spherically symmetric porous clump of alumina, as illustrated in Figure 4.2. We choose to track the concentration of alumina in the cryolite, and the porosity of the solid alumina clump using equations that are valid both inside and outside the clump — an alternative approach would be to treat inside and outside the clump separately. This has the advantage that we do not need to explicitly track the location of the boundary. We denote the time from the start of dissolution by t and we will use r for the radial distance from the centre of the spherical clump.

We denote by $\phi(r,t)$ the volume fraction of the pore space and we denote by $C(r,t)$ the concentration of alumina in the cryolite, that is, the mass of the alumina contained in a unit volume of liquid. Our model comprises equations that describe conservation of mass of dissolved alumina in the liquid cryolite and conservation of mass of solid

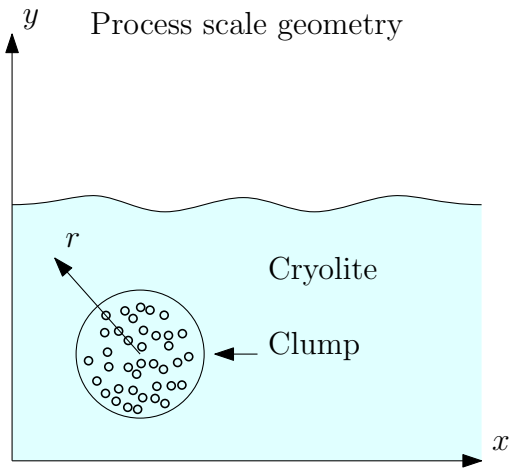

Figure 4.2: Schematic showing the process scale geometry.

alumina, which read

$$\frac{\partial}{\partial t}(\phi C) = \frac{1}{r^2}\frac{\partial}{\partial r}\left(\phi r^2 D \frac{\partial C}{\partial r}\right) + \mathfrak{D}, \tag{4.2.1}$$

$$\rho_p \frac{\partial}{\partial t}(1-\phi) = -\mathfrak{D}, \tag{4.2.2}$$

for $r > 0, t > 0$, where D is the diffusivity of alumina in the liquid cryolite, $\mathfrak{D}$ is the dissolution rate of alumina, and ρ_p is the constant density of the solid alumina. We note that, for simplicity, we neglect in (4.2.1) the flow of liquid induced by the density change caused by the dissolution of the alumina into the liquid cryolite. This reduces the complexity of our model, since we do not have to write down any equations describing how the liquid flows. However, it is unlikely to be true in practice, since the concentration change driving the reaction is similar to the density change causing the flow.

We assume that the dissolution reaction occurs when the concentration of alumina in the cryolite is lower than saturation concentration C_s and that no precipitation of alumina occurs when the concentration is greater than C_s. We further assume that the rate is proportional to the local surface area of the porous clump $(1-\phi)^{2/3}$. Thus we write that $\mathfrak{D}$ is

$$\mathfrak{D} = \nu(1-\phi)^{2/3}(C_s - C)_+, \tag{4.2.3}$$

where $(\square)_+$ denotes the positive part of $\square$, C_s is the saturation concentration, and ν is the reaction coefficient. We note that (4.2.3) is a simple constitutive law for the dissolution, and that it would be interesting to explore and derive a more accurate law by homogenising an appropriate mass transfer problem at the microscale, such as the single-particle model described in Chapter 2.

We assume that the concentration is bounded at the centre of the clump, and that the concentration far away from the clump is known. Hence we write

$$C = O(1) \quad \text{as} \quad r \to 0, \tag{4.2.4}$$

$$C = C_f \quad \text{as} \quad r \to \infty, \tag{4.2.5}$$

where the C_f denotes the far-field concentration. Note that in the numerical scheme we will apply the boundary condition (4.2.5) at some large finite value L. Finally, we assume that the liquid cryolite infiltrates the clump over a much shorter timescale than that associated with the dissolution reaction, and thus we assume that the clump is completely filled with cryolite initially and that the initial concentration of alumina is constant and everywhere equal to the far-field bulk concentration. We also assume that the initial porosity of the clump is known. Thus, we write

$$C = C_f \quad \text{at} \quad t = 0, \tag{4.2.6}$$

$$\phi = \begin{cases} \phi_0 & r \leq R_0 \\ 1 & r > R_0 \end{cases} \quad \text{at} \quad t = 0, \tag{4.2.7}$$

where ϕ_0 is the initial porosity inside the clump, which has an initial radius R_0.

4.3 Dimensionless model

We nondimensionalise our model using the scalings

$$C = C_f + (C_s - C_f)\hat{C}, \quad r = R_0\hat{r}, \quad t = \frac{\rho_p}{\nu(C_s - C_f)}\hat{t}, \tag{4.3.1}$$

where we chose the timescale by balancing the two terms in (4.2.2). Dropping the hats, the dimensionless model may be written in the form

$$\frac{\partial\left(\phi(C-\beta)\right)}{\partial t} = \frac{\alpha}{r^2}\frac{\partial}{\partial r}\left(r^2\phi\frac{\partial C}{\partial r}\right), \tag{4.3.2}$$

$$\frac{\partial\phi}{\partial t} = (1-\phi)^{2/3}(1-C)_+, \tag{4.3.3}$$

for $r > 0$, with boundary conditions

$$C = O(1) \quad \text{as} \quad r \to 0, \tag{4.3.4}$$

$$C = 0 \quad \text{as} \quad r \to \infty, \tag{4.3.5}$$

and initial conditions given by

$$C = 0 \quad \text{at} \quad t = 0, \tag{4.3.6}$$

$$\phi = \begin{cases} \phi_0 & r \le 1 \\ 1 & r > 1 \end{cases} \quad \text{at} \quad t = 0. \tag{4.3.7}$$

We have introduced two dimensionless quantities,

$$\alpha = \frac{\rho_p D}{\nu R_0^2\left(C_s - C_f\right)}, \quad \beta = \frac{\rho_p - C_f}{C_s - C_f}, \tag{4.3.8}$$

where α is the ratio of the reactive and the diffusive timescales, and β represents the amount of alumina stored in the particles divided by the carrying capacity of the cryolite fluid. For large values of β, (4.3.2) suggests that the concentration should be close to saturation inside the porous particle except near its edge. We assume that the parameters take the following values

$$\begin{gathered} C_s \approx 164\,\mathrm{kg\,m^{-3}}, \quad C_f \approx 62\,\mathrm{kg\,m^{-3}}, \quad D \approx 1.5\times 10^{-9}\,\mathrm{m^2\,s^{-1}}, \\ \rho_p \approx 2000\,\mathrm{kg\,m^{-3}}, \quad R_0 \approx 50\,\mu\mathrm{m}. \end{gathered} \tag{4.3.9}$$

We do not have an accurate estimation for the reaction coefficient ν. However, we assume that the the reactive timescale is smaller than the diffusive timescale, which we estimate to be 0.083 s, thus we pick an indicative value of $\nu = 100/\mathrm{s}$. We use the values to calculate that

$$\beta \approx 20, \quad \alpha \approx 0.1. \tag{4.3.10}$$

4.4 Numerical solution

We discretize (4.3.2)–(4.3.6) using a uniform grid on a truncated domain, namely $r \in [0, L]$, and solve the resulting set of ODEs using an adaptive backward differentiation method with `NDSolve` implemented in `Mathematica 12.1`. We check for convergence of the results by varying the spatial step size and we use the stepsize beyond which the results do not change. In the numerical codes we solve for $Q = \phi C$ using the formulation

$$\frac{\partial Q}{\partial t} = \frac{\alpha}{r^2}\frac{\partial}{\partial r}\left(r^2\left(\frac{\partial Q}{\partial r} - \frac{\partial \phi}{\partial r}\frac{Q}{\phi}\right)\right) + \beta\frac{\partial \phi}{\partial t} \quad \text{in} \quad 0 < r < L, \tag{4.4.1}$$

$$\frac{\partial \phi}{\partial t} = (1-\phi)^{2/3}(1 - Q/\phi)_+ \quad \text{in} \quad 0 < r < L, \tag{4.4.2}$$

with

$$Q = \mathrm{O}(1) \quad \text{at} \quad r = 0, \tag{4.4.3}$$

$$Q = 0 \quad \text{as} \quad r = L, \tag{4.4.4}$$

$$Q = 0 \quad \text{for} \quad 0 < r < L \quad \text{at} \quad t = 0, \tag{4.4.5}$$

$$\phi = \begin{cases} \phi_0 & 0 < r < 1 \\ 1 & 1 < r < L \end{cases} \quad \text{at} \quad t = 0. \tag{4.4.6}$$

A representative solution is shown in Figure 4.3 (left), where we plot the concentration field along with the porosity as a function of the radius for different times for parameters $\alpha = 1$, $\beta = 1$. We see that the porosity increases with time and $\phi \to 1$ everywhere as $t \to \infty$, indicating that the porous clump completely dissolves. Meanwhile, the concentration is initially zero, grows to a maximum, then finally decreases to zero, corresponding to all the alumina diffusing away from the region. In Figure 4.3 (right) we plot the concentration at the centre of the sphere which first increases (due to the dissolution reaction), then decreases (due to the diffusion) at the end of the evolution. We note that $C(0,t)$ never reaches the saturation concentration (which we show as the dashed line).

In Figure 4.4 we investigate the case where $\alpha = 0.1$, $\beta = 20$. We plot the concentration and the porosity at (left) early times and (right) late times. In this case, the behaviour is different. We see that, for early times, the porosity inside the particle remains spatially uniform and increases slightly with time. The concentration also remains spatially uniform, except in a layer near $r = 1$, and increases towards the saturation concentration ($C = 1$). After this early transient behaviour, the porosity changes in a thin, moving, region that propagates into the particle and has a similar shape throughout the rest of the evolution. Inside the particle, we see that the concentration is approximately constant at the saturation concentration, and that

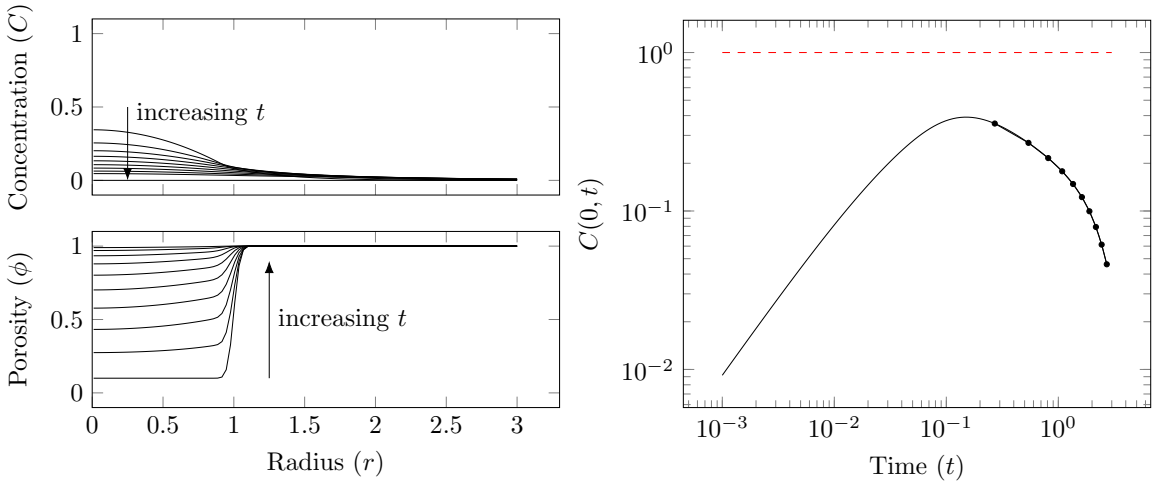

Figure 4.3: Left: Concentration and the porosity as a function of radius for $t = 0.28, \ldots, 2.8$. The concentration curve corresponding to $t = 0$ is the horizontal line at $C = 0$. Right: Concentration at the centre of the clump as a function of time. The dashed line denotes the saturation concentration. The dots correspond to the values of $C(0, t)$ shown in the lines in the left-hand figure. The parameters are $\alpha = \beta = 1$ and $\phi_0 = 0.1$.

outside it decreases as the alumina diffuses away. This behaviour continues until the front reaches $r = 0$, when, finally, the porous particle completely dissolves and the concentration field tends to zero. In order to see what happens as α decreases, we show in Figure 4.5 the concentration and the porosity at (left) early times and (right) late times, for $\alpha = 0.01$ and $\beta = 20$. We see that, at late time, the width of the travelling front is smaller. In Figure 4.6 we show the concentration at the centre of the sphere as a function of time for both sets of parameters. In both cases we see that the alumina concentration swiftly increases to the saturation concentration (shown as a dashed red line), stays there for the majority of the evolution, and then rapidly decreases as the particle completely dissolves. In Section 4.5 we will explore the early-time behaviour of the model, while in Section 4.6 we will derive an approximate travelling front solution when $\alpha \ll 1$.

In Figure 4.7 we plot the location of the boundary $r = s(t)$, which we define here to be the point where $\phi = 1/2$. We plot the evolution for three different pairs

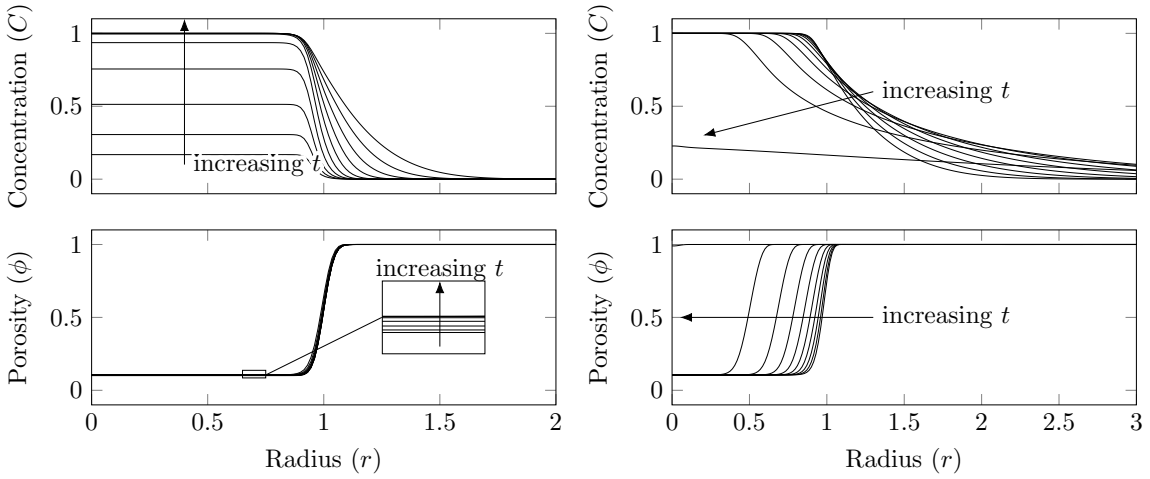

Figure 4.4: Concentration and the porosity as a function of radius at early times given by $t = 10^{-3}, \ldots, 1$ (left) and late times (right) $t = 1, \ldots, 86.69$. The parameters are $\alpha = 0.1$, $\beta = 20$ and $\phi_0 = 0.1$.

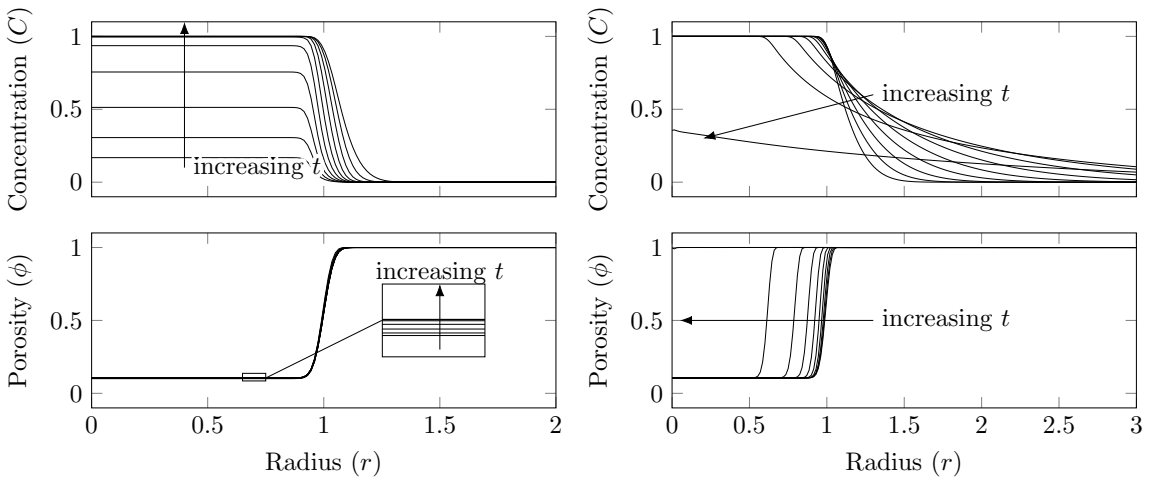

Figure 4.5: Concentration and the porosity as a function of radius at early times given by $t = 10^{-3}, \ldots, 1$ (left) and late times (right) $t = 1, \ldots, 772.095$. The parameters are $\alpha = 0.01$, $\beta = 20$ and $\phi_0 = 0.1$.

of parameter values (α, β), which illustrate that the dissolution is fastest when the dominant effect is bulk dissolution (left curve), and that at higher values of β the dissolution is slower.

In Figure 4.8 we show the dissolution time t_{diss} (which we define to be the time when $\phi = 1$ at $r = 0$) as a function of the nondimensional parameters. We see that, for the majority of the parameter space, the dissolution time is similar. This is because

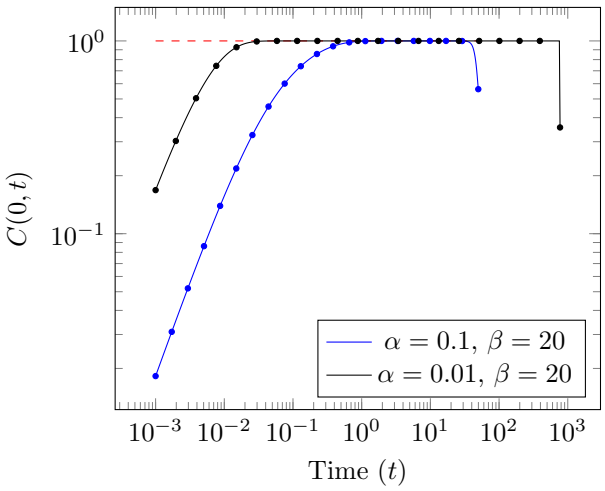

Figure 4.6: Concentration at the centre of the clump as a function of time. The dashed line denotes the saturation concentration. The dots correspond to the values of t for each line shown in Figures 4.4 and 4.5. The parameters for the black curve are $\alpha = 0.01$, $\beta = 20$, while for the blue curve $\alpha = 0.1$, $\beta = 20$, for both we take $\phi_0 = 0.1$.

in these regions, the problem is not diffusion limited and the process is controlled by dissolution in the bulk of the porous medium. However, in the top left corner of (α, β) space, corresponding to large β and small α, the dissolution time increases. This is because, for large β and small α, the problem becomes diffusion-limited, which inhibits the bulk dissolution, so the behaviour changes to a travelling front.

In order to use matched asymptotics for approximating the solution in the case where $\alpha \ll 1$, we need to figure out the scaling involved with the width of the travelling front which we call interior layer. Immediately the question arises: How does the total dissolution time and interior layer thickness scale with α? We plot the dissolution time t_{diss}, found by running multiple simulations, in Figure 4.9 (left). In Figure 4.9 (right) we plot the interior layer thickness δ_{inner} calculated by taking the difference between the positions at which the porosity is $\phi = 1 - \varepsilon$ and $\phi = \bar{\phi} + \varepsilon$, where $\bar{\phi}$ is the porosity on the solid side of the boundary and we use $\varepsilon = 10^{-3}$. We see that the interior layer size scales with $\sqrt{\alpha}$, and that the timescale for dissolution scales with α^{-1}. We will use this information in Section 4.6 to motivate the scalings in our matched asymptotic analysis for $\alpha \ll 1$.

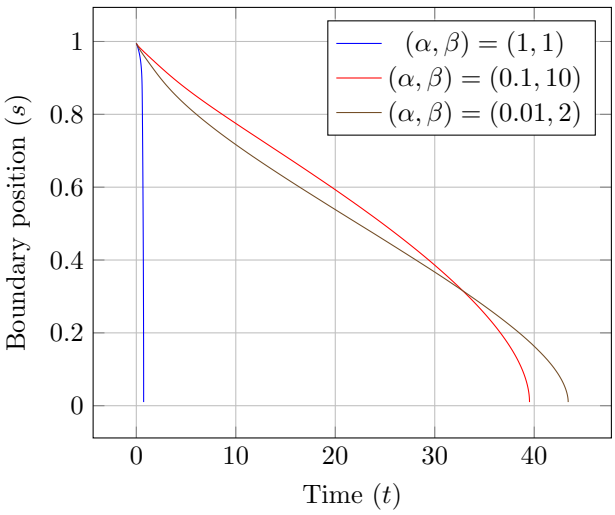

Figure 4.7: Location of the edge of the clump as a function of time for three different parameter values. $(\alpha, \beta) = (1, 1)$, $(0.1, 10)$, and $(0.01, 2)$ in order from left to right.

4.5 Small diffusion, $\alpha \ll 1$

Given that, for the operating parameters, we estimated in (4.3.10) that α is small, we now investigate the limit $\alpha \ll 1$ with the aim of understanding how the choice of β determines whether we have bulk dissolution or travelling front solutions. We consider the leading-order equations in the small-α limit by expanding $\phi \sim \phi^{(0)}$, $C \sim C^{(0)}$ as $\alpha \to 0$, giving

$$\frac{\partial \left(\phi^{(0)} \left(C^{(0)} - \beta\right)\right)}{\partial t} = 0, \tag{4.5.1}$$

$$\frac{\partial \phi^{(0)}}{\partial t} = (1 - \phi^{(0)})^{2/3}(1 - C^{(0)})_+, \tag{4.5.2}$$

with initial conditions

$$\phi^{(0)} = \begin{cases} \phi_0 & 0 < r < 1 \\ 1 & 1 < r < \infty \end{cases} \quad \text{at} \quad t = 0, \tag{4.5.3}$$

$$C^{(0)} = 0 \quad \text{at} \quad t = 0. \tag{4.5.4}$$

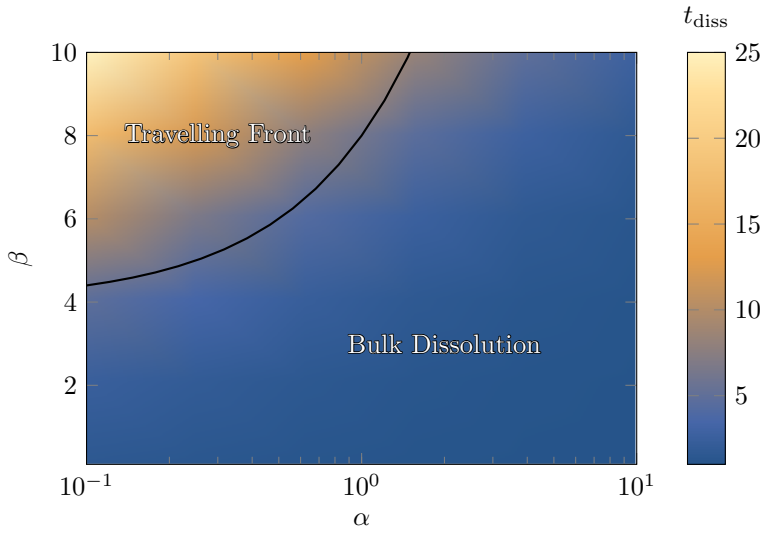

Figure 4.8: Dissolution time as a function of nondimensional parameters α and β. The colour denotes the dissolution time, with blue values indicating shorter dissolution times.

Since (4.5.1) and (4.5.2) are simply ODEs in time, we consider the cases $r < 1$ and $r > 1$ separately. For $r > 1$, since $\phi^{(0)} = 1$ at $t = 0$, equation (4.5.2) tells us that $\phi^{(0)} = 1$ everywhere, while (4.5.1) tells us that $C^{(0)} = 1$. For $r < 1$, we integrate (4.5.1) and apply the initial conditions (4.5.3) and (4.5.4) to find that

$$C^{(0)} = \frac{\beta}{\phi^{(0)}}(\phi^{(0)} - \phi_0). \tag{4.5.5}$$

We substitute (4.5.5) into (4.5.2) which results in a single ODE for $\phi^{(0)}$, namely

$$\frac{\partial \phi^{(0)}}{\partial t} = F(\phi^{(0)}) = (1 - \phi^{(0)})^{2/3} \left(1 - \frac{\beta}{\phi^{(0)}} \left(\phi^{(0)} - \phi_0\right)\right)_+. \tag{4.5.6}$$

We see from (4.5.6) that, if $\beta < 1$, $\partial\phi^{(0)}/\partial t > 0$ for all $\phi^{(0)} \in (0, 1)$, while if $\beta > 1$, $\partial\phi^{(0)}/\partial t > 0$ if $\phi^{(0)} \in \left(0, \min(1, \bar{\phi})\right)$ where $\bar{\phi} = \beta\phi_0/(\beta - 1)$, and $\partial\phi^{(0)}/\partial t = 0$ otherwise. Thus for $\beta > 1$, there is a critical value of β, given by $\beta_c = 1/(1 - \phi_0)$, below which $\partial\phi^{(0)}/\partial t > 0$ for all $\phi^{(0)} \in (0, 1)$. In Figure 4.10 we plot $\partial\phi^{(0)}/\partial t$ as a function of $\phi^{(0)}$ for $\beta = 0.5$ and $\beta = 2$, with $\phi_0 = 0.3$, these being representative of

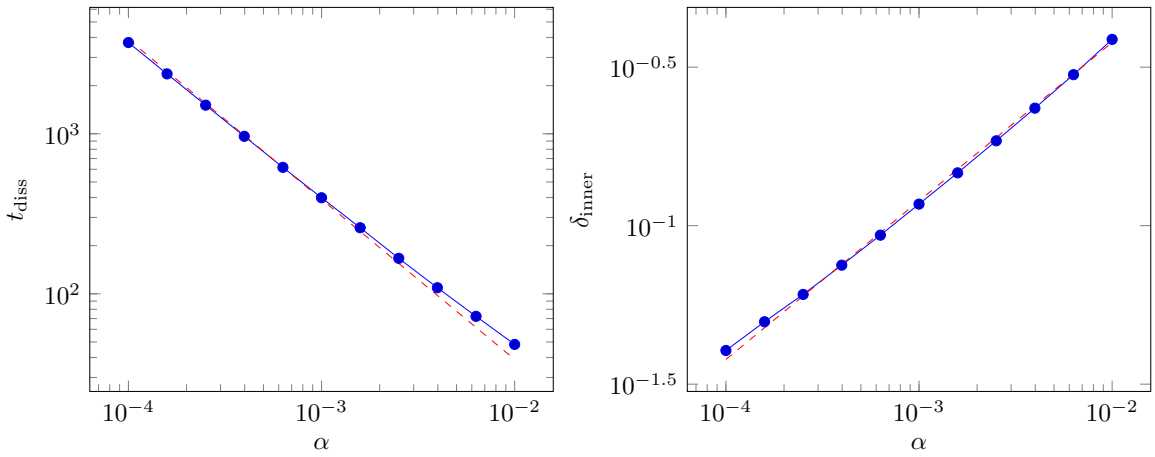

Figure 4.9: Left: Graph showing how t_{diss} varies with α. For comparison the dashed line shows $t_{\text{diss}} = 1/\alpha$. Right: Graph showing how δ_{inner} varies with α. For comparison the dashed line shows $\delta_{\text{inner}} = \sqrt{\alpha}$. $\beta = 10$ in these plots.

the cases $\beta < 1$ and $\beta > 1$, respectively. We see that, when $\beta < 1$, all the curves go through the point $\phi^{(0)} = 1$ and $\partial\phi^{(0)}/\partial t = 0$, while for $\beta > 1$, $\partial\phi^{(0)}/\partial t = 0$ at $\bar{\phi}(\beta)$. Hence, given the initial condition $\phi^{(0)} = \phi_0 < 1$, we deduce that, for $\beta < 1$, $\phi^{(0)} \to 1$ and, from (4.5.5), $C^{(0)} \to \beta\left(1 - \bar{\phi}\right)$ as $t \to t_{\text{diss}}$ (some critical time), while, for $\beta > 1$, $\phi^{(0)} \to \bar{\phi}$ and, from (4.5.5), $C^{(0)} \to 1$ as $t \to \infty$.

We further explore the steady states of (4.5.6) by carrying out a local analysis. First, we substitute $\phi^{(0)} = 1 - \varepsilon\phi_1^{(0)}$ and $t = \varepsilon^{1/3}T$ into (4.5.6) and consider the leading-order equation in ε, which reads

$$\frac{\mathrm{d}\phi_1^{(0)}}{\mathrm{d}T} = -(1 - \beta(1 - \phi_0))\phi_1^{(0)^{2/3}}, \tag{4.5.7}$$

which has the solution

$$\phi_1^{(0)} = \frac{1}{27}\left((1 - \beta(1 - \phi_0))(T_c - T)\right)^3, \tag{4.5.8}$$

for a positive constant T_c, at which $\phi_1^{(0)} = 0$. Thus, we conclude that the steady state $\phi^{(0)} = 1$ is reached in finite time.

Next, for the steady state $\phi^{(0)} = \bar{\phi}$, we substitute $\phi^{(0)} = \bar{\phi} - \varepsilon\phi_1^{(0)}$ into (4.5.6) to

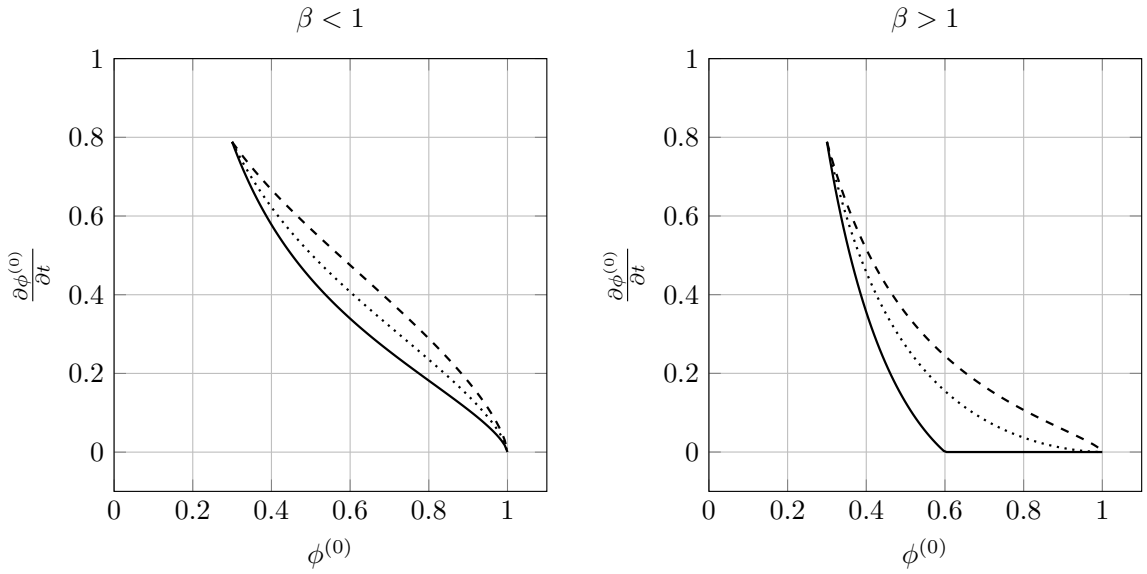

Figure 4.10: Plot of $\partial\phi^{(0)}/\partial t$ as a function of $\phi^{(0)}$ in (4.5.6) for $\beta = 0.25$ (dashed), $\beta = 0.5$ (dotted), $\beta = 0.75$ (solid) (left) and $\beta = 1.1$ (dashed), $\beta_c = 10/7$ (dotted), $\beta = 2$ (solid) (right), for $\phi_0 = 0.3$.

find that $\phi_1^{(0)}$ satisfies

$$\frac{\mathrm{d}\phi_1^{(0)}}{\mathrm{d}t} = -\frac{(\beta-1)^2}{\beta\phi_0}\left(\frac{\beta(1-\phi_0)-1}{\beta-1}\right)^{2/3}\phi_1^{(0)}, \tag{4.5.9}$$

which has the solution

$$\phi_1^{(0)} = C\exp\left(-\frac{(\beta-1)^2}{\beta\phi_0}\left(\frac{\beta(1-\phi_0)-1}{\beta-1}\right)^{2/3}t\right), \tag{4.5.10}$$

for some constant C. Thus we see that, $\phi_1^{(0)} \to 0$ as $t \to \infty$, so reaching the steady states takes infinite amount of time. We solve (4.5.6) in $\phi^{(0)} \in (\phi_0, \min(1, \bar{\phi}))$ to find that

$$\begin{aligned} t = {} & \frac{3\left(\sqrt[3]{1-\phi^{(0)}} - \sqrt[3]{1-\phi_0}\right)}{\beta-1} \\ & + \frac{3\beta\phi_0}{2(\beta-1)^2}\left(\frac{{}_2F_1\left(\frac{2}{3},1;\frac{5}{3};\frac{\beta(\phi_0-1)+1}{(\beta-1)(\phi^{(0)}-1)}\right)}{(1-\phi^{(0)})^{2/3}} - \frac{{}_2F_1\left(\frac{2}{3},1;\frac{5}{3};\frac{\beta(\phi_0-1)+1}{(\beta-1)(\phi_0-1)}\right)}{(1-\phi_0)^{2/3}}\right), \end{aligned} \tag{4.5.11}$$

which provides an implicit solution for $\phi^{(0)}$ as a function of t; here ${}_2F_1$ is a hypergeometric function (and we note that the first hypergeometric function in (4.5.11) tends to infinity as $\phi \to \bar{\phi}$). We plot the solution for $\phi^{(0)}$ and $C^{(0)}$ given by (4.5.5) and (4.5.11), for various values of β, in Figure 4.11; the critical value of $\beta_c = 10/7$. We see that both the concentration and the porosity increases with time. For $\beta < \beta_c$, we see that $\phi^{(0)} \to 1$ and $C^{(0)} \to \beta(1-\phi_0)$ as $t \to t_{\text{diss}}$, while for $\beta = \beta_c$, both $\phi^{(0)} \to 1$ and $C^{(0)} \to 1$ as $t \to \infty$, and finally, for $\beta > \beta_c$, $\phi^{(0)} \to \bar{\phi}$ and $C^{(0)} \to 1$.

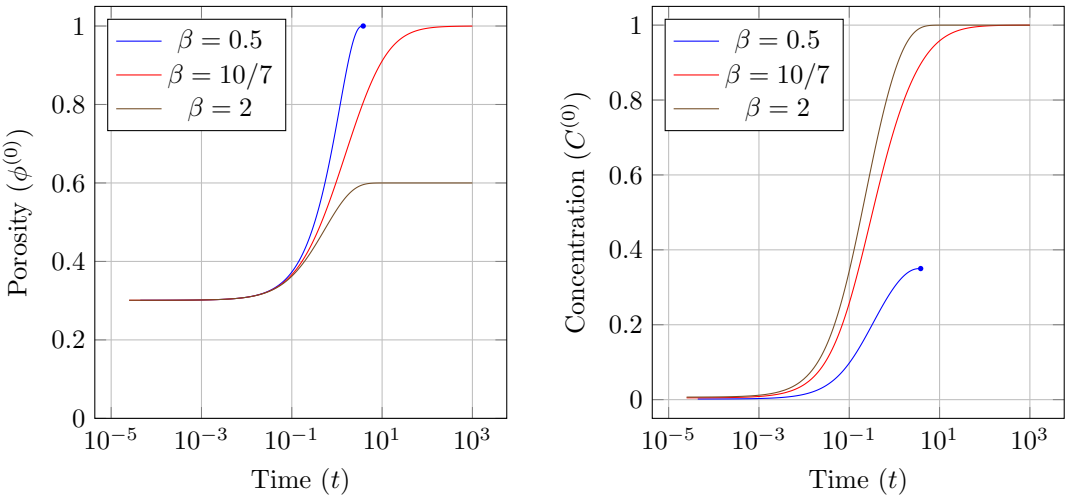

Figure 4.11: Graph of $\phi^{(0)}$ and $C^{(0)}$ given by (4.5.5) and (4.5.11) as a function of time for three different values of $\beta = 0.2, 10/7, 2$ with $\phi_0 = 0.3$. The $\beta_c = 10/7$ is the value at which the behaviour changes. The dots marks the points at which $t = t_{\text{diss}}$.

In Figure 4.12 we compare the asymptotic solution given by (4.5.5) and (4.5.11) with the numerical solution of (4.4.1)–(4.4.6) in the case where $\alpha = 0.1$ and we see that there is excellent agreement between these solutions at early time, except very close to the edge of the clump.

When $\beta < \beta_c$, we use the explicit formula (4.5.11) to calculate the dissolution time,

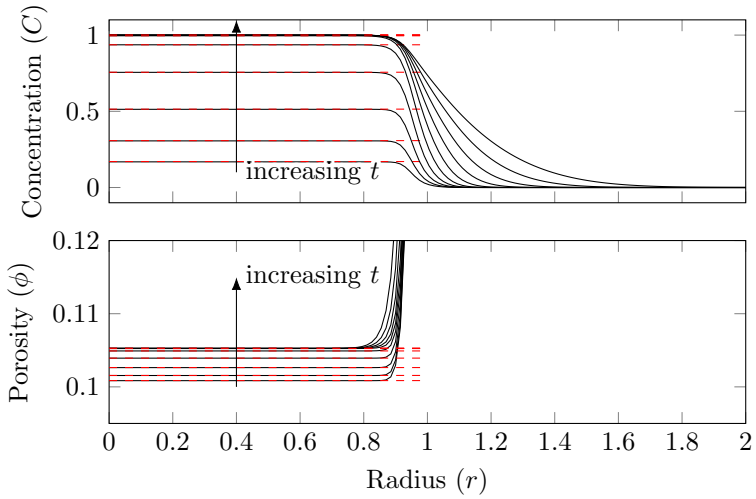

Figure 4.12: Concentration and the porosity as a function of radius for $t = 0, \ldots, 1$. The initial concentration is a horizontal line and the red dashed lines denote the solutions of (4.5.5) and (4.5.11) in $r < 1$. The parameters are $\alpha = 0.1$, $\beta = 20$, and $\phi_0 = 0.1$.

t_{diss}, which is

$$t_{\text{diss}} = \frac{\beta\left(\frac{4\pi\phi_0\left(\frac{\beta(-\phi_0)+\beta+\phi_0-1}{\beta(\phi_0-1)+1}\right)^{2/3}}{\sqrt{3}} + 6\phi_0 - 6\right) - 3\beta\phi_0\,{}_2F_1\left(\frac{2}{3}, 1; \frac{5}{3}; \frac{\beta(\phi_0-1)+1}{(\beta-1)(\phi_0-1)}\right) - 6\phi_0 + 6}{2(\beta-1)^2\left(1-\phi_0\right)^{2/3}}. \tag{4.5.12}$$

In Figure 4.13 we show t_{diss} as a function of β and ϕ_0 and we see that, as we approach the curve $\beta = \beta_c(\phi_0)$, the dissolution time tends to infinity.

We summarize all of the behaviours by plotting in Figure 4.14 the phase plane of (4.5.1) and (4.5.2) for 4 different values of β. We show the trajectories for the solutions presented in Figure 4.10 as dotted lines; all trajectories emanate from the left-hand axis of the phase plane. Since the phase plane enables us to consider all values of ϕ_0 simultaneously, we invert the critical β relationship and write $\phi_c = (\beta_c - 1)/\beta_c$, which we plot as a red line, when it exists. When $\beta > 1$, we see that solutions above the red line reach $\phi^{(0)} = 1$ and $C^{(0)} = \beta(1 - \phi_0)$, while solutions below the red line reach $\phi^{(0)} = \bar{\phi}$ and $C^{(0)} = 1$. When $\beta \leq 1$ we see that all solutions reach $\phi^{(0)} = 1$ and

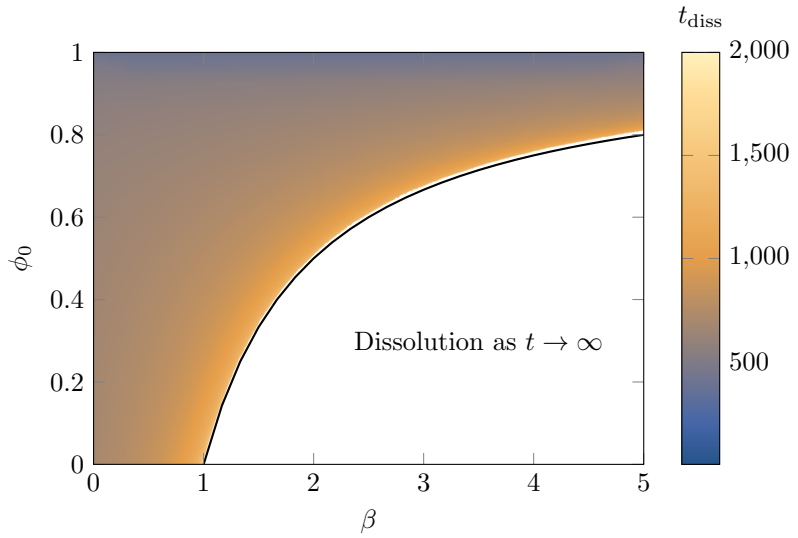

Figure 4.13: Dissolution time given by (4.5.12) as a function of β and ϕ_0. The colour denotes the dissolution time, with blue values indicating shorter dissolution times. The black line is $\beta = \beta_c(\phi_0)$.

$C^{(0)} = \beta(1 - \phi_0)$ and we note that no trajectories can pass the line $C^{(0)} = \beta$ shown in blue.

We note that our solution is not able to reproduce the longer time behaviour seen in Figures 4.4 and 4.5 and that both $\phi^{(0)}$ and $C^{(0)}$ are discontinuous at $r = 1$ when $\beta > \beta_c$. Thus, from (4.3.2), we expect there to be a diffusive interior layer of width $\sqrt{\alpha}$ around $r = 1$ that smoothes this sharp interface and becomes a travelling front. We will analyse the motion of this travelling front in the next section, where we will consider the behaviour of the system on a longer timescale.

4.6 Small diffusion – large time solution

From the numerical solutions presented in Section 4.4, the solution exhibits travelling front behaviour when $\alpha \ll 1$ and $\beta > \beta_c$. We anticipate that the leading-order problem in α outside the particle will be similar to the solid dissolution model analysed in Chapter 2. We consider $\alpha \ll 1$ and we take $\beta \sim \mathrm{O}(1) > \beta_c$.

As illustrated in Figure 4.15, we introduce a front into the problem, located at

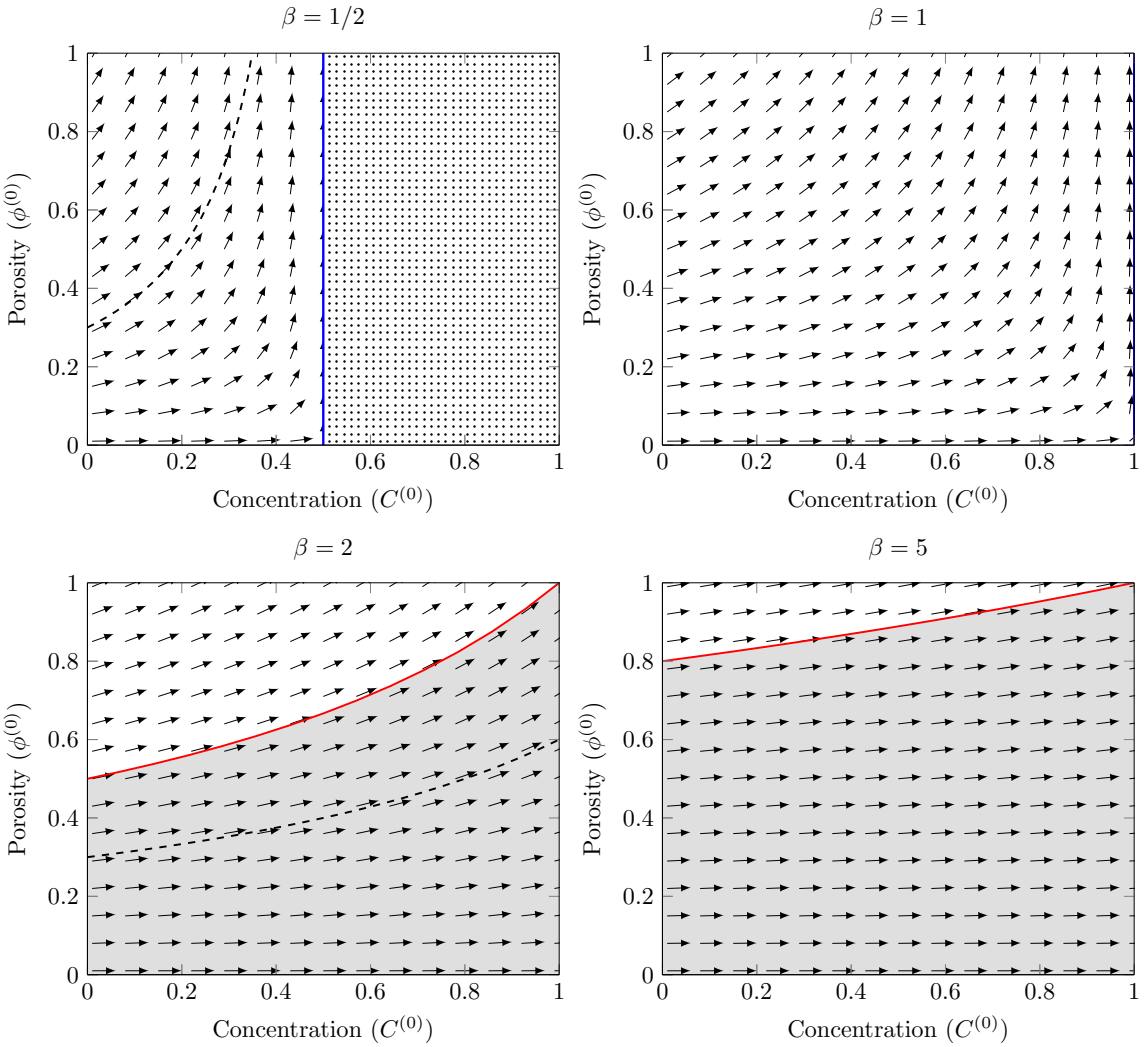

Figure 4.14: Phase plane of (4.5.1) and (4.5.2) for four different β values given by $1/2, 1, 2, 5$. The separatrices are shown in red lines. The dashed lines are two trajectories in Figure 4.10. States that cannot be achieved from the initial condition $C^{(0)} = 0$ are shown by a dotted background.

$r = s(t)$, which separates the domain into three regions: A porous region ahead of the front in $r < s(t)$, a fluid region in $r > s(t)$, and an interior layer connecting these at $r \sim s(t)$, with thickness $\sqrt{\alpha}$ (using the numerical solution as a guide). For clarity we use subscripts to distinguish the solutions in each of the regions using subscript p for the porous region, subscript f for the interior layer, and o for the fluid region outside. Since we know that the movement of the front happens on a timescale $t \sim 1/\alpha$ as

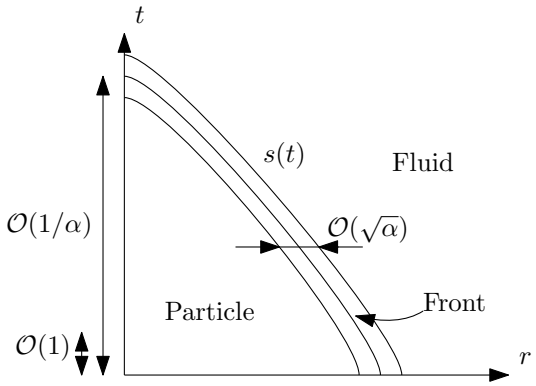

Figure 4.15: Sketch of the asymptotic structure of the moving front case.

$\alpha \to 0$, we scale time in (4.3.2)–(4.3.7) by this value, introducing

$$t = T/\alpha. \tag{4.6.1}$$

In the next few sections, we present and solve the problem in each of the three regions. Before proceeding, we establish the initial conditions for the problem on the T timescale. We write $\phi_p = \phi_p^{(0)} + \sqrt{\alpha}\phi_p^{(1)} + \cdots$, $C_p = C_p^{(0)} + \sqrt{\alpha}C_p^{(1)} + \cdots$ as $\alpha \to 0$, and match the leading-order-in-α terms with the long-time solution to the early time problem presented in Section 4.5. Thus our initial conditions are

$$\phi_p^{(0)} \sim \bar{\phi}, \quad C_p^{(0)} \sim 1 \quad \text{in} \quad r < 1 \quad \text{as} \quad T \to 0. \tag{4.6.2}$$

Meanwhile, for $r > 1$ the porosity and the concentration do not evolve on the short timescale, so we write $\phi_o = \phi_o^{(0)} + \sqrt{\alpha}\phi_o^{(1)} + \cdots$, $C_o = C_o^{(0)} + \sqrt{\alpha}C_o^{(1)} + \cdots$ as $\alpha \to 0$, giving leading-order-in-α initial conditions as

$$\phi_o^{(0)} \sim 1, \quad C_o^{(0)} \to 0 \quad \text{in} \quad r > 1 \quad \text{as} \quad T \to 0. \tag{4.6.3}$$

4.6.1 Inside the particle

Inside the particle, equations (4.3.2) and (4.3.3) may be written in the form

$$\frac{\partial}{\partial T}\left(\phi_p(C_p-\beta)\right)=\frac{1}{r^2}\frac{\partial}{\partial r}\left(r^2\phi_p\frac{\partial C_p}{\partial r}\right), \tag{4.6.4}$$

$$\alpha\frac{\partial \phi_p}{\partial T}=(1-\phi_p)^{2/3}(1-C_p)_+, \tag{4.6.5}$$

for $0<r<S(T)$, $T>0$, with boundary conditions

$$C_p=O(1) \quad \text{as} \quad r\to 0, \tag{4.6.6}$$

and initial conditions given by

$$C_p\to 1 \quad \text{for} \quad 0<r<1 \quad \text{as} \quad T\to 0, \tag{4.6.7}$$

$$\phi_p\to\bar{\phi} \quad \text{for} \quad 0<r<1 \quad \text{as} \quad T\to 0. \tag{4.6.8}$$

Additionally, we require that the solution for C_p and ϕ_p match with the interior layer solution as $r\to s(T)$. We now expand in powers of $\sqrt{\alpha}$ (where the exponent of α is chosen so that we can match with the inner solution in space) with $C_p\sim C_p^{(0)}$, $\phi_p\sim\phi_p^{(0)}$, as $\alpha\to 0$ and find that the leading-order problem of (4.6.4) and (4.6.5) is given by

$$\frac{\partial}{\partial T}\left(\phi_p^{(0)}(C_p^{(0)}-\beta)\right)=\frac{1}{r^2}\frac{\partial}{\partial r}\left(r^2\phi_p^{(0)}\frac{\partial C_p^{(0)}}{\partial r}\right), \tag{4.6.9}$$

$$(1-\phi_p^{(0)})^{2/3}(1-C_p^{(0)})_+=0. \tag{4.6.10}$$

Since $\phi_p^{(0)}=\bar{\phi}<1$ at sufficiently small times, (4.6.10) gives $C_p^{(0)}=1$ initially; but then (4.6.9) then gives $\partial\phi_p^{(0)}/\partial T=0$ initially, and we deduce therefore that $\phi_p^{(0)}=\bar{\phi}$ and $C_p^{(0)}=1$ inside the particle for $r<s^{(0)}(T)$ and all $T>0$.

4.6.2 Outside the particle

Outside the particle, in $r > s(T)$, after rescaling time with $t = T/\alpha$, the system is similar to the one inside the particle given by (4.6.4) and (4.6.5), and reads

$$\frac{\partial}{\partial T}\left(\phi_o(C_o - \beta)\right) = \frac{1}{r^2}\frac{\partial}{\partial r}\left(r^2\phi_o\frac{\partial C_o}{\partial r}\right), \tag{4.6.11}$$

$$\alpha\frac{\partial \phi_o}{\partial T} = (1-\phi_o)^{2/3}(1-C_o)_+. \tag{4.6.12}$$

with boundary condition

$$C_o \to 0 \quad \text{as} \quad r \to \infty, \tag{4.6.13}$$

and the initial condition is

$$C_o \to 0, \quad \phi_o = 1 \quad \text{for} \quad r > s(0) = 1 \quad \text{as} \quad T \to 0. \tag{4.6.14}$$

The final boundary condition comes from matching the solution to (4.6.15), (4.6.17) and (4.6.18) with the corresponding solution in the interior layer.

We expand the variables in power series of the form $C_o = C_o^{(0)} + \sqrt{\alpha}C_o^{(1)} + \cdots$ and $\phi_o = \phi_0^{(0)} + \sqrt{\alpha}\phi_o^{(1)} + \cdots$ which gives

$$\frac{\partial}{\partial T}\left(\phi_o^{(0)}(C_o^{(0)} - \beta)\right) = \frac{1}{r^2}\frac{\partial}{\partial r}\left(r^2\phi_o^{(0)}\frac{\partial C_o^{(0)}}{\partial r}\right), \tag{4.6.15}$$

$$(1-\phi_o^{(0)})^{2/3}(1-C_o^{(0)})_+ = 0, \tag{4.6.16}$$

with boundary condition

$$C_o^{(0)} \to 0 \quad \text{as} \quad r \to \infty, \tag{4.6.17}$$

and the initial condition is

$$C_o^{(0)} \to 0, \quad \phi_o^{(0)} \to 1 \quad \text{for} \quad r > s(0) = 1 \quad \text{as} \quad T \to 0. \tag{4.6.18}$$

Since the solution of (4.6.16) cannot be $C_o^{(0)} = 1$ because this would violate (4.6.17) and (4.6.18), we instead conclude that $\phi_o^{(0)} = 1$. Thus, equation (4.6.15) simplifies to the standard heat equation.

4.6.3 Interior layer

Motivated by the results from Figure 4.9, we introduce the inner scaling as

$$r = s(T) + \sqrt{\alpha}x, \quad C = C_f(x,t), \tag{4.6.19}$$

giving the following rescaled equations

$$\alpha\frac{\partial\left(\phi_f(C_f-\beta)\right)}{\partial t} - \sqrt{\alpha}\frac{\mathrm{d}s}{\mathrm{d}T}\frac{\partial\left(\phi_f(C_f-\beta)\right)}{\partial x} = \frac{\partial}{\partial x}\left(\phi_f\frac{\partial C_f}{\partial x}\right) + \frac{2\sqrt{\alpha}\phi_f}{x\sqrt{\alpha}+s(T)}\frac{\partial C_f}{\partial x}, \tag{4.6.20}$$

$$\alpha\frac{\partial\phi_f}{\partial t} - \sqrt{\alpha}\frac{\mathrm{d}s}{\mathrm{d}T}\frac{\partial\phi_f}{\partial x} = (1-\phi_f)^{2/3}(1-C_f)_+. \tag{4.6.21}$$

We expand in powers of $\sqrt{\alpha}$ using

$$C_f \sim C_f^{(0)} + \sqrt{\alpha}C_f^{(1)} + \cdots, \quad \phi \sim \phi_f^{(0)} + \sqrt{\alpha}\phi_f^{(1)} + \cdots, \quad s \sim s^{(0)} + \sqrt{\alpha}s^{(1)} + \cdots, \tag{4.6.22}$$

as $\alpha \to 0$, to give the O(1) equations

$$\frac{\partial}{\partial x}\left(\phi_f^{(0)}\frac{\partial C_f^{(0)}}{\partial x}\right) + \beta(1-\phi_f^{(0)})^{2/3}(1-C_f^{(0)})_+ = 0, \tag{4.6.23}$$

$$(1-\phi_f^{(0)})^{2/3}(1-C_f^{(0)})_+ = 0, \tag{4.6.24}$$

for $-\infty < x < \infty$. From (4.6.24) we see that the solution is either $C_f^{(0)} = 1$ and $\phi_f^{(0)} = f(x,t)$ for some function f, or $\phi_f^{(0)} = 1$ and $C_f^{(0)} = A(t)x + B(t)$ for some functions $A(t)$ and $B(t)$. However, applying the matching conditions with the particle (that will be verified in the next section) give the far-field boundary conditions given

by

$$C_f^{(0)} \to 1, \quad \phi_f^{(0)} \to \bar{\phi} \quad \text{as} \quad x \to -\infty. \tag{4.6.25}$$

Applying these gives that the solution in the interior layer is $C_f^{(0)} = 1$ and $\phi_f^{(0)} = f(x,t)$. To find the unknown function f and close the system, we use the $\mathrm{O}(\sqrt{\alpha})$ equations given by

$$-(1-\beta)\frac{\mathrm{d}s^{(0)}}{\mathrm{d}T}\frac{\partial \phi_f^{(0)}}{\partial x} = \frac{\partial}{\partial x}\left(\phi_f^{(0)}\frac{\partial C_f^{(1)}}{\partial x}\right), \tag{4.6.26}$$

$$-\frac{\mathrm{d}s^{(0)}}{\mathrm{d}T}\frac{\partial \phi_f^{(0)}}{\partial x} = -C_f^{(1)}(1-\phi_f^{(0)})^{2/3}, \tag{4.6.27}$$

for $-\infty < x < x^*$, where x^* is a finite value at which $\phi_f^{(0)}$ reaches unity (see Figure 4.16 for a sketch of the solution), with far-field conditions given by

$$\phi_f^{(0)} \to \bar{\phi}, \quad C_f^{(1)} \to 0 \quad \text{as} \quad x \to -\infty. \tag{4.6.28}$$

We integrate (4.6.26), apply the far-field conditions on the left (ahead of the front), and find that

$$\phi^{(0)}\frac{\partial C_f^{(1)}}{\partial x} = \frac{\mathrm{d}s^{(0)}}{\mathrm{d}T}\,(\beta-1)(\phi_f^{(0)} - \bar{\phi}), \tag{4.6.29}$$

giving an autonomous phase-plane system (4.6.27) and (4.6.29) for $C_f^{(1)}(x,T)$ and $\phi_f^{(0)}(x,T)$.

In $x > x^*$ the governing equations can be written as

$$\frac{\partial}{\partial x}\left(\phi_f^{(0)}\frac{\partial C_f^{(1)}}{\partial x}\right) = 0 \tag{4.6.30}$$

$$\frac{\partial \phi_f^{(0)}}{\partial x} = 0, \tag{4.6.31}$$

which, by using the assumed continuity of $\phi_f^{(0)}$, $C_f^{(1)}$, and $\partial C_f^{(0)}/\partial x$ at $x = x^*$ has the

solution

$$\phi_f^{(0)} = 1, \tag{4.6.32}$$

$$C_f^{(1)} = \frac{\mathrm{d}s^{(0)}}{\mathrm{d}T}\,(\beta - 1)(1 - \bar{\phi})(x - x^*) + C_f^{(1)}\Big|_{x=x^*}. \tag{4.6.33}$$

We note that, in this expression, x^* and $C_f^{(1)}\Big|_{x=x^*}$ are degrees of freedom one of which cannot be determined by solving the autonomous phase-plane system (4.6.27) and (4.6.29) subject to (4.6.25). In order to determine x^* we solve (4.6.26) and (4.6.27) starting at $x = 0$ and find the point where $\phi_f^{(0)} = 1$. We then read off $C_f^{(1)}\Big|_{x=x^*}$. Having found the solution for $C_f^{(1)}$ and $\phi_f^{(0)}$, we then translate the solution to align with the numerical solution. An alternative approach would be to fix $x^* = 0$, and define $s^{(0)}(T)$ to be the point at which $\phi_f^{(0)} = 1$.

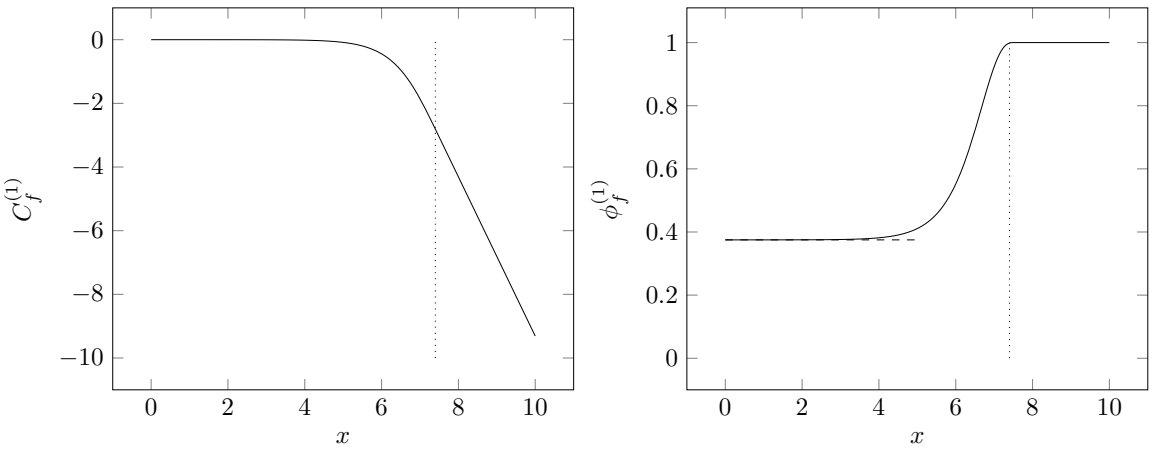

Figure 4.16: Graph of the concentration and the porosity in the interior layer as a function of position for (4.6.27) and (4.6.29). The dashed line on the right denote $\bar{\phi}$, while the dotted vertical lines mark $x = x^*$, the left of this is (4.6.29), while to the right of this line (4.6.32) and (4.6.33) is valid. The parameters are $\phi = 0.3$, $\beta = 5$ and $\frac{\mathrm{d}s^{(0)}}{\mathrm{d}T} = -1$.

4.6.4 Matching the solutions

We need to match together the asymptotic expansions that hold in each of the regions in order to determine the problem that governs the evolution of $r = s^{(0)}$. The

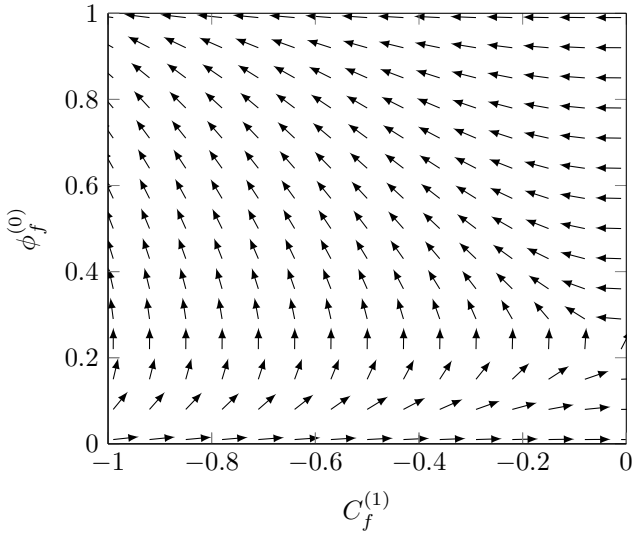

Figure 4.17: Phase plane of the inner problem (4.6.27) and (4.6.29) for $\beta = 10$.

expansions in the different regions as $\alpha \to 0$ are given by

$$C_p(r) = 1 + \mathrm{O}(\alpha^{1/2}), \quad \phi_p(r) = \frac{\beta}{\beta - 1}\phi_0 + \mathrm{O}(\alpha^{1/2}), \tag{4.6.34}$$

$$C_f(x) = 1 + \mathrm{O}(\alpha^{1/2}), \quad \phi_f(x) = \phi_f^{(0)}(x) + \mathrm{O}(\alpha^{1/2}), \tag{4.6.35}$$

$$C_o(r,T) = C_o^{(0)}(r,T) + \mathrm{O}(\alpha^{1/2}), \quad \phi_o(r) = 1 + \mathrm{O}(\alpha^{1/2}), \tag{4.6.36}$$

where $\phi_f^{(0)}(x)$ is the solution of the system (4.6.27) and (4.6.29) and $C_o^{(0)}$ obeys the diffusion equation (4.6.15) outside.

First, we match the particle solution and the front solution which gives

$$\lim_{r \to s(T)} C_p^{(0)}(r,T) = 1 = \lim_{x \to -\infty} C_f^{(0)}(x,T), \tag{4.6.37}$$

$$\lim_{r \to s(T)} \phi_p^{(0)}(r,T) = \frac{\beta\phi_0}{\beta - 1} = \lim_{x \to -\infty} \phi_f^{(0)}(x,T). \tag{4.6.38}$$

This yields the far-field condition (4.6.25) that closes the inner problem. Then we

match the front solution with the solution outside of the spherical clump to obtain

$$\lim_{x\to\infty} C_f^{(0)}(x,T) = 1 = \lim_{r\to s(T)} C_o^{(0)}(r,T), \tag{4.6.39}$$

$$\lim_{x\to\infty} \phi_f^{(0)}(x,T) = 1 = \lim_{r\to s(T)} \phi_o^{(0)}(r,T). \tag{4.6.40}$$

These matching conditions are not enough to close the system because $\mathrm{d}s^{(0)}/\mathrm{d}T$ is still unknown. The missing condition is the matching condition for the flux

$$\lim_{x\to\infty} \frac{\partial C_f^{(1)}}{\partial x} = \lim_{r\to s(T)} \frac{\partial C_o^{(0)}}{\partial r}, \tag{4.6.41}$$

which gives the final condition for the outer problem $C_o^{(0)}$: using (4.6.33) we deduce that

$$\frac{\partial C_o^{(0)}}{\partial r}\,(s^{(0)},T) = (1-\bar{\phi})(\beta-1)\frac{\mathrm{d}s^{(0)}}{\mathrm{d}T}, \tag{4.6.42}$$

which physically means that the flux of alumina into the liquid region is dependent on the jump in the porosity, the reaction rate β, and the speed of the front.

With this condition, we now defined a system for $r > s(T)$ and $T > 0$ given by

$$\frac{\partial C_o^{(0)}}{\partial T} = \frac{1}{r^2}\frac{\partial}{\partial r}\left(r^2\frac{\partial C_o^{(0)}}{\partial r}\right), \tag{4.6.43}$$

$$C_o^{(0)} \to 0 \quad \text{as} \quad r\to\infty, \tag{4.6.44}$$

$$C_o^{(0)} = 1, \quad \frac{\partial C_o^{(0)}}{\partial r}\,(s^{(0)},T) = (1-\bar{\phi})(\beta-1)\frac{\mathrm{d}s^{(0)}}{\mathrm{d}T} \quad \text{at} \quad r = S^{(0)}(T), \tag{4.6.45}$$

$$C_o^{(0)} = 0 \quad \text{for} \quad r > S^{(0)}(0) = 1 \quad \text{at} \quad T = 0, \tag{4.6.46}$$

which can be used to track the moving boundary in the sharp interface limit, without the need to solve the system in the whole region. We note that this outer problem is identical to problem (2.4.2) presented in Chapter 2 if we scale $\tau = \sigma T$, and set $\sigma = (1-\bar{\phi})(\beta-1)$ and $\rho_r = 1$. We compare the numerical solution to (4.3.2)–(4.3.6)

(obtained using the method of lines) with the numerical solution to the reduced travelling front problem (4.6.43)–(4.6.46) (also obtained using the method of lines) in Figure 4.18. We show the numerical solution of (4.3.2)–(4.3.6) with solid lines, using circles for the travelling front solution given by (4.6.43)–(4.6.46) and using a red-dashed line for the solution of the inner problem given by (4.6.27) and (4.6.29), fixing the translational invariance by fitting the curve to the appropriate position using least squares (we initiate the fitting by setting $x^* = S^{(0)}(T)$). We see that the travelling wave solution agrees well with the full numerical solution, except at early and late-times. We further see that there is excellent agreement between the solution of the inner problem and the full numerical solution. Similarly, in Figure 4.19 we compare the interior layer solution for the porosity to the numerical solution and find that there is good agreement. We note that, as the front approaches $r = 0$, the interior layer solution is no longer valid, and hence we omit the last curve.

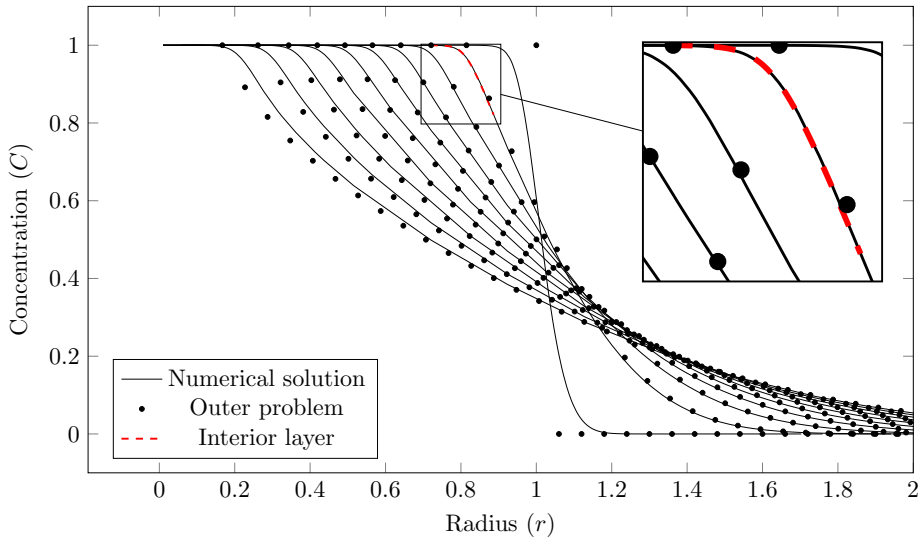

Figure 4.18: Graph showing the concentration as a function of radial position for different times. The solid lines are the numerical solutions of (4.4.1)–(4.4.6) using the method of lines; the dots denote the solution of (4.6.43)–(4.6.46), and the red dashed line is the solution of the inner problem near the front given by (4.6.27) and (4.6.29). Parameters are $\beta = 2$, $\phi_0 = 0.1$, and $\alpha = 10^{-3}$.

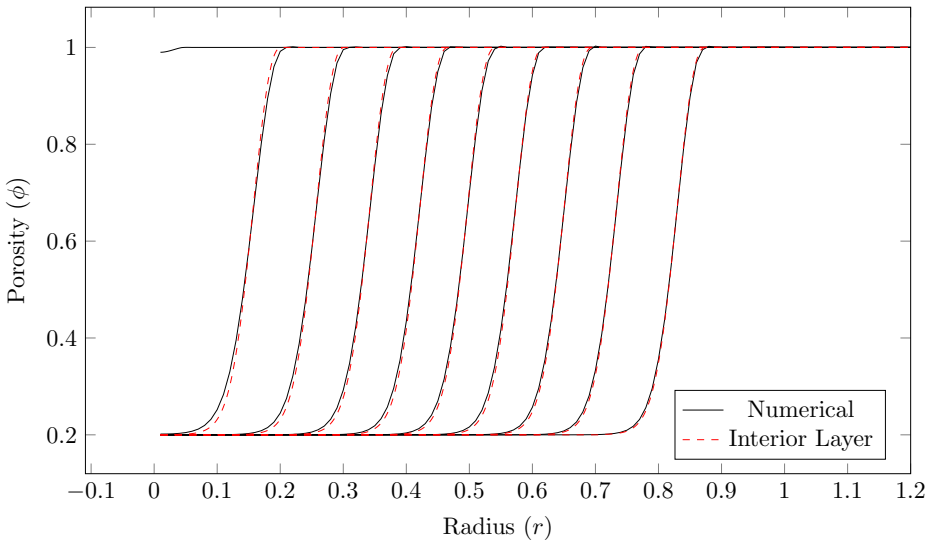

Figure 4.19: Graph showing the porosity as a function of radial position for different times. The solid lines are the numerical solutions of (4.4.1)–(4.4.6) using the method of lines and the red dashed lines are the solutions of the interior layer problem near the front given by (4.6.27) and (4.6.29). Parameters are $\beta = 2$, $\phi_0 = 0.1$, and $\alpha = 10^{-3}$.

4.7 Conclusions

In this chapter, we investigated the dissolution of a spherical clump of alumina in a cryolite bath. We formulated a mathematical model which depends on the dimensionless parameters

$$\alpha = \frac{\rho_p D}{\nu R_0^2 \left(C_s - C_f\right)}, \quad \beta = \frac{\rho_p - C_f}{C_s - C_f}, \tag{4.7.1}$$

along with the initial porosity, ϕ_0, and obtained numerical solutions for various values of α and β using the method of lines. We identified two qualitatively distinct cases: bulk and surface dissolution. In the case of bulk dissolution, the porous medium dissolves at every point uniformly, while in the case of surface dissolution, the clump saturates with alumina, and dissolves from its side and the solution is of travelling front form. We found that the time to completely dissolve the clump in these two cases is given by

$$t_{\text{bulk}} \sim \frac{\rho_p}{\nu(C_s - C_f)} (= \alpha\, t_{\text{front}}), \quad t_{\text{front}} \sim \frac{R_0^2}{D}, \tag{4.7.2}$$

respectively.

We explored the behaviour of the system in the limit $\alpha \ll 1$, which corresponds to large reaction rate, using asymptotic analysis. We use phase-plane analysis to find that, when $\beta < \beta_c$, the clump undergoes bulk dissolution, while if $\beta > \beta_c$, the clump undergoes surface dissolution. We investigated the travelling front case using sharp-interface asymptotics and derived a simplified model similar to the one in Chapter 2. We compared the solution of the original system to the simplified moving boundary case and noted that there is excellent agreement between them in the majority of the evolution.

Chapter 5

Infiltration of a spherical clump

Synopsis

In this chapter, we formulate a mathematical model for the infiltration of molten cryolite into an initially cold, gas-filled, spherical, porous alumina, clump. We investigate two sub-limits: firstly, when the molten cryolite infiltrates without freezing, and secondly when the molten cryolite is partially frozen inside the porespace as it infiltrates. We find that, in both cases, the pressure of the gas increases, which slows down the infiltration. In the second case, the slowdown of the infiltrating front promotes freezing in the porespace and ultimately yields finite time clogging at the infiltration front.

5.1 Introduction

In the previous chapter, we studied the dissolution of a saturated spherical clump of alumina placed instantaneously in a cryolite bath. We now turn our attention to the initial behaviour of a porous spherical clump of alumina immersed instantaneously in molten cryolite, building on the insight gained in Chapters 2 and 3. We saw in Chapter 3 that the combination of infiltration and solidification can result in interesting behaviours, such as the existence of multiple solutions or the nonexistence of a solution, and, for certain parameters values, clogging in finite time. Our goal in this chapter is

to investigate a key effect that we have previously neglected, namely the presence of trapped gas.

In Chapter 3, we neglected the presence of the gas because the rafts are open to the atmosphere and so any gas inside the raft when it enters the cryolite bath can freely exit through the top surface. However, this is not true in general when a clump is submerged sufficiently rapidly that the gas does not have time to escape. Our main area of interest is how the presence of gas inhibits the infiltrating front.

Research into the infiltration of porous materials was discussed in detail in Chapter 3, but we revisit the key references here, for completeness. Models for infiltration of porous spheres are presented in [5, 52, 107], where they investigate experimentally the motion of infiltrating fronts into spherical agglomerates for various fluids. They compare their experimental measurements with explicit predictions from a model based on Darcy's law (for cases where the gas pressure does not increase considerable inside the cavity); they find good agreement between the predictions and the measurements. Often the effect of gas transport and non-equilibrium thermodynamics are included in mathematical models for heat transfer in porous media. The most well-known method for this is to write down a two-temperature model [47, p. 403], which has been used successfully in many contexts [47]. Often multi-phase and complex flow models are derived using homogenisation theory to generate macroscale equations, such as during evaporation [65] or complex flows [74]. The flow of ideal gas inside a porous reservoir was investigated by Muskat and Botset [68] who formulate a mathematical model for radially symmetric injection and solve it using a quasi-steady approximation; subsequent articles refine this approach [69, 70].

We will present the mathematical model in Section 5.2 and nondimensionalise it in Section 5.3. We analyse the model in two different limits. First, we will consider the non-phase changing infiltration limit in Section 5.4 and then we will consider how the solution changes when phase-change is included in Section 5.5. Finally, we summarise

the results and present the conclusions in Section 5.6.

5.2 Mathematical Model

We now describe the mathematical model that we will use to investigate the infiltration of a stationary spherical clump of radius R_0 submerged in cryolite (as shown in Figure 5.1). As before, we will use t to denote the time from the placement of the clump into the liquid. We assume that an infiltration front forms at $r = c(t)$ which separates the clump into two regions: (i) a dry core region in $r < c(t)$ which consists of gas (air in our case) in the pore space between the alumina particles, and (ii) a mushy region in $c(t) < r < R_0$, which consists of liquid and frozen cryolite and alumina particles. We summarize the constituents in each of the regions visually in Figure 5.2. We note that, in this chapter, we will use the small-superheat approximation right from the start in order to not overcomplicate our model, since we have seen in Chapters 2 and 3 that the superheat only changes the behaviour on a longer timescale. In the following sections, we will describe the governing equations in each of these regions using appropriate conservation laws and constitutive relations, and present the boundary and initial conditions.

5.2.1 Dry core

In the dry core region $r < c(t)$, we use a two-temperature formulation for the porous medium [47, p.403]. We assume that, at any given macroscale position, the gas phase and the solid phase can have different temperatures and that there is an exchange of heat between them which manifests as source and sink terms in the governing heat equations. Appealing to conservation of energy and assuming that the heat transfer is proportional to the temperature difference between the two constituents [47], the

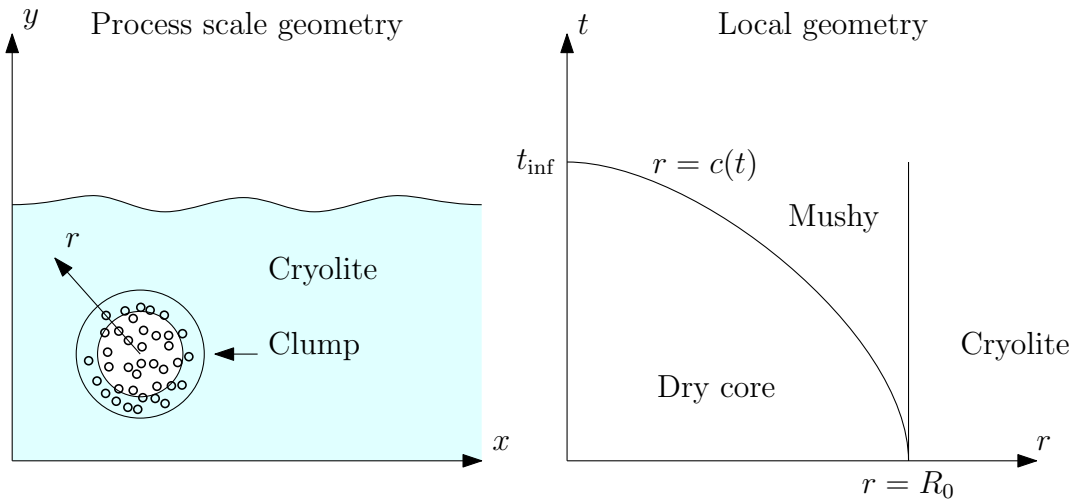

Figure 5.1: Schematic of the cell-scale geometry (left), showing a spherical porous clump of alumina particles inside the cryolite bath, and the local geometry (right), showing the spatial coordinate on the horizontal and the temporal evolution vertically. The moving front is located at $r = c(t)$, and the radius of the porous clump is R_0.

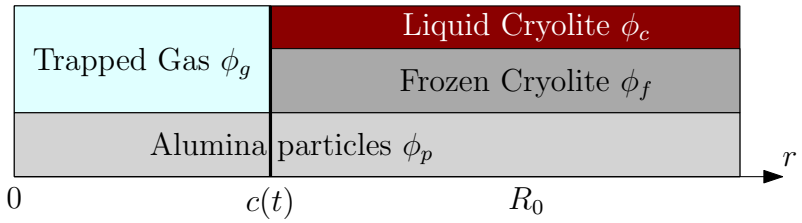

Figure 5.2: Schematic showing the constituents in the two regions in the mathematical model. The infiltration front is shown by a thick black line. On the left of that front is the dry core region containing trapped gas and alumina particles, while to the right is the mushy region with three different constituents, namely the molten cryolite, frozen cryolite, and alumina particles.

equation for the temperature, T_p, of the particles can be written as

$$\phi_p \rho_p c_p \frac{\partial T_p}{\partial t} = \frac{1}{r^2} \frac{\partial}{\partial r} \left(r^2 k_p \frac{\partial T_p}{\partial r} \right) + h \left(T_g - T_p \right), \tag{5.2.1}$$

where ϕ_p is the volume fraction of alumina particles, ρ_p is the density of the alumina, c_p is the heat capacity of the alumina, k_p is the effective heat conductivity of the alumina that takes into account the microscale geometry (here we use $k_p = \phi_p k_a$ rather than (3.2.7) since we have not averaged over the phases in the temperature fields),

and h is the heat transfer coefficient between the gas and the particles.

Similarly, including convection, the gas temperature T_g obeys

$$\phi_g c_g \frac{\partial}{\partial t}\left(\rho_g T_g\right) + \frac{1}{r^2}\frac{\partial}{\partial r}\left(r^2 \phi_g \rho_g c_g T_g u_g\right) = \frac{1}{r^2}\frac{\partial}{\partial r}\left(r^2 k_g \frac{\partial T_g}{\partial r}\right) - h\left(T_g - T_p\right), \quad (5.2.2)$$

where ϕ_g is the gas volume fraction, ρ_g is the density of air, c_g is the heat capacity of air, k_g is the effective heat conductivity of air (given by $k_g = \phi_g k_{air}$), and u_g is the radial gas velocity in the porous medium. We assume that there are no voids in the core so that

$$\phi_g + \phi_p = 1, \quad (5.2.3)$$

and we further assume that ϕ_p, and hence ϕ_g, is constant. Assuming that the air flow is governed by Darcy's law as in, e.g., [68], conservation of mass and momentum for the gas phase can be written as

$$\frac{\partial}{\partial t}\left(\phi_g \rho_g\right) + \frac{1}{r^2}\frac{\partial}{\partial r}\left(r^2 \phi_g \rho_g u_g\right) = 0, \quad (5.2.4)$$

$$\phi_g u_g = -\frac{K(\phi_g)}{\mu_g}\frac{\partial p_g}{\partial r}, \quad (5.2.5)$$

where p_g is the pressure of the gas, K is the permeability function, and μ_g is the viscosity of the gas. We consider that the permeability function can be modelled using the Carman-Kozeny relationship (see, e.g., [47]) given by

$$K(\phi_g) = \frac{a^2 \phi_g^3}{180(1-\phi_g)^2}, \quad (5.2.6)$$

where a is the characteristic size of the pores.

Equations (5.2.1), (5.2.2), (5.2.4) and (5.2.5) provide four equations for the five unknowns T_p, T_g, p_g, ρ_g, u_g. The additional equation that we need is an equation of state for the gas. We assume that the ideal gas law applies locally at every point in

the porous medium, and thus write

$$p_g = \rho_g T_g R_{gas}, \tag{5.2.7}$$

where the R_{gas} is the specific gas constant (which is the universal gas constant divided by the molar mass of the gas).

5.2.2 Mushy region

In the mushy region, $c(t) < r < R_0$, where frozen and molten cryolite both coexist, we make *a priori* the small superheat approximation as in Chapter 3, so that the temperature of the frozen cryolite T_f, of the molten cryolite T_c, and of the porous medium T_p, are everywhere at the melting temperature, T_m, of the cryolite, i.e. $T_f = T_c = T_p = T_m$ in $c(t) < r < R_0$. We appeal to conservation of mass for the solid and for the liquid, assume Darcy flow, and no voids, and thus write

$$\frac{\partial \phi_f}{\partial t} = 0, \tag{5.2.8}$$

$$\frac{\partial \phi_c}{\partial t} + \frac{1}{r^2}\frac{\partial}{\partial r}\left(r^2 \phi_c u_c\right) = 0, \tag{5.2.9}$$

$$\phi_c u_c = -\frac{K(\phi_c)}{\mu_c}\frac{\partial p_c}{\partial r}, \tag{5.2.10}$$

$$\phi_c + \phi_f + \phi_p = 1, \tag{5.2.11}$$

where ϕ_f is the volume fraction of frozen cryolite, ϕ_c is the volume fraction of molten cryolite, u_c is the radial velocity of the molten cryolite, μ_c is the viscosity of the molten cryolite, and p_c is the liquid pressure. We note that, here, ϕ_p is constant.

5.2.3 Boundary and initial conditions

At the centre of the sphere we assume that the temperatures and the gas density are bounded, so we write

$$T_g, T_p, p_g, \rho_g \quad \text{bdd} \qquad \text{at} \quad r = 0. \tag{5.2.12}$$

At the infiltration front, $r = c(t)$, we ensure that we conserve the mass of the gas, the mass of the cryolite, and energy. Further, we assume that the temperatures of all of the phases are at the melting temperature, and that the pressure at this front is given by the difference between the gas pressure and the capillary pressure. Conserving the mass of the gas, we write

$$u_g = \dot{c} \quad \text{at} \quad r = c(t), \tag{5.2.13}$$

while conservation of liquid mass implies

$$\rho_c \phi_c (u_c - \dot{c}) - \rho_f \phi_f \dot{c} = 0 \quad \text{at} \quad r = c(t), \tag{5.2.14}$$

where ρ_c is the density of the molten cryolite, ρ_f is the density of the frozen cryolite, and we account for the phase-change between the liquid and frozen cryolite.

Continuity of temperature across the moving front is given by

$$T_p = T_g = T_c = T_f = T_m \quad \text{at} \quad r = c(t), \tag{5.2.15}$$

while conservation of energy at the interface reads

$$-k_p \frac{\partial T_p}{\partial r} - k_g \frac{\partial T_g}{\partial r} = \rho_c \phi_c h_c (u_c - \dot{c}) - \rho_f \phi_f h_f \dot{c} \quad \text{at} \quad r = c(t), \tag{5.2.16}$$

where h_c and h_f are the enthalpies of the liquid and solid cryolite, respectively. We

simplify (5.2.16) using (5.2.14) and

$$h_c - h_f = L \quad \text{at} \quad T = T_m, \tag{5.2.17}$$

where L is the latent heat, to give

$$-k_p \frac{\partial T_p}{\partial r} - k_g \frac{\partial T_g}{\partial r} = \rho_f L \phi_f^+ \dot{c} \quad \text{at} \quad r = c(t), \tag{5.2.18}$$

The right-hand side accounts for the contribution due to the phase-change of the cryolite at the front, while the left-hand side is the heat flux out of the dry region. The pressures in the liquid and the air are connected at the moving front by the capillary pressure and so we write

$$p_c = p_g - P_c \quad \text{at} \quad r = c(t), \tag{5.2.19}$$

where P_c is the capillary pressure generated by the microscopic menisci, given by $P_c = \gamma/a$, where γ is the surface tension of cryolite and a is the pore size. We note that here, for simplicity, we consider the capillary pressure to be constant, in contrast with Chapter 3.

We assume that the radius of the clump is much smaller than the depth, H, of the clump below the approximate horizontal free boundary of the bath, so that the hydrostatic pressure does not change much around the clump, i.e we write

$$p_c = p_0 + \rho_c g H \quad \text{at} \quad r = R_0, \tag{5.2.20}$$

where p_0 is the ambient pressure outside the bath.

We assume that, initially, the gas pressure p_{g0} is constant, that the clump is at a

given temperature, T_0, and that there is no infiltration. Thus, at $t = 0$,

$$p_g = p_{g0}, \quad T_p = T_g = T_0 \quad \text{in} \quad r < R_0, \tag{5.2.21}$$

$$c = R_0. \tag{5.2.22}$$

The model for ρ_g, ϕ_c, ϕ_f, p_c, p_g, u_c, u_g, T_g, T_p, and c is now fully specified, by the PDEs (5.2.1)–(5.2.10), the boundary conditions (5.2.12)–(5.2.20), and the initial conditions (5.2.21) and (5.2.22).

5.3 Nondimensionalisation

We nondimensionalize (5.2.1)–(5.2.22) using the following scalings and subsequently drop the hats

$$t = \frac{\mu_c R_0^2}{\phi_0 a^2 \left(p_0 + \rho_c g H + P_c\right)} \hat{t}, \quad r = R_0 \hat{r}, \quad c = R_0 \hat{c}, \quad \rho_g = \frac{p_{g0}}{T_0 R_{gas}} \hat{\rho}_g, \tag{5.3.1}$$

$$u_g = \frac{\phi_0 a^2 R_0 \left(p_0 + \rho_c g H + P_c\right)}{\mu_c R_0^2} \hat{u_g}, \quad u_c = \frac{\phi_0 a^2 R_0 \left(p_0 + \rho_c g H + P_c\right)}{\mu_c R_0^2} \hat{u_c}, \tag{5.3.2}$$

$$p_c = \left(p_0 + \rho_c g H + P_c\right) \hat{p_c} - P_c, \quad p_g = p_{g0} \hat{p_g}, \quad K = a^2 \hat{K}, \tag{5.3.3}$$

$$T_p = (T_m - T_0)\hat{T}_p + T_0, \quad T_g = (T_m - T_0)\hat{T}_g + T_0. \tag{5.3.4}$$

With these scalings we keep the dominant balance in (5.2.5) and (5.2.10), scale the temperatures between the two achievable extremes, and the gas pressure and density with the initial conditions. The timescale that we chose corresponds to the cryolite infiltration timescale.

5.3.1 Dry core

With these scalings, the equations (5.2.1), (5.2.2), (5.2.4), (5.2.5) and (5.2.7) in the dry core in $r < c(t)$ read

$$\frac{\partial T_p}{\partial t} = \frac{C}{r^2}\frac{\partial}{\partial r}\left(r^2\frac{\partial T_p}{\partial r}\right) + D(T_g - T_p), \tag{5.3.5}$$

$$\frac{\partial}{\partial t}\left(\rho_g T_g\right) + \frac{1}{r^2}\frac{\partial}{\partial r}\left(r^2\rho_g T_g u_g\right) = \frac{A}{r^2}\frac{\partial}{\partial r}\left(r^2\frac{\partial T_g}{\partial r}\right) - B(T_g - T_p), \tag{5.3.6}$$

$$\frac{\partial \rho_g}{\partial t} + \frac{1}{r^2}\frac{\partial}{\partial r}\left(r^2\rho_g u_g\right) = 0, \tag{5.3.7}$$

$$\mu_{gc}\phi_g u_g = -\mathcal{A}K(\phi_g)\frac{\partial p_g}{\partial r}, \tag{5.3.8}$$

$$p_g = \rho_g(1 + \mathcal{T}T_g), \tag{5.3.9}$$

where the nondimensional parameters, written in terms of the liquid cryolite infiltration timescale

$$\tau = \frac{\mu_c R_0^2}{\phi_0 a^2\left(p_0 + \rho_c g H + P_c\right)}, \tag{5.3.10}$$

are given by

$$A = \frac{\tau k_g T_0 R_{gas}}{R_0^2 p_{g0} c_g \phi_g}, \qquad B = \frac{\tau h T_0 R_{gas}}{p_{g0} c_g \phi_g}, \qquad C = \frac{\tau k_p}{R_0^2 \rho_p c_p \phi_p}, \tag{5.3.11}$$

$$D = \frac{h\tau}{c_p \rho_p \phi_p}, \qquad \mathcal{T} = \frac{T_m - T_0}{T_0}, \qquad \mu_{gc} = \frac{\mu_g}{\mu_c}; \tag{5.3.12}$$

here A is the ratio of the liquid cryolite infiltration timescale to the timescale for thermal diffusion of the gas; B is the ratio of the liquid cryolite infiltration timescale to the timescale for the gas/alumina heat transfer; C is the ratio of the liquid cryolite infiltration timescale to the timescale for the thermal diffusion of the alumina; D is the ratio of the liquid cryolite infiltration timescale to the timescale for the cryolite heat transfer; $\mathcal{T}$ is the ratio of the superheat to the initial temperature; and μ_{gc} is the

ratio of the gas viscosity to the cryolite viscosity.

5.3.2 Mushy region

Meanwhile, equations (5.2.8)–(5.2.10) in the mushy region $c(t) < r < 1$ read

$$\frac{\partial \phi_c}{\partial t} = 0, \tag{5.3.13}$$

$$\frac{1}{r^2}\frac{\partial}{\partial r}\Big(r^2 \phi_c u_c\Big) = 0, \tag{5.3.14}$$

$$\phi_c u_c = -K(\phi_c)\frac{\partial p_c}{\partial r}, \tag{5.3.15}$$

where we note that we have used (5.2.11) to replace ϕ_f in (5.3.13), which subsequently simplifies (5.3.14), and where

$$K(\phi_c) = \frac{\phi_c^3}{180(1-\phi_c)^2}. \tag{5.3.16}$$

We note that the temperature is equal to one everywhere in this region.

5.3.3 Boundary and initial conditions

Finally, the scaled boundary conditions (5.2.12)–(5.2.14) are

$$\rho_g, p_g, T_g, T_p \quad \text{bdd} \qquad \text{at} \quad r = 0, \tag{5.3.17}$$

$$u_g = \dot{c} \quad \text{at} \quad r = c(t), \tag{5.3.18}$$

$$u_c = \dot{c}\left(1 + \rho_r \frac{\phi_f}{\phi_c}\right) \quad \text{at} \quad r = c(t), \tag{5.3.19}$$

where $\rho_r = \rho_f/\rho_c$. Since $|u_c| \geq |\dot{c}|$, the liquid speed is faster than the front speed, which is appropriate physically, because part of the pores are filled with solid, so that the liquid has to move faster than the front. Remembering that, at the infiltration

front, the temperatures $T_g = T_p = 1$, conservation of energy (5.2.14) reads

$$-\dot{c}\phi_f = \mathrm{St}\left(\frac{\partial T_g}{\partial r} + \bar{k}\frac{\partial T_p}{\partial r}\right) \quad \text{at} \quad r = c(t), \tag{5.3.20}$$

where we note that, if St is small, so that it is hard to change the phase of the material, then either the front moves slowly or there is a small amount of freezing, giving ϕ_f small. Finally the remaining boundary conditions (5.2.15), (5.2.19) and (5.2.20) are given by

$$T_p = T_g = 1 \quad \text{at} \quad r = c(t), \tag{5.3.21}$$

$$p_c = \mathcal{A}p_g \quad \text{at} \quad r = c(t), \tag{5.3.22}$$

$$p_c = 1 \quad \text{at} \quad r = 1. \tag{5.3.23}$$

The initial conditions (5.2.21) and (5.2.22) at $t = 0$ are straightforwardly given by

$$p_g = 1, \quad T_p = T_g = 0 \quad \text{in} \quad r < 1, \quad c = 1 \quad \text{at} \quad t = 0. \tag{5.3.24}$$

We have introduced a further three dimensionless parameters, namely

$$\mathcal{A} = \frac{p_{g0}}{p_0 + \rho_c g H + P_c}, \quad \mathrm{St} = \frac{\tau k_g (T_m - T_0)}{\rho_s L R_0^2}, \quad \bar{k} = \frac{k_p}{k_g}, \tag{5.3.25}$$

where $\mathcal{A}$ represents the ratio of the initial pressure of the gas compared to the total pressure drop from the ambient pressure, St is a modified Stefan number, which is the ratio of the solidification timescale to the timescale of liquid infiltration, and $\bar{k}$ is the ratio of the particle heat conductivity to that of the gas.

If $\mathcal{A} = 1$, the gas pressure balances with the pressure outside, and hence the front does not move because, from (5.3.14), (5.3.15), (5.3.22) and (5.3.24), the pressure is uniform. If $\mathcal{A} < 1$, the pressure inside the dry region is smaller than the gas pressure and hence infiltration is possible. Finally, if $\mathcal{A} > 1$, the inner pressure is larger than

the driving pressure, which would drive out the gas inside. We expect $\mathcal{A} < 1$ for most situations of practical interest. We summarize the values of each of the dimensionless parameters in Table 5.1, and note that B, D and St are all small.

Parameter		Value
Timescale ratio	A	67
Timescale ratio	B	2.075
Timescale ratio	C	0.02
Timescale ratio	D	7.9×10^{-4}
Overheat	$\mathcal{T}$	3.4
Pressure drop	$\mathcal{A}$	0.79
Modified Stefan number	St	0.5×10^{-4}
Conductivity ratio	$\bar{k}$	37
Viscosity ratio	μ_{gc}	0.02

Table 5.1: Dimensionless parameters using the mean physical properties presented in Table 1.1.

In the following sections we will consider two sublimits of our model, namely (i) isothermal infiltration (in Section 5.4, given by $\mu_{gc} \ll 1$, $\mathcal{T} \ll 1$, $\mathrm{St} \ll 1$), and (ii) phase-changing infiltration (in Section 5.5, given by $\mu_{gc} \ll 1$, $D \ll 1$, $\bar{k} \gg 1$, $\mathcal{T} \ll 1$).

5.4 Isothermal infiltration

We first consider the case in which there is no phase change, the gas viscosity is small compared to that of the invading liquid, and the temperature change in the gas is negligible, i.e.

$$\mu_{gc} \ll 1, \quad \mathcal{T} \ll 1, \quad \mathrm{St} \ll 1. \tag{5.4.1}$$

In order to simplify the algebra, we rescale time using $t = \phi_c / K(\phi_c)\hat{t}$. Neglecting the corresponding small terms in (5.3.5)–(5.3.24), we obtain at leading order the following

model: in the dry core region, equations (5.3.7)–(5.3.9) imply

$$\frac{K(\phi_c)}{\phi_c}\frac{\partial \rho_g}{\partial t} + \frac{1}{r^2}\frac{\partial}{\partial r}\left(r^2 \rho_g u_g\right) = 0 \quad \text{in} \quad 0 < r < c(t), \tag{5.4.2}$$

$$\mathcal{A} K(\phi_g)\frac{\partial p_g}{\partial r} = 0 \quad \text{in} \quad 0 < r < c(t), \tag{5.4.3}$$

$$p_g = \rho_g \quad \text{in} \quad 0 < r < c(t), \tag{5.4.4}$$

and, in the mushy region, equations (5.3.13)–(5.3.15) give

$$\frac{\partial \phi_f}{\partial t} = 0 \quad \text{in} \quad c(t) < r < 1, \tag{5.4.5}$$

$$\phi_c u_c = -K(\phi_c)\frac{\partial p_c}{\partial r} \quad \text{in} \quad c(t) < r < 1, \tag{5.4.6}$$

$$\frac{1}{r^2}\frac{\partial}{\partial r}\left(r^2 \phi_c u_c\right) = 0 \quad \text{in} \quad c(t) < r < 1. \tag{5.4.7}$$

The boundary conditions (5.3.19)–(5.3.23) become

$$p_g \quad \text{bdd} \quad \text{at} \quad r = 0, \tag{5.4.8}$$

$$u_g = \frac{K(\phi_c)}{\phi_c}\dot{c} \quad \text{at} \quad r = c(t), \tag{5.4.9}$$

$$u_c = \frac{K(\phi_c)}{\phi_c}\dot{c} \quad \text{at} \quad r = c(t), \tag{5.4.10}$$

$$\phi_f = 0 \quad \text{at} \quad r = c(t), \tag{5.4.11}$$

$$p_c = \mathcal{A} p_g \quad \text{at} \quad r = c(t), \tag{5.4.12}$$

$$p_c = 1 \quad \text{at} \quad r = 1, \tag{5.4.13}$$

and the initial condition (5.3.24) becomes

$$p_g = 1, \quad c = 1 \quad \text{at} \quad t = 0. \tag{5.4.14}$$

5.4.1 Analysis

First, we use conservation of momentum (5.4.6) and conservation of cryolite mass (5.4.7) to find

$$\frac{1}{r^2}\frac{\partial}{\partial r}\left(r^2\frac{\partial p_c}{\partial r}\right) = 0 \quad \text{in} \quad c(t) < r < 1, \tag{5.4.15}$$

then we use conservation of solid mass (5.4.5) and boundary condition (5.4.11) to find that $\phi_f = 0$ in the mushy region, as expected. Conservation of momentum of the gas (5.4.3) yields that p_g is spatially uniform in the dry region. Next, we integrate conservation of mass of the gas (5.4.2) from $r = 0$ to $r = c(t)$ and use boundary condition (5.4.9) to find that the total mass of the gas is conserved, i.e

$$\frac{\mathrm{d}}{\mathrm{d}t}\int_0^{c(t)} r^2 p_g(t)\,\mathrm{d}r = 0. \tag{5.4.16}$$

This expression can be integrated using the fact that p_g is only a function of time, giving

$$c^3 p_g(t) = 1. \tag{5.4.17}$$

We integrate the pressure equation (5.4.15), apply the boundary conditions (5.4.12) and (5.4.13) and use (5.4.17). We find that the pressure inside the infiltrated region is given by

$$p_c = \frac{c(t)^3 - r\,c(t)^2 + \mathcal{A}(r-1)}{r(c(t)-1)c(t)^2}. \tag{5.4.18}$$

We substitute (5.4.18), and the pressure given by (5.4.6), into (5.4.10), which provides a nonlinear ODE for $c(t)$ given by

$$\dot{c} = \frac{c(t)^3 - \mathcal{A}}{(c(t)-1)c(t)^4}. \tag{5.4.19}$$

We solve (5.4.19) to find that

$$t + C = \frac{1}{6}\left(\mathcal{A}^2\left(\log\left(\mathcal{A}^2 + \mathcal{A}c + c^2\right) + 2\mathcal{A}\log\left(c^3 - \mathcal{A}^3\right)\right.\right.$$
$$\left.\left. - 2\log(\mathcal{A} - c) - 2\sqrt{3}\arctan\left(\frac{\mathcal{A} + 2c}{\sqrt{3}\mathcal{A}}\right)\right) + c^2(2c - 3)\right), \tag{5.4.20}$$

where the constant C is determined by applying (5.4.14) and is found to be

$$C = \frac{\mathcal{A}^2}{6}\left(\log\left(1 + \mathcal{A} + \mathcal{A}^2\right) + 2\mathcal{A}\log\left(1 - \mathcal{A}^3\right) - 2\log(\mathcal{A} - 1)\right.$$
$$\left. - 2\sqrt{3}\arctan\left(\frac{\mathcal{A} + 2}{\sqrt{3}\mathcal{A}}\right) - \frac{1}{\mathcal{A}^2}\right). \tag{5.4.21}$$

In Figure 5.3 we plot the solution for c given by (5.4.20) and (5.4.21) for various values of $\mathcal{A}$. We see that, for $\mathcal{A} > 0$, the front moves into the porous clump and approaches a finite-radius steady state as $t \to \infty$, as is to be expected. The steady-state front location c^*, where the gas pressure counteracts the infiltration, is calculated from (5.4.19) to be

$$c^* = \mathcal{A}^{1/3}, \tag{5.4.22}$$

and we show these steady states using red dashed lines in Figure 5.3.

Furthermore, in the limit $\mathcal{A} \to 0$, equation (5.4.19) can be written as

$$\dot{c} = \frac{1}{(c(t) - 1)c(t)}, \tag{5.4.23}$$

which has the implicit solution

$$t = \frac{1}{6} - \frac{c^2}{2} + \frac{c^3}{3}, \tag{5.4.24}$$

which we show using a green line. In this limit, the front reaches the centre of the particle in finite time, in contrast to the $\mathcal{A} \neq 0$ case. The limit is thus singular and we do not expect it to be representative of the $\mathcal{A} \neq 0$ behaviour. We see in Figure 5.3 the

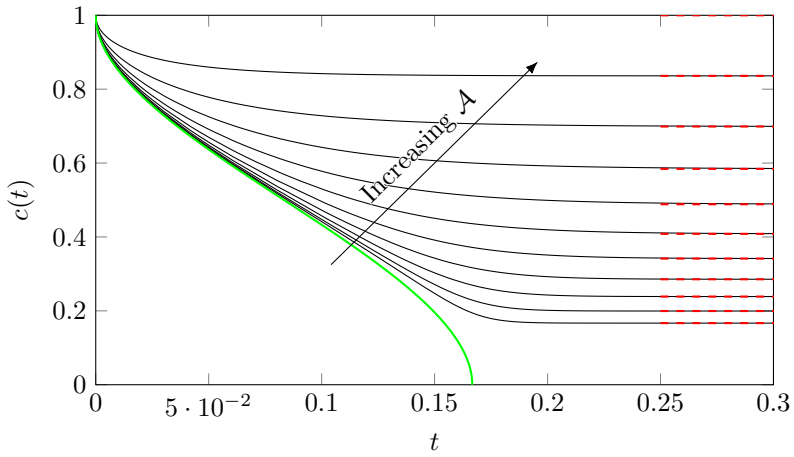

Figure 5.3: Graph showing the front position as a function of time. The black lines are the analytical solutions of (5.4.20) and (5.4.21) for $\mathcal{A} = 10^{-3}, \cdots, 1$ (10 logarithmically distributed points), the green line is the solution when $\mathcal{A} = 0$, given by (5.4.24), and the red dashed lines denote the equilibrium radii given by (5.4.22).

divergence between the $\mathcal{A} = 0$ and $\mathcal{A} > 0$ solutions, as anticipated. This expression, for $\mathcal{A} = 0$, was also derived by Levresse et al. [52, Eq. 7], where they neglect the contribution of gas pressure. In the next section, we will investigate how phase change modifies this behaviour.

5.5 Infiltration with phase-change

We next consider the case in which the viscosity of the gas is small compared to that of the liquid, the gas-solid heat exchange is negligible, the overheat is small, and the heat conductivity of the solid is much greater than that of the gas, i.e.

$$\mu_{gc} \ll 1, \quad D \ll 1, \quad \mathcal{T} \ll 1, \quad \bar{k} \gg 1. \tag{5.5.1}$$

In this limit, the leading-order equations (5.3.5) and (5.3.7)–(5.3.9) are

$$\frac{\partial T_p}{\partial t} = C \frac{1}{r^2} \frac{\partial}{\partial r} \left(r^2 \frac{\partial T_p}{\partial r} \right) \quad \text{in} \quad 0 < r < c(t), \tag{5.5.2}$$

$$\frac{K(\phi_c)}{\phi_c}\frac{\partial \rho_g}{\partial t} + \frac{1}{r^2}\frac{\partial}{\partial r}\left(r^2 \rho_g u_g\right) = 0 \quad \text{in} \quad 0 < r < c(t), \tag{5.5.3}$$

$$\mathcal{A} K(\phi_g)\frac{\partial p_g}{\partial r} = 0 \quad \text{in} \quad 0 < r < c(t), \tag{5.5.4}$$

$$p_g = \rho_g \quad \text{in} \quad 0 < r < c(t), \tag{5.5.5}$$

and, in the mushy region, equations (5.3.13)–(5.3.15) give

$$\frac{\partial \phi_c}{\partial t} = 0 \quad \text{in} \quad c(t) < r < 1, \tag{5.5.6}$$

$$\phi_c u_c = -K(\phi_c)\frac{\partial p_c}{\partial r} \quad \text{in} \quad c(t) < r < 1, \tag{5.5.7}$$

$$\frac{1}{r^2}\frac{\partial}{\partial r}\left(r^2 \phi_c u_c\right) = 0 \quad \text{in} \quad c(t) < r < 1. \tag{5.5.8}$$

The boundary conditions (5.3.17) and (5.3.19)–(5.3.23) for these are

$$T_p \quad \text{bdd} \quad \text{as} \quad r \to 0, \tag{5.5.9}$$

$$u_g = \dot{c} \quad \text{at} \quad r = c(t), \tag{5.5.10}$$

$$\dot{c}(\rho_r \phi_f + \phi_c) = -K(\phi_c)\frac{\partial p_c}{\partial r} \quad \text{at} \quad r = c(t), \tag{5.5.11}$$

$$\phi_f \dot{c} = -\mathrm{St}\bar{k}\frac{\partial T_p}{\partial r} \quad \text{at} \quad r = c(t), \tag{5.5.12}$$

$$T_p = 1 \quad \text{at} \quad r = c(t), \tag{5.5.13}$$

$$p_c = \mathcal{A} p_g(t) \quad \text{at} \quad r = c(t), \tag{5.5.14}$$

$$p_c = 1 \quad \text{at} \quad r = 1, \tag{5.5.15}$$

and the initial conditions (5.3.24) are

$$T_p = 0 \quad \text{in} \quad r < 1, \quad c = 1 \quad \text{at} \quad t = 0. \tag{5.5.16}$$

In this limit, phase-change is possible at the infiltration front and we have to track the temperature in the porous alumina clump, in contrast to the model in Section 5.4.

5.5.1 Analysis

We solve the problem using a method similar to the one presented in Chapter 3. First, we combine (5.5.7) and (5.5.8) to get

$$\frac{1}{r^2}\frac{\partial}{\partial r}\left(r^2\hat{K}(\phi_c(r))\frac{\partial p_c}{\partial r}\right) = 0 \quad \text{in} \quad c(t) < r < 1, \tag{5.5.17}$$

which we then integrate to find that p_c is given by

$$p_c = 1 + \frac{\mathcal{A}p_g(t) - 1}{I(t)} \int_1^r \frac{\mathrm{d}\hat{r}}{\hat{r}^2\hat{K}(\phi_c(\hat{r}))} \quad \text{in} \quad c(t) < r < 1, \tag{5.5.18}$$

in order to satisfy the pressure boundary conditions (5.5.14) and (5.5.15), where I is defined to be

$$I(t) = \int_1^{c(t)} \frac{1}{\hat{r}^2\hat{K}(\phi_c(\hat{r}))}\,\mathrm{d}\hat{r}\,. \tag{5.5.19}$$

We use the differentiation rule to derive an evolution equation for I given by

$$\dot{I}(t) = \frac{\dot{c}}{\hat{K}(\phi_c(c(t)))c(t)^2}, \quad \text{with} \quad I(0) = 0. \tag{5.5.20}$$

Note that, if $\hat{K} = 1$, equation (5.5.18) reduces to the expression (5.4.18) for isothermal infiltration. We differentiate (5.5.18) to find

$$\left.\frac{\partial p_c}{\partial r}\right|_{r=c(t)} = \frac{\mathcal{A}p_g(t) - 1}{I(t)c(t)^2\hat{K}(\phi_c(c(t)))}, \tag{5.5.21}$$

which we substitute into the conservation of mass boundary condition (5.5.11) to obtain

$$\dot{c}c^2(\rho_r\phi_f + \phi_c) = -\frac{\mathcal{A}p_g(t) - 1}{I(t)}. \tag{5.5.22}$$

Finally, similarly to the isothermal case, we integrate conservation of mass of the

gas (5.4.2) from $r = 0$ to $r = c(t)$ and use boundary condition (5.4.9) to obtain

$$c^3 p_g(t) = 1. \tag{5.5.23}$$

With these manipulations and defining $\phi_f^*(t) = \phi_f(c(t))$, we now have a heat equation for the temperature in the alumina clump with three straightforward boundary conditions given by

$$\frac{\partial T_p}{\partial t} = \frac{C}{r^2}\frac{\partial}{\partial r}\left(r^2 \frac{\partial T_p}{\partial r}\right) \quad \text{in} \quad r < c(t), \tag{5.5.24}$$

$$T_p \quad \text{bdd} \qquad \text{at} \quad r = 0, \tag{5.5.25}$$

$$T_p = 1 \quad \text{at} \quad r = c(t), \tag{5.5.26}$$

together with the ODEs for $c(t)$ and $I(t)$ given by

$$c^5 \dot{c}((\rho_r - 1)\phi_f^* + 1 - \phi_a) = -\frac{\mathcal{A} - c^3}{I}, \tag{5.5.27}$$

$$\dot{I} = \frac{\dot{c}}{\hat{K}(1 - \phi_a - \phi_f^*)c^2}, \tag{5.5.28}$$

where ϕ_f^* is given by

$$\phi_f^* = -\frac{\mathrm{St}\bar{k}}{\dot{c}} \left.\frac{\partial T_p}{\partial r}\right|_{r=c}, \tag{5.5.29}$$

with initial conditions

$$T_p = 0 \quad \text{in} \quad r < 1, \quad c = 1, \quad I = 0 \quad \text{at} \quad t = 0, \tag{5.5.30}$$

After this point, making further analytical progress is hard, so we investigate the behaviour numerically. Since the initial condition is discontinuous, we initiate our numerics with the early-time solution that we will now present in the next section.

5.5.2 Early-time solution

At early times, we seek an asymptotic self-similar solution to the system (5.5.24)–(5.5.30) of the form

$$T_p \sim g(\eta), \quad c \sim 1 + 2\lambda_c\sqrt{t}, \quad I \sim 2\lambda_I\sqrt{t}, \quad \phi_f^* \sim \Phi, \tag{5.5.31}$$

where $\eta = (r-1)/(2\sqrt{t})$ and the function $g(\eta)$ and constants λ_c (< 0), λ_I, and Φ are to be determined. It follows from (5.5.24) and (5.5.26), and (5.5.30) that the system that we need to solve is

$$Cg'' + 2\eta g' = 0 \quad \text{in} \quad \eta < \lambda_c, \tag{5.5.32}$$

with

$$g = 1 \quad \text{on} \quad \eta = \lambda_c, \quad g \to 0 \quad \text{as} \quad \eta \to -\infty, \tag{5.5.33}$$

and, because we are considering early time, the boundedness condition (5.5.25) is also applied as $\eta \to -\infty$, and is consistent with (5.5.33). Equations (5.5.32) and (5.5.33) have the solution

$$g(\eta) = \frac{1 + \operatorname{erf}(\eta/\sqrt{C})}{1 + \operatorname{erf}(\lambda_c/\sqrt{C})}. \tag{5.5.34}$$

Appealing to (5.5.27)–(5.5.29), we find that the unknowns λ_c, λ_I, and Φ are given by solving

$$2\Phi\lambda_c + \bar{k}\mathrm{St}g'(\lambda_c) = 0, \tag{5.5.35}$$

$$-1 + A = -2\lambda_I\lambda_c(1 - \phi_a + \Phi(\rho_r - 1)), \tag{5.5.36}$$

$$\lambda_I = \frac{\lambda_c}{\hat{K}(1 - \Phi - \phi_a)}. \tag{5.5.37}$$

We use these equations as initial conditions for our numerical solution, applying them at a small, yet finite, time. We combine (5.5.36) and (5.5.37) and eliminate λ_I to find

that

$$\lambda_c = -\sqrt{\frac{(1-A)\hat{K}(1-\Phi-\phi_a)}{2(1-\phi_a+\Phi(\rho_r-1))}}, \tag{5.5.38}$$

where we take $\lambda_c < 1$ on physical grounds. In Figure 5.4, motivated by (5.5.35), we plot $-2\Phi\lambda_c/g'(\lambda_c)$ and $\bar{k}\mathrm{St}$ for the parameters in Table 5.1 in order to determine whether or not there are solutions for a given set of parameters. As in Section 3.5, we find that there is a critical value of $\bar{k}\mathrm{St}$ above which there are no solutions and, below this value, two solutions exist.

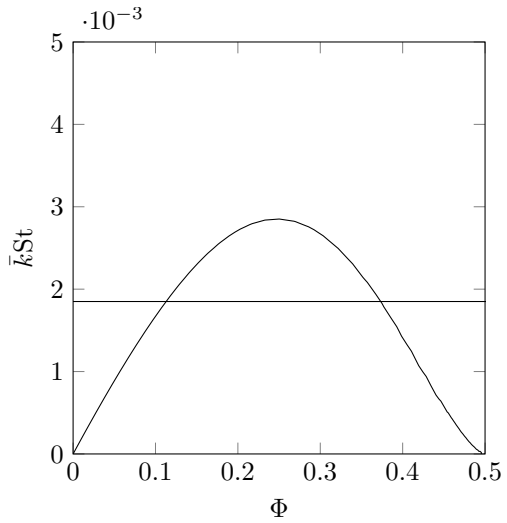

Figure 5.4: Graph of $-2\Phi\lambda_c/g'(\lambda_c)$ in the Φ, $\bar{k}\mathrm{St}$ plane using (5.5.35) and (5.5.38). The intersection of these two curves give the two different early time solutions.

5.5.3 Numerical results

We map the region $0 < r < c(t)$ onto a fixed domain using $r = \xi\, c(t)$, then discretize using finite differences. As in Chapters 2 and 3, since initially there is no infiltrated region, we use the early-time asymptotic solutions in Section 5.5.2 to resolve the initial behaviour and to start our simulation. We expect that the temperature gradient near the moving front needs to be calculated accurately, so we use a nonuniform grid in which there are more points near $r = c(t)$. For our numerical calculations, we use a

geometric point density increase given by

$$\xi_i = \frac{q^{i+1} - 1}{q^{N+1} - 1} \quad \text{for} \quad i = 0, \ldots, N, \tag{5.5.39}$$

where N is the number of discretisation points, and $q < 1$ is a number that controls the geometric sequence which we took to be 0.98. We undertook the usual convergence tests by refining the spatial grid and refining the numerical tolerances used by `Mathematica`.

In Figure 5.5, we show how c and ϕ_f vary with time and we see that there are two possible solutions. We also show the solutions to the early-time problem (5.5.34)–(5.5.37) using red and green dashed lines. We see that the numerical solution initiated from the larger volume fraction diverges from the initial condition more quickly than the one initiated from the smaller volume fraction. Thus we speculate that the solution with smaller volume fraction is stable (in line with Section 3.8). We note that both fronts stop at finite time, which occurs when ϕ_f reaches 1/2.

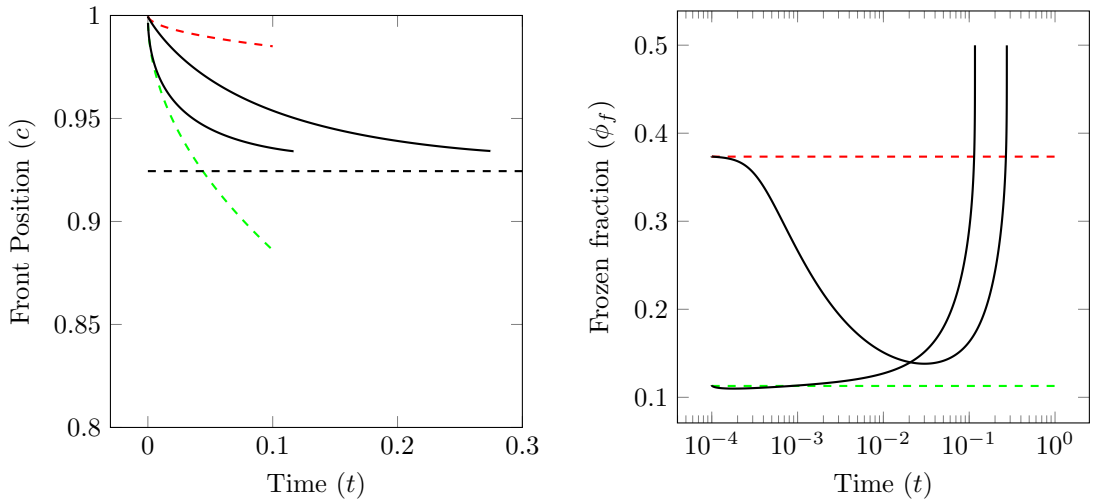

Figure 5.5: Comparison of the two different solutions at early-times. The solid lines are the numerical integration of (5.5.24)–(5.5.30) with initial conditions chosen by the two solutions of (5.5.34)–(5.5.37), the red and green dashed lines are the two solutions of (5.5.34)–(5.5.37), while the black dashed line on the left is the steady-state front location given by (5.4.22). The parameters for this plot are given in Table 5.1.

In Figure 5.6 (left), we show the solution for T_p as a function of r at different times.

We see that, as time progresses, the edge of the clump heats up as it is infiltrated — the infiltration front is located at $T_p = 1$ for each curve. However, clogging occurs quite swiftly and the centre of the clump remains cold througout the evolution. In Figure 5.6 (right), we show how c, I, and ϕ_f^* vary with time (we note that we have plotted $-I$ and the scale for I is different from the scale for c and ϕ_f^*). We see that, initially, c and I decrease and ϕ_f^* increases with time but, while the progression of the infiltrating front slows as time increases, we see that ϕ_f^* starts to increase faster and, as it approaches $\phi_f^* = 1 - \phi_a = 0.5$, this generates a rapid change in the gradient of I which becomes infinite at some finite time, t_c, after which we stop the simulation.

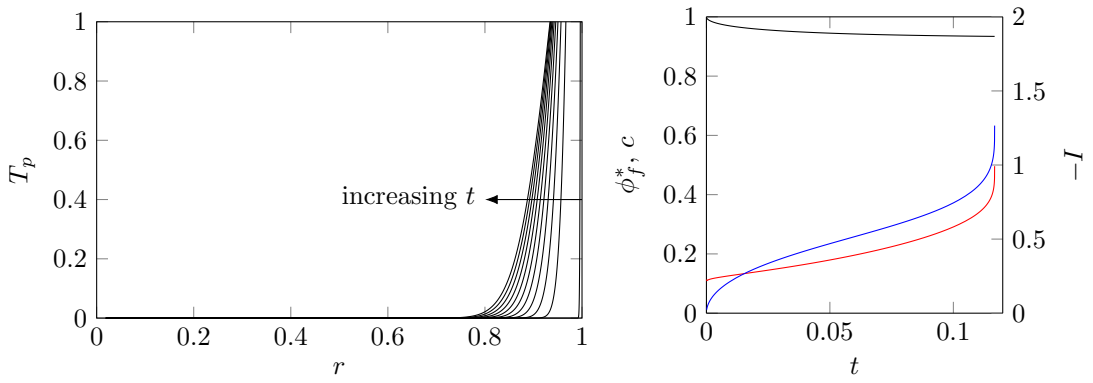

Figure 5.6: (Left) Graph of T_p as a function of r for different times. (Right) Graphs showing the evolution of c (black), ϕ_f^* (red), and $-I$ (blue) as a function of time. The parameters for this plot are given in Table 5.1.

In order to see if the model can exhibit qualitatively different behaviour, for example, whether the temperature can rise in the particle, in Figure 5.7 we plot T_p, c, ϕ_f^*, and I for an artificial parameter set, where we have increased St and C and decreased $\mathcal{A}$ and $\bar{k}$. We see the same qualitative behaviour for c, ϕ_f^*, and I as we have previously observed, but now the infiltration front gets much deeper into the clump and the temperature at the centre has risen singificantly by the time clogging occurs.

In Figure 5.8, we compare the solution in the isothermal case to the solution in the phase-changing case for two different values of $\mathcal{A}$ and we see that including phase-change significantly slows down the infiltration, and in the appropriate limit

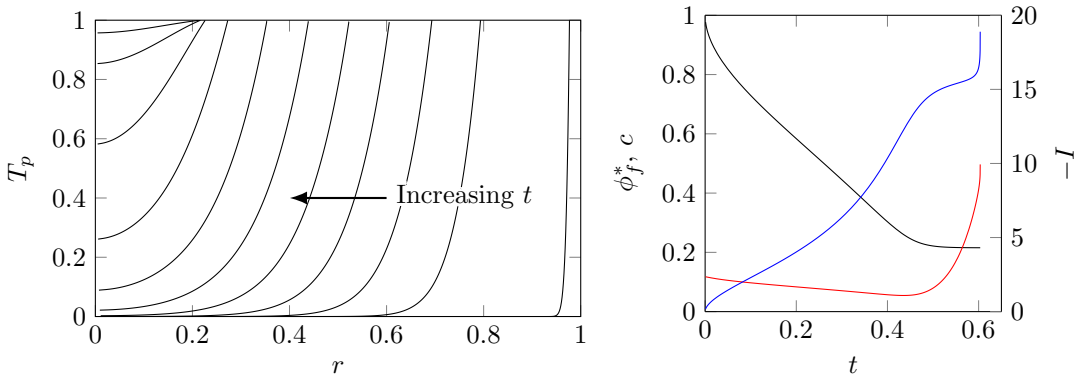

Figure 5.7: (Left) Graph of T_p as a function of r for different times. (Right) Graphs showing the evolution of c (black), ϕ_f^* (red), and $-I$ (blue) as a function of time. The parameters for this plot are $\mathrm{St} = 10^{-2}$, $\mathcal{A} = 10^{-2}$, $C = 10^{-1}$, $\phi_a = 1/2$, $\bar{k} = 1$.

(when $\mathrm{St} \to 0$), the two solutions coincide. We note that, irrespective of the value of St, the final position of the front in the phase-changing case is the same as the steady-state front position in the isothermal case.

In Figure 5.9, we plot the evolution of the flux I (left) and frozen fraction ϕ_f^* (right) as a function of time for five different Stefan numbers. We see that the clogging time decreases as St decreases (the solution with the smallest amount of solid at early times clogs the earliest). As $\mathrm{St} \to 0$, I and ϕ_f^* both approach some limiting behaviour: in the case of ϕ_f^* the solution is approximately constant initially, then rapidly increases to $1 - \phi_a$.

5.6 Conclusions

In this chapter, we investigated a mathematical model combining the spherical geometry in Chapter 2 with the model for infiltration in Chapter 3 in order to evaluate the effect of the enclosed dry core on the evolution of the infiltration front. We considered two cases: isothermal infiltration, in which there is no freezing, and phase-changing infiltration, in which we have to track the volume fractions of solid and liquid cryolite as well as the temperature of the porous material. We solved the isothermal infiltration

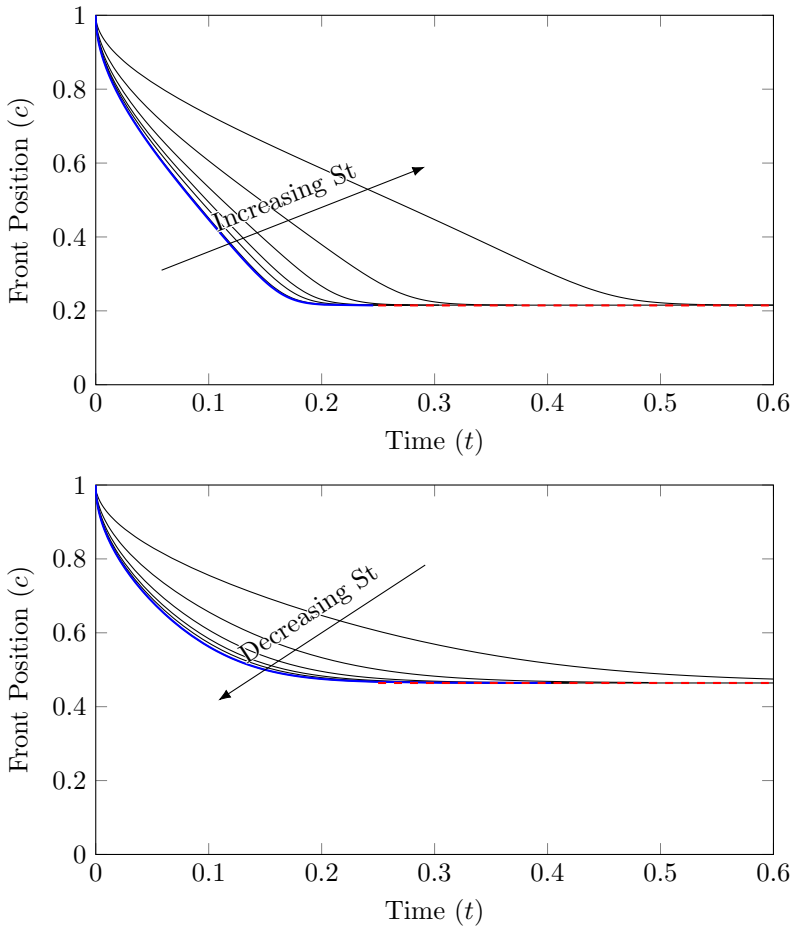

Figure 5.8: Front position as a function of time for the different cases for two different values of $\mathcal{A}$ ($\mathcal{A} = 10^{-2}$ in the top figure, and $\mathcal{A} = 0.3$ in the bottom one). The black lines are the numerical solutions of the phase-changing case for different values of $\mathrm{St} = 1/100, 1/200, 1/400, 1/800, 1/1600$, the blue line is the isothermal case given by (5.4.20) and (5.4.21), and the red dashed line is the equilibrium given by (5.4.22). The rest of the parameters for this plot are $C = 10^{-1}$, $\phi_a = 1/2$, and $\bar{k} = 1$.

problem analytically, which shows that, in the presence of the gas core, the infiltration slows down and reaches a steady state, because the gas pressure increases and results in an opposing force, which ultimately stops the infiltration. We showed that our model agrees with the model in [52] in the limit in which the pressure of the trapped air is negligible.

In the phase-changing case, we employed a similar methodology to that presented in Chapter 3 in order to find the early-time evolution of the model. We found that

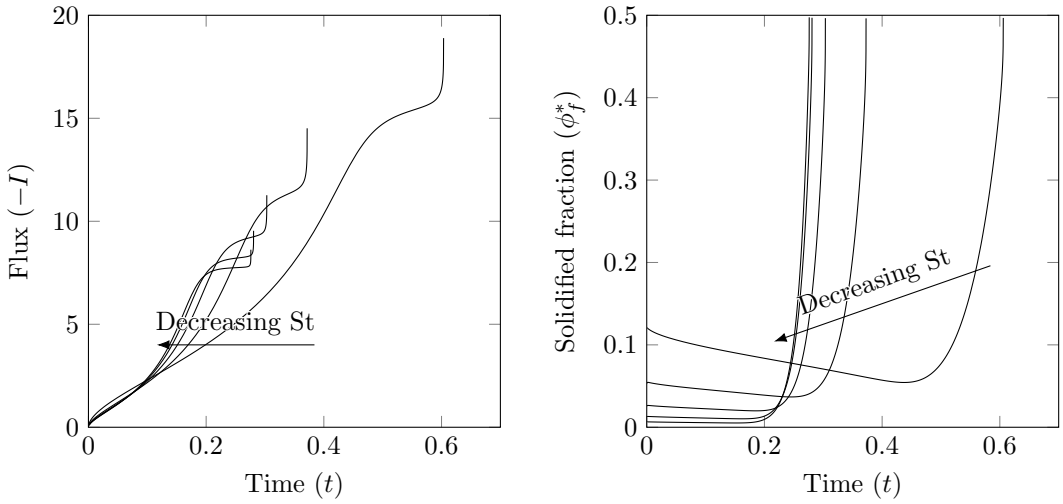

Figure 5.9: Value of $-I$ (left) given by (5.5.19) and the solidified fraction, ϕ_f^*, (right) given by (5.5.22) as a function of time, for different values of St $= 1/100, 1/200, 1/400, 1/800, 1/1600$. Note that at the time of clogging the flux approaches a finite value and does not blow up — the clogging happens at $\phi_f = 1 - \phi_a$. The rest of the parameters for this plot are $\mathcal{A} = 10^{-2}$, $C = 10^{-1}$, $\phi_a = 1/2$, $\bar{k} = 1$.

multiple solutions were again possible and we speculated that the solution with smaller initial volume fraction of solid cryolite is stable. Our numerical solutions showed that the front always clogs at finite time, and away from the centre of the sphere. This is in contrast with the results in Chapter 3, where there is a possibility of complete infiltration. We compared the solutions to the phase-changing problem for different Stefan numbers to the solution to the isothermal problem; the positions of the infiltration front agree as St $\to 0$. We note that the equilibrium position is reached at finite time in the phase-changing case in contrast to the isothermal case where it is reached as $t \to \infty$.

We note that, regardless of whether we consider isothermal or phase-changing infiltration, the presence of the gas core changes the qualitative behaviour from complete infiltration of a spherical clump to partial infiltration with clogging.

Chapter 6

Conclusions

In this thesis, we have focused on the modelling of one part of the Hall-Héroult process for turning alumina into aluminium, namely the microenvironment around an individual alumina particle or a raft of particles in a cryolite bath. Our aim was to understand the heat and mass transfer processes taking place, in order to provide insight into how to control the process.

In Chapter 2, we examined the problem of the dissolution of a cold alumina particle in a bath of hot cryolite. Initially, the dissolution is inhibited by the formation of a frozen layer of cryolite which forms around the particle. We developed a spherically symmetric model to describe the heat and mass transfer between the particle and the surrounding material, allowing for freezing and melting of the cryolite close to the particle, and the particle's subsequent dissolution. We solved this model numerically using the method of lines by using the early-time asymptotic solution to initiate the numerical scheme. We explored the behaviour as we varied the key dimensionless parameters. We find that the temperature perturbation is localised to within 5–10 particle radii. We also considered the problem in the limits of small superheat and of small Stefan number. Using these asymptotic solutions, we found approximate expressions for the freezing, melting, and dissolution times, with freezing being the

fastest effect and dissolution the slowest. In addition, using the early-time solution we determined constraints on the parameters for which shell growth is possible. Our results predict that increasing the superheat or decreasing the particle size should decrease the time it takes for a particle to dissolve, in accordance with practical experience.

In Chapter 3, we formulated a one-dimensional model for the phase-changing infiltration into a porous raft, placed on top of the cryolite. The model comprises of equations describing the temperature in the whole raft, the cryolite velocity, and the volume fraction of frozen cryolite, which we assume can coexist with liquid cryolite in a mushy region. We simplify our model in the limit of small-superheat and solve the equations in a similar way to Chapter 2 using the method of lines and initiating the numerical scheme using the early-time asymptotic solution. The early-time behaviour highlights that the model can exhibit multiple solutions for a given parameter set, one of which is stable and the other one is unstable. We find that, if the Nusselt number is smaller than a critical value that depends on the external temperature the infiltrating front moves completely through the raft leaving behind a region with partially frozen cryolite. For Nusselt numbers above the critical value the model undergoes a discontinuous change in behaviour which corresponds to the clogging of the pore space. Furthermore, near clogging, the volume fraction of frozen cryolite is described by a power law that is dependent on the form of the permeability function; for our choice of permeability, this gave a $t^{1/4}$ power law. This, in turn, influences the short-time behaviour of a backwards propagating clogging front, which has a $t^{4/5}$ front propagation speed, as opposed to the well-known $\sqrt{t}$ behaviour for standard Stefan problems. We also find that there is a critical value of one of the dimensionless parameters, A (which represents how easy it is to freeze the cryolite), below which there are no solutions to the early-time problem. This critical parameter depends very weakly on the Bejan number (which represents the pressure drop at the infiltration

front). When no solutions exist, we expect the cryolite to freeze on the external surface of the raft.

In Chapter 4, we formulated a model for the disintegration of a porous clump of alumina and solved the problem numerically using the method of lines. The numerical solutions have a travelling dissolution front in one parameter regime and bulk dissolution in another. We investigated the travelling dissolution front situation in the case where the reaction rate is large and the diffusion is small by using the method of matched asymptotic expansions to reduce the full problem to a simpler case. The asymptotic expressions match well with the numerical solutions. Our asymptotic analysis yielded a simplified problem analogous to the solid particle problem but for the case of a porous sphere, and we identified the two important timescales in the problem, describing the reaction-limited (bulk dissolution) and diffusion-limited (travelling front) dissolution.

In Chapter 5, we formulated a model for the infiltration of cryolite into a submerged, spherical, clump to see what effect the trapped gas at the centre of the clump will have on the behaviour. We again worked in the limit of small superheat. We simplified this model and compare two cases: (i) isothermal infiltration, and (ii) infiltration with freezing of the cryolite. We solved the isothermal infiltration problem analytically and the phase-changing infiltration problem numerically using the method of lines. We see that, in both cases, the infiltration front stops moving since the pressure of the gas rises and balances the capillary pressure, resulting in a dry core in the centre. In the case where phase change is possible, we observe that the infiltration front propagates slower than in the isothermal infiltration case, and that the front clogs after some finite time since the gas slows down the propagation of the front.

Our overarching question was to determine how long would it take to dissolve an alumina dose completely when it was introduced into a cryolite bath. We answered this question for three relevant geometries (solid particle, porous raft, and porous

clump) and presented timescales for each of them that our industrial collaborators can modify to improve the process.

We were also interested in how much cryolite freezes during the process, which we clarified by finding the maximum radius of a cryolite crust in the case of an impermeable sphere of alumina and the frozen volume fraction of cryolite in the cases of porous rafts and clumps. In the porous raft case, we found out that the infiltrating front can clog, that is, completely freeze, depending on the properties of the raft. This is connected to the question of whether the raft will float or sink since a colder environment promotes front infiltration which increases the weight of the raft and makes it more prone to sinking.

The last question that we wanted to answer is whether the dose will aggregate or disperse. If the infiltrating solution does not exist in the early-time evolution of the raft infiltration model, then we expect that the dose will be frozen at the surface of the cryolite, inhibiting dissolution, while if the infiltrating solution exists, we expect that the dose can disperse after a brief infiltration period, and hence the raft will be consumed.

For a more detailed non-technical summary, we refer the reader to Chapter 7, where these key results are explained in more detail.

6.1 Extensions

A complete description of the feeding of alumina is difficult because many different qualitative changes occur during the process which makes mathematical modelling difficult. Multiple research avenues could be explored in order to build a more complete picture of the process.

In all of our models, we have focused on macroscale problems and assumed that they are governed by averaged physical quantities, such as the average heat

conductivity, that smooth out any porescale variations. Obtaining values for these averaged quantities is not straightforward. A natural next step would be to zoom in to the porescale and systematically average models that hold on the porescale in order to capture the influence of the microscale geometry. We now turn our attention to specific extensions for each chapter.

First, in Chapter 2, we neglected the effect of bulk flow around the alumina particle. Including the bulk flow in the mathematical model would introduce asymmetry and enable a more accurate, non-radially-symmetric prediction for the evolution of the shape of the particle. We also only considered a single particle. Incorporating additional particles, moderately spaced, and assessing the influence of one particle on its neighbours would be useful for describing the local freezing and dissolution processes at higher particle density.

In Chapter 3, we restricted our investigation to one-dimensional rafts. In order to account for infiltration near to the edges of the raft, we would need to explore the behaviour of a two-dimensional analogue of the model that we presented. We anticipate that the increase in the dimensionality of the problem would make both the early-time evolution and the late-time numerical solution much more complicated to solve. Our focus thus far has been on infiltration of rafts. Nevertheless, dissolution should also be incorporated. For simplicity, we used the Kozeny-Carman relation to describe the permeability. It would be useful to explore how other constitutive equations for the permeability would alter the power-law behaviours near clogging.

In Chapter 4, for simplicity we neglected the flow of cryolite generated by the dissolution of the alumina particles. This is unlikely to be negligible in practice, and so including this flow is the key extension to this chapter. We anticipate that including the flow will not alter the general structure of the solution. In addition, the simple relationship describing the dissolution could be replaced by one obtained via systematic averaging of the processes occurring on the porescale.

In Chapter 5, we focused on a spherical clump. The next step would be to apply this model to a two dimensional raft as mentioned earlier. In this model we also ignored the interplay between trapped water and cryolite. Another natural extension would be to include the change of phase from water to steam that occurs when cryolite meets the water, and the subsequent increase in the pressure in the gas phase.

More broadly, there are numerous additional phenomena that we have neglected that could form the basis of future investigations. These include:

(i) Granular Flow

In order to make our investigations simpler, we made the assumption that the alumina particles are either isolated or have been formed into rafts or clumps. This is not true initially, since the alumina flows out of the feeder as a powder and impacts on the surface of the liquid cryolite. We expect that the initial behaviour of the alumina particles upon impacting the cryolite surface is what generates the rafts and clumps, so it would be interesting to explore raft formation by considering the motion of the free-flowing cold powder onto the surface of the hot cryolite. This granular flow problem is hard, even without any phase change in the cryolite. A realistic constitutive model would need to be identified for the bulk movement of the alumina particles which will influence how this powder impacts, and moves into, the liquid cryolite. At one extreme, if the density of the powder is extremely low then the model in Chapter 2 would describe the dissolution, while if the density is high, a modified version of the model in Chapter 3 would be required. In between these regimes, the interplay between individual particles will be crucial for understanding their motion and subsequent dissolution. Such a model could be used to give insight into whether or not a raft forms, which would help our industry collaborators understand how to optimise the feeding part of the process. With a suite of additional such models, it would be possible to answer questions such as: (i) How does the freezing of the cryolite

effect the initial spreading of the powder, or (ii) what is the difference between a cold and hot powder impacting a liquid? These would give more information on how the process parameters, (such as the typical particle size, the height from which the dose is added, the frequency of addition, and the dose size) influence the properties of rafts and clumps.

(ii) Multi-component infiltration

We have focused on the infiltration and freezing of cryolite, assuming that it is a 'pure' liquid. However, cryolite is a multi-component molten salt containing many different molecules [100] and has a complex behaviour that depends heavily on the different chemicals that are added to it. The presence of these chemicals mean that the phase-diagram of the cryolite is not straightforward and local hot spots in the concentration of some of the components are likely to alter the infiltration and freezing behaviour. Capturing these variations, possibly by extending our raft infiltration model to include multiple species and concentration-dependent mushy region behaviour, would be an interesting next step.

It would be interesting to explore how a more complicated phase-diagram changes the infiltration behaviour, and how it affects the presence of multiple solutions and the clogging. When combined with the granular flow model, this would be then a close approximation of the real system.

(iii) Radiation

The Hall-Héroult cell is at such a high temperature that heat transfer via radiation start to become important [83]. Since the cryolite is partly transparent, the boundary conditions that we have prescribed on the boundaries of the porous media in the current thesis are not quite right. For this topic we could draw upon related work on glass manufacture (e.g. [89]), and extend Chapters 2 and 3 to include a radiative Stefan condition. This would enable us to provide more accurate predictions for the

heat transfer times. We expect that including radiation would speed up the melting timescales and make the shells thinner, so we expect that our model give an upper bound for these.

Summary

In this thesis, we have set out to shed new light on the topic of alumina dissolution into molten cryolite in Hall-Héroult cells and we addressed some unanswered questions. We expect that this work will be used by our industrial partners as a stepping stone towards improving the understanding and efficiency of Hall-Héroult cells and, ultimately, benefitting the world by providing a more energy-efficient and cheaper way to produce aluminium, one of the most important materials in today's society.

Chapter 7

Industrial recommendations

7.1 Solid alumina particle

The problem of the feeding of alumina particles into a cryolite bath in the Hall-Héroult process is complicated. Hence, to get a basic understanding of the process, we first investigated the related, but geometrically simpler, problem of placing a single cold alumina particle into a large pool of cryolite [50]. The particle is colder than the liquid and so it removes heat from it. A shell of frozen cryolite thus forms on the particle as shown in the schematic in Figure 7.1. This leads us to the question, how big is this shell, and how fast does it form? Using the mathematical model we have formulated, we provide an answer for these in the form of the following simple equations:

$$\text{maximum size of the shell,} \quad R = a\sqrt[3]{1 + \frac{\rho_p c_p (T_c^* - T_p^*) k_s}{\rho_s k_s L}}, \tag{7.1.1}$$

$$\text{time for shell to reach maximum size,} \quad t_F \approx \frac{a^2 c_p \rho_p}{\pi^2 k_p} \log\left(\frac{2(T_m - T_p^*)k_p}{(T_c^* - T_m)k_c}\right), \tag{7.1.2}$$

where a is the initial size of the particle, c_p is the alumina specific heat capacity, ρ_p is the density of the alumina particle, k_p is the heat conductivity of the alumina particle, T_m is the melting temperature of the cryolite, T_p^* is the initial temperature of the

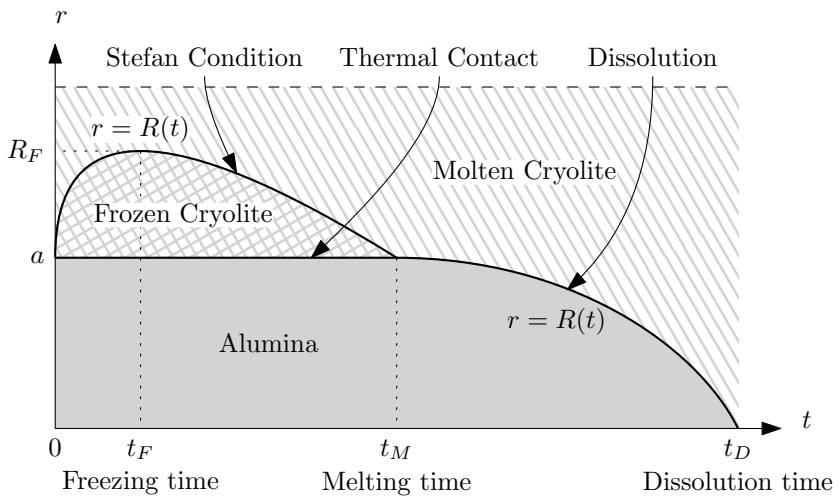

Figure 7.1: Schematic of the geometry used in the mathematical model using time and the radial coordinate.

alumina particle, T_c^* is the temperature of the cryolite liquid far from the particle, k_c is the heat conductivity of the cryolite liquid, k_s is the heat conductivity of the frozen cryolite, ρ_s is the density of the frozen cryolite, and L is the latent heat of solidification for the cryolite. We summarize the dependency of the timescales on these parameters in Figure 7.2 using a dimensionless parameter grouping on the horizontal axis. Using realistic parameters, we find that $t_F \approx 500\,\mu s$ and $R \approx 75\,\mu m$.

We note that the time it takes the cryolite layer to freeze scales with the square of the size of the particle, so small changes in the particle size can change the freezing time substantially. We further note that the radius of the frozen shell scales with the size of the particle and depends only weakly on the other parameters, so is less sensitive to change.

After the frozen shell forms, since the liquid is still hot far away from the sphere, the system gradually heats up and the shell melts. Our model predicts that the time to get back to having no frozen cryolite, t_M, is given by

$$t_M \sim \frac{a^2 c_p \rho_p}{3k_p} \frac{(T_m - T_p^*)k_p}{(T_c^* - T_m)k_c} \approx 100\,\text{ms}, \tag{7.1.3}$$

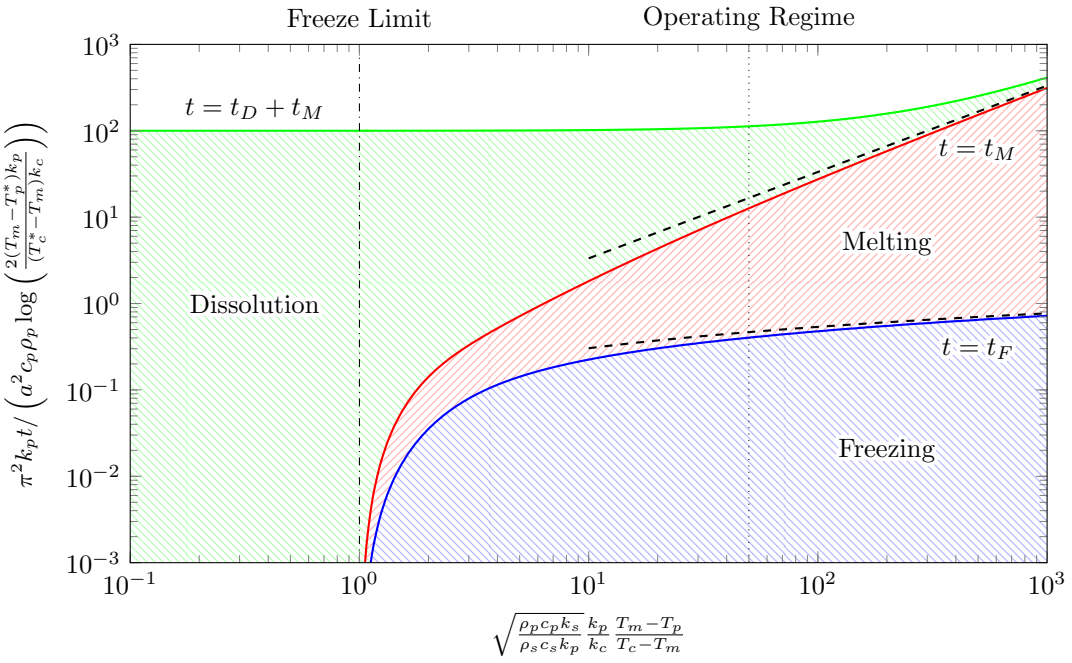

Figure 7.2: Schematic of the different regimes based on the parameters.

(using typical parameters). Once the shell has melted, we find that the temperature of the cryolite is constant. We see that we can decrease the time for melting by increasing the superheat $T_c^* - T_m$ (that is, the difference between the bath temperature and the melting temperature of the cryolite), or by decreasing the particle size a.

After the shell has melted, the liquid cryolite and the alumina particle are in contact, and we use a dissolution model to predict that the time, t_D, taken for the particle to completely dissolve is given by

$$t_D \sim \frac{a^2 \rho_p (1 - C_s/\rho_c)}{2D(C_s - C_f)} \approx 17\,\text{s}, \tag{7.1.4}$$

(using typical parameters), where C_s is the saturation concentration of alumina in the cryolite, D is the diffusivity of alumina in the cryolite, and C_f is the alumina concentration far from the particle.

Thus, in order to minimize the time of dissolution, we should minimize the particle size, a, or increase the saturation concentration, C_s, by changing the cryolite

composition or modifying the temperature.

To assess how valid our 'single particle' model is, we evaluate how far the particle influences the environment. We find that the temperature of the cryolite only decreases in a 5-10 radii region around the particle, which means that if the particles are well separated the evolution will be well captured by our model, but if the particles are closer together, then more detailed models that capture the influence of particles on each other are necessary.

7.2 Porous alumina raft

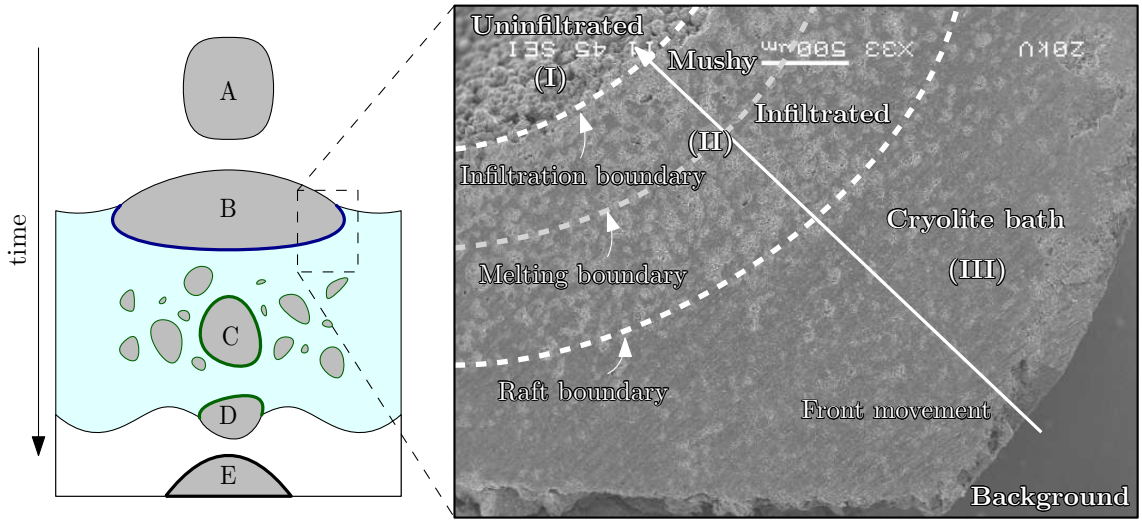

Figure 7.3: Schematic of the geometry focused in this section. The background image (right) is an experiment by [44].

Our next approach was to investigate the infiltration of cryolite into a porous raft of alumina that is floating on top of the liquid as shown in Figure 7.3, since rafts are prevalent in the Hall-Héroult process. Typical questions that industry would like to be answered are: Under what circumstances does a raft form? How long does it take for the raft to disappear? What are the mechanisms determining whether it floats or sinks into the liquid? As a first step towards answering some of these questions, we formulate a mathematical model for the infiltration of liquid cryolite into a porous

raft in order to gain insight into how phase change affects the infiltration.

There are (at least) two things that can happen. Either the liquid freezes on the surface of the raft leading to a frozen-layer-growth problem, similar to the solid particle case, or the liquid infiltrates into the porous medium and freezes inside. We formulate a model for the second scenario and investigate its behaviour. Our model allows for the coexistence of liquid and frozen cryolite within the porous media in a "mushy region".

We find that the infiltration front that moves into the porous medium has a slightly lower speed compared to the speed for an infiltrating front of an isothermal liquid and, in fact, there are two solutions to our model. To decide which one happens in reality, we investigate the stability of these solutions and find that only one of them, which has a faster propagating front and lower volume fraction of frozen cryolite, is stable.

A key result of the model is that we determine (see Figure 7.4) the parameters where the infiltrating solutions cease to exist (which we hypothesise corresponds to a shift to external layer growth). We notice that the industrially relevant parameters put the operating regime, shown as a shaded region with size related to the uncertainty in the physical parameters, near the transition line. This means that small changes in operating conditions may significantly alter the qualitative behaviour of the rafts. This suggests that more research (further refining the transition line) in these marginal cases would be very useful for industrial designs. The controlling parameters for the process are

$$\mathrm{A} = \frac{(1-\phi_a)\rho_s L}{\phi_a \rho_a c_a (T_c - T_a)}, \quad \mathrm{Be} = \frac{\rho_a c_a a^2 (1-\phi_a)(\sigma/a + \rho_c g H)}{180 \mu_c k_p}, \tag{7.2.1}$$

where ϕ_a is the volume fraction of alumina particles, ρ_s is the density of the solidified cryolite, L is the latent heat of solidification of the cryolite, ρ_a is the density of alumina particles, c_a is the isobaric heat capacity of alumina, T_c is the cryolite temperature,

T_a is the initial temperature of the alumina particles, a is the particle size, σ is the cryolite-alumina capillary pressure, ρ_c is the density of the liquid cryolite, g is the gravitational acceleration, H is the depth at which the particle is placed, μ_c is the viscosity of the cryolite, and k_p is the heat conductivity of the alumina particle.

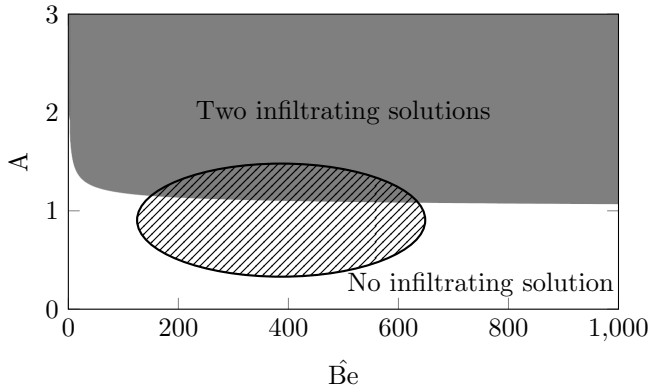

Figure 7.4: Regime diagram for the different solutions, and dashed region shows the operating regime. The definitions of A and $\hat{Be}$ are given in the text.

7.3 Dissolution of a porous clump

Often clumps of alumina particles split from rafts and sink into the cryolite. We next built a mathematical model to explore the dissolution of a submerged, saturated, porous clump. We restrict ourselves to considering spherical clumps.

When a clump separates, we assume that it is already completely infiltrated with liquid, and the liquid then starts to dissolve the constituent particles. Here the question that we can ask is how long does it take to dissolve the clump? We find that, depending on the parameters, there are two qualitatively different behaviours that can occur. If the reaction speed is fast, then the cryolite inside the clump saturates with alumina which slows down the internal dissolution, and the main route for dissolution is through the surface of the clump, similarly to the solid sphere case that we investigated previously. However, if the reaction speed is slow enough, then the clump dissolves from within, at the same rate everywhere. We provide the timescales

for both cases and the regime diagram showing the different behaviours depending on the parameters of the process. The two timescales are given by

$$t_{\text{bulk}} \sim \frac{\rho_p}{\nu(C_{sat} - C_f)}, \quad t_{\text{front}} \sim \frac{a^2}{D}, \tag{7.3.1}$$

where ρ_p is the density of the alumina, ν is the reaction rate, C_f is the far-field concentration of alumina in cryolite, C_{sat} is the saturation concentration of alumina in cryolite, a is the size of the clump, and D is the diffusion coefficient of alumina in cryolite. In the model, we assume the simplest possible form for the dissolution reaction, namely $D = \nu(1-\phi)^{2/3}(C_{\text{sat}} - C_f)$. The reaction rate, ν is not known *apriori*; it would need to be determined by fitting with experimental data.

Our model suggests that, if the goal is to speed up the dissolution of the clumps as much as possible, the bulk alumina concentration should be decreased, or the reaction rate increased by modifying the composition or temperature. Other approaches would be to spread out the clumps or to introduce stirring.

7.4 Infiltration of a gas-filled spherical clumps

Finally, we revisit the behaviour of the clump to see how the presence of gas enclosed at the centre of an alumina clump submerged in cryolite alters the infiltration. The initial behaviour is the same as for a raft: a front that moves into the clump. However, as it moves into the clump, the volume of gas inside decreases. This volume change increases the pressure, which slows down and stops the front propagation resulting in a dry core inside the clump. This effect is present for infiltration when the cryolite remains liquid, but even more pronounced when the cryolite freezes, since this decreases the size of the pores even further.

Using the isothermal model, we calculate how long it takes for liquid cryolite to completely infiltrate into the spherical clump, using realistic parameters for a

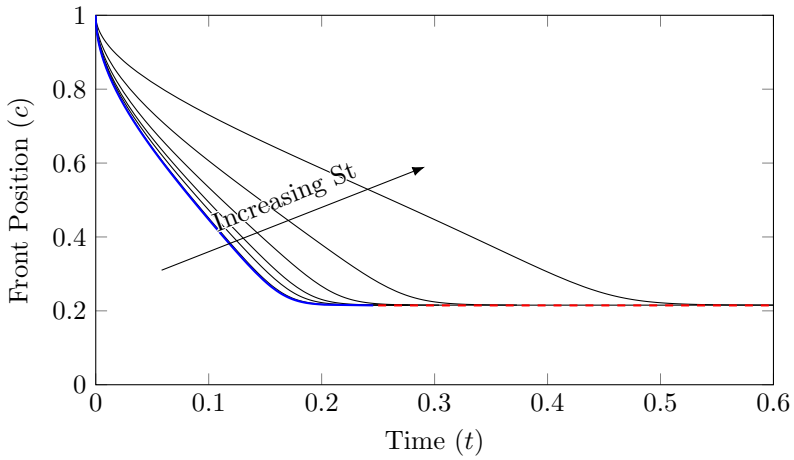

Figure 7.5: Front position shown as a function of time for different values of the Stefan number. The blue line is the solution of the isothermal problem, the red dashed line is the equilibrium front position of the isothermal problem, and the black lines are the solutions of the phase changing model.

centimetre size clump gives

$$t_{\text{inf}} \sim \frac{a^2 \mu}{(p_0 + \rho_c g H + p_c) K} \approx 868\,\mu\text{s}, \tag{7.4.1}$$

where a is the size of the clump, μ is the viscosity of the cryolite, p_0 is the atmospheric pressure, ρ_c is the density of the cryolite, H is the depth at which the clump is placed (10 cm), p_c is the capillary pressure, and K is the permeability of the porous medium. With the typical parameters, the infiltration and the temperature variations are confined to a thin region near the edge of the clump, and therefore most of the clump is cold when the infiltration stops. As we increase the influence of phase-change we find that the infiltration time, t_{inf}, increases (see Figure 7.5).

7.5 Conclusions & Further Work

We have investigated the feeding of alumina into a Hall-Héroult cell. We have formulated mathematical models for a single particle, a floating raft, and a porous clump. We solved all of these models numerically and, where applicable, analytically.

We have identified the important timescales for each of the models and how the solutions of these models behave.

The production of alumina is a complex process and our research can be extended in many different ways. We neglected the effect of bulk flow in our models. Including such flow would enable a more accurate, non-radially-symmetric prediction for the evolution of the shape of the particles and clumps. We focused initially on the heat and mass transfer problem for freezing and melting around, and dissolution of, a single particle. A natural next step is to consider multiple particles in order to determine the influence of particles on each other. We have only considered one-dimensional rafts and are thus not able to capture the infiltrating behaviour near corners. Our model could be easily extended to the two-dimensional analogue which would enable corner infiltration to be studied. Another extension would be to incorporate dissolution into the raft model. In our model for the dissolution of spherical clumps, we neglected the induced flow caused by the dissolution. This is likely to be important and so including flow will be essential for a complete picture on how clumps evolve. It would also be interesting to extend our gas-filled phase-changing infiltration model to describe submerged rafts and to include the reaction between the cryolite and bound water contained within the structure. All our models were formulated at the macroscale level, and involved averaged physical quantities, such as the heat conductivity. In order to more accurately capture the influence of the microscale geometry and chemistry, a key next step is to formulate the appropriate equations on the microscale and systematically average them to find these physical quantities. There are also additional phenomena that we could take into account. For example, introducing granular flow would give more accurate information about the formation of rafts, incorporating the multi-component nature of cryolite would give more insights into the mushy layers, and introducing radiation would more accurately reflect the heat-transfer mechanisms.

We hope that our models and their results increase understanding of particle infiltration and show new perspectives in the field of alumina feeding, ultimately helping our industrial partners to become more energy efficient.

Bibliography

[1] R. Almanza, P. Hernández, I. Martínez, and M. Mazari (2009). *Development and mean life of aluminum first-surface mirrors for solar energy applications*, Solar Energy Materials and Solar Cells 93 (9):1647–1651.

[2] AzoMaterials (2019). *Azo Materials*.

[3] J. M. Back (2016). *Stefan problems for melting nanoscaled particles*. PhD thesis. Queensland University of Technology.

[4] A. J. Bernoff and T. P. Witelski (2010). *Stability and dynamics of self-similarity in evolution equations*, Journal of Engineering Mathematics 66:11–31.

[5] F. Bohin, I. Manas-Zloczower, and D. L. Feke (1994). *Penetration of Silicone Polymers into Silica Agglomerates and Its Influence on Dispersion Mechanism*, Rubber Chemistry and Technology 67 (4):602–609.

[6] V. Bojarevics (2019). *Dynamic Modelling of Alumina Feeding in an Aluminium Electrolysis Cell*, in *Light Metals 2019*. Springer International Publishing, p. 675–682.

[7] M. A. Bunk and J. R. King (2003). *Spreading melts with basal solidification*, ZAMM Zeitschrift fur Angewandte Mathematik und Mechanik 83 (12):820–843.

[8] J. Chadam, D. Hoff, E. Merino, P. Ortoleva, and A. Sen (1986). *Reactive Infiltration Instabilities*, IMA Journal of Applied Mathematics 36 (3):207–221.

[9] V. Dassylva-Raymond, L. Kiss, S. Poncsák, P. Chartrand, J.-F. Bilodeau, and S. Guérard (2014). *Modeling the Behavior of Alumina Agglomerate in the Hall-Héroult Process*, Light Metals:603–608.

[10] J. J. Derksen, G. Reynolds, A. Crampton, Z. Huang, and J. Booth (2015). *Simulations of dissolution of spherical particles in laminar shear flow*, Chemical Engineering Research and Design 93:66–78.

[11] J. N. Dewynne and J. M. Hill (1986). *Integral formulations and bounds for two phase Stefan problems initially not at their fusion temperature*, Acta Mechanica 58:201–228.

[12] F. Dierich and P. A. Nikrityuk (2012). *Euler-Lagrange modelling of melting and solidification with moving solid particles*, Progress in Computational Fluid Dynamics, An International Journal 12 (2/3):112.

[13] F. Dierich, P. A. Nikrityuk, and S. Ananiev (2011). *2D modeling of moving particles with phase-change effect*, Chemical Engineering Science 66 (22):5459–5473.

[14] D. A. Drew and S. L. Passman (1999). *Theory of Multicomponent Fluids*. Springer New York.

[15] J. L. Duda and J. S. Vrentas (1969). *Mathematical analysis of bubble dissolution*, AIChE Journal 15 (3):351–356.

[16] J. L. Duda and J. S. Vrentas (1971). *Heat or mass transfer-controlled dissolution of an isolated sphere*, International Journal of Heat and Mass Transfer 14 (3):395–407.

[17] O. Ehrich, C. Yun-Ken, and K. Schwerdtfeger (1978). *The melting of metal spheres involving the initially frozen shells with different material properties*, International Journal of Heat and Mass Transfer 21 (3):341–349.

[18] K. E. Einarsrud, I. Eick, W. Bai, Y. Feng, J. Hua, and P. J. Witt (2017). *Towards a coupled multi-scale, multi-physics simulation framework for aluminium electrolysis*, Applied Mathematical Modelling 44:3–24.

[19] Elysis Technologies (2020). *Elysis Technologies*.

[20] M. Epstein (1977). *Stability of a Submerged Frozen Crust*, Journal of Heat Transfer 99 (4):527.

[21] M. Epstein and F. B. Cheung (1982). *On the Prediction of Pipe Freeze-Shut in Turbulent Flow*, Journal of Heat Transfer 104:381–384.

[22] M. Epstein and F. B. Cheung (1983). *Complex Freezing-Melting Interfaces in Fluid Flow*, Annual Review of Fluid Mechanics 15:293–319.

[23] D. L. Feltham, N. Untersteiner, J. S. Wettlaufer, and M. G. Worster (2006). *Sea ice is a mushy layer*, Geophysical Research Letters 33 (14).

[24] F. Font (2014). *Beyond the classical Stefan problem*. PhD thesis. Universitat Politecnica de Catalunya.

[25] H. Fujita (1953). *Diffusion with a sharp moving boundary*, The Journal of Chemical Physics 21 (4):700–705.

[26] H. Gan, J. J. Feng, and H. H. Hu (2003). *Simulation of the sedimentation of melting solid particles*, International Journal of Multiphase Flow 29 (5):751–769.

[27] M. Gaune-Escard and K. R. Seddon (2010). *Molten salts and ionic liquids*. Wiley & Sons, Inc.

[28] K. Grjotheim (1982). *Aluminium Electrolysis. Fundamentals of the Hall-Heroult Process*. Aluminium-Verlag.

[29] K. Grjotheim and H. Kvande (1993). *Introduction to Aluminium Electrolysis*. Aluminium-Verlag.

[30] L. Grünhaupt, M. Spiecker, D. Gusenkova, N. Maleeva, S. T. Skacel, I. Takmakov, F. Valenti, P. Winkel, H. Rotzinger, W. Wernsdorfer, A. V. Ustinov, and I. M. Pop (2019). *Granular aluminium as a superconducting material for high-impedance quantum circuits*, Nature Materials 18 (8):816–819.

[31] S. C. Gupta (2003). *The Classical Stefan Problem*. Elsevier.

[32] D. W. Hahn and M. N. Ozisik (2012). *Heat conduction*. John Wiley & Sons, Inc.

[33] W. E. Haupin (2016). *Principles of Aluminum Electrolysis*. Springer International Publishing.

[34] R. Haverkamp and B. Welch (1998). *Modelling the dissolution of alumina powder in cryolite*, Chemical Engineering and Processing: Process Intensification 37 (2):177–187.

[35] M. A. Herrero and J. J. L. Velázquez (1997). *On the Melting of Ice Balls*, SIAM Journal on Mathematical Analysis 28 (1):1–32.

[36] E. J. Hinch and B. S. Bhatt (1990). *Stability of an acid front moving through porous rock*, Journal of Fluid Mechanics 212:279.

[37] T. Hofer (2011). *Numerical Simulation and Optimization of the Alumina Distribution in an Aluminium Electrolysis Pot*. PhD thesis. École polytechnique fédérale de Lausanne.

[38] S. D. Howison (2005). *Practical Applied Mathematics*. Cambridge University Press.

[39] H. E. Huppert (1989). *Phase changes following the initiation of a hot turbulent flow over a cold solid surface*, Journal of Fluid Mechanics 198:293–319.

[40] H. E. Huppert (1990). *The fluid mechanics of solidification*, Journal of Fluid Mechanics 212:209–240.

[41] Hydro Aluminium (2019). *Internal Communications*.

[42] S. W. Jessen (2008). *Mathematical Modeling of a Hall Héroult Aluminum Reduction Cell*. MSc. thesis. Technical University of Denmark.

[43] Q. Kang, L. Chen, A. J. Valocchi, and H. S. Viswanathan (2014). *Pore-scale study of dissolution-induced changes in permeability and porosity of porous media*, Journal of Hydrology 517:1049–1055.

[44] C. Kaszás, L. Kiss, S. Poncsák, S. Guérard, and J.-F. Bilodeau (2017). *Spreading of Alumina and Raft Formation on the Surface of Cryolitic Bath*, Light Metals. The Minerals, Metals & Materials Series:473–478.

[45] C. Kaszás, L. I. Kiss, S. Guérard, and J.-F. Bilodeau (2015). *Behavior of Powders on the Surface of a Liquid*, Light Metals:637–642.

[46] C. Kaszás, L. I. Kiss, S. Poncsák, and J.-F. Bilodeau (2016). *Flotation and Infiltration of Artificial Alumina Rafts on the Surface of Molten Cryolite*, in *The International Committee for Study of Bauxite, Alumina & Aluminium*, p. 1–9.

[47] M. Kaviany (1995). *Principles of Heat Transfer in Porous Media*. September. Springer New York.

[48] L. V. Kim (1990). *Determination of heat-transfer coefficients in porous media*, Journal of Engineering Physics 59 (5):1423–1426.

[49] J. F. King (2001). *The aluminium industry*. Woodhead Publishing Limited.

[50] A. Kovács, C. Breward, K. Einarsrud, S. Halvorsen, E. Nordgård-Hansen, E. Manger, A. Münch, and J. Oliver (2020). *A heat and mass transfer problem for the dissolution of an alumina particle in a cryolite bath*, International Journal of Heat and Mass Transfer 162:120232.

[51] P. Lavoie, M. P. Taylor, and J. B. Metson (2016). *A Review of Alumina Feeding and Dissolution Factors in Aluminum Reduction Cells*, Metallurgical and Materials Transactions B 47 (4):2690–2696.

[52] P. Levresse, I. Manas-Zloczower, D. L. Feke, Y. Bomal, and D. Bortzmeyer (1999). *Observation and analysis of the infiltration of liquid polymers into calcium carbonate agglomerates*, Powder Technology 106 (1-2):62–70.

[53] Y. Li, L. Gong, M. Xu, and Y. Joshi (2020). *Enhancing the performance of aluminum foam heat sinks through integrated pin fins*, International Journal of Heat and Mass Transfer 151:119376.

[54] B. Lindman, G. Karlström, and L. Stigsson (2010). *On the mechanism of dissolution of cellulose*, Journal of Molecular Liquids 156 (1):76–81.

[55] A. López-Ortega, J. L. Arana, E. Rodríguez, and R. Bayón (2018). *Corrosion, wear and tribocorrosion performance of a thermally sprayed aluminum coating modified by plasma electrolytic oxidation technique for offshore submerged components protection*, Corrosion Science 143:258–280.

[56] R. N. Lumley (2010). *Fundamentals of aluminium metallurgy: Production, processing and applications*. Woodhead Publishing Limited.

[57] D. Markl and J. A. Zeitler (2017). *A Review of Disintegration Mechanisms and Measurement Techniques*, Pharmaceutical Research 34 (5):890–917.

[58] S. W. McCue, J. R. King, and D. S. Riley (2003). *Extinction behaviour for two-dimensional inward-solidification problems*, Proceedings of the Royal Society A: Mathematical, Physical and Engineering Sciences 459 (2032):977–999.

[59] S. W. McCue, B. Wu, and J. M. Hill (2008). *Classical two-phase Stefan problem for spheres*, Proceedings of the Royal Society A: Mathematical, Physical and Engineering Sciences 464 (2096):2055–2076.

[60] G. J. McIntosh, G. E. K. Agbenyegah, M. M. Hyland, and J. B. Metson (2015). *Adsorptive capacity and evolution of the pore structure of alumina on reaction with gaseous hydrogen fluoride*, Langmuir 31 (19):5387–5397.

[61] C. R. Meyer and I. J. Hewitt (2017). *A continuum model for meltwater flow through compacting snow*, The Cryosphere Discussions 11 (6):1–24.

[62] W. S. Miller, L. Zhuang, J. Bottema, A. J. Wittebrood, P. De Smet, A. Haszler, and A. Vieregge (2000). *Recent development in aluminium alloys for the automotive industry*, Materials Science and Engineering A 280 (1):37–49.

[63] A. Mortensen, L. J. Masur, J. A. Cornie, and M. C. Flemings (1989). *Infiltration of fibrous preforms by a pure metal: Part I. Theory*, Metallurgical Transactions A 20 (11):2535–2547.

[64] A. Mortensen and V. J. Michaud (1990). *Infiltration of fiber preforms by a binary alloy: Part I. Theory*, Metallurgical transactions. A, Physical metallurgy and materials science 21 A (7):2059–2072.

[65] K. Mosthaf (2013). *Modeling and Analysis of Coupled Porous-Medium and Free Flow with Application to Evaporation Processes*. PhD thesis. University of Stuttgart.

[66] N. Moussa, D. Gobin, H. Duval, and B. Goyeau (2017a). *Infiltration of a porous matrix by a solidifying liquid metal: A local model*, International Journal of Thermal Sciences 120:481–490.

[67] N. Moussa, B. Goyeau, H. Duval, and D. Gobin (2017b). *Macroscopic model for solidification in porous media*, International Journal of Heat and Mass Transfer 113:704–715.

[68] M. Muskat and H. G. Botset (1931). *Flow of gas through porous materials*, Journal of Applied Physics 1 (1):27–47.

[69] M. Muskat (1934). *The flow of compressible fluids through porous media and some problems in heat conduction*, Journal of Applied Physics 5 (3):71–94.

[70] M. Muskat (1937). *The Flow of Fluids Through Porous Media*, Journal of Applied Physics 8 (4):274–282.

[71] T. G. Myers, J. P. F. Charpin, and S. J. Chapman (2002). *The flow and solidification of a thin fluid film on an arbitrary three-dimensional surface*, Physics of Fluids 14 (8):2788–2803.

[72] P. N. Østbø (2002). *Evolution of Alpha Phase Alumina in Agglomerates upon Addition to Cryolitic Melts*. PhD thesis. Norwegian University of Science and Technology.

[73] R. I. Pedroso and G. A. Domoto (1973). *Perturbation Solutions for Spherical Solidification of Saturated Liquids*, Journal of Heat Transfer 95 (1):42.

[74] H. H. Ramaiah (2013). *Homogenization of complex flows in porous media and applications*:209.

[75] D. S. Riley, F. T. Smith, and G. Poots (1974). *The inward solidification of spheres and circular cylinders*, International Journal of Heat and Mass Transfer 17 (12):1507–1516.

[76] D. R. Sadoway (2001). *Inert anodes for the Hall-Héroult cell: The ultimate materials challenge*, JOM 53 (5):34–35.

[77] L. Samain, A. Jaworski, M. Edén, D. M. Ladd, D. K. Seo, F. Javier Garcia-Garcia, and U. Häussermann (2014). *Structural analysis of highly porous γ-Al2O3*, Journal of Solid State Chemistry 217:1–8.

[78] L. E. Scriven (1959). *On the dynamics of phase growth*, Chemical Engineering Science 10 (1-2):1–13.

[79] J. A. Sherratt (2010). *On the form of smooth-front travelling waves in a reaction-diffusion equation with degenerate nonlinear diffusion*, Mathematical Modelling of Natural Phenomena 5 (5):64–79.

[80] J. Siepmann and F. Siepmann (2013). *Mathematical modeling of drug dissolution*, International Journal of Pharmaceutics 453 (1):12–24.

[81] K. Smith, P. Watson, and T. H. Topper (1970). *Stress-strain function for the fatigue of metals*, Journal of Materials 5 (4):767–778.

[82] A. Solheim (2009). *Aluminium Electrolysis: Main Principles and Technology*. SINTEF.

[83] A. Solheim, H. Gudbrandsen, N.-H. Giskeødegård, S. Kolås, E. Manger, and N. J. Holt (2017). *Thermal Radiation towards the Sideledge in Alumina Reduction Cells*, in *The International Committee for Study of Bauxite, Alumina & Aluminium*.

[84] A. M. Soward (1980). *A Unified Approach to Stefan's Problem for Spheres and Cylinders*, Proceedings of the Royal Society A: Mathematical, Physical and Engineering Sciences 373 (1752):131–147.

[85] M. Stefanoni, U. M. Angst, and B. Elsener (2019). *Kinetics of electrochemical dissolution of metals in porous media*, Nature Materials 18 (9):942–947.

[86] K. Stewartson and R. T. Waechter (1976). *On Stefan's Problem for Spheres*, Proceedings of the Royal Society A: Mathematical, Physical and Engineering Sciences 348 (1655):415–426.

[87] L. Su, H. Liu, G. Yao, and J. Zhang (2019). *Experimental study on the closed-cell aluminum foam shock absorption layer of a high-speed railway tunnel*, Soil Dynamics and Earthquake Engineering 119:331–345.

[88] P. Szymczak and A. J. C. Ladd (2012). *Reactive-infiltration instabilities in rocks. Fracture dissolution*, Journal of Fluid Mechanics 702:239–264.

[89] M. Taroni, C. J. W. Breward, L. J. Cummings, and I. M. Griffiths (2013). *Asymptotic solutions of glass temperature profiles during steady optical fibre drawing*, Journal of Engineering Mathematics 80:1–20.

[90] J. Thonstad, F. Nordmo, and J. B. Paulsen (1972). *Dissolution of alumina in molten cryolite*, Metallurgical and Materials Transactions B 3 (2):407–412.

[91] J. Thonstad, A. Solheim, S. Rolseth, and O. Skar (1988). *The Dissolution of Alumina in Cryolite Melts*, Light Metals:105–111.

[92] F. Tisseur and K. Meerbergen (2006). *The quadratic eigenvalue problem Problem*, Society for Industrial and Applied Mathematics 43:235–286.

[93] G. G. Tsypkin (2003). *Mathematical model of salt precipitation due to groundwater evaporation*, Doklady Physics 48 (4):198–201.

[94] G. G. Tsypkin (2005). *Two-Valued Solutions in the Problem of Salt Precipitation during Groundwater Evaporation*, Fluid Dynamics 40 (4):593–599.

[95] G. G. Tsypkin and A. W. Woods (2004). *Vapour extraction from a water-saturated geothermal reservoir*, Journal of Fluid Mechanics 506:315–330.

[96] G. G. Tsypkin and A. W. Woods (2005). *Precipitate formation in a porous rock through evaporation of saline water*, Journal of Fluid Mechanics 537:35.

[97] D. Vella (2015). *Floating Versus Sinking*, Annual Review of Fluid Mechanics 47:115–135.

[98] D. Vella and H. E. Huppert (2007). *The waterlogging of floating objects*, Journal of Fluid Mechanics 585:245–254.

[99] V. R. Voller, J. B. Swenson, and C. Paola (2004). *An analytical solution for a Stefan problem with variable latent heat*, International Journal of Heat and Mass Transfer 47 (24):5387–5390.

[100] D. I. Walker (1993). *Alumina in Aluminum Smelting and its behaviour after addition to cryolite-based electrolytes*. PhD thesis. University of Toronto.

[101] J. I. Wang and W. D. Oliver (2019). *An aluminium superinductor*, Nature Materials 18 (8):775–776.

[102] E. W. Washburn (1921). *The Dynamics of Capillary Flow*, Physical Review 17 (3):273–283.

[103] B. J. Welch and G. I. Kuschel (2007). *Crust and alumina powder dissolution in aluminum smelting electrolytes*, JOM 59 (5):50–54.

[104] A. J. Wells, J. R. Hitchen, and J. R. G. Parkinson (2019). *Mushy-layer growth and convection, with application to sea ice*, Philosophical Transactions of the Royal Society A: Mathematical, Physical and Engineering Sciences 377 (2146):20180165.

[105] M. G. Worster (1992). *The Dynamics of Mushy Layers*, in *Interactive Dynamics of Convection and Solidification*. Springer Netherlands, p. 113–138.

[106] M. G. Worster (1997). *Convection in mushy layers*, Annual Review of Fluid Mechanics 29 (1):91–122.

[107] H. Yamada, I. Manas-Zloczower, and D. L. Feke (1998). *Observation and analysis of the infiltration of polymer liquids into carbon black agglomerates*, Chemical Engineering Science 53 (11):1963–1972.

[108] Y. Yang, B. Gao, Z. Wang, Z. Shi, and X. Hu (2015). *Study on the Dissolution of Alumina in Cryolite Electrolyte Using the See-Through Cell*, Light Metals.

[109] H. Zhang, S. Yang, H. Zhang, J. Li, and Y. Xu (2014). *Numerical simulation of alumina-mixing process with a multicomponent flow model coupled with electromagnetic forces in aluminum reduction cells*, Jom 66 (7):1210–1217.

[110] Q. Zhang, M. P. Taylor, and J. J. Chen (2015). *Computational Modeling of Thermochemical Evolution of Aluminum Smelter Crust*, Metallurgical and Materials Transactions B: Process Metallurgy and Materials Processing Science 46 (3):1520–1534.

[111] C. B. Zhao, B. Hobbs, and A. Ord (2020). *Transient-state instability analysis of dissolution-timescale reactive infiltration in fluid-saturated porous rocks: Purely mathematical approach*, Science China Technological Sciences 63 (2):319–328.

[112] C. Zhao, B. Hobbs, and A. Ord (2019). *A unified theory for sharp dissolution front propagation in chemical dissolution of fluid-saturated porous rocks*, Science China Technological Sciences 62 (1):163–174.

[113] C. Zhao, T. Poulet, K. Regenauer-Lieb, and B. E. Hobbs (2013). *Computational modeling of moving interfaces between fluid and porous medium domains*, Computational Geosciences 17 (1):151–166.

[114] Y. Zhou, Y.-j. J. Wang, and W.-k. K. Bu (2014). *Exact solution for a Stefan problem with latent heat a power function of position*, International Journal of Heat and Mass Transfer 69:451–454.

[115] S. Zhu, Y. Wu, Q. Chen, Z. Yu, C. Wang, S. Jin, Y. Ding, and G. Wu (2006). *Dissolution of cellulose with ionic liquids and its application: A mini-review*, Green Chemistry 8 (4):325–327.